AD-775 225

STRUCTURE AND PROPERTY CONTROL THROUGH RAPID QUENCHING OF LIQUID METALS

N. J. Grant, et al

Massachusetts Institute of Technology

Prepared for:

Advanced Research Projects Agency

22 Jun 1973

DISTRIBUTED BY:

NTIS

National Technical Information Service
U. S. DEPARTMENT OF COMMERCE
5285 Port Royal Road, Springfield Va. 22151

DOCUMENT CONTROL DATA - R&D

(Security classification of title, body of abstract and indexing annotation must be entered when the overall report is classified)

ORIGINATING ACTIVITY (Corporate author) Massachusetts Institute of Technology Cambridge, Massachusetts 02139	2a. REPORT SECURITY CLASSIFICATION unclassified 2b. GROUP

REPORT TITLE

Structure and Property Control Through Rapid Quenching of Liquid Metals

DESCRIPTIVE NOTES (Type of report and inclusive dates)

AUTHOR(S) (Last name, first name, initial)

Grant, N.J.; Pelloux, Regis M.; Flemings, M.C.; Argon, A.S.

REPORT DATE June 22, 1973	7a. TOTAL NO. OF PAGES 411	7b. NO. OF REFS
CONTRACT OR GRANT NO. DAHC 70 C 0283 PROJECT NO. ARPA Order #1608 Program Code #0D10	9a. ORIGINATOR'S REPORT NUMBER(S)	
	9b. OTHER REPORT NO(S) (Any other numbers that may be assigned this report)	

AVAILABILITY/LIMITATION NOTICES

SUPPLEMENTARY NOTES	12. SPONSORING MILITARY ACTIVITY Advanced Research Projects Agency 1400 Wilson Blvd. Washington, D.C. 22209

ABSTRACT

This report summarizes the results and accomplishments of a three year research program investigating the processing of billets from rapidly quenched liquid metals.

Various powder metallurgy (P/M) and quench-casting techniques have been employed to generate extremely fine dendrite arm spacings and homogeneous structures. Iron, nickel and cobalt-base alloy powders, produced by steam atomization (coarse powders), argon atomization, vacuum atomization, and the rotating electrode process, have been consolidated into dense billets by hot isostatic pressing (HIP) and/or extrusion.

The hot working properties of P/M billets and quench-cast bars have been evaluated by high strain rate tests and creep (superplastic) testing. Two P/M superalloys, MAR-M-509 (cobalt-base) and IN-100 (nickel-base) after HIP and hot extrusion demonstrated excellent hot workability under high strain rate and creep forming conditions.

Detailed analyses of microstructures, heat treatments and mechanical properties are presented for all P/M alloys and compared to equivalent cast materials.

Reproduced by
NATIONAL TECHNICAL
INFORMATION SERVICE
U S Department of Commerce
Springfield VA 22151

DD FORM 1 JAN 64 1473

Security Classification

Rapid Quenching
Structure and Segregation Control
Powder Metallurgy

INSTRUCTIONS

1. ORIGINATING ACTIVITY: Enter the name and address of the contractor, subcontractor, grantee, Department of Defense activity or other organization *(corporate author)* issuing the report.

2a. REPORT SECURITY CLASSIFICATION: Enter the overall security classification of the report. Indicate whether "Restricted Data" is included. Marking is to be in accordance with appropriate security regulations.

2b. GROUP: Automatic downgrading is specified in DoD Directive 5200.10 and Armed Forces Industrial Manual. Enter the group number. Also, when applicable, show that optional markings have been used for Group 3 and Group 4 as authorized.

3. REPORT TITLE: Enter the complete report title in all capital letters. Titles in all cases should be unclassified. If a meaningful title cannot be selected without classification, show title classification in all capitals in parenthesis immediately following the title.

4. DESCRIPTIVE NOTES: If appropriate, enter the type of report, e.g., interim, progress, summary, annual, or final. Give the inclusive dates when a specific reporting period is covered.

5. AUTHOR(S): Enter the name(s) of author(s) as shown on or in the report. Enter last name, first name, middle initial. If military, show rank and branch of service. The name of the principal author is an absolute minimum requirement.

6. REPORT DATE: Enter the date of the report as day, month, year; or month, year. If more than one date appears on the report, use date of publication.

7a. TOTAL NUMBER OF PAGES: The total page count should follow normal pagination procedures, i.e., enter the number of pages containing information.

7b. NUMBER OF REFERENCES: Enter the total number of references cited in the report.

8a. CONTRACT OR GRANT NUMBER: If appropriate, enter the applicable number of the contract or grant under which the report was written.

8b, 8c, & 8d. PROJECT NUMBER: Enter the appropriate military department identification, such as project number, subproject number, system numbers, task number, etc.

9a. ORIGINATOR'S REPORT NUMBER(S): Enter the official report number by which the document will be identified and controlled by the originating activity. This number must be unique to this report.

9b. OTHER REPORT NUMBER(S): If the report has been assigned any other report numbers *(either by the originator or by the sponsor)*, also enter this number(s).

10. AVAILABILITY/LIMITATION NOTICES: Enter any limitations on further dissemination of the report, other than those imposed by security classification, using standard statements such as:

(1) "Qualified requesters may obtain copies of this report from DDC."

(2) "Foreign announcement and dissemination of this report by DDC is not authorized."

(3) "U. S. Government agencies may obtain copies of this report directly from DDC. Other qualified DDC users shall request through _____."

(4) "U. S. military agencies may obtain copies of this report directly from DDC. Other qualified users shall request through _____."

(5) "All distribution of this report is controlled. Qualified DDC users shall request through _____."

If the report has been furnished to the Office of Technical Services, Department of Commerce, for sale to the public, indicate this fact and enter the price, if known.

11. SUPPLEMENTARY NOTES: Use for additional explanatory notes.

12. SPONSORING MILITARY ACTIVITY: Enter the name of the departmental project office or laboratory sponsoring *(paying for)* the research and development. Include address.

13. ABSTRACT: Enter an abstract giving a brief and factual summary of the document indicative of the report, even though it may also appear elsewhere in the body of the technical report. If additional space is required, a continuation sheet shall be attached.

It is highly desirable that the abstract of classified reports be unclassified. Each paragraph of the abstract shall end with an indication of the military security classification of the information in the paragraph, represented as *(TS)*, *(S)*, *(C)*, or *(U)*.

There is no limitation on the length of the abstract. However, the suggested length is from 150 to 225 words.

14. KEY WORDS: Key words are technically meaningful terms or short phrases that characterize a report and may be used as index entries for cataloging the report. Key words must be selected so that no security classification is required. Identifiers, such as equipment model designation, trade name, military project code name, geographic location, may be used as key words but will be followed by an indication of technical context. The assignment of links, rules, and weights is optional.

GPO 886-551

Security Classification

Final Technical Report

STRUCTURE AND PROPERTY CONTROL THROUGH RAPID QUENCHING OF LIQUID METALS

Sponsored by

Advanced Research Projects Agency

Contract No.: ~~DACH17~~ 70 C 0283

DAHC-15

ARPA Order No.: 1608

Program Code No.: 0D10

Contractor:

Massachusetts Institute of Technology
Cambridge, Massachusetts 02139

Principal Investigator:

N. J. Grant
(617) 253-5638

and Industrial Materials Technology
Woburn, Massachusetts 01801
(617) 933-1124

DDC
RECEIVED
MAR 8 1974

Effective date of Contract: June 22, 1970
Contract Expiration Date: June 21, 1973

Total Amount of Contract: $470,300
ARPA Order No. 1608

The views and conclusions contained in this document are those of the authors and should not be interpreted as necessarily representing the official policies, either expressed or implied, of the Advanced Research Projects Agency or the U.S. Government.

DISTRIBUTION STATEMENT
Approved for public release;
distribution unlimited

TABLE OF CONTENTS

	Page Number
TASK I PROCESSING OF ALLOYS	
Hot Isostatic Pressing of Modern Alloys Powders	1
I. Introduction	1
II. Process Description	2
A. Powder Characterization	2
B. Canning	3
C. Equipment	5
D. Process Cycle	5
E. Compaction Mechanics	6
III. Applications	7
IV. Metallurgy	8
V. Conclusions	10
Tables	12
Figures	13
Canning Practice and Argon Contamination in Hot Isostatic Pressing	22
I. Introduction	22
II. Theory of Leaks	22
A. Flow Characteristics of Capillaries	22
B. Leak Rates Through Capillaries at 1 Atmosphere and 1000 Atmospheres for He and Ar	24
C. Total Argon Leakage Flow	25
D. Argon Contamination Levels in Compacts	25
E. Other Causes	25
F. Summary	29
III. Leak Detection	29
IV. Experimental	30

V. Conclusions 32

Tables 34

Figures 41

TASK II SOLIDIFICATION RESEARCH 46

PART I 48

I. Introduction 49

II. Experimental Procedure 51

A. Maraging 300 Alloy Cast at Different Cooling Rates 51
B. Atomization Processes 53

III. Results and Discussion 54

A. D.A.S. Versus Cooling Rate 54
B. Evaluation of Atomized Powders 55
C. Heat Flow During Atomization 57

IV. Conclusions 60

Appendix 62

Tables 65

Figures 66

PART II 74

I. Introduction 75

II. Apparatus and Procedure 76

III. Results and Discussion 78

A. Powder Formation 78
B. Structures of Atomized Powders 81
C. Extrusion Billets 82

IV. Conclusions 82

Table 85

Figures 86

PART III-Refining by Partial Solidification 95

TASKS III AND IV THERMOMECHANICAL TREATMENT, MICROSTRUCTURE AND MECHANICAL PROPERTIES 103

Liquid Metal Atomization for Hot Working Preforms 104

I. Introduction 105

II. Cooling Rates and Solidification Structures 105

III. Powder Cleanliness 107

IV. Powder Consolidation 108

V. Structure and Properties of Alloys Processed from Quenched Powders 109

A. Aluminum Alloys 109
B. IN-100 111
C. MAR-M-509 and a Hafnium Modification 112

VI. Discussion 114

Tables 117

Figures 120

Properties of IN-100 Processed by Powder Metallurgy 128

I. Introduction 128

II. Characterization of Metal Powders 133

III. Powder Consolidation 135

IV. Results and Discussion 137

V. Conclusions 145

Tables 149

Figures 153

Properties of Maraging Steel 300 Produced by Powder Metallurgy 170

I. Introduction 171

II. Materials 172

III. Experimental Procedures and Results 174

IV. Discussion 175

A. Tensile Properties 175
B. Fracture Toughness Properties 178
C. Fatigue Properties 179

V. Conclusions 180

Tables 182

Figures 189

Fracture Toughness and Fatigue Crack Growth Rates of IN-100 Processed by Powder Metallurgy 191

I. Introduction 191

II. Materials and Test Procedures 191

A. Materials 191
B. Processing 191
C. Microstructure 193
D. Mechanical Properties 193
E. Fracture Toughness (K_{IC}) Tests 194

III. Fatigue Crack Propagation (da/dn vs. ΔK) 195

IV. Conclusions 197

Tables 198

Figures 201

The Deformation of Hot Isostatically Pressed IN-100 at High Temperatures and High Strain Rates 213

I. Introduction 213

II. Materials and Powder Consolidation 214

III. Experimental Procedure 215

IV. Results and Discussion 217

A. Short Time Stress Rupture Behavior 217
B. High Temperature Fracture 219
C. Rupture Life Versus Deformation Rate 220
D. Ductility 221

V. Conclusions 223

Tables 226

Figures 235

Distribution of Plastic Strain and Triaxial Tensile Stress in Necked Steel and Copper Bars 251

I. Introduction 252

II. Bounds for the Stress and Strain Distribution in the Neck Region of a Bar 253

A. Non-Strain Hardening, Rigid Plastic Material 254
B. Linearly Hardening Material with Zero Yield Stress 256

III. Experiments on Neck Profiles 257

IV. Numerical Computation of the Stress and Strain Distribution in Necked Bars of Steel and Copper 260

A. Stress Strain Curves for Steel and Copper 260
B. Numerical Results for Stress and Strain Distributions in Smooth Bars and Bars with an Initial Necking Profile 261

V. Discussion 263

Appendix - Extension of the Bridgman Solution for Triaxial Stress Distribution Along the Axis of a Necked Bar 266

Tables 269

Figures 275

Cavity Formation from Inclusions in Ductile Fracture 287

I. Introduction 289

II. Criteria for Inclusion Separation 291

A. Assessment of Earlier Developments 291
B. Critical Stress Criteria Based on Continum Deformation 294
C. Critical Stress Criteria Based on Dislocation Models 300

III. Experiments 310

IV. Discussion 312

Appendix A.1 Interfacial Stresses Around Large Spherical Inclusions 316

Appendix A.2 Interacting Inclusions 318

Tables 320

Figures 322

Separation of Inclusions in Spheroidized 1045 Steel, Cu-0.6% Cr Alloy, and Maraging Steel in Plastic Straining 336

I. Introduction 337

II. Experimental Procedure 338

III. Experimental Results 342

A. Spheroidized 1045 Steel 342
B. Copper with Cu-Cr Inclusions 345
C. Unaged Maraging Steel 346
D. Spheroidized 1045 Steel at Elevated Temperature 348

IV. Discussion 350

Tables 358

Figures 361

LIST OF TABLES

Table Number		Page Number
TASK I		
Hot Isostatic Pressing of Modern Alloy Powders		
I	IN-100 Low Carbon Chemistry	12
Canning Practice and Argon Contamination in Hot Isostatic Pressing		
I	Capillary Leakage Flow Rates	34
II	Total Argon Leakage Flow	35
III	Argon Analysis	36
IV	HIP Container Design Study vs. Leakage and Argon Contamination	37
V	Expected Argon Contamination Level vs. Initial 1 Atmosphere He Leakage Rate for ≈27 Gram Compact (Net)	40
TASK II		
Part II		
I	List of Atomization Experiments	85
Part III		
I	Refining of an Aluminum Alloy by Gravity Draining of the Aluminum-Rich Liquid	100
TASKS III AND IV		
Liquid Metal Atomization for Hot Working Preforms		
I	Maximum Metastable Solubilities Observed at Cooling Rate of ≈ 10^6 °C/second	117
II	Al-Si Alloys Tested at 20°C	117
III	Structural Characteristics of 2024 Alloy	117
IV	Room Temperature Properties of Al Alloy 2024-T4	118
V	Room Temperature Properties of IN-100	118
VI	Stress Rupture Data at 982°C for IN-100	118
VII	Room Temperature and 982°C Properties of MAR-M-509	119
VIII	Stress Rupture Properties at 982°C for MAR-M-509	119

Table Number		Page Number
	Properties of IN-100 Processed by Powder Metallurgy	
I	IN-100 Chemistries (w/o)	149
II	Size Range and Screen Analysis (% retained) of the Powders as Received from the Manufacturers	150
III	Etchants	151
IV	IN-100 Room Temperature Properties	152
	Properties of Maraging Steel 300 Produced by Powder Metallurgy	
I	Chemical Composition of the Maraging Steels 300 Used in This Work	182
II	Processing Variables of the Materials	183
III	Tensile Properties of 300 Grade Maraging Steels	184
IVa	Fracture Toughness Measurements of 300 Grade Maraging Steels - Crack Parallel to the R.D.	185
IVb	Fracture Toughness Measurements of 300 Grade Maraging Steels - Crack Perpendicular to R.D.	186
V	Life (number of cycles to failure X1000) of Fatigue Specimens Tested in Tension-Compression at the Stress Amplitude Levels Indicated	187
	Fracture Toughness and Fatigue Crack Growth Rates of IN-100 Processed by Powder Metallurgy	
I	Chemical Composition of IN-100	198
II	Gas Analysis in ppm by Weight	199
III	HIP (pressure-temperature-time) Processing Parameters	199
IV	Heat Treatment for IN-100	200
V	Mechanical Properties of IN-100	200
VI	Fracture Toughness Properties of IN-100	200
	The Deformation of Hot Isostatically Pressed IN-100 at High Temperatures and High Strain Rates	
I	IN-100 Composition	226
II	Size Range and Screen Analysis	227
III	Results of 1800°F (982°C) Testing	228
IV	Results of 1900°F (1038°C) Testing	230
V	Results of 2000°F (1093°C) Testing	232
VI	Comparison of Rupture Strength Superiority with HIP Time	234
	Distribution of Plastic Strain and Triaxial Tensile Stress in Necked Steel and Copper Bars	
I	Equivalent Plastic Strain and Triaxial Tensile Stress Distribution in a 1045 Steel Bar	269
II	Equivalent Plastic Strain and Triaxial Tensile Stress Distribution in a 1045 Steel Bar	270
III	Equivalent Plastic Strain and Triaxial Tensile Stress Distribution in a 1045 Steel Bar	271

Table Number		Page Number
IV	Equivalent Plastic Strain and Triaxial Tensile Stress Distribution in a Cu-0.6% Cr Bar	272
V	Equivalent Plastic Strain and Triaxial Tensile Stress Distribution in a Cu-0.6% Cr Bar	273
VI	Equivalent Plastic Strain and Triaxial Tensile Stress Distribution in a Cu-0.6% Cr Bar	274
	Cavity Formation from Inclusions in Ductile Fracture	
Ia	Normalized Radial Stresses σ_{rr}/k Around the Inclusion, Measured from a Point Under the Tensile Direction	320
Ib	Normalized Tangential Stresses $\sigma_{\theta\theta}/k$ Around the Inclusion, Measured from a Point Under the Tensile Direction	320
Ic	Magnitude of Normalized Tangential Shear Strain $\gamma_{r\theta}/(k/G)$ Around the Inclusion, Measured from a Point Under the Tensile Direction	321
	Separation of Inclusions in Spheroidized 1045 Steel, Cu-0.6% Cr Alloy, and Maraging Steel in Plastic Straining	
I	Spheroidized 1045 Steel, Stress for Separation of Fe_3C Inclusions	358
II	Cu-0.6% Cr, Stress for Separation of Cu-Cr Inclusions	359
III	Unaged Maraging (VM300) Steel, Stress for Separation of TiC Inclusions	360

LIST OF FIGURES

Figure Number		Page Number
TASK I		
Hot Isostatic Pressing of Modern Alloys Powders		
1	IN-100/low carbon steel interdiffusion zone.	13
2	IN-100 LC forging billet compact, 8"ϕ X 4" high	13
3	Heating and cooling of HIP furnace and load, schematic.	14
4	Process cycles, schematic.	15
5	Pressure "Activation" of sintering.	16
6	Test bar compact, 3/4"ϕ X 11" long.	17
7	Extrusion billet compact, 3-3/4"ϕ X 9-1/2" long.	17
8	Sheet bar compact, 2" X 4-1/2" X 12".	17
9	IN-100 LC press forged HIP billets. Top: HIP'ed at 2150°F, 15 ksi, 5 hrs., middle: HIP'ed at 2200°F, 15 ksi, 5 hrs., bottom: HIP'ed at 2250°F, 15 ksi, 5 hrs. Chemistry, see Table I.	18
10	IN-100 LC, REP powder. -35 mesh. Left: HIP'ed at 2000°F, 29 ksi, 2 hrs. As pressed, etched. Center: 2 hrs. at 2275°F, A.C., etched. Right: 5 hrs. at 2275°F, A.C., etched.	18
11	IN-100 LC REP powder, -60 mesh. Left: HIP'ed at 2250°F, 15 ksi, 5 hrs. plus press forge. Right: HIP'ed at 2200°F, 15 ksi, 5 hrs. plus press forge.	18
12	HIP process cycle, Type II, low pressure heat up. (Plot of actual data)	19
13	HIP process cycle, Type III, high pressure heat up. (Plot of actual data)	20
14	IN-100 LC REP powder, -60 mesh. Left: Type II cycle, Figure 12. Right: Type III cycle, Figure 13. Etched. Chemistry, see Table I.	21

Figure Number		Page Number
15	Same as Figure 14. Note coarse γ', Type II cycle, finer γ', Type III cycle.	21
	Canning Practice and Argon Contamination in Hot Isostatic Pressing	
1	Idealized capillary leak.	41
2	Argon contamination levels versus total leakage flow for various compact sizes.	42
3	Argon penetration in solid metal at 2100°F, 15,000 psi, 5 hours.	43
4	Test Can Designs	44
5	HIP'ed compacts after machining argon analysis samples.	45
TASK II		
Part I		
1	Sketch of levitation melting and casting apparatus.	66
2	Variation of microstructure with cooling rate for Maraging 300 alloy. (a) gas quench, (b) liquid quench, (c) chill cast. Magnification 200X.	67
3	Secondary dendrite arm spacing versus cooling rate in Maraging 300 steel alloy.	68
4	Spin atomized powders of Maraging 300 steel alloy; (a) and (b) are SEM micrograph views at 19X and 240X, respectively, (c) is a photomicrograph of a polished and etched cross-section at 200X.	69
5	SEM micrograph views of atomized powder particles of IN-100 alloy; (a) and (b) show spin atomized powders at 56X and 215X, respectively. (c) and (d) show vacuum atomized powders at 57X and 22.5X, respectively, (e) and (f) show inert gas atomized fine powders at 210X and 1050X, respectively.	70
6	Secondary dendrite arm spacing versus powder particle diameter of Maraging 300 steel alloy obtained by different atomization processes.	71
7	Calculated radial fraction liquid and volume fraction solid versus free fall time and distance for different size powder particles of Maraging 300 steel alloy.	72

Figure Number		Page Number
8	Photomicrographs showing examples of duplex dendritic structures obtained in atomized powders; (a) steam atomized coarse powder of Maraging 300 steel alloy at 75X, (b) spin atomized powder of IN-100 alloy at 200X.	73
Part II		
1	Schematic of atomization apparatus used in this study.	86
2	SEM view of pure aluminum powders emerging from a sintered Al_2O_3 filter, Run #1, (a) 23X, (b) 208X.	87
3	SEM view of pure aluminum powders emerging from a sintered Al_2O_3 filter; (a) and (b) are from Run #15 at 20X and 90X, respectively, (c) is from Run #16 at 75X.	88
4	Size distributions of spherical 7075 aluminum alloy powders made utilizing Al_2O_3 filters; (a) Run #9, T_F = 700°C, (b) Run #14, T_F = 742°C.	89
5	Photomicrograph showing filtration of aluminum oxide from a 7075 aluminum alloy melt.	90
6	Structures of atomized pure aluminum powders made in Run #1; (a) and (b) are SEM views of different size powders at 50X, (c) is a representative microstructure of the powders.	91
7	Surface irregularities of atomized pure aluminum powders; (a) Run #1, 590X, (b) Run #15, 500X, (c) Run #16, 590X.	92
8	Atomized powder of 7075 aluminum alloy from Run #14; (a) and (b) are SEM views at 110X and 200X, respectively, (c) is a photomicrograph of a polished and etched cross-section at 100X.	93
9	Microstructure of 7075-T6 extrusion made from atomized spherical powders, 100X' (a) and (b) are transverse and longitudinal cross-sections, rbspectively.	94
Part III		
1	Schematic illustration of two Rheorefining processes. In both processes, partial solidification is accompanied by vigorous agitation. Separation of solid from liquid in the slurry is achieved by: (a) atomization, (b) preferential draining of the liquid.	101
2	Composition versus powder mesh size of Sn-15% Pb alloy Rheorefined by atomization at 0.4 fraction solid.	102

Figure Number		Page Number
TASKS III AND IV		
Liquid Metal Atomization for Hot Working Preforms		
1	Dendrite arm structure as a function of cooling rate for aluminum and aluminum alloys.	120
2	Polished and etched sections of IN-100 showing dendritic patterns (a) powder particle by rotating electrode process, 200X; (b) precision cast tensile bar, 100X.	121
3	Replica electron micrographs of as-HIP FM powder showing extensive carbide phase surrounding prior particle boundaries, 4000X.	122
4	High strain rate tests of IN-100 at 1150°C (2100°F). (a) HIP condition, (b) hot extruded condition, 200X.	123
5	As-extruded test bars superplastically deformed at 1038°C (1900°F) at strain rates from 0.5 to 0.01 min^{-1}. Bar at top is size of undeformed tensile specimen.	124
6	MAR-M-509 at 1178°C (2150°F) and 2000 atmospheres (28 ksi) for 2 hours. Tension test at 20°C. (a) cross section (b) longitudinal section at fracture.	124
7	Cobalt-1 atom percent HfC P/M alloy comparing (a) HIP + extruded structures with (b) same material re-HIP at 1260°C (2300°F) for 1 hour.	125
Properties of IN-100 Processed by Powder Metallurgy		
1	As-received FM powders as viewed in SEM: (a) 138X, (b) 680X.	153
2	As-received HM powders as viewed in SEM: (a) 24X, (b) 245X.	154
3	As-received NM powders as viewed in SEM: (a) 63X, (b) 253X.	155
4	Polished and etched section of as-received FM powders showing dendritic structure. 500X.	156
5	Polished and etched section of as-received HM powders showing dendritic structure. 50X.	156
6	Polished and etched section of as-received NM powders showing dendritic structure. 200X.	157

Figure Number		Page Number
7	Polished and etched cross-section of as-cast tensile bar showing dendritic structure. 100X.	157
8	As-cast IN-100 microstructure. 1000X	158
9	As-HIP FM powder. 100X.	158
10	Replica electron micrographs of as-HIP FM powder showing extensive carbide phase surrounding prior particle boundaries. (a) 4000X, (b) 5000X.	159
11	Longitudinal section of as-extruded FM powder. 200X.	160
12	Longitudinal section of as-extruded NM powder. 200X.	160
13	Grain-coarsened NM powder extrusion. 24 hours at 2270°F. 500X.	161
14	High strain rate log stress vs. log rupture time at various temperatures for as-extruded IN-100.	162
15	High strain rate log stress vs. log deformation rate at various temperatures for as-extruded IN-100.	163
16	High strain rate effect of deformation rate on elongation at various temperatures for as-extruded IN-100.	164
17	High strain rate fracture cross-section of HIP FM powder test bar at 2100°F. Polished. 200X.	165
18	High strain rate fracture cross-section of extruded NM powder test bar pulled at 1100°F. Polished and etched. 200X.	165
19	As-extruded test bars superplastically deformed at 1900°F at strain rates from 0.5 min^{-1} to 0.01 min^{-1}. Bar at top is size of undeformed tensile specimen.	166
20	Superplastic deformation of as-extruded IN-100 at various temperatures plotted as log true flow stress vs. log strain rate.	167
21	Microstructure of superplastically deformed as-extruded material pulled at 1900°F. 1000X.	168
22	1800°F stress-rupture properties for various grain sizes of cast IN-100 and extruded IN-100 powders.	169

Figure Number		Page Number
	Properties of Maraging Steel 300 Produced by Powder Metallurgy	
1	Fracture surface of fracture toughness specimens. From left to right: Vascomax 300, fracture plane parallel to the rolling direction, HR69 fracture plane parallel and perpendicular to the rolling direction, respectively. Specimen thickness 1.27 cm (0.5 inch).	188
2	Fracture surface of fracture toughness specimens. From left to right: Vascomax 300 fracture plane perpendicular to the rolling direction HR83 fracture plane parallel and perpendicular to the rolling direction, respectively. Specimen thickness .625 cm (0.25 inch).	188
3	Fracture surface of fracture toughness specimens. From left to right: HR91, VM82 and VM82A, fracture plane parallel to the rolling direction in each specimen. Specimen thickness .635 cm (.25 inch).	189
4	S-N curves of Vascomax 300 and of a powder metallurgy product produced by hot isostatic pressing and extrusion.	190
	Fracture Toughness and Fatigue Crack Growth Rates of IN-100 Processed by Powder Metallurgy	
1	Microstructure of as-received cast IN-100 (40X).	201
2	Microstructure of heat treated cast IN-100 (40X).	201
3	Microstructure of as-received cast plus HIP IN-100 (40X).	202
4	Microstructure of heat treated cast plus HIP IN-100 (40X).	202
5	Overall view of typical IN-100 powder processed by REP technique (500X).	203
6	Microstructure of typical IN-100 powder processed by REP technique (1000X).	203
7	IN-100 billet processed by powder metallurgy and HIP and forged.	204
8	Microstructure of as-received P/M plus HIP and forged IN-100 (40X).	204
9	Microstructure of as-received P/M plus HIP and forged IN-100 (200X).	205

Figure Number		Page Number
10	Pores in P/M plus HIP and forged IN-100 (200X).	205
11	Microstructure of heat treated P.M plus HIP and forged IN-100 (400X).	206
12	Microstructure of heat treated P/M plus HIP and forged IN-100 (1000X).	206
13	Compact-tension specimen used for fracture toughness testing.	207
14	Orientation of fracture toughness and fatigue specimens in forged P/M billet of IN-100.	208
15	Fracture surface of cast IN-100 (630X).	209
16	Fracture surface of cast plus HIP IN-100 (600X).	209
17	Single-edge-crack specimen used for fatigue crack propagation testing.	210
18	Fatigue crack propagation in P/M, cast and cast plus HIP IN-100 at room temperature and 1400°F.	211
19	Branching of the fatigue crack in cast IN-100 (40X).	212

The Deformation of Hot Isostatically Pressed IN-100 at High Temperatures and High Strain Rates

1a	Typical REP IN-100 powder particle (500X).	235
1b	Dendrite structure in REP IN-100 powder (300X).	235
2a	Typical microstructure of IN-100 HIP at 2100°F (1170°C) for 2 hours at 15 ksi (103.4 N/mm^2). Designation: (3A68-2) (200X).	236
2b	Typical microstructure of IN-100 HIP at 2250°F (1250°C) for 5 hours at 15 ksi (103.4 N/mm^2). Designation: (2L43-1) (200X). Taken after testing.	236
3	Stress vs. deformation rate plot for IN-100 HIP at 2050°F (1140°C) for 2 and 5 hours.	237
4	Stress vs. deformation rate plot for IN-100 HIP at 2100°F (1170°C) for 2 and 5 hours.	237
5	Stress vs. deformation rate plot for IN-100 at 2150°F (1195°C) for 2 and 5 hours.	238

Figure Number		Page Number
6	Stress vs. deformation rate plot for IN-100 HIP at 2200°F (1220°C) for 2 and 5 hours.	238
7	Stress vs. deformation rate plot for IN-100 HIP at 2250°F (1250°C) for 2 and 5 hours.	239
8	Typical post-test photomicrograph of IN-100 HIP at 2250°F (1250°C) for 2 hours; designation (2L49-2); tested at 2000°F (1093°C); 106 ksi (73.1 N/mm^2). Deformation rate: 5.7 X 10^{-5} sec^{-1} (400X).	240
9	Typical post-test photomicrograph of IN-100 HIP at 2250°F (1250°C) for 2 hours; designation (2L43-2); tested at 1900°F (1038°C); 335 ksi (231 N/mm^2). Deformation rate: 3.1 X 10^{-4} sec^{-1}. (200X).	240
10	Typical post-test photomicrograph of IN-100 HIP at 2250°F (1250°C) for 5 hours; designation (2L46-1); tested at 1800°F (982°C); 248 ksi (170.9 N/mm^2). Deformation rate: 4.6 X 10^{-6} sec^{-1}. (200X).	241
11	Typical post-test photomicrograph of IN-100 HIP at 2200°F (1220°C) for 5 hours; designation (2L42-2); tested at 1900°F (1038°C); 148 ksi (111.8 N/mm^2). Deformation rate: 2.3 X 10^{-5} sec^{-1}. (200X).	241
12	Typical post-test photomicrograph of IN-100 HIP at 2150°F (1195°C) for 2 hours; designation (2K12-4); tested at 1900°F (1038°C); 189 ksi (130.3 N/mm^2). Deformation rate: 2.7 X 10^{-4} sec^{-1}. (200X).	242
13	Typical post-test photomicrograph of IN-100 HIP at 2050°F (1140°C) for 5 hours; designation (3A53-3); tested at 1900°F (1038°C); 232 ksi (160 N/mm^2). Deformation rate: 2.0 X 10^{-3} sec^{-1}. (200X).	242
14	Typical SEM fractograph of IN-100 HIP at 2200°F(1220°C) for 5 hours; designation (2L52-4); tested at 2000°F (1093°C); 80 ksi (55 N/mm^2). Deformation rate: 1.4 X 10^{-4} sec^{-1}. (130X).	243
15	Typical SEM fractograph of IN-100 HIP at 2150°F (1195°C) for 2 hours; designation (2K12-4); tested at 1900°F (1038°C); 189 ksi (130.3 N/mm^2). Deformation rate: 2.7 X 10^{-4} sec^{-1}. (119X).	243
16	Typical post-test photomicrograph of IN-100 HIP at 2150°F (1195°C) for 2 hours; designation (2K12-4); tested at 1900°F (1038°C); 189 ksi (130.3 N/mm^2). Deformation rate: 2.7 X 10^{-4} sec^{-1}. (1000X).	244

Figure Number		Page Number
17	Typical rupture time vs. deformation rate plot (Monkman-Grant) for material HIP at 2050°F (1140°C) for 2 and 5 hours. Tested at 1800°F (982°C).	244
18	Stress vs. elongation curve for IN-100 HIP at 2050°F (1140°C) tested at 1800°F (982°C).	245
19	Stress vs. elongation curve for IN-100 HIP at 2250°F (1250°C) tested at 1800°F (982°C).	245
20	Stress vs. elongation curve for IN-100 HIP at 2050°F (1140°C) tested at 1900°F (1038°C).	246
21	Stress vs. elongation curve for IN-100 HIP at 2250°F (1250°C) tested at 1900°F (1038°C).	246
22	Stress vs. elongation curve for IN-100 HIP at 2050°F (1140°C) tested at 2000°F (1093°C).	247
23	Stress vs. elongation curve for IN-100 HIP at 2250°F (1250°C) tested at 2000°F (1093°C).	247
24	Elongation vs. rupture time curve for IN-100 HIP at 2050°F (1140°C) tested at 1900°F (1038°C).	248
25	Elongation vs. rupture time curve for IN-100 HIP at 2100°F (1170°C) tested at 1900°F (1038°C).	248
26	Elongation vs. rupture time curve for IN-100 HIP at 2150°F (1195°C) tested at 1900°F (1038°C).	249
27	Elongation vs. rupture time curve for IN-100 HIP at 2200°F (1220°C) tested at 1900°F (1038°C).	249
28	Elongation vs. rupture time curve for IN-100 HIP at 2250°F (1250°C) tested at 1900°F (1038°C).	250

Distribution of Plastic Strain and Triaxial Tensile Stress in Necked Steel and Copper Bars

1	Changes of neck profile with deformation in a tension specimen.	275
2	Changes of shape of a grid inscribed on the surfaces of two specimens with initially machined natural neck profiles of $(a/R)_i = 0.5$.	276
3	True stress-true strain plot for two spheroidized 1045 steel specimens.	277

Figure Number		Page Number
4	True stress-true strain plot for two fully aged specimens of Cu-0.6% Cr.	278
5	Nodal points in finite element grids for bars with initially machined natural neck profiles, a) $(a/R)_i$ = 0.5, b) $(a/R)_i$ = 1.0.	279
6	Distribution of equivalent plastic strain (a), and triaxial tensile stress (b) for 1045 steel bar with $(a/R)_i = 0$, $(a/R)_f = 0.95$, $\varepsilon_y = 0.0072$, $n = 8$.	280
7	Distribution of equivalent plastic strain (a), and triaxial tensile stress (b) for 1045 steel bar with $(a/R)_i = 0.5$, $(a/R)_f = 1.65$, $\varepsilon_y = 0.0094$, $n = 4$.	281
8	Distribution of equivalent plastic strain (a), and triaxial tensile stress (b) for 1045 steel bar with $(a/R)_i = 1.0$, $(a/R)_f = 2.4$, $\varepsilon_y = 0.0094$, $n = 4$.	282
9	Distribution of equivalent plastic strain (a), and triaxial tensile stress (b) for Cu-0.6% Cr bar with $(a/R)_i = 0$, $(a/R)_f = 0.95$, $\varepsilon_y = 0.00$, $n = 3$.	283
10	Distribution of equivalent plastic strain (a), and triaxial tensile stress (b) for Cu-0.6% Cr bar with $(a/R)_i = 0.5$, $(a/R)_f = 2.75$, $\varepsilon_y = 0.00416$, $n = 2.5$.	284
11	Distribution of equivalent plastic strain (a), and triaxial tensile stress (b) for Cu-0.6% Cr bar with $(a/R)_i = 1.0$, $(a/R)_f = 3.82$, $\varepsilon_y = 0.00416$, $n = 2.5$.	285
12	Distribution of triaxial tensile stress, σ_T, flow stress, Y, and triaxiality, σ_T/Y, in: (a) Steel with $(a/R)_i = 0$, at $a/a_i = 0.75$; (b) Steel with $(a/R)_i = 0.5$, at $a/a_i = 0.60$; (c) Steel with $(a/R)_i = 1.0$, at $a/a_i = 0.60$; (d) Cu-0.6% Cr with $(a/R)_i = 0$, at $a/a_i = 0.45$; (e) Cu-0.6% Cr with $(a/R)_i = 0.5$, at $a/a_i = 0.50$; (f) Cu-0.6% Cr with $(a/R)_i = 1.0$, at $a/a_i = 0.50$.	286

Cavity Formation from Inclusions in Ductile Fracture

1	Idealization of actual plastic behavior by two limiting forms on non-hardening rigid plastic, and linear behavior.	322
2	One quadrant of grid for finite element solution of initiation of plastic flow in pure shear around a rigid cylinder.	323

Figure Number		Page Number
3	Spreading of the plastic region (shaded) with increasing boundary displacements for elastic, non-hardening plastic idealization: (a) $u_1 = u_0$ where plastic flow is just initiated, (b) $u_1 = 1.1\ u_0$, (c) $u_1 = 1.2\ u_0$, (d) $u_1 = 1.3\ u_0$, (e) $u_1 = 1.4\ u_0$, (f) $u_1 = 1.5\ u_0$.	324
4	Change of maximum interfacial tensile stress with increasing boundary strain in non-hardening material.	325
5	Distribution of interfacial tensile stress and shear strain around a rigid particle in an incompressible linear matrix.	326
6	The distribution of principal total strain ε_{xx} parallel to the tension direction for the elastic, non-hardening plastic material, the linear incompressible material, and experimental measurements on a model copper specimen with a hardened cylindrical Cu-Be "inclusion"	327
7	Ashby's model of the production of a secondary plastic zone to dissipate the elastic shear stresses arising from the interfacial displacement incompatibility upon plastic straining of the matrix.	328
8	(a) Idealization of the cylindrical plastic punching by a cylinder elastically or plastically extended in a rigid cavity against wall friction; (b) Plastic punching between two interacting particles.	329
9	Change of interfacial stress with increasing distant plastic strain for an elastic plug and a plastic, strain hardening plug.	330
10	Dependence of interfacial stress on local second phase particle concentration, (a) for copper, $n = 2.5$, (b) for 1045 steel, $n = 4$.	331
11	Probability $(1-P(c/\bar{c}))$ of finding a local second phase particle concentration in excess of c, when the overall average is $\bar{c}$.	333
12	The dependence of the critical strain ratio for particle interactions as a function of local second phase concentration for two hardening exponents.	334
13	Experimental arrangement for determining local plastic strains in a copper block with a hardened, cylindrical Cu-Be "inclusion".	335

Figure Number		Page Number
	Separation of Inclusions in Spheroidized 1045 Steel, Cu-0.6% Cr Alloy, and Maraging Steel in Plastic Straining	
1	Fe_3C inclusions in spheroidized 1045 steel (bar is 10μ).	361
2	Cu-Cr inclusions in a plastically strained sample of Cu-0.6% Cr alloy (bar is 10μ).	361
3	Stress-strain curve of unaged maraging VM300 steel.	362
4	Section of maraging steel showing fracture surface outline and large internal holes from which TiC inclusions have been removed in the course of polishing (bar is 50μ).	363
5	Cumulative density distribution of diameters of Fe_3C inclusions: upper curve, prior to straining; middle curve, separated inclusions underneath fracture surface; lower curve, separated inclusions, a distance $z = 0.32\ a_0$ away from fracture surface.	364
6	Cumulative distribution of net nearest neighbor distances between Fe_3C inclusions.	365
7	Frequency distribution of the ρ/λ_c ratio of Fe_3C.	366
8	(a) Fe_3C inclusions and holes on axial section of fractured specimen; (b) fracture surface dimples (bar is 5μ).	367
9	Density of separated Fe_3C inclusions, and fraction of inclusions separated along axes of spheroidized steel specimens: (a) $(a/R)_i = 0$; (b) $(a/R)_i = 0.5$; (c) $(a/R)_i = 1.0$.	368
10	Cumulative density distribution of diameters of Cu-Cr inclusions in Cu-0.6% Cr alloy: upper curve, prior to straining; lower curve separated inclusions underneath fracture surface.	371
11	Dimples on fracture surface of copper with Cu-Cr inclusions (bar is 10μ).	372
12	Density of separated Cu-Cr inclusions and fraction of inclusions separated along axes of Cu-0.6% Cr alloy: (a) $(a/R)_i = 0$; (b) $(a/R)_i = 0.5$; (c) $(a/R)_i = 1.0$.	373
13	Density of separated TiC inclusions, and fraction of inclusions separated along axes of maraging steel: (a) $(a/R)_i = 0.1$ and $(a/R)_i = 0.25$; (b) $(a/R)_i = 0.5$ and $(a/R)_i = 1.0$.	376

Figure Number		Page Figure
14	Dimples on fracture surface of maraging steel showing large dimples of TiC inclusions, and small dimples of Ni_3Mo inclusions (bar is 10μ).	378
15	Fe_3C inclusions and holes in specimen strained at 450°C (bar is 5μ).	379
16	Fe_3C inclusions and holes in specimen strained at 630°C (bar is 5μ).	379
17	Cumulative density distribution of effective diameters of Fe_3C inclusions in material strained at 450°C: upper curve, prior to straining; lower curve, separated inclusions underneath fracture surface.	380
18	Cumulative density distribution of effective diameters of Fe_3C inclusions in material strained at 630°C: upper curve, prior to straining; lower curve, separated inclusions underneath fracture surface.	381
19	Density of separated Fe_3C inclusions and fraction of inclusions separated along axes of 1045 steel specimens strained at 450°C and 630°C.	382
20	Dimples on fracture surface of Fe_3C-bearing 1045 steel, Fractured at 450°C (bar is 10μ).	383
21	Dimples on fracture surface of Fe_3C-bearing 1045 steel, fractured at 630°C (bar is 10μ).	383
22	Probability of finding a local concentration of second phase in excess of c in specimen with average concentration $\bar{c}$, as a function of $c/\bar{c}$. Circles are experimental, broken curve from theory of Argon, et.al. (10).	384
23	Construction for determination of the distribution of separated Fe_3C inclusions along the axis of a fractured specimen of spheroidized 1045 steel containing a large concentration of interacting inclusions.	385
24	Fraction of separated inclusions as a function of equivalent plastic strain: Dots determined from specimens 5 and 6 of 1045 steel, curve obtained from construction given in Figure 23.	386

TASK I

PROCESSING OF ALLOYS

P.E. Price
R. Widmer

Hot Isostatic Pressing of Modern Alloy Powders

I. INTRODUCTION

In modern metallurgy continued development of high performance materials, characterized most generally by extensive use of scarce and expensive components, has been limited in some areas by basic physical phenomena. An example of such a limitation is the tendency of highly alloyed compositions to undergo macro and micro segregation during solidification from the melt. The dimensional scale and "intensity" of such segregation tends to increase with decreased cooling rate of liquid metal, a condition which occurs generally with increasing casting size. In production of wrought products from cast ingots or bars, adverse effects on workability and the uniformity of structure and properties may result from solidification induced inhomogeneities in configurations surprisingly small.

Alloy improvements for "state-of-the-art" aircraft gas turbine engine discs are expected to employ increasing amounts of refractory metals such as tungsten, tantalum, columbium, molybdenum and hafnium in a nickel alloy base. Some developmental compositions are even now so heavily alloyed that the "cast and wrought" process route is "closed out". Further progress requires process routes employing prealloyed metal powders. The technical aspects of achieving compositional uniformity and structural refinement by use of prealloyed powder have been discussed.[1,2,3,4]

Prealloyed powder production achieves in effect sufficient reduction in dimensional scale of segregation of alloying elements in each powder particle that subsequent process steps produce "fully" homogeneous structures. Phase relationships are maintained during processing, however, and insoluble phases such as carbides may persist although "refined" in dimension. Full utilization of the properties of superalloy powder requires, however, the critical step of consolidation. In the present paper, the method of hot isostatic pressing of alloy powders will be discussed.

II. PROCESS DESCRIPTION

Hot isostatic pressing of prealloyed powders consists of consolidation by application of fluid pressure at elevated temperature. Configurations may include "net-shape", forging preforms, extrusion billets, hot rolling billets, test bar material, etc. In the case of net-shape production, careful dimensional control is required to achieve maximum economy in powder utilization. For forging billets, the same condition applies because subsequent forging practice requires consistent billet dimensions. Basic elements of the pressing include powder characterization, encapsulation, and process cycle.

A. Powder Characterization

Powder properties which affect subsequent processing include particle shape, size, size distribution, and chemistry. Workability and property response require close specification of these variables. Immediate specification of "packing density" of superalloy powder after being "tapped" or vibrated is required for design of encapsulation containers. Powder packing density is defined as the ratio of apparent density of "tapped" powder to density of "100% dense" material. Values of the latter are generally taken as those of cast or wrought material. Thus,

$$D = \frac{\rho'}{\rho}$$

where

D = packing density

ρ' = apparent density of tapped powder, grs/cc

ρ = density of 100% dense material, grs/cc

Since in hot isostatic pressing the "empty space" between powder particles is "squeezed out", the volume shrinkage per unit volume during HIP is given by

$$\frac{\Delta V}{V} = \frac{\rho - \rho'}{\rho} = 1 - \frac{\rho'}{\rho} = 1-D \qquad (1)$$

Linear dimensional shrinkage can be approximated to first order from the relationship for a unit volume

$$V = l^3 \qquad (2)$$

$$\frac{\Delta V}{V} = \frac{3\Delta l}{l} \tag{3}$$

and

$$\frac{\Delta l}{l} = \frac{1}{3}\frac{\Delta V}{V} = \frac{1-D}{3} \tag{4}$$

Thus, for a powder with D = 0.7, the linear shrinkage after full compaction is given by:

$$\frac{\Delta l}{l} \cong \frac{1-0.7}{3} \cong 0.1 \tag{5}$$

With such a powder, the starting dimension to produce a specific finish dimension is estimated as:

$$L_i = \frac{L_f}{1-\frac{\Delta l}{l}} = \frac{L_f}{0.9} \tag{6}$$

where

L_i = initial linear powder dimension

L_f = desired final compact dimensions

Allowances must be made for stock for forging and/or finish machining as well as removal of the interaction zone between the can and its compacted contents. Complications arise in maintaining geometry control if powder packing density is $<$.5-.6 due to flake and/or hollow particle morphology. Thin sections distort readily during compaction of low packing density powder.

B. Canning

In hot isostatic compaction of powder, the loose powder is encapsulated in a container which functions first as a vacuum container and then as a leak proof high temperature - high pressure plastic envelope. Factors which are critical in design and execution of such containers include:

1. Liquid phase formation. Can material must be selected to avoid liquid phase formation in the powder/can system at process temperature. For nickel base alloys, low carbon and stainless steel have been used. Iron does not lower the solidus temperature of IN-100 significantly, for example. Hot isostatic pressing has been

carried out within 30°F of the nominal incipient melting point of IN-100 with limited can/powder interaction, Figure 1. Some nickel base alloys may be processed slightly above their solidus temperatures. In these cases, phase relationships of the container/alloy system must be carefully considered. A more critical case is that of titanium alloy powders in low carbon steel cans. The Fe/Ti system shows a 1980°F binary eutectic. A safety margin of 150°F to allow for process temperature control and "other impurities" depressing the system solidus fixes maximum HIP process temperature at 1800°F in spite of the much higher melting points of the separate components.

2. Container material availability. Low carbon steel seamless tubing is the first choice because of the large selection of standard diameters and wall thicknesses available commercially. Seamless stainless tubing is available in standard but more limited sizes. Refractory metals and nickel base alloy "standard" tubing sizes are available in limited sizes, usually small.

3. Fabricability. If special circular symmetry shapes and sizes are required, spinning, hydroforming, rolling and welding must be able to be easily carried out. Low carbon steel "spinning" grade sheet in 14 and 16 gauge has been used to manufacture containers of this type for IN-100 forging preforms, Figure 2. Both the "can" and the "cover" were spun.

4. Weldability. Vacuum and pressure tightness of powder containers depend critically on the integrity of their weld joints. Welding techniques are well established for low carbon and stainless steels, and may be applied without extensive development. Meticulous attention to joint fit up and surface preparation is essential.

5. Leak detection. In fabrication of containers for powder compaction, it must be generally assumed that vacuum and/or pressure leaks, however small, are present in each and every can. Container design and fabrication must be planned to facilitate leak detection. The criticality of leakage in compaction technology is discussed in a separate paper.

C. Equipment

Boyer, Orcutt, and Conaway[5] have described the basic features of hot isostatic pressing equipment. A major aspect of process control which is critical for nickel base superalloys is measurement of "actual" temperature of the parts or billets being processed. HIP unit furnace winding control thermocouples for batch operation in an 8" ø furnace starting at room temperature lead the load by as much as several hundred ^{0}F and times of the order of 1-2 hours depending on load configuration, Figure 3. Because of transfer and capacity lags[6], workpiece temperatures must be measured by "closely thermally coupled" thermocouples. Where possible, temperatures at the load O.D. at the top and center at the bottom must be measured to prevent both overheating and underheating. Thermocouples must be maintained to the highest standards of calibration because convective flow in a HIP unit serves to effectively transport harmful thermocouple contaminants to the smallest and most remote locations.

D. Process Cycles

There are many possible hot isostatic process cycles which vary in the relationship of temperature and pressure application. Cycle variations include those shown schematically in Figure 4 and described as follows:

I. Pressurize by pumping cold to ~1/3 required process pressure. Isolate vessel and heat to process temperature. Pressure rises due to increased gas temperature under constant volume constraint. The "~1/3" figure applies for argon gas at ~2200^{0}F process temperature.

II. Heat work to process temperature while maintaining process pressure low, 100-1000 psi. Pressurize to required level by pumping cold gas into hot system.

III. Pressurize system to required level by pumping cold. Follow by heating system to process temperature while bleeding process gas back to storage to maintain required pressure level.

IV. Heat and pressurize simultaneously.

Final pressure in all cycles may be "trimmed" by pumping or bleeding. Cycle I is used most often because it permits exact process control and minimizes equipment wear. Cycle III requires extreme care in operation to prevent over pressurization of equipment. This cycle also exposes powder containers to maximum risk of argon leakage since full pressure is applied before the can material is sufficiently plastic to flow and seal small leaks. Conversely, Cycle II minimizes leakage risk since full can plasticity is attained before application of substantial pressure. Cycle II is also noted as similar to an idealized model of a process whereby full pre-heating of billets is carried out in a furnace outside the hot isostatic press. Cycle IV is designed to minimize overall process time.

E. Compaction Mechanics

With the exception of compacts specifically designed for porous structures, it may generally be assumed that "100%" density is the normal objective for hot isostatic pressing of powder compacts. There is no general theoretical description of the complete densification process during hot isostatic pressing, but Coble[7] has discussed the "final stage" of sintering with applied pressure. The driving force for densification in this stage is given by the author as:

$$D.F. = \frac{2\gamma}{r} + \frac{P_a}{D} \qquad (7)$$

where

γ = surface energy, ergs/cm^2

r = pore radius, cm

P_a = applied pressure, dynes/cm^2

D = relative density, dimensionless

When pore radius becomes sufficiently small, the applied pressure term can be neglected. If an order of magnitude (factor 10^1) difference is selected where the pressure term is to be discarded, a region of pressure independent sintering in final stage is defined by

$$\frac{P_a}{D} \leqq (10^{-1}) \frac{2\gamma}{r} \tag{8}$$

Since $D \cong 1$ in final stage, $P_a r \leqq .2$ (9)

defines the lower boundary of "pressure enhanced" sintering conditions. Fundamental assumptions required for Coble's model are location of all pores on grain boundaries and absence of gas trapped within closed pores. The second assumption must generally be questioned in hot isostatic pressing and is safely established only by chemical analysis.

A plot of equation 9 is given in Figure 5 for $\gamma = 1000$ ergs/cm^2. The locus of $P_a/D = \frac{2\gamma}{r}$ defines equal contribution to the driving force for densification of both the pressure and the surface energy terms. The significance of Figure 5, as derived from Coble's model, is that final elimination of porosity proceeds substantially independently of applied pressure. For pores small enough to be uninfluenced by applied pressure, there is no restriction on number or distribution of such "species". Thus, arrays of such pores may occur at interparticle boundaries or precisely where the greatest bonding integrity is required. Figure 5 defines the size of pores which may remain at these boundaries to be eliminated by surface tension "driven" diffusion processes.

Implicit in the application of Coble's model to hot isostatic pressing is the assumption that the applied pressure is transmitted throughout the powder compact. This condition may not hold for "large" nickel base powder compacts at "low" compaction temperatures where creep strength is high enough to partially support an applied load for times of the order of 1 hour. Conversely, HIP processing at a temperature where partial melting occurs would insure transmission of applied pressure via the liquid phase.

III. APPLICATIONS

Four types of HIP powder compacts utilized to produce material for processing and test are shown in Figures 2, 6, 7, and 8 respectively. Test bars, 3/4"ø, were used for plasticity, property, microstructural and heat treatment studies primarily of IN-100 and cobalt base alloys. Extrusion billets were HIP'ed

to provide "full" interparticle bonding prior to extrusion as well as maximizing the amount of solid core material in the billet. Sheet bars in maraging steel and cobalt base alloy powders were hot rolled to ~3/8" plate for test. Three IN-100 powder compacts as shown in Figure 2 were press forged at Wyman-Gordon Company to produce flat ~12" ø discs, Figure 9.

IV METALLURGY

Metallographic study of HIP compacts was carried out in three areas as follows: 1. direct HIP compaction of IN-100 powder for high temperature (≥1500°F) applications, 2. investigation of forging rolling, and extrusion billets and products, and 3. effect of HIP cycle on microstructure.

A processing goal established for "good" high temperature (≥1500°F) properties of IN-100 powder compacts was as large a grain size as possible. Two process routes were explored: 1. HIP below the γ' solvus and heat treatment above it for grain growth and 2. HIP above the γ' solvus directly with additional heat treatment optional. Full details have been covered in a previous report[8] but structure results are summarized in Figure 10. Structure produced by HIP, which is typical, consists of mixed grain size material, the finest grain size of the order of ~10μ originating in highly deformed and recrystallized powder particles, and the coarsest of the order of 50μ originating as the cast grain size of those powder particles undeformed during HIP compaction. Heat treatment above the γ' solvus produced a ~300μ g.s. and a unique "unstable" grain boundary structure (center, Figure 10) as well as some pores. Further heat treatment nearly eliminated the "unstable" grain boundary structure and replaced it with scattered "large" pores near or on grain boundaries (right, Figure 10). Similar grain boundary "instability" and pore formation was also observed in IN-100 LC powder HIP'ed @ 2275°F (above γ' solvus) and heat treated @ 2275°F following HIP.

The origin of thermally induced porosity ("TIP") was sought in analysis of compacted material for argon. TIP was found to occur in IN-100 LC at argon levels as low as 0.1 ppm by a vacuum fusion - mass spec analysis method.

This 0.1 ppm level was, however, close to the detectability limit of the analytical method so that the conclusions drawn from this finding are tentative. Normal carbon (.15%C) IN-100 HIP'ed and heat treated above the γ' solvus did not show TIP when argon was less than the detectability limit ($\leq$ 0.1ppm).

Metallographic examination of the forgings shown in Figure 9 was carried out and two center radial sections are shown in Figure 11. HIP @ 2250°F produced a uniform g.s. of ~200μ which forged without cracking except at the edges. The 2200°F HIP'ed preform showed cracking throughout, primarily at the boundaries of undeformed prior powder particles. Analysis for argon of material adjacent to that in the micros showed 2.6 ppm in the 2250°F HIP'ed billet and 62 ppm in the 2200°F HIP'ed billet. The latter level is considered sufficient to prevent full densification during HIP and cause crack growth during forging originating in pores in the compact.

Effect of HIP process cycle on microstructure was investigated with IN-100 LC for two types of relationships between temperature and pressure application. In the first (type II cycle, Fig. 4), starting with as low a pressure as practical (~500 psi) the sample was heated to 2030°F, then pressurization to 15 ksi was carried out by pumping as fast as possible. A plot of time/temperature/pressure is shown in Figure 12. Note the temperature lag of the load behind the furnace windings. In the second cycle (type III cycle, Fig. 4), the HIP unit was pressurized to 15 ksi "cold" (~100°F) then heated as fast as possible to 2030°F. A plot of cycle parameters is shown in Figure 13. The time scale is interrupted to permit complete plotting. Note that at high pressure the temperature lag of the load is reduced. In both cases, a dwell time of 2 hours and "rapid as possible" cool was used. Samples were canned as test bar compacts 3/4" ϕ x 6" long (see Figure 6). IN-100 LC remelt stock chemistry of the powder used in these tests is given in Table I.

A difference in structure between type II cycle and type III cycle IN-100 LC material was observed. Figures 14 and 15 detail these findings. The low pressure heat up material (left both figures) showed coarser recrystallized grain size for both

γ matrix and γ' phase than for high pressure heat up material (right both figures). Recrystallization of deformed powder particles is considered "dynamic" in both cycles, but with full pressure applied before heat up (type III) the temperature at which Rx occurs in this case would tend to be the lowest at which small amounts of deformation occur. This could be 1700-1900°F considering that this range is traversed relatively slowly (~1/2 hour, see Figure 13). With a low pressure heat up (type II), however, negligible deformation occurs below 2030°F, and at 2030°F only as the pressure builds up. Dynamic recrystallization at the higher temperature produces a generally coarser structure. Similar effects are observed in extrusion. The practical value of such structural characteristics requires further study.

CONCLUSIONS

The effects of process details on the structure of hot isostatically pressed powder compacts have been discussed. Factors which have been shown to be significant but must be further explored to permit advancement of this unique process method include heat transfer within the system, accurate workpiece temperature measurement, kinetics of final pore closure, container leakage, and time/temperature/pressure relationships of the HIP cycle.

REFERENCES

1. "Structure and Property Control through Rapid Quenching of Liquid Metals". MIT Center for Materials Science and Engineering ARPA Contract No. DAHC15 70 C 0283. Semi-Annual Reports 1,2,3,4 & 5.

2. Burke, J. J. & Weiss, V. eds; Powder Metallurgy for High-Performance Applications, Syracuse University Press 1972.

3. Friedman, G. I. & Ansell, G. S.; The Superalloys ed by C. T. Sims & W. C. Hagel, Wiley 1972 pg. 427-450.

4. Proceedings Second International Conference on Superalloys, September 1972. Battelle Report No. MCIC-72-10

5. Boyer, C. B., Orcutt, F. D., and Conaway, R. M.; "High Temperature High Pressure Autoclaves", Chemical Engineering Progress, Vol. 62, No. 5, May 1966, pg. 99-106.

6. Schumann Jr., R., Metallurgical Engineering Principles, Vol. I, Addison Wesley 1952, pg. 277-282.

7. Coble, R. L., Journal of Applied Physics, Vol. 41, No. 12, Nov. 1970, pg. 4798-4807.

8. ARPA Contract No. DAHC15 70 C 0283. Semi-Annual Report No. 4.

Table I

IN-100 Low Carbon Chemistry

C	Mn	Si	Cr	Ni
.02	.10	.10	9.10	Bal.
Mo	**Co**	**Fe**	**S**	**V**
2.93	14.6	.37	.007	1.04
Ti	**Al**	**B**	**Ti & Al**	
4.88	5.64	.016	10.5	

Figure 1. IN-100/low carbon steel interdiffusion zone.

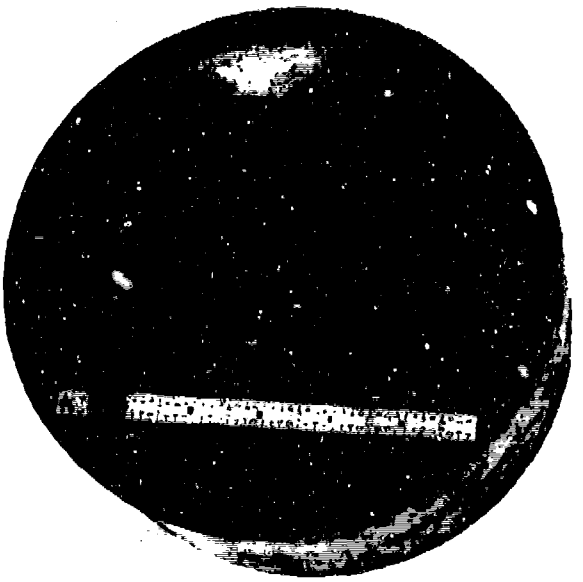

Figure 2. IN-100 LC forging billet compact, 8" ϕ x 4" high.

Figure 3. Heating and cooling of HIP furnace and load, schematic.

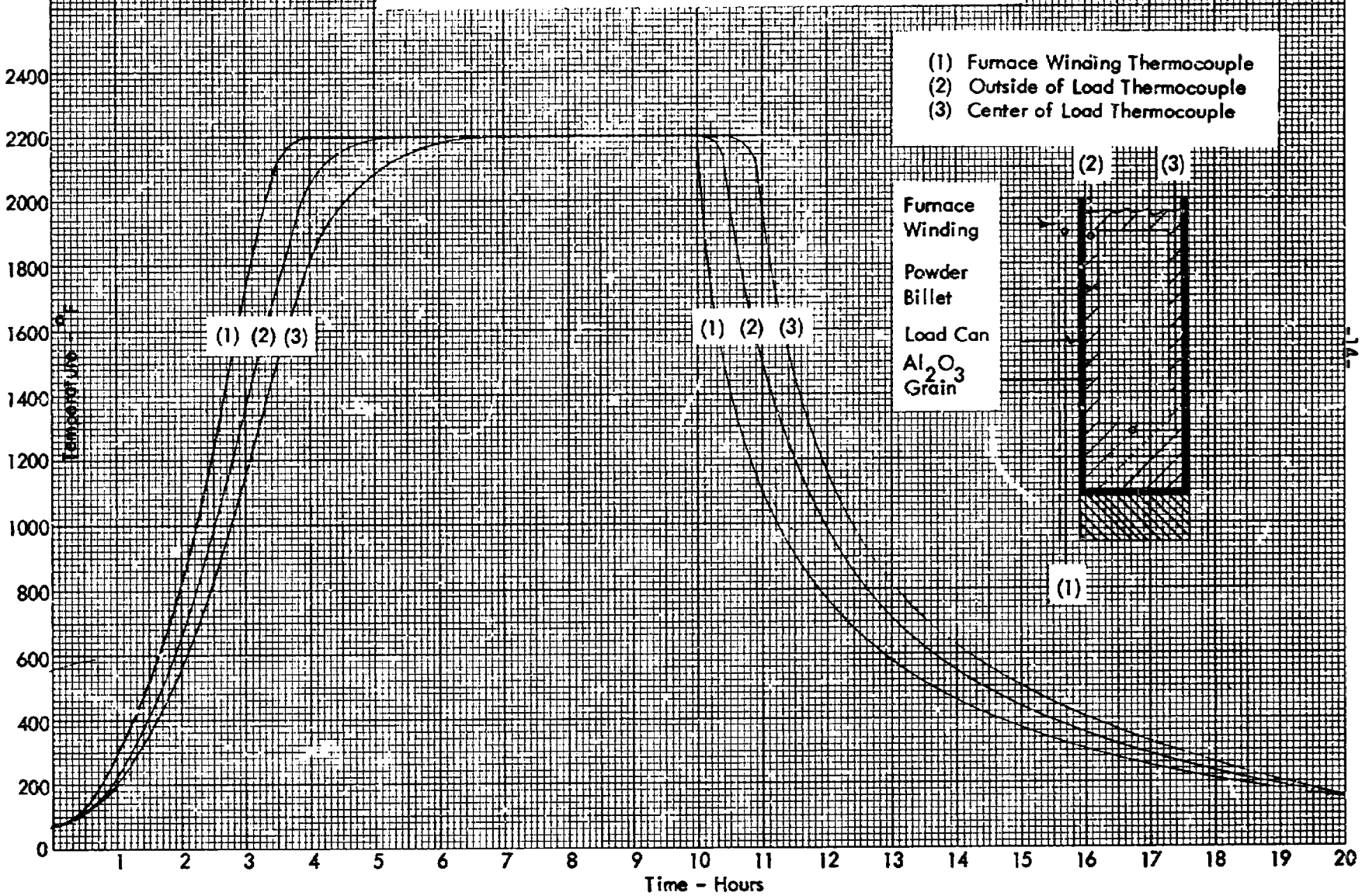

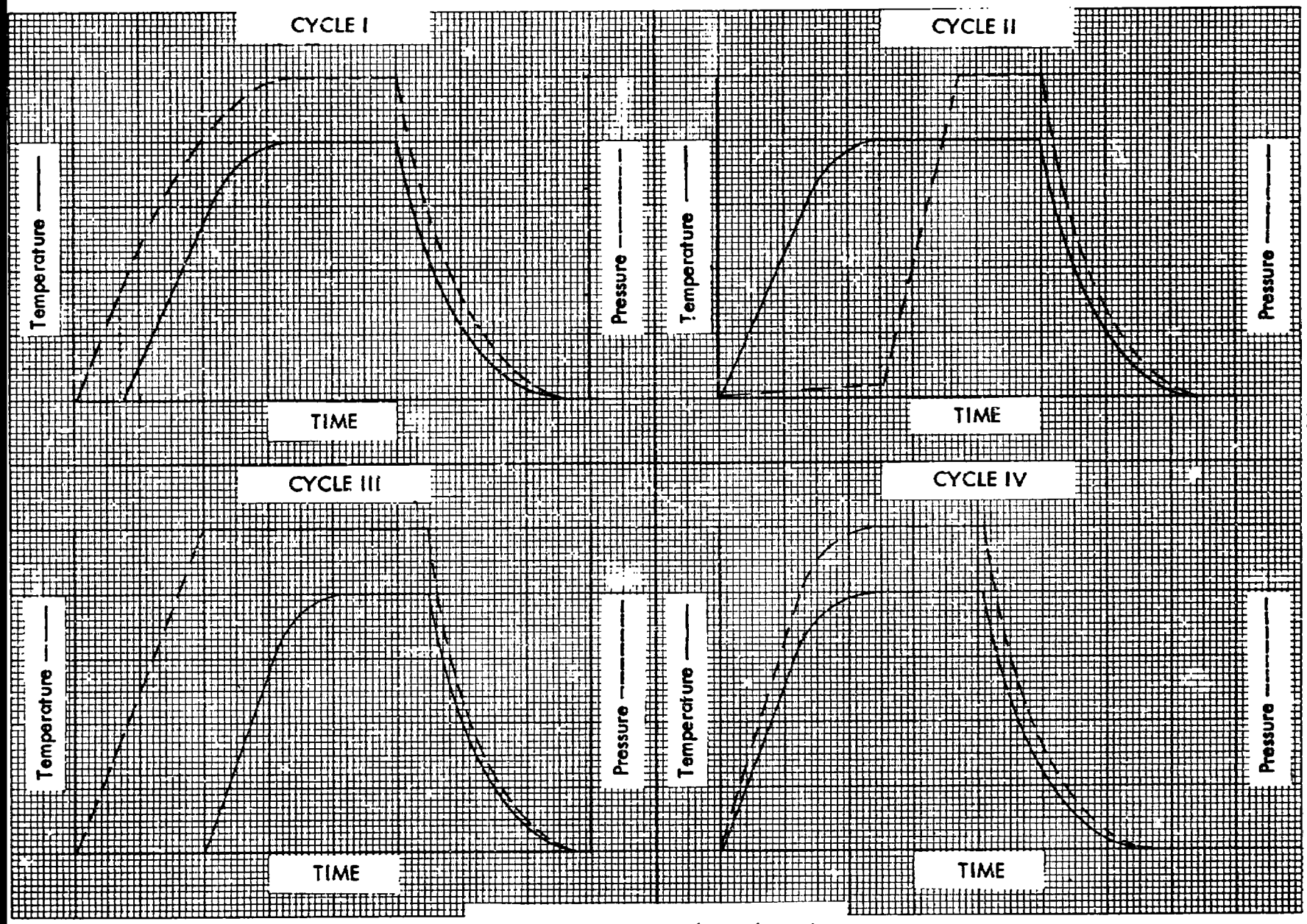

Figure 4. Process cycles, schematic.

Figure 5. Pressure "Activation" of Sintering

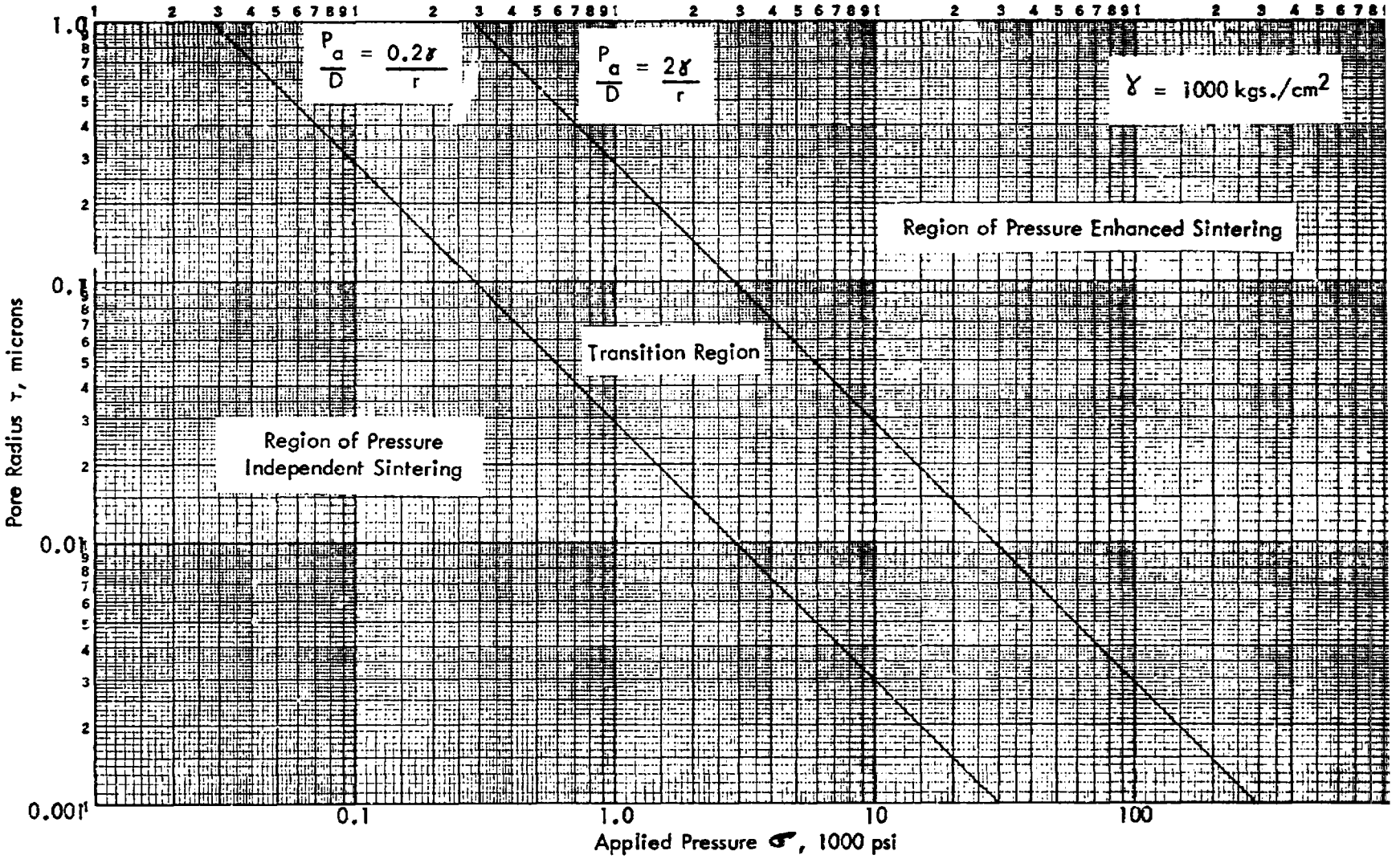

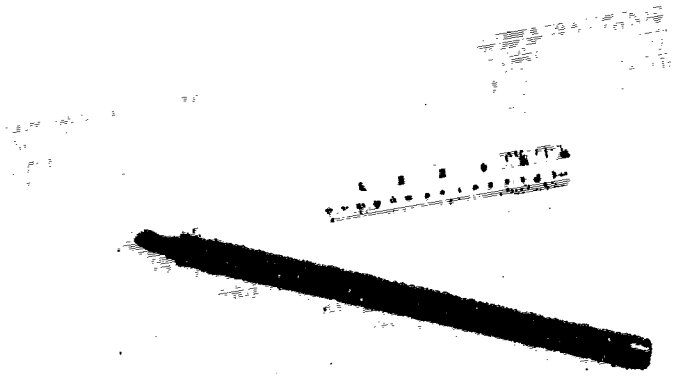

Figure 6.

Test bar compact, 3/4" ϕ x 11" long.

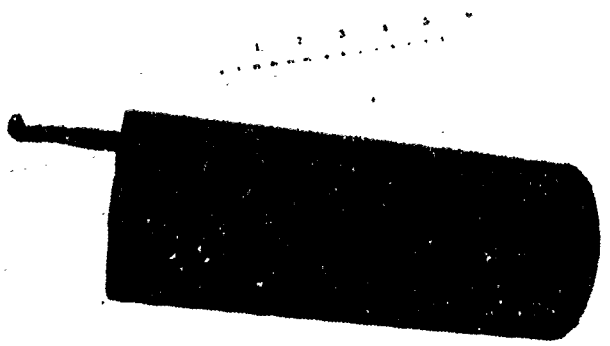

Figure 7.

Extrusion billet compact, 3-3/4" ϕ x 9-1/2" long.

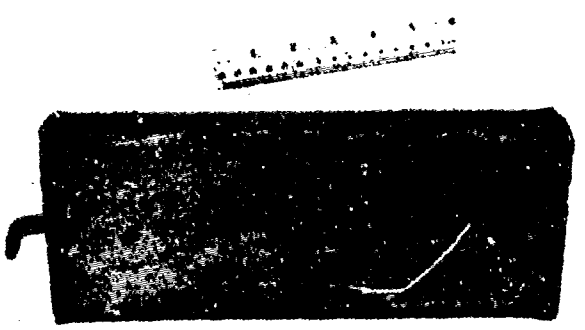

Figure 8.

Sheet bar compact, 2" x 4-1/2" x 12".

Reproduced from best available copy.

Figure 9.

IN-100 LC press forged HIP billets. Top: HIP'ed at 2150°F, 15 ksi, 5 hrs.; middle: HIP'ed at 2200°F, 15 ksi, 5 hrs.; bottom: HIP'ed at 2250°F, 15 ksi, 5 hrs. Chemistry, see Table I.

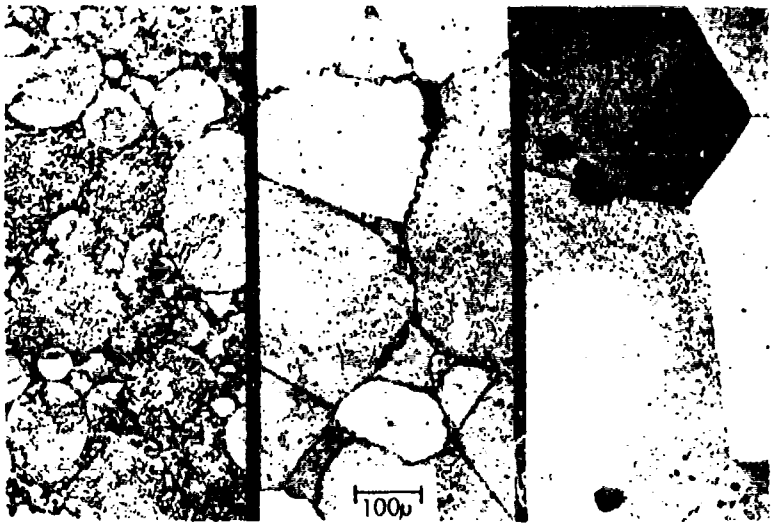

Figure 10.

IN-100 LC, R.E.P. powder, -35 mesh. Left: HIP'ed at 2000°F, 29 ksi, 2 hrs. As Pressed, etched. Center: 2 hrs. at 2275°F, A.C., etched. Right: 5 hrs. at 2275°F, A.C., etched.

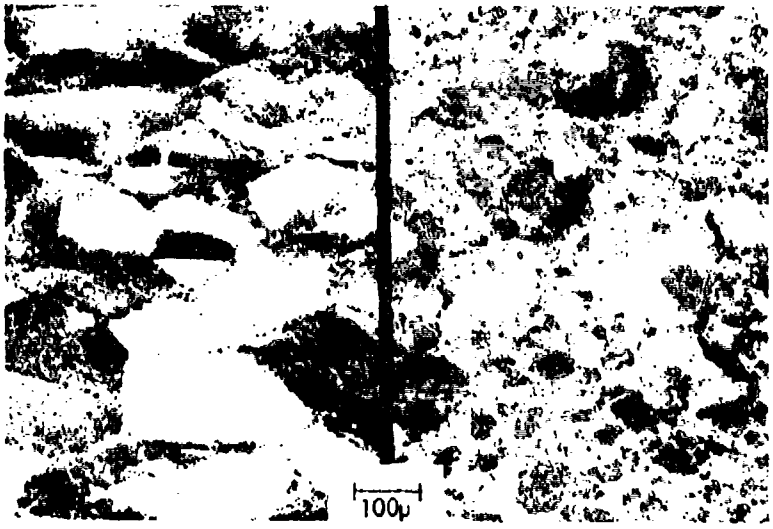

Figure 11.

IN-100 LC R.E.P. powder, -60 mesh. Left: HIP'ed at 225[illegible], 15 ksi, 5 hrs. plus press forge. Right: HIP'ed at 2200°F, 15 ksi, 5 hrs. plus press forge.

Figure 12. HIP process cycle, Type II, low pressure heat up.
(Plot of actual data)

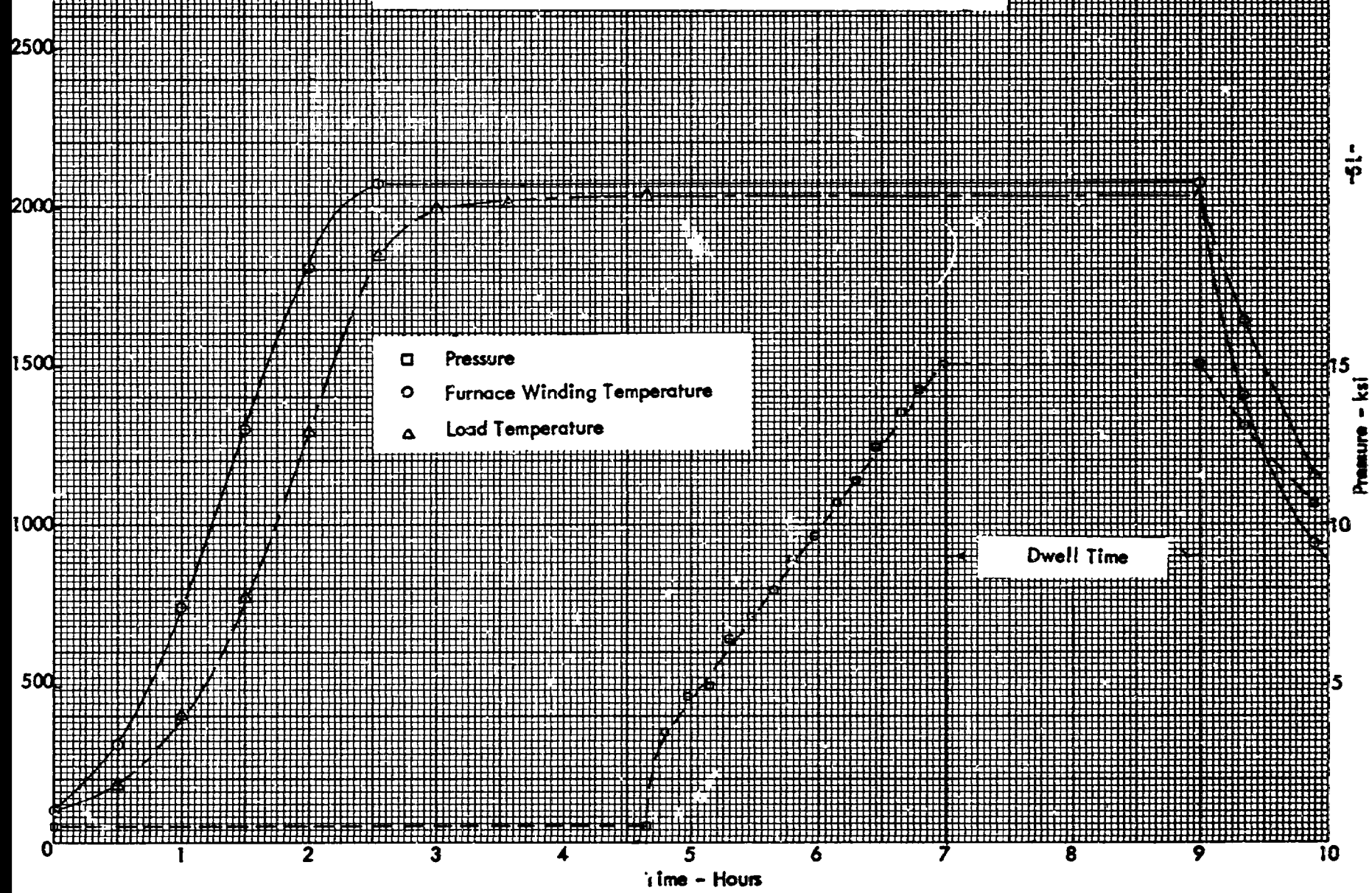

Figure 13. HIP process cycle, Type III, high pressure heat up.
(Plot of actual data)

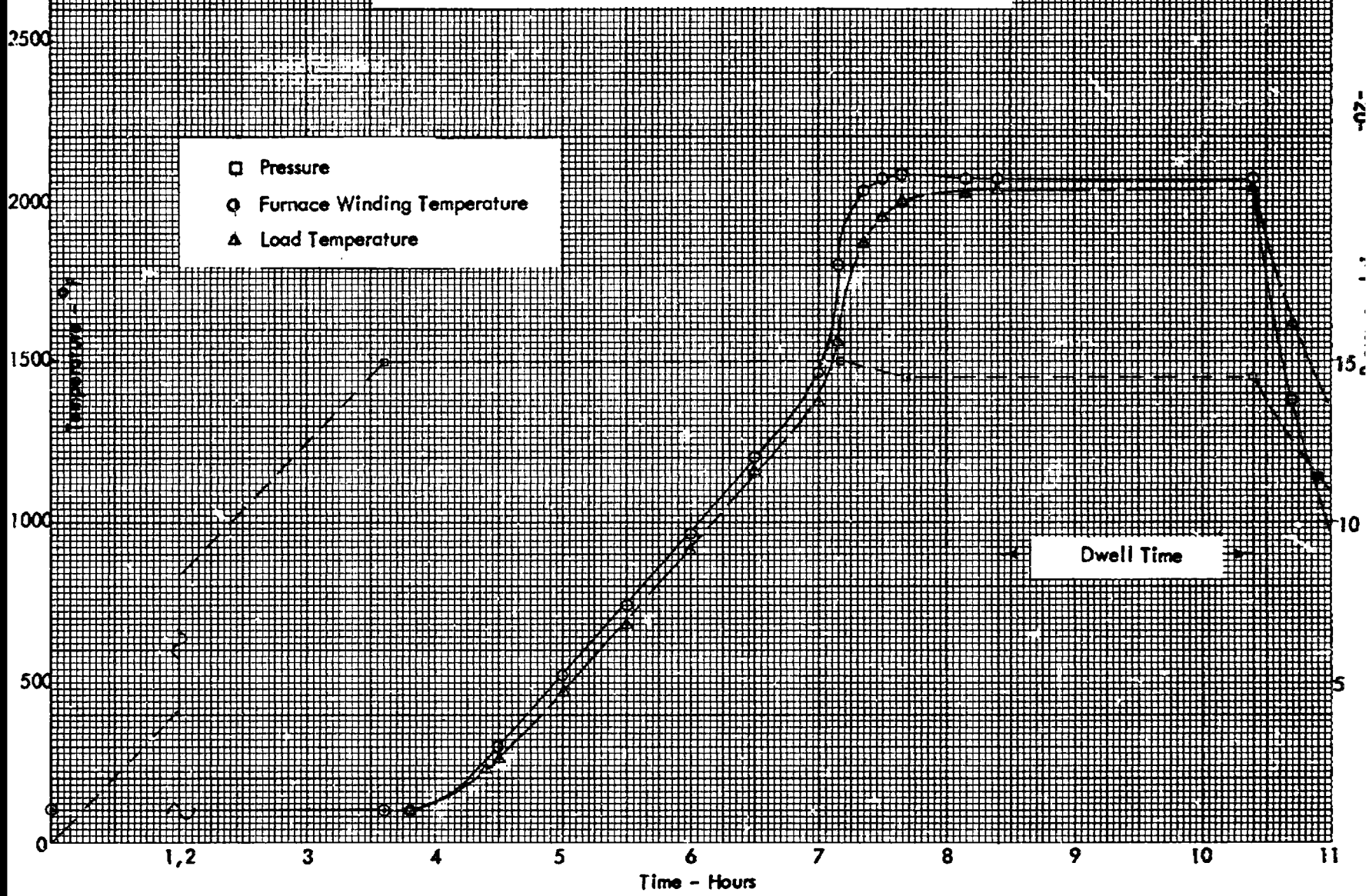

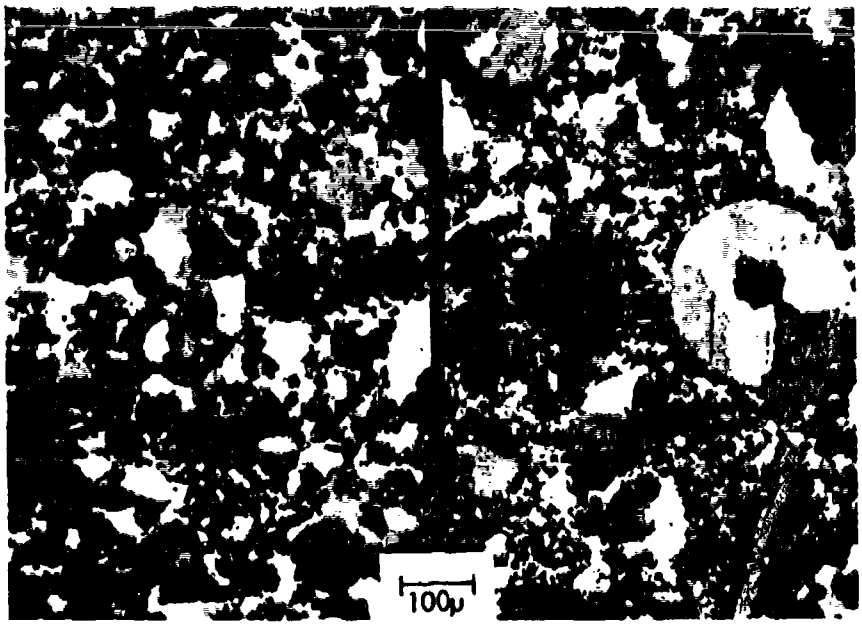

Figure 14. IN-100 LC R.E.P. powder, -60 mesh. Left: Type II cycle, Figure 12. Right: Type III cycle, Figure 13. Etched. Chemistry, see Table I.

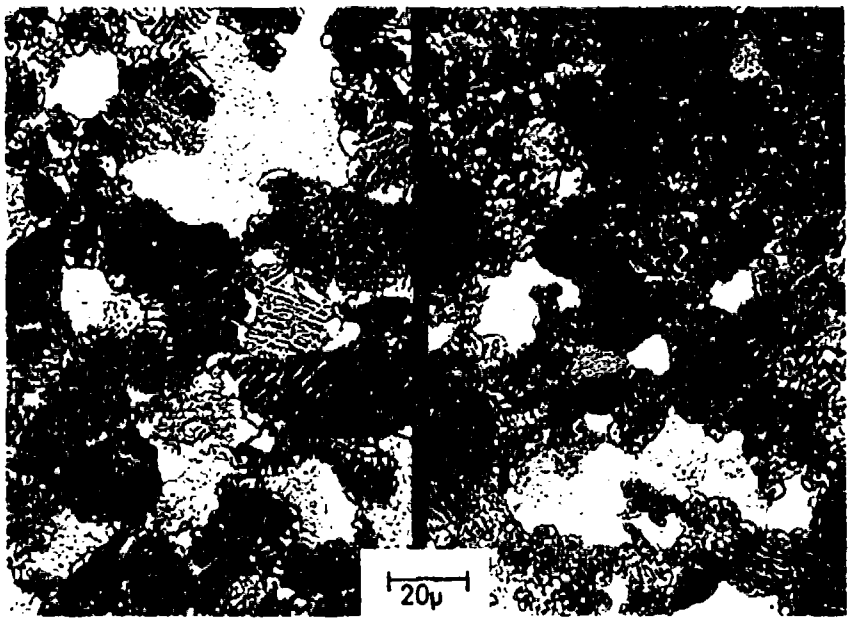

Figure 15. Same as Figure 14. Note coarse γ', Type II cycle, finer γ', Type III cycle.

Canning Practice and Argon Contamination in Hot Isostatic Pressing

I INTRODUCTION

The usefulness of hot isostatic pressing as a cost effective process method for producing "close-to-net" shapes or forging preforms in modern P/M superalloy materials is currently being recognized by interested parties. Experience over the last three years at Industrial Materials Technology with canning and hot isostatic pressing of powders and composite structures has shown a variety of manufacturing errors which may occur. The most common is container leakage. In general, there is a spectrum of defects ranging from grossly leaking cans which do not compact at all, to cans which contain powder compacted apparently to "100%" density but in fact, have porosity detectable metallographically either before or after high temperature heat treatment. Such compacts may contain argon at levels from 0.1 to 100 ppm. Porosity associated with argon in P/M superalloy products may severely decrease hot plasticity of forging preforms and/or lead to decreased creep and fatigue properties.

Process conditions in hot isostatic pressing are unique in superalloy metallurgy because leak proof integrity of a can or envelope must be maintained at pressures up to 30,000 psi and temperatures up to ~2250°F. Accordingly, the theory of leaks in HIP cans has been examined and subjected to experimental test. Findings have contributed to understanding of process limitations and defined questions for further exploration.

II THEORY OF LEAKS

A. Flow Characteristics of Capillaries

For purposes of discussion, a single leak in a HIP container is approximated as a small straight cylindrical capillary perpendicular to the can wall. Schematically, this is shown in Figure 1. Guthrie and Loevinger[1] have described the flow characteristic of a cylindrical capillary as

$$Q = \frac{1}{L}\left[C_1 P^2 + C_2 P + C_3 \ln(1 + C_4 P)\right]_{P_2}^{P_1} \tag{1}$$

where

Q = flow rate, cgs units

P_1 = high pressure outside leak, cgs units

P_2 = lowest pressure inside capillary, cgs units

L = capillary length, cgs units

$$C_1 = \frac{\pi D^4}{256\eta}$$

$$C_2 = .34\sqrt{\frac{kT}{m}}\ D^3$$

$$C_3 = .065\eta\frac{kT}{m}\ D^2$$

$$C_4 = 1.24\sqrt{\frac{m}{kT}}\ \frac{D}{\eta}$$

η = viscosity of gas

k = Boltzmanns constant

T = absolute temperature

m = mass of gas molecule

For $P_2 = 0$, the case of an evacuated and sealed can with a "small" leak, and P_1 "large", the case of such a can in a hot isostatic press under 15,000 psi pressure or under 15 psi during leak test, Eq. 1 becomes

$$Q = \frac{1}{L}\left[\frac{\pi D^4}{256\eta} P_1^2 + .34\sqrt{\frac{kT}{m}}\ D^3 P_1 + .065\eta\frac{kT}{m} D^2 \ln\left(1 + 1.24\sqrt{\frac{m}{kT}}\frac{D}{\eta}P_1\right)\right] \tag{2}$$

Since Eq. 2 is derived from Knudsen's equation[2], it strictly applies only in the viscous and molecular flow regions. Transition from turbulent flow to viscous flow occurs when Reynolds number

$$Re = \frac{DV\rho}{\eta} \text{ is } < 1{,}200 \qquad (3)$$

where

V = gas velocity, cgs units

ρ = gas density, cgs units

η = gas viscosity, cgs units

D = capillary diameter, cm

It is necessary therefore, to establish the applicability of Eq. (2) by determining Re for various calculated leakage flow rates.

B. Leak Rates Through Capillaries at 1 Atmosphere and 1,000 Atmospheres For He and Ar.

Flow rates at room temperature have been calculated for idealized capillaries with diameters covering the range which may occur in practice. A standard capillary length L = 1 cm has been used as well as the stated values of physical parameters and constants. Reynolds number has been calculated for various conditions to verify use of Knudsen's equation. Parameter values used were:

ηHe @ 20°C, 1 atm = 194×10^{-6} poise (gr/cm sec)

ηAr @ 20°C - 1300°C, 1000 atm = 700×10^{-6} poise

mHe = 6.64×10^{-24} grs/molecule

mAr = 66.2×10^{-24} grs/molecule

$k = 1.38 \times 10^{-16}$ dyne-cm/degree (Boltzmann's constant)

T = 293°K

1 atm = 1.01×10^{6} dynes/cm^2

Table I gives values of leakage flow rates for He at 1 atmosphere (~15 psig) and for Ar at 1000 atmospheres (~15,000 psig) for five capillary diameters, D, and two values of wall thickness L. These calculations clearly indicate the major problem in leak checking HIP containers, i.e. the leakage flow rate of argon through a capillary at 1000 atmospheres process pressure may be up to five orders of magnitude greater than the flow rate during any practical leak checking procedure applied before HIP. Thus, the sensitivity of leak checking methods becomes critical for the integrity of HIP compacts.

Reynolds number values (Table I) for the calculated flow rates show that only for a 10μ capillary under 1000 atm argon pressure is the Knudsen equation invalid. A hole of this size is detectable by several methods so that consequent container leakage should not occur in practice.

C. Total Argon Leakage Flow

Total flow through a single leak has been estimated using the assumption that P_2 (Figure 1) remains negligible. Times have been taken as 1000 sec (16.7 min) and 10,000 sec (167 min, ~3 hrs) the latter comparable to those of process cycles frequently used. It should be noted that in practice, multiple capillary leaks may occur. Table II summarizes these calculations.

D. Argon Contamination Levels in Compacts.

Contamination levels in powder compacts of various sizes for various total leakage flows may be estimated using Figure 2. Derivation of Figure 2 is as follows. Assume a 10 lb. (net) superalloy powder compact with a 1 ppm (by wt.) level of argon contamination. Total argon contained is 4.54×10^{-3} grams. Since the density of argon is $\sim 1.78 \times 10^{-3}$ grs/cc at standard temperature and pressure (STP), 1 ppm argon in a 10 lb. compact is equivalent to ~2.5 std cc.

Comparison of total argon leakage flow for a 0.1μ diameter capillary x 0.1 cm (.040") long and 10,000 seconds flow time from Table II (56 cc-atm) shows that a 1000 lb. compact would be contaminated to a level of ~0.26 ppm Ar and a 100 lb. compact to ~2.6 ppm Ar. The significance of various argon contamination levels in superalloy powder compacts remains largely unexplored at this time. In general, argon would be expected to be found after HIP compaction in micropores, which in turn may adversely affect forgeability and high temperature properties.

E. Other Causes

To put the overall problem of argon contamination of compacts in perspective, it is necessary to assess the significance of sources other than leaks. Possibilities which might produce results similar to actual leaks include:

1. Contaminated powder
2. Insufficient evacuation of compacts
3. Permeation of argon through solid "defect free" can walls

These points are discussed below:

1. Powder may pick up argon in manufacturing (argon atomization) and/or handling. Air is nominally 9000 ppm argon by weight (~1%). Powder handling in inert gas or air may lead to physical adsorption of gas particularly in powder particle capillaries which are surface connected and originate in solidification shrinkage[3]. Details of this behavior require full investigation using appropriate surface chemistry techniques. Hot extraction and vacuum fusion-mass spec readout analysis of argon atomized IN-100 LC was carried out to characterize argon atomized powder. In hot extraction, the powder sample was heated under vacuum at high temperature for a given period of time and the evolved gas analyzed. Results are in Table III and indicate that a significant amount of argon cannot be "pumped off" even at very high temperature and is "released" only by fusion. It is to be noted that samples for analysis are normally handled in air so that "adsorbed" argon is negligible (first and second analyses, Table III) compared to "trapped" or "occluded" argon.

2. Insufficient evacuation of compacts may lead to contamination by residual gas and its proportional fraction of argon. It is to be noted immediately that since pumping out of a compact is a dynamic process with pressure being measured at the compact outlet or the pump inlet, there may be one or more orders of magnitude pressure difference from compact to pump. Furthermore, a real leak could be pumped "fast enough" through the high impedance powder bed and exit tube to give an apparently "acceptable" seal-off pressure. Such a leak would continue however, to admit air after seal-off of the evacuation tube.

In the case of a theoretically leak tight can, an expression may be derived giving the estimated contamination level as a function of residual gas pressure and temperature.

$$P_{pm_{contaminant}} \equiv \frac{M_c}{M_m} \times 10^6$$

where

$M_c \equiv$ mass of gas contaminant per unit volume of loose compact

$M_m \equiv$ mass of metal per unit volume of loose compact

$M_m = \rho'$

and

$\rho' \equiv$ tap density of powder, grs/cc

For the gas

$$M_c = \frac{PfvM}{RT}$$

where

$P \equiv$ total pressure in compact, μ Hg

$v \equiv$ free volume per unit volume

$f \equiv$ fractional gas composition, i.e. air - 0.2 O_2 $f = 0.2$

$M \equiv$ molecular wt. of species, grs/mole

$R \equiv$ gas constant, 82.06 cc-atm/^oK

$T \equiv$ absolute temperature, ^oK

Note that

$v = 1 - \rho'/\rho$

$\rho \equiv$ true density of metal, grs/cc

Thus

$$P_{pm_{contaminant}} = \frac{1.32\ MPf}{RT} \quad \frac{1 - \rho'/\rho}{\rho'}\ ;\ P \text{ in } \mu \text{ Hg}$$

The residual pressure for 1 ppm total gas contamination from air may be calculated using:

$M_{air} \equiv 29$ grs/mole

$T = 600^oK$ ($327^oC = 620^oF$)

$\rho = 8.0$ grs/cc

$\rho' = 5.2$ grs/cc

Then

$$P_{pm} = 5.2 \times 10^{-5} P \quad (P, \mu\ Hg)$$

For $P_{pm} = 1$

$$P = 1.9 \times 10^{4}\ \mu\ Hg$$

$$\cong 19\ mm\ Hg$$

Since the normal total gas content of "good" superalloy powders is of the order of 50-100 ppm, it is clear that a residual compact pressure of 19 mm Hg does not appreciably increase that average contamination level above the initial value. For argon, which is ~ 1% of air, contamination level is given by

$$P_{pm_{Ar}} \cong 7.2 \times 10^{-7}\ P \quad (P, \mu\ Hg)$$

For

$$P_{pm_{Ar}} = 1$$

$$P = 1.4 \times 10^{6}\ \mu\ Hg$$

$$\cong 1.8\ atm$$

Since this pressure is greater than 1 atm, it is clear that insufficient evacuation leading to 1 ppm argon contamination is extremely unlikely.

3. Although there is no known mechanism by which argon should permeate defect free carbon or stainless steel, commercial steel products contain a wide assortment of "defects" including grain boundaries, inclusions, second phases, dislocation, vacancies, etc. Furthermore, it might be assumed that under the high pressure (15,000 psi) and high temperature (2200°F) conditions existing in a hot isostatic press, argon fluid might interact with steel in a sufficiently non-ideal way to produce new effects. Accordingly, argon permeation as an alternative to capillary leaks, was investigated experimentally.

Solid cylindrical bars of low carbon and 304 stainless steel were HIP'ed at 2100°F, 15,000 psi for 5 hours. Ten successive machine chips .0025" thick were taken with a lathe off the exterior cylindrical surface of the sample bars. Chips numbers 1, 2, 3, 5 and 10 were analyzed for argon by a vacuum fusion-mass spectrometer readout method. Blank samples were taken by the same method

of adjacent bar material not HIP'ed. Results are shown in Figure 3. All sample levels were above the detectability limit of the equipment at the time analysis was performed. The only HIP samples appreciably above blank levels were in the first chips taken .0025" deep in from the outer surface. From .005" in to a depth of .025" argon samples were substantially independent of depth from the surface. These data indicate that permeation of argon through "defect free" material does not occur to depths greater than .005" for the conditions tested. The blank values are surprisingly high but may be traceable steelmaking practice. On the basis of present data, it is concluded that since HIP can walls are generally $>$ .065" thick and that there is essentially no argon concentration gradient inside a depth of .005" for low carbon and stainless steel, the probability of substantial contamination of compacts by argon permeation of defect free can walls is negligible. Conversely, the use of 1-5 mil thin wall cans or "coatings" would be questionable on the basis of present data.

F. Summary

On the basis of theoretical and experimental considerations, the most likely sources of argon contamination of superalloy powder compacts arise in base argon content of powder and encapsulation container leaks.

III LEAK DETECTION

Table I indicates that leakage flow rates under pressing conditions (1000 atm) may be several orders of magnitude greater than under pressure conditions (1 atm) usually used for leak testing. The sensitivity or detection limit of various leak checking methods is therefore critical in insuring low leakage encapsulation cans. Guthrie[4] has listed the sensitivities of various methods. Several methods require special operating conditions not easily adaptable to HIP containers. Three methods and their estimated sensitivities in terms of leak size warrant discussion: 1. Soap bubbles, 5×10^{-5} std cc/sec, 2. Halogen leak detector, 10^{-6} std cc/sec, and 3. Helium leak detector, $\sim 10^{-10}$ std cc/sec.

From Table I, it may be seen that methods (1) and (2) above may be used to find 10μ capillaries but not 1μ (or smaller) capillaries. The helium leak detector

should find 1μ and 0.1μ capillaries. Since Table II shows that for a 1μ (10^{-4}cm) capillary total leakage flow may significantly contaminate compacts of all sizes (see Figure 2), the only method that has useable sensitivity for the problem is the helium detection method.

Leak detection has been fully discussed by Guthrie[5]. Maximum sensitivity of a helium mass spec leak detector is achieved only by operation in the "vacuum testing" mode (see reference). Briggs and Burnett[6] have analyzed the method whereby a sealed container is exposed to up to 5-10 atmospheres of helium. The interior "free" volume is thus "charged" and leakage back out after charging is tested. This method would appear ideally suited for sealed HIP containers. However, analysis shows that for a 10 lb. (net) powder compact with a real leak of 10^{-7} std cc/sec at 1 atm pressure ($D=10^{-4}$ Table I), powder at an apparent density of 5.2 grs/cc (8.0 grs/cc fully dense), and detection within 1 second after charging, a charging time of ~17 hours at 150 psi would be required to generate back leakage just detectable with a helium leak detector (10^{-11}std cc/sec). The "charging" method for leak detection in sealed HIP capsules clearly has only limited application for small (~1 lb.) compacts, and is unsuitable for larger compacts.

IV EXPERIMENTAL

An experimental study was carried out wherein 72 small cans embodying "best practice" test variables of can design, can wall thickness, material, and welding technique were filled, welded, leak checked, evacuated, sealed, HIP'ed, and the IN-100 LC cores analyzed for argon. Figure 4 shows details of the can designs tested. End plugs for cans in carbon steel were machined from "special quality" 1117 hot rolled bar which experience has shown to have less centerline porosity than "merchant quality" bar.

Processing sequence included the following:

1. Machine tubes, end plugs and exit tubes
2. Vapor degrease
3. TIG weld in exit tubes
4. H_2 anneal welded assemblies (except stainless steel) and end plugs, 1700°F, 1 hour.

5. Insert steel wool exit tube plug
6. Fill with IN-100 LC R.E.P. powder, ~ 27 grs (.059 lbs.) per can
7. Insert end plugs and weld
8. Helium mass spec leak check using Varian NRC925 equipment
9. Evacuate cold, then heat to ~1200°F while continuing evacuation
10. Seal exit tube and cut off excess length
11. Hot isostatically press
12. Machine samples from IN-100 core
13. Argon analyze using vacuum fusion-mass spec. readout

Figure 5 shows HIP'ed compacts after machining for chemical analysis samples.

Compilation of leak test and argon analysis results is presented in Table IV. Can type (see Figure 4) and HIP conditions are indicated. A large number of cans were carried through leak testing to obtain estimates of process reproducibility. A reduced number of argon analyses were run to limit cost.

Expected argon contamination levels for leakage rates of the order found experimentally (Table IV) were estimated as shown in Table V. As an example a 1 atm He leak rate of 10^{-8} std cc/sec should have allowed sufficient argon leakage flow at 450 atm. to raise the argon level in the 27 gram (net) compact to 18 ppm, a value well within the detectability limit of the analysis method. No such high values of argon were found for any samples, a variance from theoretical expectations. Analytical values of argon were uniformly low and independent of initial leak rate and pressurization cycle. What is not known, is whether the measured leakage rates were valid after hot evacuation of the cans at 1200°F (Step 9 in processing sequence). Since the cans were heated in air, oxidation occurred and may have acted to seal existing capillary leaks. The theory of argon leakage thus remains incompletely tested. Nevertheless, the can designs and process sequences used have been shown to produce "HIP'ed" IN-100 powder substantially free of argon.

V CONCLUSIONS

Powder manufacturing processes employing argon and container leakage under high pressure during HIP appear as the primary sources of argon contamination of powder compacts. Experiment has indicated the need for further testing of leakage theory. A "best practice" has been established which yields substantially argon free compacts by hot isostatic pressing. Related areas of investigation which require further work include: 1. definition of the precision and accuracy of analytical methods for argon in superalloy compacts, 2. establishment of standard reference "knowns" for analysis, and 3. determination of superalloy property variations as a function of argon content at low levels ($\ll$ 10 ppm).

REFERENCES

1. Guthrie, A. and Wakerling, R. K., "Vacuum Equipment and Techniques", McGraw Hill 1949, pg 191 - 194.

2. Ibid, pg 27.

3. Berman, S. J., S. M. Metallurgy Thesis. MIT Department of Metallurgy, August 1973, pg 76a.

4. Guthrie, A., "Vacuum Technology", Wiley 1963, pg 472.

5. Ibid, Chapter 15.

6. Briggs, W. E., and Burnett, S. G., "Helium Leak Testing: A New Analysis". Vacuum Division, Varian Associates Pub. No. VR-69, June 1969.

Table I

Capillary Leakage Flow Rates

Q, cc-atm/sec

Reynolds Number, Re, for Flow Rate & Capillary

D cm, μ, A°	He, P_1 = 1 atm			Ar, P_1 = 1000 atm		
	L = 1 cm	L = 0.1 cm	Re, L = 0.1cm	L = 1 cm	L = 0.1 cm	Re, L=0.1cm
10^{-7}, .001, 10^{1}	1.8×10^{-16}	1.8×10^{-15}	1.9×10^{-8}	2.3×10^{-15}	2.3×10^{-14}	7.0×10^{-7}
10^{-6}, .01, 10^{2}	9.8×10^{-14}	9.8×10^{-13}	1.1×10^{-6}	6.1×10^{-12}	6.1×10^{-11}	1.8×10^{-4}
10^{-5}, .1, 10^{3}	2.6×10^{-11}	2.6×10^{-10}	2.8×10^{-5}	5.7×10^{-8}	5.7×10^{-7}	1.7×10^{-1}
10^{-4}, 1, 10^{4}	7.1×10^{-9}	7.1×10^{-8}	7.7×10^{-4}	5.6×10^{-4}	5.6×10^{-3}	170
10^{-3}, 10, 10^{5}	2.2×10^{-5}	2.2×10^{-4}	2.4×10^{-2}	5.6	56	1.7×10^{6}

Table II

Total Argon Leakage Flow

Q x t, cc - atm

Argon, P_1 = 1000 atm

D, cm	L = 1 cm		L = 0.1 cm	
	1000 sec	10,000 sec	1000 sec	10,000 sec
10^{-7}	2.3×10^{-12}	2.3×10^{-11}	2.3×10^{-11}	2.3×10^{-10}
10^{-6}	6.1×10^{-9}	6.1×10^{-8}	6.1×10^{-8}	6.1×10^{-7}
10^{-5}	5.7×10^{-5}	5.7×10^{-4}	5.7×10^{-4}	5.7×10^{-3}
10^{-4}	5.6×10^{-1}	5.6	5.6	56
10^{-3}	5.6×10^{3}	5.6×10^{4}	56×10^{3}	56×10^{4}

Table III

Argon Analysis

Argon atomized IN 100 LC, -80 mesh, Mass spec. readout

		Ppm	wt.
1.	Vacuum extraction 15 min @ 2000°F	ND	.5*
2.	Vacuum extraction 15 min @ 2200°F (same sample as 1 above)	ND	.5*
3.	Vacuum fusion (same sample as 1 and 2 above)	1.6	.5*

* .5 ppm limit of detectability
ND None detected

Sample size ~1 gram

Table IV

HIP Container Design Study vs Leakage and Argon Contamination

Can No. Internal Code	Type (see Fig.4) SS, CS[1]	Leak Rate std cc/sec 1 atm He pressure	Process Cycle 2250°F, 2 hrs. ___ ksi	Argon Level, Ppm. Vacuum fusion, mass spec analysis
3E79	1-SS	3.8×10^{-9}	30^{3}	NA
3E80	1-SS	4.2×10^{-8}	15^{4}	NA
3E81	1-SS	3.6×10^{-8}	30^{3}	ND, 0.1 (see Note 7)
3E82	1-SS	4.8×10^{-8}	15^{2}	ND, 0.1
3E83	1-SS	2.1×10^{-8}	15^{2}	ND, 0.1
3E84	1-SS	7.2×10^{-8}	15^{4}	NA
3E85	1-CS	3.0×10^{-8}	15^{2}	ND, 0.1
3E86	1-CS	5.2×10^{-8}	15^{2}	ND, 0.1
3E87	1-CS	4.6×10^{-8}	15^{4}	NA
3E88	1-CS	4.6×10^{-8}	15^{4}	NA
3E89	1-CS	3.2×10^{-8}	15^{3}	ND, 0.1
3E90	1-CS	4.0×10^{-8}	30^{3}	NA
3E67	2-SS	$< 1.0 \times 10^{-9}$	30^{3}	ND, 0.1
3E68	2-SS	9.4×10^{-9}	30^{3}	NA
3E69	2-SS	4.6×10^{-8}	15^{4}	ND, 0.1
3E70	2-SS	$< 1.0 \times 10^{-9}$	15^{4}	NA
3E71	2-SS	4.2×10^{-8}	15^{2}	ND, 0.1
3E72	2-SS	9.4×10^{-9}	15^{2}	ND, 0.1
3E73	2-CS	$< 1.0 \times 10^{-9}$	30^{3}	NA
3E74	2-CS	$< 1.0 \times 10^{-9}$	15^{4}	ND, 0.1
3E75	2-CS	6.8×10^{-9}	15^{2}	ND, 0.1
3E76	2-CS	9.4×10^{-9}	15^{3}	ND, 0.1
3E77	2-CS	3.2×10^{-8}	30^{2}	ND, 0.1
3E78	2-CS	$< 1.0 \times 10^{-9}$	15^{4}	NA

Table IV continued

3E55	3-SS	2.5×10^{-8}	30^{3}	ND, 0.1
3E56	3-SS	3.4×10^{-8}	15^{4}	NA
3E57	3-SS	3.2×10^{-8}	15^{4}	0.2
3E58	3-SS	$< 1.0 \times 10^{-9}$	15^{2}	ND, 0.1
3E59	3-SS	$< 1.0 \times 10^{-9}$	30^{3}	NA
3E60	3-SS	No Test	15^{2}	ND, 0.1
3E61	3-CS	$< 1.0 \times 10^{-9}$	30^{3}	ND. 0.1
3E62	3-CS	$< 1.0 \times 10^{-9}$	15^{2}	ND, 0.1
3E63	3-CS	$< 1.0 \times 10^{-9}$	15^{4}	ND, 0.1
3E64	3-CS	$< 1.0 \times 10^{-9}$	15^{2}	ND, 0.1
3E65	3-CS	4.2×10^{-8}	30^{3}	NA
3E66	3-CS	No Test	15^{4}	NA
3E91	4-SS	6.6×10^{-8}	30^{3}	ND, 0.1
3E92	4-SS	2.5×10^{-8}	15^{4}	NA
3E93	4-SS	8.0×10^{-8}	15^{2}	ND, 0.1
3E94	4-SS	6.2×10^{-8}	30^{3}	NA
3E95	4-SS	5.6×10^{-8}	15^{4}	NA
3E96	4-SS	5.2×10^{-8}	15^{2}	ND, 0.1
3E97	4-CS	3.2×10^{-8}	15^{4}	NA
3E98	4-CS	1.1×10^{-7}	15^{2}	ND, 0.1
3E99	4-CS	5.2×10^{-8}	15^{3}	ND, 0.1
3E100	4-CS	5.8×10^{-8}	30^{3}	ND, 0.1
3E101	4-CS	3.0×10^{-8}	15^{2}	NA
3E102	4-CS	2.6×10^{-8}	15^{4}	NA
3E37	5	1.2×10^{-8}	30^{3}	NA
3E38	5	8.4×10^{-9}	30^{3}	NA
3E39	5	8.4×10^{-9}	15^{4}	NA
3E40	5	8.6×10^{-9}	15^{4}	NA
3E41	5	1.0×10^{-8}	15^{3}	ND, 0.1
3E42	5	7.4×10^{-9}	30^{3}	NA
3E43	5	9.2×10^{-9}	15^{4}	ND, 0.1
3E44	5	8.8×10^{-9}	15^{2}	NA
3E45	5	1.2×10^{-8}	30^{3}	ND, 0.1
3E46	5	8.0×10^{-9}	15^{2}	ND, 0.1
3E47	5	7.2×10^{-9}	15^{2}	ND, 0.1
3E48	5	8.2×10^{-9}	15^{4}	ND, 0.1
			15^{2}	ND, 0.1

Table iV continued

3E25	6	1.1×10^{-8}	15[2]	ND[5], 0.1
3E26	6	$< 1.0 \times 10^{-9}$	15[4]	NA[6]
3E27	6	1.1×10^{-8}	15[4]	ND, 0.1
3E28	6	1.2×10^{-9}	15[3]	NA
3E29	6	$< 1.0 \times 10^{-9}$	30[4]	NA
3E30	6	7.8×10^{-9}	15[3]	NA
3E31	6	9.0×10^{-9}	30[3]	NA
3E32	6	$< 1.0 \times 10^{-9}$	30[2]	ND, 0.1
3E33	6	7.2×10^{-9}	15[3]	ND, 0.1
3E34	6	8.8×10^{-8}	30[2]	NA
3E35	6	1.1×10^{-9}	15[2]	ND, 0.1
3E36	6	2.4×10^{-9}	15[2]	ND, 0.1

1. SS 304 stainless steel filler rod used on welds
   CS No filler rod used. Carbon steel weld metal only.

2. Cycle: Pump cold to 6400 psi. Turn on heat. Pressure → 15,000 psi, temperature → 2250°F.

3. Cycle: Pump cold to 9600 psi. Turn on heat. Pressure → 30,000 psi, temperature → 2250°F.

4. Cycle: Pressurize cold to 1000 psi. Turn on heat. Temperature → 2250°F, pressure 11,000 psi.
   Turn on compressor. Pressure → 15,000 psi.

5. ND = none detected, less than

6. NA = not analyzed

7. IN-100 R.E.P. base powder analysis, Ppm, wt.: Nitrogen ND, 10; Oxygen 50; Argon ND, 0.1; Hydrogen 3.1; Helium ND, 2

Table V

Expected Argon Contamination Level vs
Initial 1 Atmosphere He Leakage Rate
for ~ 27 Gram Compact (Net)

	1000 atm Ar			675 atm Ar[1.]			450 atm Ar[2.]		
Leak Rate 1 atm. He Std cc/sec	Leak Rate Std cc/sec	1000 sec Leakage Fl. cc-atm	Ppm Argon 27 Gram compact	Estimated Leak Rate Std cc/sec	1000 sec Leakage Fl. cc-atm	Ppm Argon 27 Gram compact	Estimated Leak Rate Std cc/sec	1000 sec Leakage Fl. cc-atm	Ppm Argon 27 Gram compact
10^{-7}	6×10^{-3}	6	406	3×10^{-3}	3	203	1.6×10^{-3}	1.6	108
10^{-8}	10^{-3}	1	67	$.5 \times 10^{-3}$	0.5	34	2.7×10^{-4}	0.27	18
10^{-9}	10^{-5}	.01	0.67	$.5 \times 10^{-5}$	0.005	.34	2.7×10^{-6}	2.7×10^{-3}	.18

1. 675 atm corresponds to 9600 psi. See Note 3, Table IV.

2. 450 atm corresponds to 6400 psi. See Note 2, Table IV.

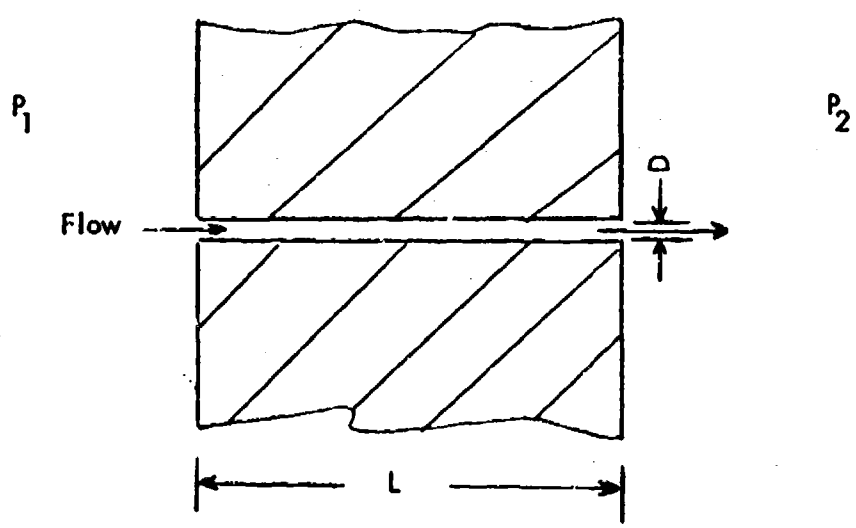

P_1 = exterior pressure (outside can)

P_2 = interior pressure (inside can)

L = capillary length = can wall thickness

D = capillary diameter = "size" of leak

$P_1 \gg P_2$ for cases of interest

Figure 1. Idealized capillary leak.

Figure 2. Argon contamination level vs. total leakage flow for various compact sizes.

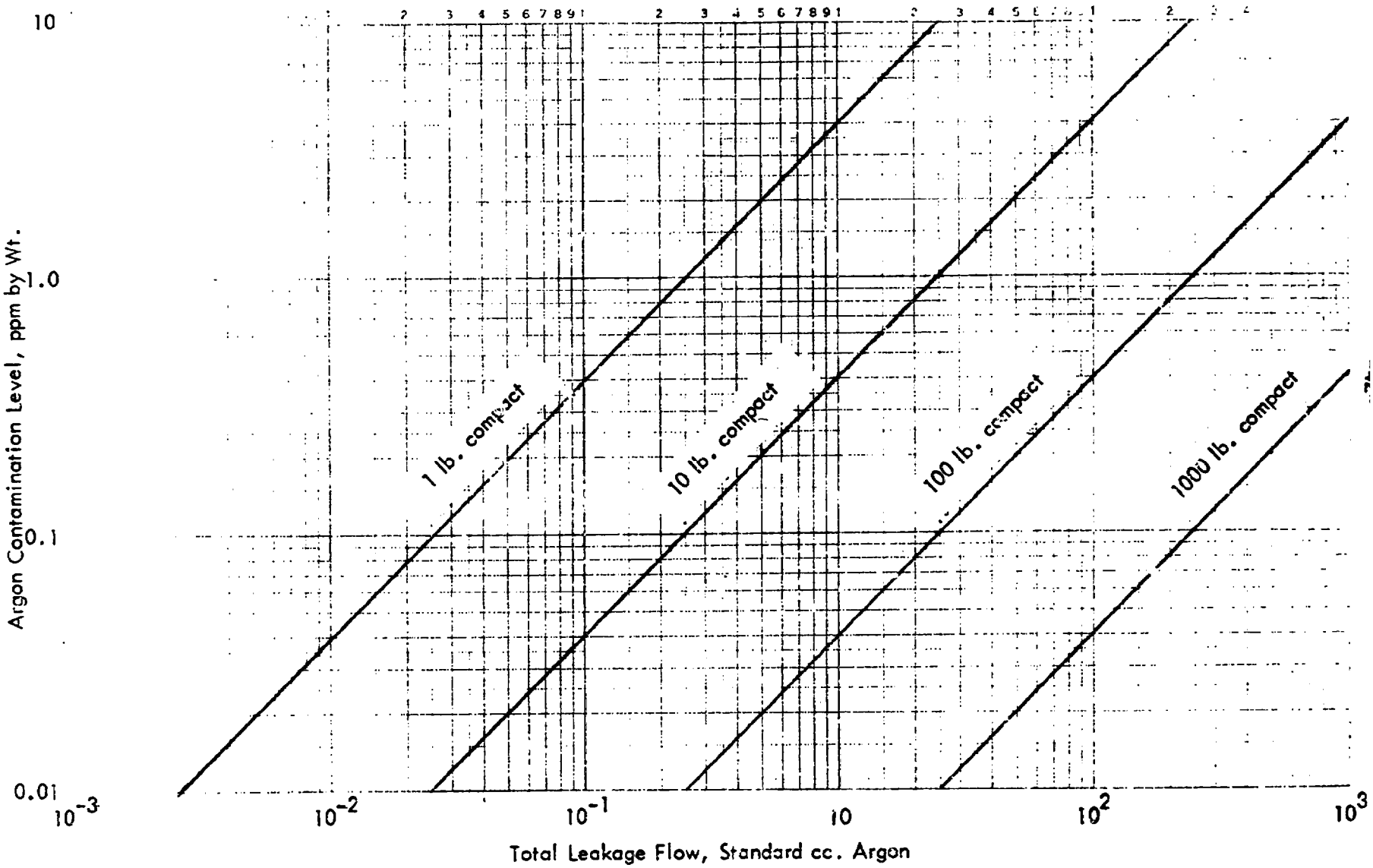

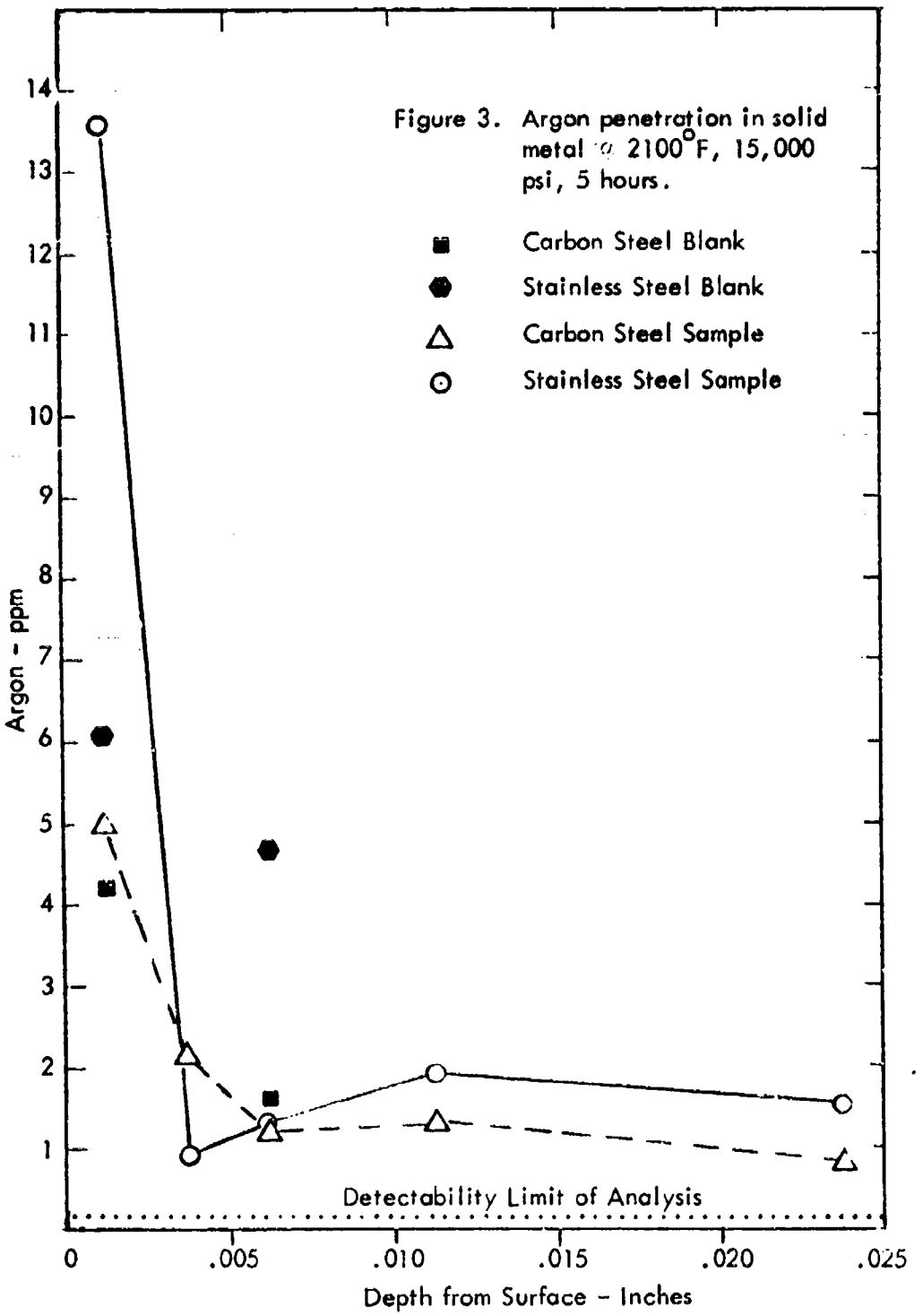

Figure 3. Argon penetration in solid metal @ 2100°F, 15,000 psi, 5 hours.

Figure 4. Test Can Designs

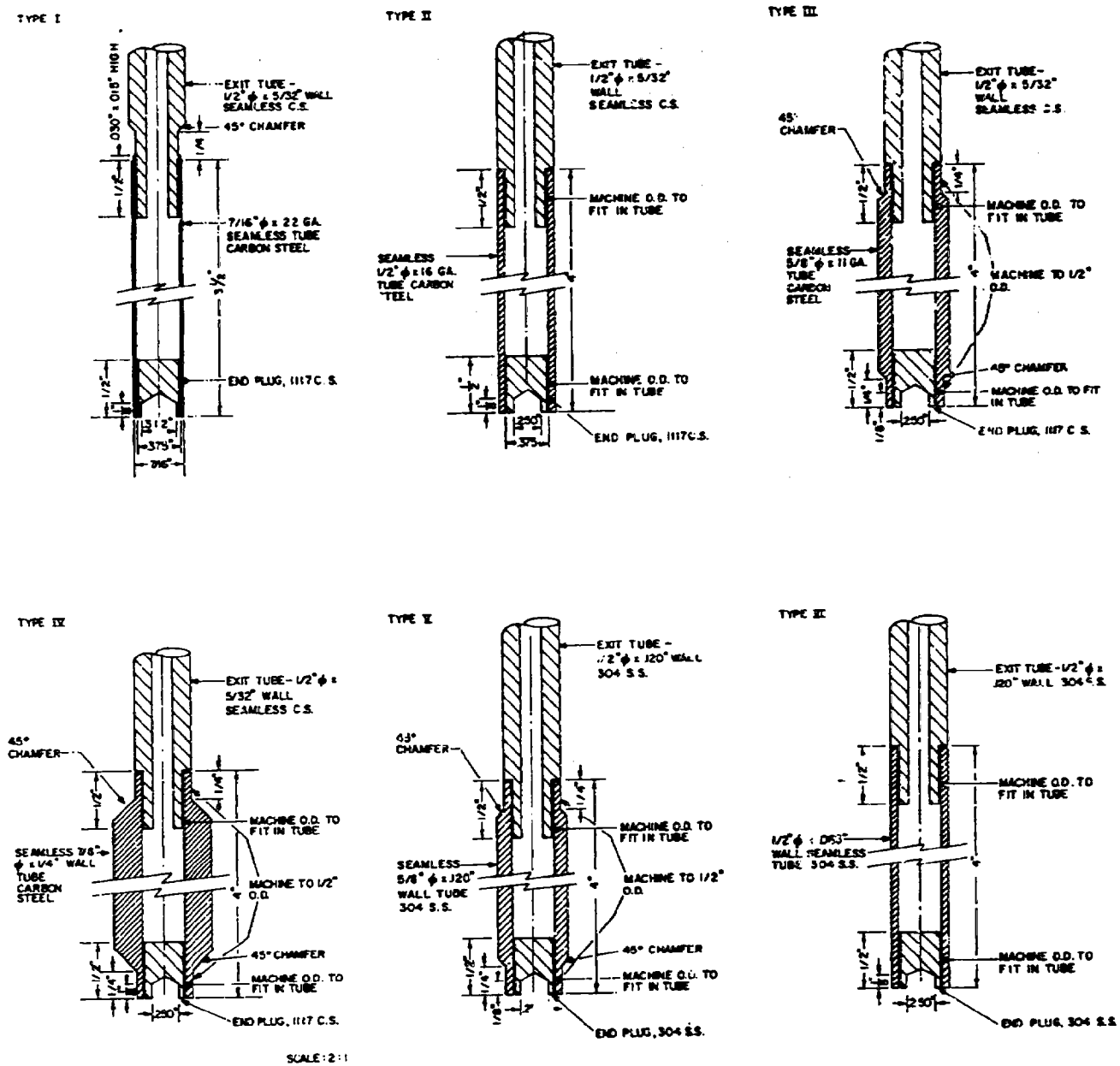

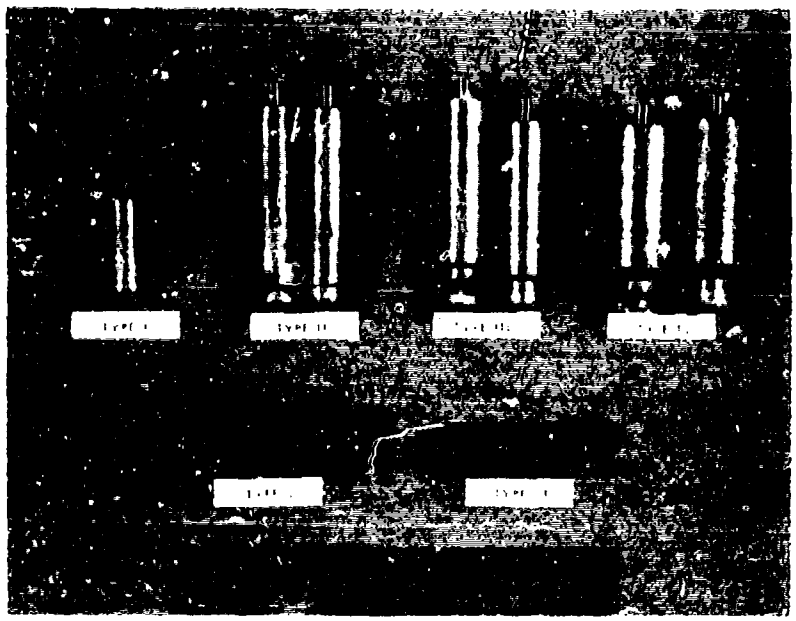

Figure 5. HIP'ed compacts after machining argon analysis samples.

TASK II

SOLIDIFICATION RESEARCH

R. Mehrabian
P.A. Joly
D. Apelian
D.R. Geiger
M.C. Flemings

INTRODUCTION

In this part of the program work was carried out to develop and evaluate new processes for atomization of metal powders. A summary of that work is reported here in three parts:

In Part I results of the investigation evaluating powders of iron, nickel, and cobalt base alloys made by different atomization processes are reported. In addition a heat flow analysis is presented that permits calculation of solidification times during atomization.

Part II describes a new type of atomization process developed in this investigation. The process combines filtration of metal alloys with powder production. Experiments were carried out in a laboratory apparatus with aluminum alloys. A patent application, #SN 310, 652, based on this process was filed through the M.I.T. patent office on November 29, 1972.

Part III describes a refining process developed in this program that utilizes atomization to separate segregated liquid from a partially solidified, vigorously agitated, alloy slurry. A patent application, #SN 221,796, based on this process was filed through the M.I.T. patent office on January 28, 1972.

PART I

ABSTRACT

Prealloyed powders of Maraging 300, IN-100, and Mar-M-509 alloys made by different atomization techniques are compared with respect to chemistry, size, morphology, and microstructure. Depending on the process employed and the size and morphology of the powders produced, measured oxygen contents and secondary dendrite arm spacings vary from 40 p.p.m. to 2000 p.p.m. and 2 to 15μ, respectively.

For the Maraging 300 alloy the relationship $d = 39.8\varepsilon^{-0.30}$ between secondary dendrite arm spacing, d, and local average cooling rate, ε, is established. A simple heat flow analysis is presented which permits calculation of heat transfer coefficients and solidification times of powders using this relationship. For example, a heat transfer coefficient $h = 10^{-2}$ $cal/cm^2 sec^{\circ}C$ is calculated for steam atomization of coarse Maraging 300 alloy powders.

I. INTRODUCTION

The two important structural parameters influencing properties of components made by direct casting or via atomization are grain size and dendrite arm spacing. While fine grain size generally improves room temperature properties, large grains sometimes with specified orientations, are preferred in high temperature applications. On the other hand, the dendritic structure within the cast grains has as great, or greater, influence on properties at all temperatures. Regions between dendrite arms are usually rich in solute, contain equilibrium and/or non-equilibrium second phases and microporosity. With decreasing dendrite arms spacings homogenization of solute segregation becomes commercially feasible, and second phases (inclusions and microporosity) become finer and more evenly distributed. Experimental evidence available for a variety of cast alloys indicates that dendrite arm spacing is influenced only by local average cooling rate or "local solidification time."* Thus, refinement of dendritic structure by increasing the rate of heat extraction during solidification of castings has become of foremost importance in solidification technology.

The most important common advantage of parts produced by compaction of atomized powders over parts directly cast to shape is the fine dendritic structures of the powders. New

* "Local solidification time" is defined as time at a given location in a casting between initiation and completion (or near completion) of solidification. It is inversely proportional to local average cooling rate at that location.

atomization techniques, developed in the past decade, are currently being applied to production of high strength, highly alloyed materials. Whether the powder metallurgy route will succeed in replacing the casting and ingot approach, in these more complex alloys, depends on the chemical integrity of the powders which influences their subsequent successful consolidation into fully dense, heat treatable parts.

The aim of this investigation was: (1) to study the relationship between rate of heat extraction during solidification and structures of atomized powders, and (2) to compare the structural features and chemical intergrity of highly alloyed materials cast by different atomization processes. The three alloys studied were iron base Maraging 300 alloy, nickel base IN-100 alloy, and cobalt base MAR-M-509 alloy. In lieu of direct experimental temperature measurements during solidification of atomized powders, solidification times versus powder particle size are calculated using heat flow expressions coupled with an experimental relationship developed between local average cooling rates and secondary dendrite arm spacings of Maraging 300 alloy. Prealloyed powders of the three alloys produced by steam, inert gas, vacuum (soluble gas), rotating electrode, and spin atomization are compared with respect to their chemistry, size, morphology, and segregate spacings.

II. EXPERIMENTAL PROCEDURE

A. Maraging 300 Alloy Cast at Different Cooling Rates

The effect of a range of cooling rates, 0.1°C/sec to 10^3°C/sec, on the secondary dendrite arm spacings of Maraging 300 alloy was determined. The various cooling rates were obtained by levitation melting and casting of small droplets (1 to 2 grams), unidirectional solidification of a 2.5 Kg ingot, and vacuum melting of 700 gram charge in an alumina crucible and furnace cooling.

Levitation Melting and Casting

Figure 1 is a sketch of the levitation melter and associated apparatus. The details of this apparatus have previously been described (1). Droplets of the Maraging 300 alloy were levitated inside the glass tube in an atmosphere of helium. The temperature of the droplets was continuously monitored using a two-color optical pyrometer. The molten levitated droplets were solidified and cooling rates measured using the following techniques:

(a) Gas Quenching. With sufficiently high flow rates of hydrogen or helium, droplets were solidified while levitated. Measured cooling rates, via the two-color optical pyrometer were of the order of 1 - 15°C/sec.

(b) Oil Quenching. Somewhat higher cooling rate was obtained by liquid quenching. The liquid quench tank was placed

below the exit port shown in Figure 1; the power to the levitation coil was turned off, and the charge dropped through the plastic seal into the liquid. A cooling rate of $\sim 140^{o}C/sec$ has previously been calculated for oil quenching (2).

(c) Chill Casting. Chill castings in a copper mold with plate shaped mold cavity of 0.08" thickness, inserted in the turntable in the enclosure in Figure 1, were made and cooling rates on the order of $10^{3o}C/sec$ were measured as previously described. (1)

Unidirectional Casting

A 2" by 2" by 5" tall unidirectional ingot of the Maraging 300 alloy was cast using a composite mold of CO_2 sand and insulating molding material, Fiberchrome. A water-cooled stainless steel chill was located at the base opening of the mold. Thermal measurements were made by utilization of four Pt/Pt-10% Rh silica shielded thermocouples located along the length of the ingot mold.

Vacuum Melting and Furnace Cooling

Several specimens of Maraging 300 alloy weighing approximately 700 grams were vacuum melted in an alumina crucible. These samples were solidified inside the crucible by decreasing the power input to the furnace at different rates and temperature profiles were recorded with a Pt/Pt-10% Rh thermocouple inserted in the melt.

B. Atomization Processes

Prealloyed vacuum cast ingots of Maraging 300, IN-100 and MAR-M-509 alloys were sent to different commercial establishments for atomization. The powders were made by:

(a) Inert gas atomization. The prealloyed ingot is vacuum remelted and atomized by a stream of high purity argon gas.

(b) Rotating electrode process. The end of a consumable rotating electrode of the alloy is arc melted in an inert atmosphere and fine droplets are flung off by centrifugal force.

(c) Spin atomization. A new propriatory process where atomization is achieved by pressurizing the whole melt as opposed to disintegration of a liquid metal stream by a quenching medium.

(d) Steam atomization. The prealloyed ingot is remelted in an atomsphere and atomized by a stream of low pressure steam.

(e) Vacuum atomization. The remelted alloy is pressurized and saturated with hydrogen. Atomization is obtained through a "pressure nozzle" operating between the hydrogen filled chamber and a vacuum chamber.

Powder particles of the three alloys, made by the different processes listed above, were analyzed by routine chemical and vacuum fusion techniques. The powders were also characterized by morphology and size distribution. Finally, standard optical metallographic and SEM techniques were used to study internal and surface structures of the powders.

III. RESULTS AND DISCUSSION

A. D.A.S. Versus Cooling Rate

The effect of cooling rate during solidification on secondary dendrite arm spacings of Maraging 300 alloy is shown in Figures 2 and 3. Generally for a wide variety of cast alloys, dendrite arm spacing is found to be inversely proportional to local average cooling rate to an exponent (or directly proportional to "local solidification time" to the same exponent). (1, 3, 4) The relationship for a given alloy is:

$$d = at_f^{\,n} = b\,(\varepsilon)^{-n} \qquad (1)$$

where d is secondary dendrite arm spacing, a and b are constants t_f is "local solidification time", ε is local average coooling rate, and the exponent, n, is usually in the range of 1/3 to 1/2.

Figure 2 shows how the microstructure of the Maraging 300 alloy is refined by increasing the local average cooling rate during solidification. Figure 3 is a plot of the secondary dendrite arm spacings versus local average cooling rates on a log-log plot. The exponent, n, in equation (1) determined for this alloy is 0.30.

B. Evaluation of Atomized Powders

Powders of the three alloys processed by different atomization techniques were characterized by chemical purity, morphology, size, and secondary dendrite arm spacings. Results of this study are presented in Table I and Figures 4-6. Examination of this data permits the following observations:

Gas Contents

Powders of all three alloys made by REP, spin, or vacuum atomization processes have oxygen contents less than 100 ppm. The argon atomized fine powder is slightly higher in oxygen content at 170 ppm. It appears that spin atomized powders are the cleanest with respect to argon, nitrogen, and hydrogen contents, while, as expected, steam atomization resulted in the highest oxygen and nitrogen contents.

Powder Size and Morphology

Both the REP and spin atomized powders were spherical in shape and had relatively narrow size ranges. For example, in the spin atomized Maraging 300 alloy, median particle size ∿430μ, 68% by weight of the particles were in the 370 to 490μ size range. Figure 4 shows scanning electron micrograph views and a photomicrograph of a polished and etched cross-section of spin atomized Maraging 300 alloy powder. The same type of smooth, well rounded, and uniform powder particles were

also obtained in the Mar-M-509 alloy.

The vacuum atomization process, while leading to production of clean powders, Table I, has little control over powder shape. The powders consist of spheres and flakes. The inert gas atomized powders are generally spherical in shape with finer particles attached to coarser particles. Figure 5 compares scanning electron micrograph views of representative powder particles of IN-100 alloy produced by spin, vacuum, and inert gas atomization processes.

Steam atomization produces coarse, spherical particles, with some included porosity, in Maraging 300 alloy. However, it is not a suitable process for Mar-M-509 and IN-100 alloys. The powders of the latter two alloys are hollow spheres and flakes, and thin sharp flakes, respectively. The flakiness of the powders is caused by the high surface oxidation of the broken liquid streams preventing their subsequent spherodization by surface tension forces.

Dendrite Arm Spacing

Figure 6 shows the measured secondary dendrite arm spacings in the Maraging 300 alloy powders obtained by different atomization processes. As expected, local average cooling rate, hence measured secondary dendrite arm spacing, is influenced primarily by the size of the particles, and to a lesser extent the coolant environment employed. For

example, average secondary dendrite arm spacings in spin and vacuum atomized powders is $\sim 5\mu$, and in coarse powders made by steam or argon atomization, it is $\sim 10\mu$ (see Table I for powder particle sizes). Results of dendrite arm spacing measurements in both the IN-100 and the Mar-M-509 alloys show the same trend.

C. Heat Flow During Atomization

During solidification of small spherical alloy droplets heat flow is interface controlled. Using Newton's law of cooling, coupled with an overall heat balance, equations (A1) and (A2) in the Appendix, an expression for radial fraction liquid remaining in a solidifying droplet versus time is obtained:

$$r/R = \{1-Ct\}^{1/3} \qquad (2)$$

where:

$$C = \frac{3h(T_M - T_o)}{R\rho_s H} \qquad (3)$$

Volume fraction liquid remaining is then equal to 1-Ct. All the terms in equations (2) and (3) are defined in the Appendix.

The combined radiation and convection heat transfer coefficient in equation (3) can be calculated using equation (A1) in the Appendix and data generated in Figure 3. For

example, for the Maraging 300 alloy, measured secondary dendrite arm spacing of a steam atomized droplet, 1 mm in diameter, is $\sim 7\mu$. From Figure 3 the corresponding cooling rate is $\sim 10^{3}$ °C/sec. Using the values of Fe-25%Ni alloy (1, 2) for ρ, and C_p, and an atomization temperature of 1500°C, the value of $h = 10^{-2}$ cal/cm^2 sec°C is calculated.

Knowing the value of the heat transfer coefficient permits prediction of solidification time from equations (2) and (3). Figure 7 shows, for Maraging 300 alloy, calculated plots of radial and volume fractions solidified versus time for different size particles.

The liquidus temperatures of the alloys used in this study are high enough that most heat flow during solidification is by radiation. To estimate contribution of radiation cooling to the heat transfer coefficient, equations developed by Szekely and Fisher (6) are used in the Appendix. As expected contribution of radiation to the heat transfer coefficient, at a given temperature, is dependent on the emissivity of the droplet. The emissivity may vary from 0.5 to 0.95 depending on whether the surface of the droplet is oxidized or not (7). For an emissivity value of 0.8 for Maraging 300 alloy a heat transfer coefficient of $h = 6.65 \times 10^{-3}$ cal/cm^2-sec°C is calculated. Hence, radiation cooling is 66% of the total for the case considered.

In general, heat transfer coefficient, h, during atomization is influenced by convection, type of coolant employed,

interaction of the coolant with surface of the sample, and temperature. A change in coolant environment, resulting in a sudden change in the heat transfer coefficient, can lead to duplex dendritic structures in powder particles. Figure 8(a) shows a portion of a steam atomized coarse powder of Maraging 300 alloy with the finer dendrites on the outside layer of the droplet and the coarser on the inside. It appears that the particle was only partially solidified in flight. The coarser structure must have resulted from stagnant steam formation around the particle as it completed solidifying in the quench water bath below. A second type of structural peculiarity caused by uneven rate of heat extraction from the surface of a solidifying powder particle is shown in Figure 8(b). In this case a large grain must have solidified from one side of the particle. Intersection of the polished surface with the convex interface of this grain has resulted in the structure observed.

Whether heat removal during solidification is controlled by convection or radiation, a value for the heat transfer coefficient and hence solidification time can be calculated following the procedure outlined here. Atomized droplets generally solidify in a "mushy" manner, rather than the plane front solidification assumed herein. The corn-on-the-cob surface of the spin atomized powder in Figure 4(b) is due to existing liquid at the droplet surface feeding shrinkage near the end of solidification.

IV. CONCLUSIONS

1. Secondary dendrite arm spacing in Maraging 300 alloy is proportional to local average cooling rate to an exponent of -0.30.
2. Prealloyed powders of Maraging 300, IN-100, and Mar-M-509 alloys were spheres and/or flakes of 75 to 2500μ in average size, had oxygen contents of 40 p.p.m. to 2000 p.p.m. and dendrite arm spacings of 2 to 15μ, depending on the atomization process.
3. REP, spin, and vacuum atomized powders have oxygen contents consistently less than 100 p.p.m.. The first two are spherical in shape with relatively narrow size ranges. Vacuum atomization while lending to production of clean powders has little control over powder shape.
4. An empirical relationship between secondary dendrite arm spacings and cooling rates coupled with a simple heat flow analysis permits accurate estimates of heat transfer coefficients and cooling rates during atomization.
5. Cooling rates during atomization of Maraging 300 alloy by different processes are in the range of $\sim 10^2$ to $\sim 10^{4}$ ^{o}C/sec with resulting dendrite arm spacings of 4 to 13μ. Calculated heat transfer coefficient for steam atomization of the alloy is 10^{-2} cal/cm^{2}sec^{o}C.

REFERENCES

1. W.E. Brower, Jr., R. Strachan, M.C. Flemings, "Effect of Cooling Rate on Structure of Ferrous Alloys", Cast Metals Research Hournal, v. 6, No. 4, 1970, pp. 176-180.

2. W.E. Brower, Jr., "Solidification Structure Fracture Relations in Inclusion Bearing Iron", Ph.D. Thesis, Department of Metallurgy and Materials Science, Massachusetts Institute of Technology, 1969.

3. T.F. Bower, H.D. Brody, M.C. Flemings, "Measurements of Solute Redistribution in Dendritic Solidification", Trans. Met. Soc., AIME, v. 236, 1966, pp. 624.

4. M.C. Flemings, D.R. Poirier, R.V. Barone, H.D. Brody, "Microsegregation in Iron-Base Alloys", J.I.S.I., v. 208, 1970, pp. 371.

5. R.K. Robinson, "Development of P/M Cobalt-Base Alloys Using Rapidly Quenched, Pre-Alloyed Powders", Sc.D. Thesis, Department of Metallurgy and Materials Science, Massachusetts Institute of Technology, 1973.

6. J. Szekely, R.J. Fisher, "On the Solidification of Metal Spheres Due to Thermal Radiation at the Bounding Surface", Met. Trans, v. 1, 1970, p. 1480.

7. H.C. Hottel, A.F. Sarofim, Radiative Transfer, McGraw-Hill Booi Co., 1967.

APPENDIX

Heat Flow During Atomization

Newton's law of cooling for a small spherical droplet of radius R with "h controlled" heat transfer is written:

$$q)_{r=R} = 4\pi R^2 h(T-T_o) = 4/3\pi R^3 C_p \frac{dT}{dt} \qquad (A1)$$

where; q = rate of heat flow at the droplet-coolant medium interface, cal/sec

R = radius of the droplet, cm

T = temperature of the droplet, ^oC

T_o = medium temperature, ^oC

ρ = density of the alloy, g/cm^3

C_p = specific heat of the alloy, cal/g^oC

h = heat transfer coefficient, <u>radiation plus convection</u>, $cal/cm^2 sec^oC$

$dT/dt = \varepsilon$ = cooling rate at temperature T, $^oC/sec$

Assuming that the rate of heat extraction during solidification is the same as during cooling of the droplet prior to solidification, the following heat balance can be established:

$$4\pi R^2 h(T_M-T_o) = 4/3\pi R^3 C_p \rho \frac{dT}{dt} = -4\pi r^2 \rho_s H \frac{dr}{dt} \qquad (A2)$$

where:

T_M = melting temperature of the droplet, ^oC

r = radial position of the solid front, cm

H = latent heat of fusion, cal/g

dr/dt = solidification velocity, negative, cm/sec

Equation (A2) further assumes that the size of the mushy zone in the alloy is small enough that solidification essentially takes place at a single temperature. With initial boundary conditions of r=R, at t=0, equation (A2) is integrated to obtain:

$$r/R = \{ 1-Ct \}^{1/3} \qquad (A3)$$

where:

$$C = \frac{3h(T_M-T_o)}{R\rho_s H} \qquad (A4)$$

For complete solidification of the droplet, r=0 and t_f=1/C.

Szekely and Fisher (6) have used a similar approach by considering heat flow due to radiation only. Using Stefan's law of radiation, equation (A3) still applies, with a new constant:

$$C' = \frac{3\sigma e(T_M^4-T_o^4)}{R\rho_s H} \qquad (A5)$$

where:

σ = Boltzmann's constant

e = emissivity

This new constant, C', is the equivalent of C, if the combined convection plus radiation transfer coefficient in

equation (A4) is replaced by:

$$h_{rad} = \sigma e (T_M + T_o) \ (T_M^{\ 2} + T_o^{\ 2}) \qquad \text{(A6)}$$

TABLE I - POWDER DESCRIPTION

	Atomization Process	Median size μ	Gas content, p.p.m. O	N	H	Ar	Shape of powders
Cobalt base alloy MAR-M-509 type alloy	spin atomized	340	45	<10	<1.0	<.2	solid spheres
	vacuum atomized	110	250-310*	10-100	5-10	<.2	flakes, solid spheres[o]
	steam atomized	2000	200-1200	100-600	11-24	<.2	flakes, hollow spheres[o]
Nickel base alloy IN-100	spin atomized	400	85	<10	<1.0	<.2	solid spheres
	vacuum atomized	~200	50	-	5	<.2	flakes, solid spheres
	R.E.P. atomized	170	70	10	5.6	.3	solid spheres
	argon atomized fine powder	75	170	7	17	1.6	solid spheres, with fine particles attached to coarser particles
Iron base alloy Maraging steel VM-300	spin atomized	430	42	-	-	-	solid spheres
	vacuum atomized	300	53	10	5	<.2	flakes, solid spheres
	R.E.P. atomized	200	40	-	5	<.2	solid spheres
	steam atomized	1980	150-2000	-	-	-	solid spheres with porosi
	argon atomized coarse powder +	2590	630	-	-	-	solid spheres with porosi

* probably from retained slag.

\+ further quenched in water tank.

[o]From R. Robinson (5).

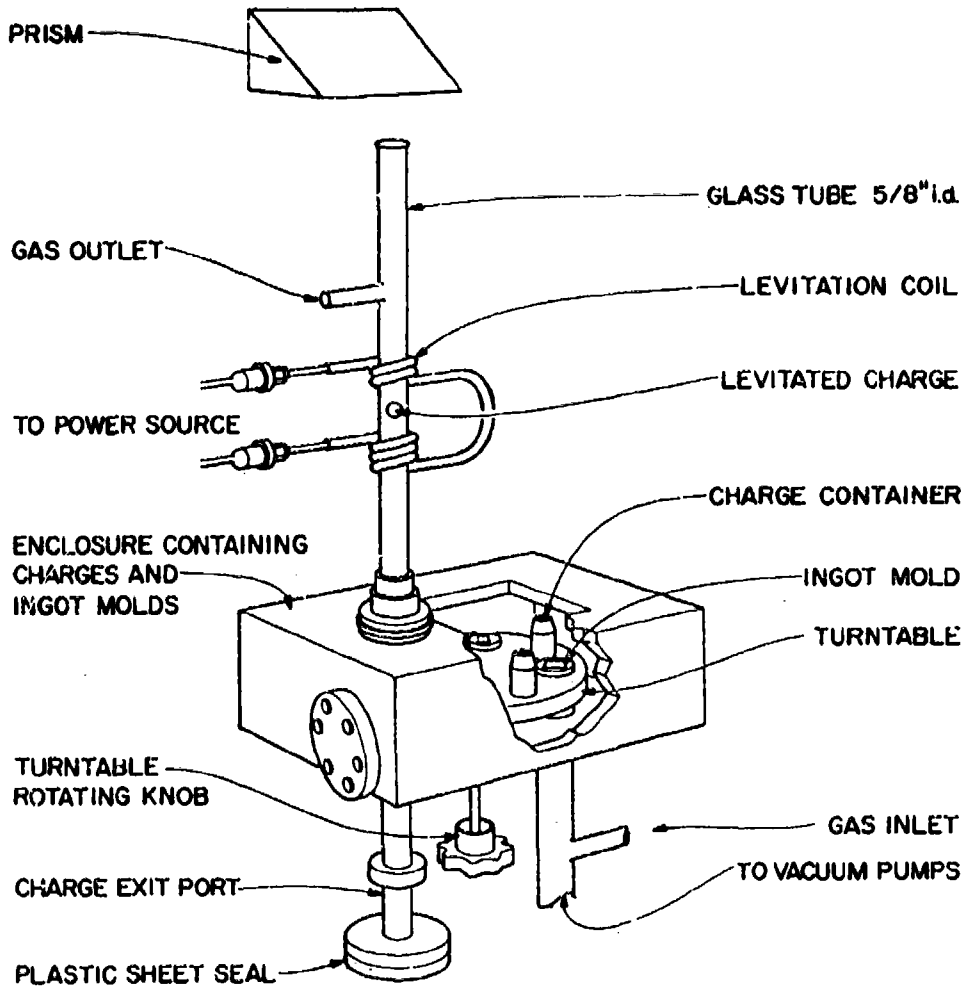

Figure 1. Sketch of levitation melting and casting apparatus.

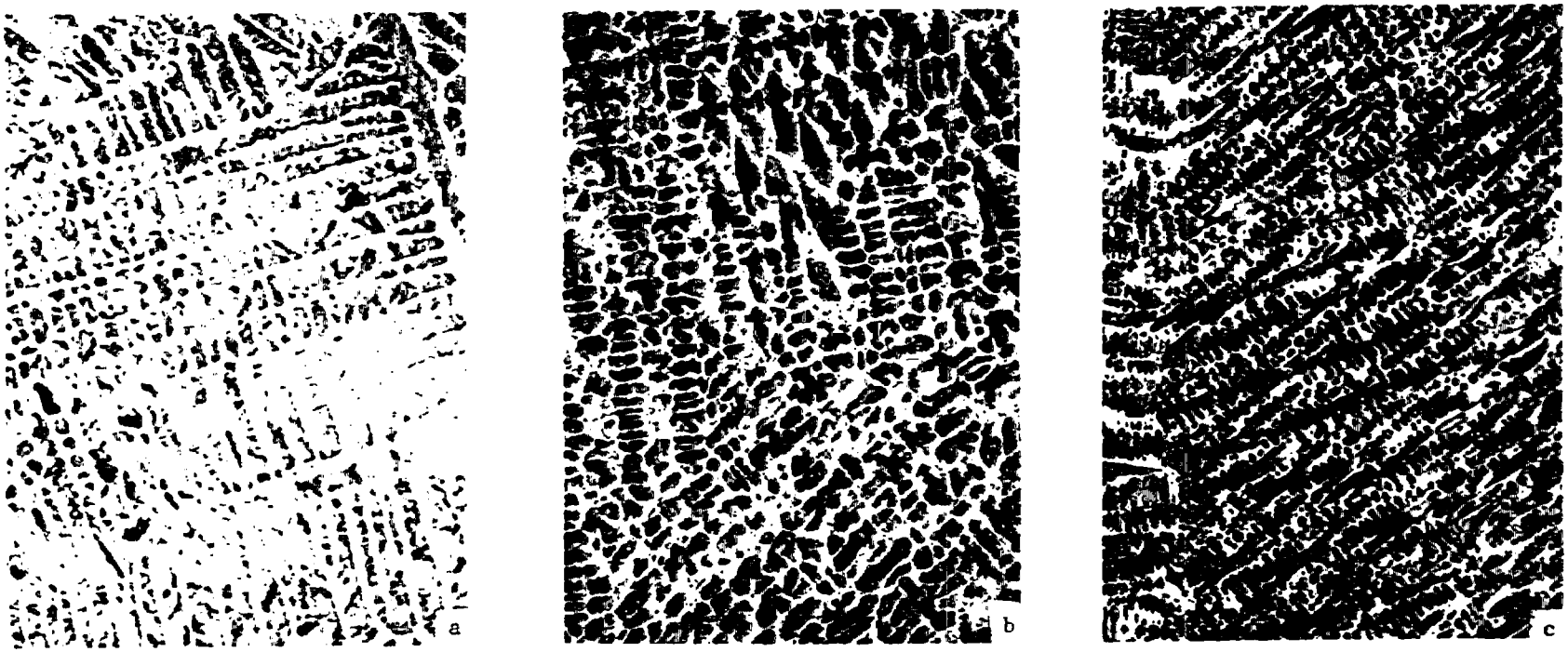

Figure 2. Variation of microstructure with cooling rate for Maraging 300 alloy. (a) Gas quench, (b) liquid quench, (c) chill cast. Magnification 200X.

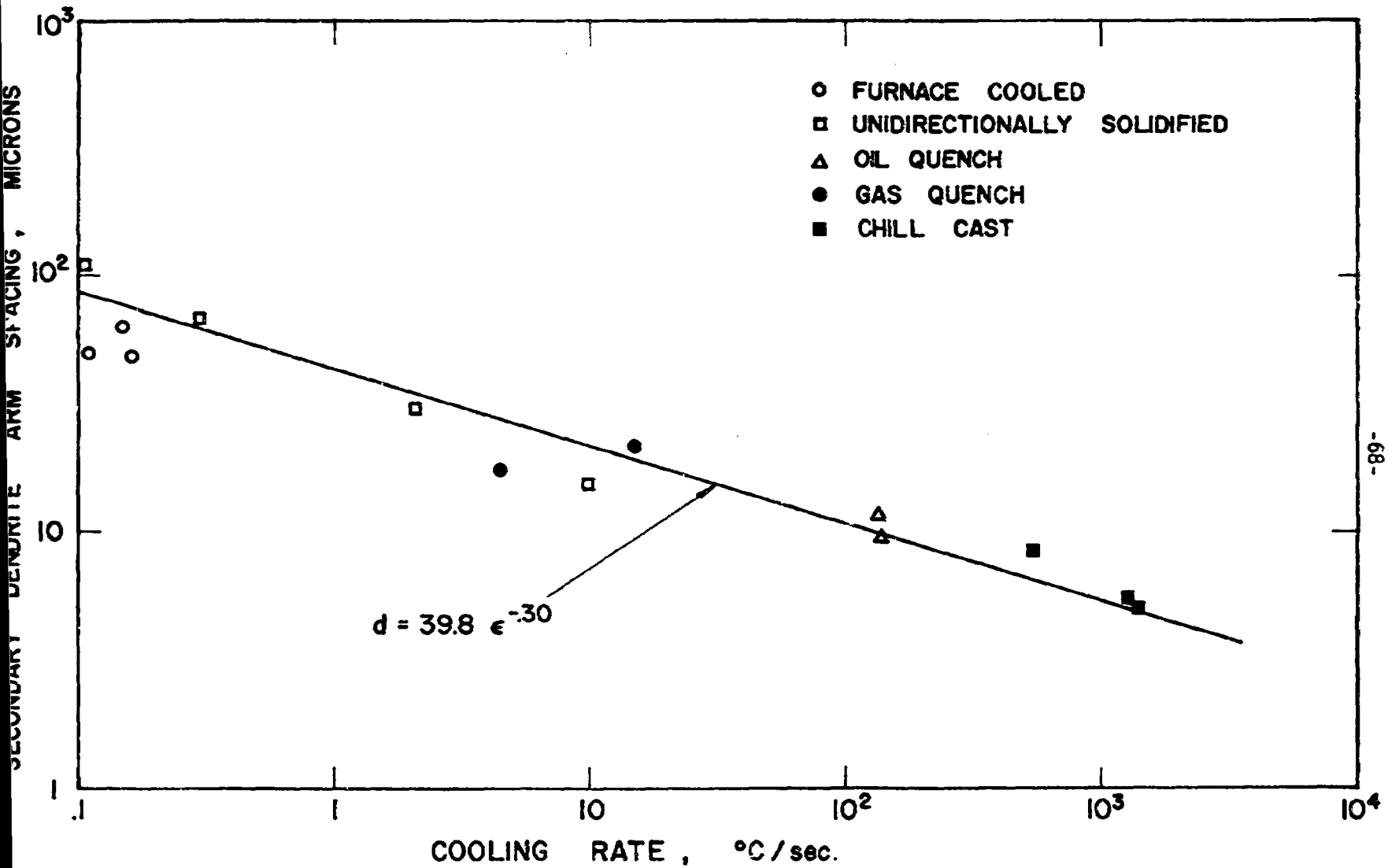

Figure 3. Secondary dendrite arm spacing versus cooling rate in Maraging 300 steel alloy.

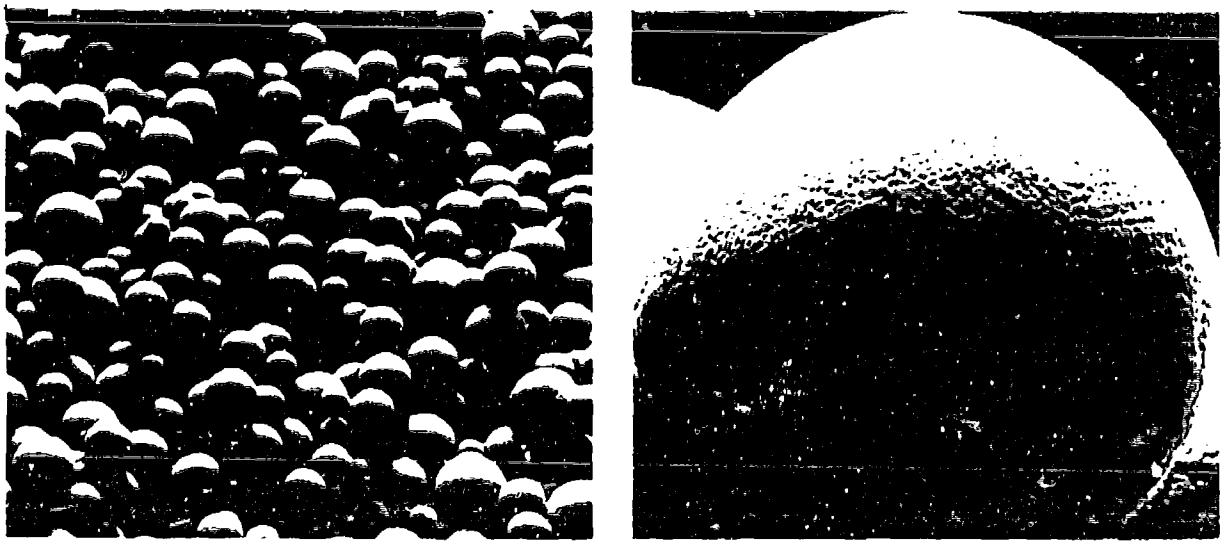

a b

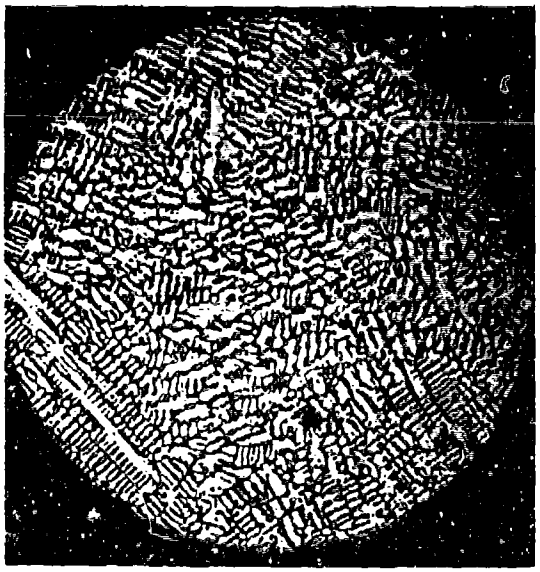

c

Figure 4. Spin atomized powders of Maraging 300 steel alloy; (a) and (b) are SEM micrograph views at 19X and 240X, respectively, (c) is a photomicrograph of a polished and etched cross-section at 200X.

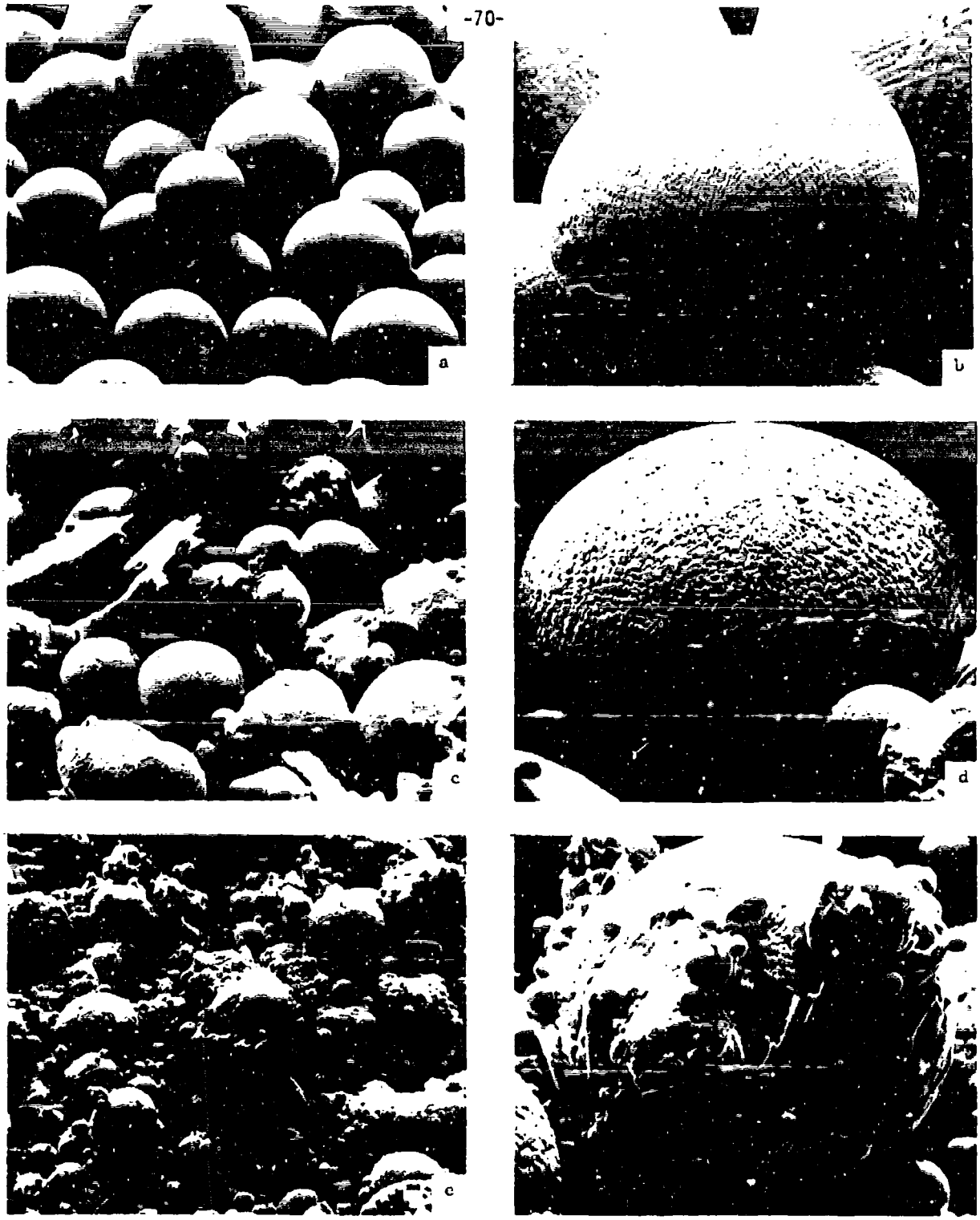

Figure 5. SEM micrograph views of atomized powder particles of IN-100 alloy; (a) and (b) show spin atomized powders at 56X and 215X, respectively, (c) and (d) show vacuum atomized powders at 57X and 22 5X, respectively, (e) and (f) show inert gas atomized fine powders at 210X and 1050X, respectively.

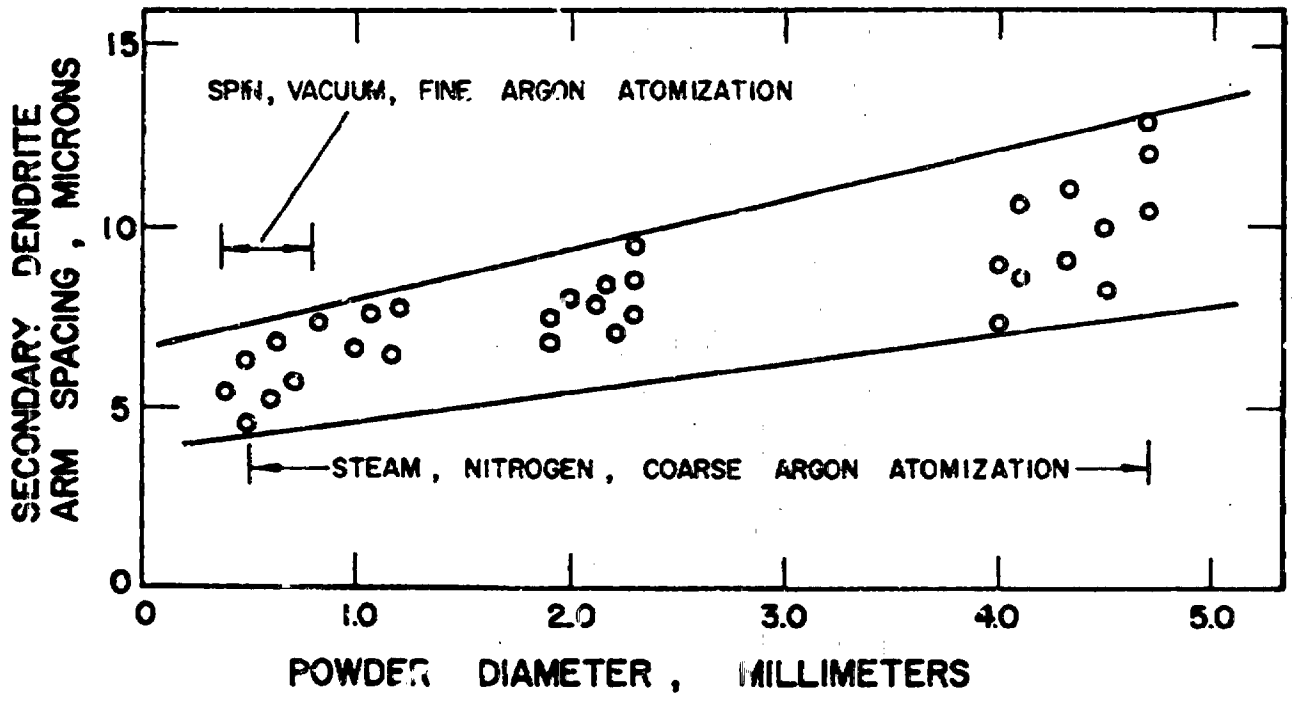

Figure 6. Secondary dendrite arm spacings versus powder particle diameter of Maraging 300 steel alloy obtained by different atomization processes.

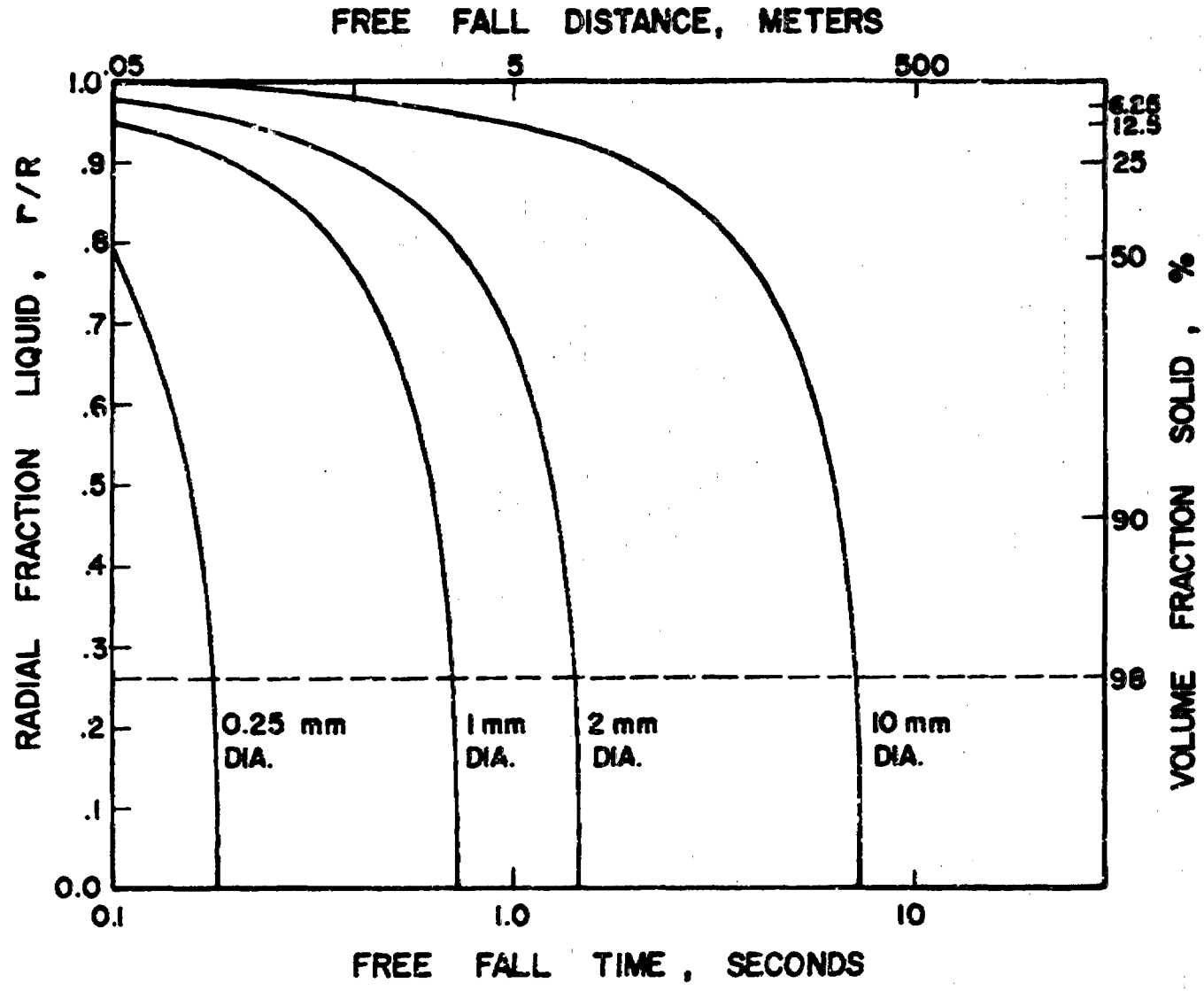

Figure 7. Calculated radial fraction liquid and volume fraction solid versus free fall time and distance for different size powder particles of Maraging 300 steel alloy.

a

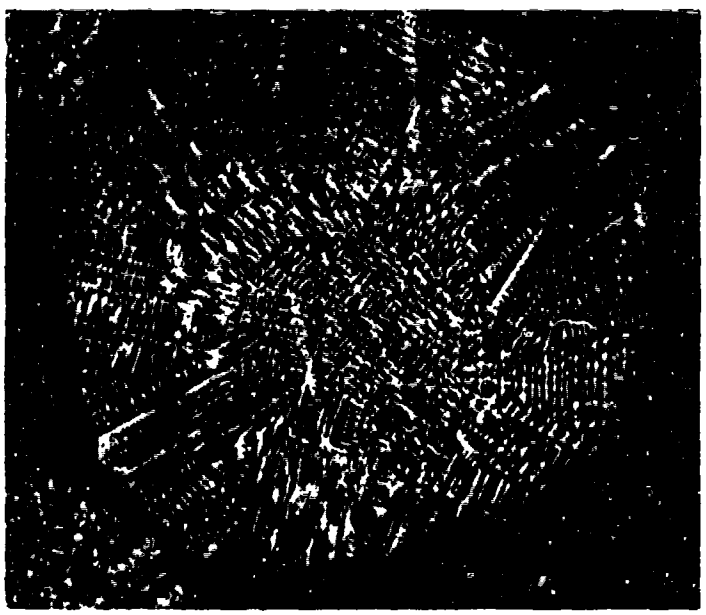

b

Figure 8. Photomicrographs showing examples of duplex dendritic structures obtained in atomized powders; (a) steam atomized coarse powder of Maraging 300 steel alloy at 75X, (b) spin atomized powder of IN-100 alloy at 200X.

PART II

ABSTRACT

A laboratory apparatus was constructed to atomize metal alloys by forcing them through sintered ceramic disc filters. The process combines filtration of oxides and/or undesirable second phase particles with atomization. Pure aluminum and 7075 aluminum alloy were atomized using sintered Al_2O_3 and SiO_2 disc filters with average pore sizes in the range of 30 to 150μ. Effect of experimental variables on the formation, and size distribution of spherical powders were determined. Spherical powders, 150 to 2000μ in size, of 7075 aluminum alloy with secondary D.A.S. spacings between 4 - 8μ, were cold compacted and extruded into a billet. Room temperature longitudinal properties of the billet in T6 condition were: Y.S. 80 Ksi, U.T.S. 94.3 Ksi, Elongation 15% and R.A. 42%.

I. INTRODUCTION

A new type of atomization process that combines filtration of metal alloys with powder production will be described. The process entails atomization of an alloy by forcing it through porous ceramic filters. Experiments were carried out on aluminum alloys to determine the governing parameters of the process. An extrusion billet made from these powders was tested for mechanical properties.

In general, for production of high quality powders of many alloys (iron, cobalt, and nickel-base superalloys being examples), surface oxides are undesirable because they cause poor bonding of the particles. Inert gas or hydrogen entrapped as porosity is undesirable because it is compacted in high temperature and hot pressurized and can subsequently expand in service at high temperature leading to failure of the material. Secondary particles formed in the melt, such as inclusions, are undesirable bacause they too result in lower mechanical properties of the final part.

Of all the various powder manufacturing processes available the particular process to be described is unique because: (i) filtration of undesired oxides, inclusions, and foreign particles occurs prior to powder drop formation, and (ii) the process can be carried out in high vacuum.

II. APPARATUS AND PROCEDURE

A schematic of the apparatus for the production of metal powders through ceramic filters is shown in Figure 1. It consists of a pressure vessel within which a graphite crucible is placed containing the metal charge and a filter assembly located below the charge. The crucible is covered with an insulating shield made out of fiberfrax. RF induction heating is employed within the chamber. The chamber is 10" in diameter by 8" high. It is placed at a height of 7 to 8 feet to allow a long enough freefall distance for the metal powders to solidify. The liquid metal, which is melted in situ, is atomized by pressuring the chamber with an inert gas.

The crucible is mounted on the base of the chamber by six stainless steel bolts utilizing an asbestos insulating gasket. With this construction, upon pressurization, the crucible is under pressure from all sides except the bottom, and a pressure differential is set within the crucible between the melt and the lower chamber.

The filter media employed (sintered discs of alumina or quartz) is completely contained within a graphite filter assembly, which in turn is mounted in the crucible with a taper fit. Hence, pressurization of the top of the melt forces liquid metal down through the filter, Figure 1.

Other specific features of the assembly shown in Figure 1 include the following:

1. An inflow and outflow valve, incorporating a pressure gauge is located on top of the chamber.

2. The chamber is connected to a vacuum pump through a ½ inch diameter pipe.

3. The copper coils for the RF heating are arranged so that a uniform temperature profile exists along the entire length of the filter container assembly.

4. A thermocouple feed through is located on the side of the chamber to permit measurement of the melt temperature.

Experiments were done with 99.99% aluminum and 7075 aluminum alloy of 7.3%Zn-3.2%Mg-2%Cu-0.25%Cr nominal composition. Filter materials were Al_2O_3 porous disc filters of 87-100μ and 31-36μ pore sizes and sintered quartz discs of 90-150μ and 40-90μ pore sizes.

The procedure was to melt about 200 grams of the alloy in a nitrogen atmosphere and superheat it to 800°C. The power was then gradually decreased reducing the melt temperature to a predetermined level, T_F. The pressure above the melt was gradually increased until metal drops (powders) started to exit from the filter. The procedure employed and the temperatures and pressures used are listed in Table I. Size distribution curves of the resulting powders obtained from the various filters were determined by sizing (sieve analysis) and weighing of the powders.

Pound lots of spherical powders and flakes were produced using various filters as described above. The spherical

powders of the 7075 alloy were cold compacted under 20,000 psi pressure into a 3 inch O.D. by 2 inch I.D. 6061-T6 aluminum can. This extrusion billet was heated to a solutionizing temperature of 476°C, held there for one hour and furnace cooled. Subsequently it was sealed, soaked at 300°C for 4 hours and extruded at the same temperature at a reduction ratio of 20 to 1.

Ten tensile test specimens were machined from the billet. These were solutionized at 475°C for 2 hours and aged at 129°C for 24 hours prior to testing.

III. RESULTS AND DISCUSSION

A. Powder Formation

An SEM view of spherical metal drops (powders) emerging from the pores of a sintered Al_2O_3 disc, with an average pore size of 87-100μ, is shown in Figure 2(a). The neck region of one of the powders is shown in Figure 2(b). The exiting stream of liquid metal becomes spherical in shape due to surface tension forces, and subsequently drop detachment occurs. Hauser and Edgerton (1) have investigated the steps of formation and detachment of drops from the end of vertical tubes. They show that a waist forms first and rapidly necks down into a stem which then breaks off close to the top of the drop.

Harkins and Brown (2) have derived an expression for drop formation using a force balance between gravity and surface tension. These types of analyses, however, do not take into account formation of an oxide skin or solidification of the droplet.

Experimental observations showed that successful formation of spherical powder particles depends on detachment of the liquid drops from the filter prior to growth and coalescence of adjacent drops. Conditions that permit liquid drops exiting from adjacent pores to coalesce result in formation of large liquid drops that do not completely solidify in flight and splat in the collector container. The different variables that affect formation and subsequent solidification of the powder particles are; (a) pressure differential across the ceramic filter, (b) superheat in the melt, (c) the wetting angle between the melt and the ceramic filter, and (d) the average pore size of the ceramic filter.

Pressure

A large number of available pores in the bottom of the filter are not utilized during drop (powder) formation, Figures 3(a) and (b). Liquid metal preferentially flows through paths of least resistance, causing a channeling phenomenon to occur. Increasing the pressure differential leads to utilization of a greater number of pores. However, increasing the pressure

head, above a critical maximum causes consolidation of drops from adjacent pores (i.e., less than one drop diameter apart), Figures 3(c). In the extreme case, consolidation of many liquid drops results in formation of large drops, or streams, which do not completely solidify in flight and splat against the collection container forming flakes.

Superheat

Direct observations of drop formation through magnifying lenses located below the filter, have shown that formation of consolidated large drops, or streams, can be correlated to superheat in the melt. In general, increasing the superheat in the melt results in formation of larger drops before detachment from the filter occurs. Sieve analysis of spherical powders of 7075 aluminum alloy produced in Runs # 9 and #14, Table I, verify these observations. Figures 4(a) and 4(b) show the size distributions of the resulting powders from Run # 9 (T_F= 700°C) and Run # 14 (T_F=742°C), respectively.

Wetting

Increased wetting between the ceramic filter and the molten alloy has an adverse effect on successful production of spherical powders. It was found that Al_2O_3 filters were more amenable to atomization than the SiO_2 filters. SiO_2 filters of 90-150μ pore size were used in Run # 6 (T_f=769°C) and Run # 7 (T_F=650°C), Table I. In both runs large drops of the 7075 alloy were formed, which in turn splatted against the collection con-

tainer below. Liquid aluminum wets SiO_2 much more readily than it does Al_2O_3 (3). Hence, liquid drops spread out more easily on the SiO_2 filters, leading to formation of consolidated drops.

Filter Pore Size

The diameter of atomized powders decrease with decreasing average pore size of the filters used. As expected, pressure differentials required are higher for the finer pore filters, Run # 2 , Table I.

One of the attractive features of this process is that filtration and drop (powder) formation occur simultaneously. Figure 5 shows the oxide "cake" retained above a sintered disc filter during atomization of 7075 aluminum alloy.

B. Structures of Atomized Powders

Figures 6(a) and 6(b) show SEM views of 150 to 300μ size pure aluminum powders obtained in Run #1, Table I. The powders are generally spherical in shape. Occasionally powders with stems or tips not completely detached were also observed, Figure 7(a). At a higher magnification, surface irregularities such as ripples, folds, and waves are observed, Figure 7. These are caused when the initial oxide layer tries to accommodate deformation experienced by the drop as solidification, shrinkage, and flight instabilities occur. Figure 6(c) shows a representative microstructure.

Figures 8(a) and 8(b) show SEM views of the 7075 aluminum

alloy powders. Figure 8(c) shows a photomicrograph of a polished and etched cross-section. These are representative structures of the powders that were cold compacted and hot extruded into a billet. Measured secondary dendrite arm spacings were between 4 - 8μ, indicating cooling rate of $\sim 10^{3}$ °C/sec (4).

C. Extrusion Billets

Spherical powders of the 7075 aluminum alloy ranging in size from 100μ to 2000μ, obtained with the Al_2O_3 filters were cold compacted and hot extruded into a billet. The billet was heat treated to a T6 condition as previously described. The transverse and longitudinal microstructures of the extruded billet are shown in Figure 9.

Room temperature average tensile properties, from multiple tests in the lingitudinal direction, were: Y.S.=80 Ksi, UTS = 94.3 Ksi, Elongation = 15%, R.A. = 42%.

IV. CONCLUSIONS

1. A new laboratory process for production of metal alloy powders was developed. The process combines filtration of oxides and undesirable second phases with atomization.
2. Pure aluminum and 7075 aluminum alloy were atomized by

forcing them through sintered Al_2O_3 and SiO_2 disc filters with pore sizes in the range of 30 to 150μ. The Al_2O_3 filters were found to be more amenable to successful droplet formation.

3. For a given sintered disc filter successful formation of metal powders below the filter depends on the applied pressure. Pressures used in this study were in the range of 2 - 6 psi.
4. Size range of powders is influenced by the amount of superheat in the melt. Increasing superheat results in formation of larger powders.
5. The longitudinal room temperature tensile properties of a 7075-T6 extrusion made from the atomized powders were: Y.S. = 80 Ksi, U.T.S. ≃ 94.3 Ksi, Elongation = 15%, R.A. = 42%.

ACKNOWLEDGMENT

The authors acknowledge financial support by the Advanced Research Projects Agency of this research program.

REFERENCES

1. E.A. Hauser, H.E. Edgerton, B.M. Holt, and J.T. Cox, Jr., J. Phys. Chem., Vol. 40, (1936) p. 973.

2. W.D. Harkins, F.E. Brown, J. Am. Chem. Soc., Vol. 41 (1919) p. 499.

3. W.D. Kingery, J. of the Amer. Ceramic Soc., Vol. 37 (1954) p. 44.

4. H. Matyja, B.C. Giessen, N.J. Grant, J. Inst. Metals, Vol. 96 (1968) p. 30.

LIST OF ATOMIZATION EXPERIMENTS

run #	sintered filters used	T_F	alloy used	pressure applied (psi)
1	Al_2O_3, 87-100μ	710°C	99.99% Al	7-8 then lowered to 4-5
2	Al_2O_3, 31-36μ	840°C	7075	7-14
3	Al_2O_3, 87-100μ	756.5°C	7075	3-5
4	Al_2O_3, 87-100μ, previously infiltrated	732.5°C	7075	3-5
5	Al_2O_3, 87-100μ	760°C	7075	3-5
6	SiO_2, 90-150μ	769°C	7075	2-4 and 10-14
7	SiO_2, 90-150μ	650°C	7075	3-4
8	Al_2O_3, 87-100μ	697°C	7075	0-6
9	Al_2O_3, 87-100μ, previously infiltrated	700°C	7075	5-6
10	Al_2O_3, 87-100μ, previously infiltrated	721°C	7075	5-6
11	SiO_2, 90-150μ	685°C	7075	3-5
12	Al_2O_3, 87-100μ, same filter as in runs # 10-12	742°C	7075	5-6
13	Al_2O_3, 87-100μ	742°C	7075	0-7
14	Al_2O_3, 87-100μ, previously infiltrated, filter from run #15	742°C	7075	4-5
15	Al_2O_3, 87-100μ	700°C	99.99% Al	7, then lowered to 4-5
16	Al_2O_3, 87-100μ	700°C	99.99% Al	7, then lowered to 4-5

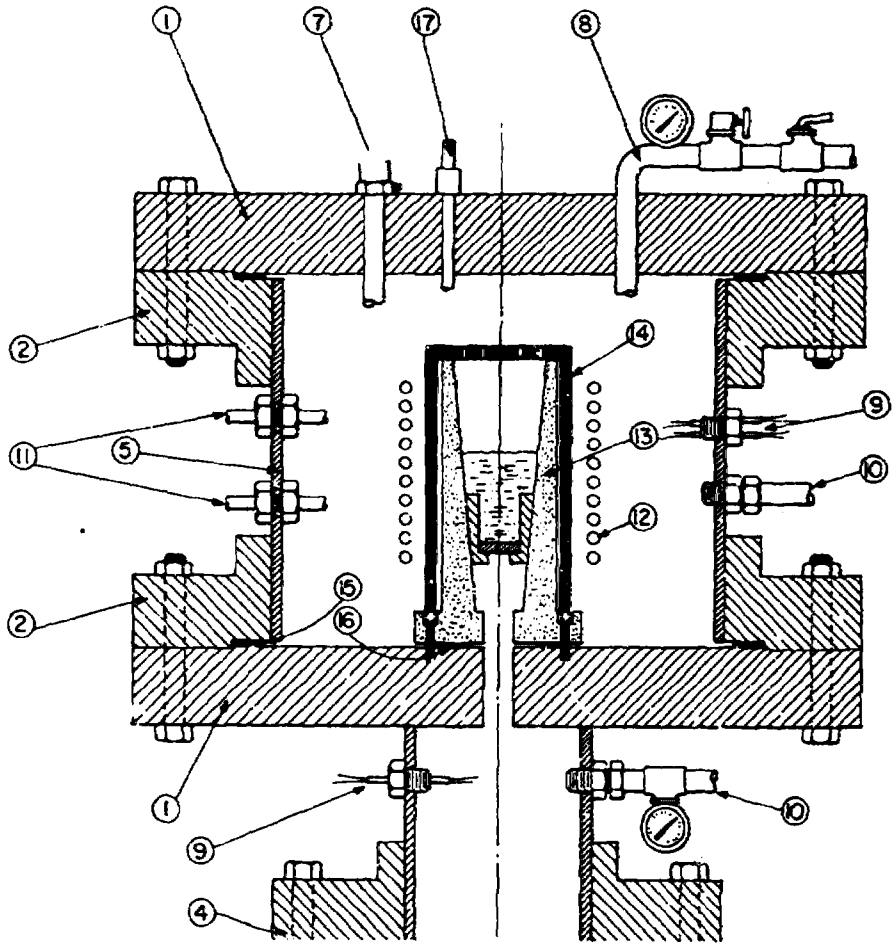

① 10"-300 LB. BLIND FLANGES
② 10"-300 LB. SLIP-ON FLANGES
③ 4"-600 LB. BLIND FLANGE
④ 4"-600 LB. SLIP-ON FLANGE
⑤ 10" SCH. 80 BLK. STEEL SEAM. A-106 PIPE, 0"-8½" PE
⑥ 4" SCH. 40 BLK. STEEL SEAM A-53 PIPE, 0'-5" PE
⑦ SAFETY VALVE
⑧ PRESSURE INFLOW AND OUTFLOW AND PRESSURE GAUGE
⑨ THERMOCOUPLE FEEDTHROUGHS
⑩ ½" PIPE TO VACUUM PUMP
⑪ WATER INFLOW AND OUTFLOW FOR RF COILS
⑫ COILS
⑬ GRAPHITE CRUCIBLE
⑭ FIBERFRAX INSULATING SHIELD
⑮ GASKETS
⑯ INSULATING GASKET
⑰ CHECK VALVE FOR ATMOSPHERE CONTROL

Figure 1: Schematic of atomization apparatus used in this study.

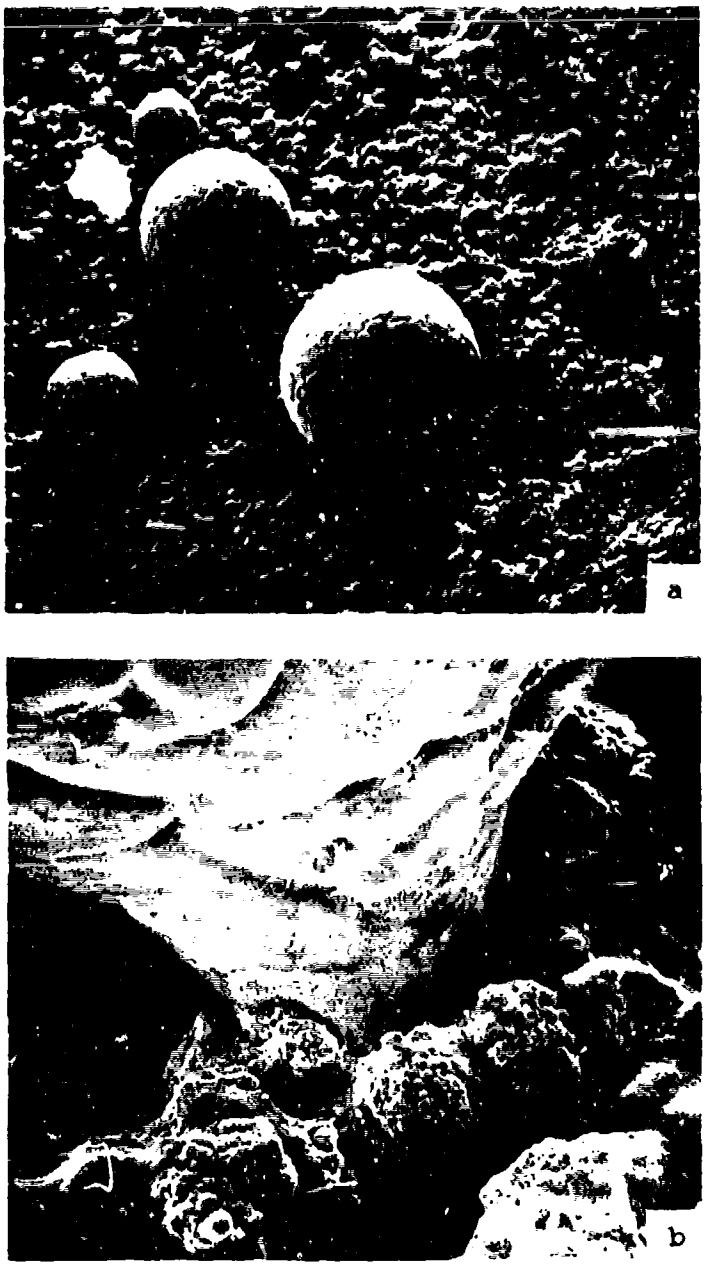

Figure 2. SEM view of pure aluminum powders emerging from a sintered Al_2O_3 filter, Run #1; (a) 23X, (b) 208X.

Figure 3. SEM view of pure aluminum powders emerging from a sintered Al_2O_3 filter; (a) and (b) are from Run #15 at 20X and 90X, respectively, (c) is from Run #16 at 75X.

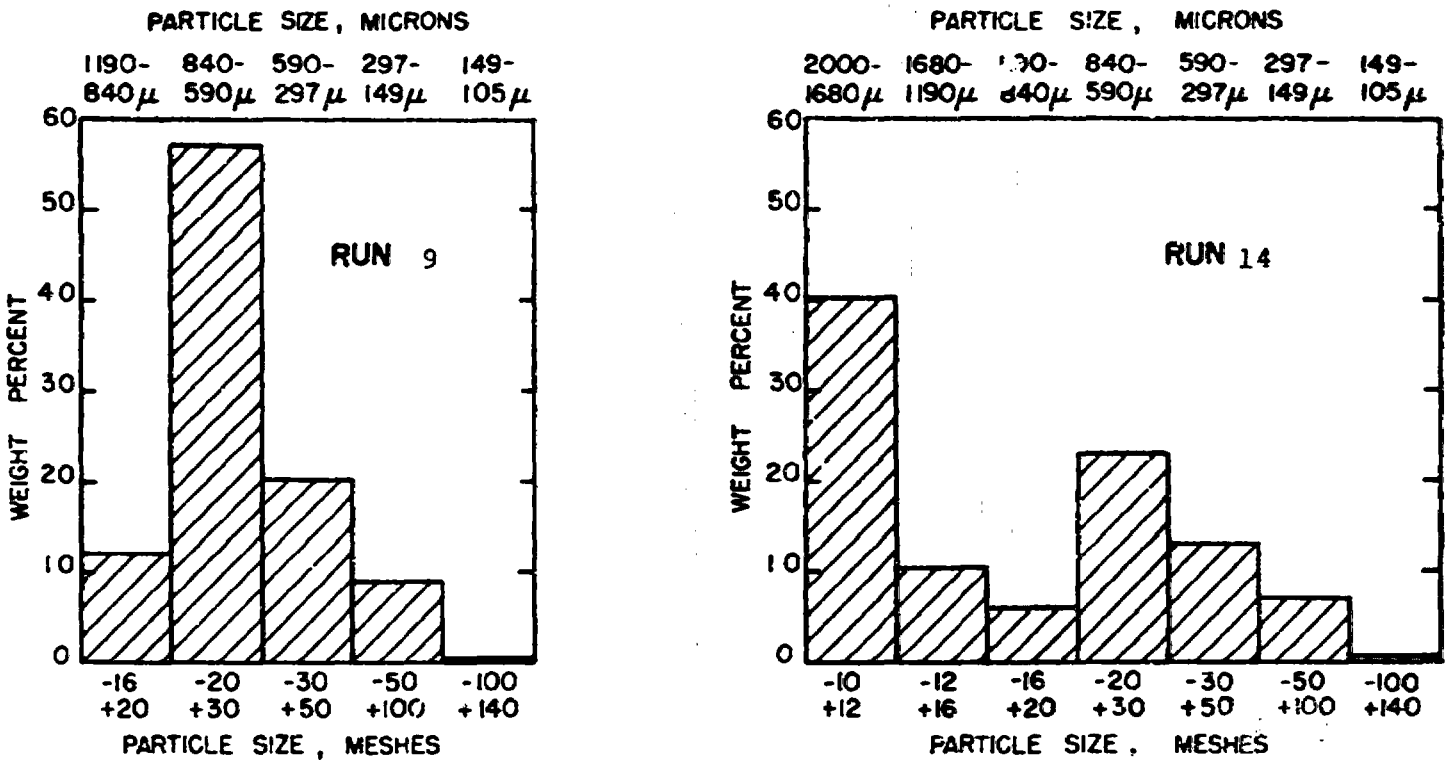

Figure 4. Size distributions of spherical 7075 aluminum alloy powders made utilizing Al_2O_3 filters; (a) Run #9, T_F=700°C, (b) Run #14, T_F=742°C

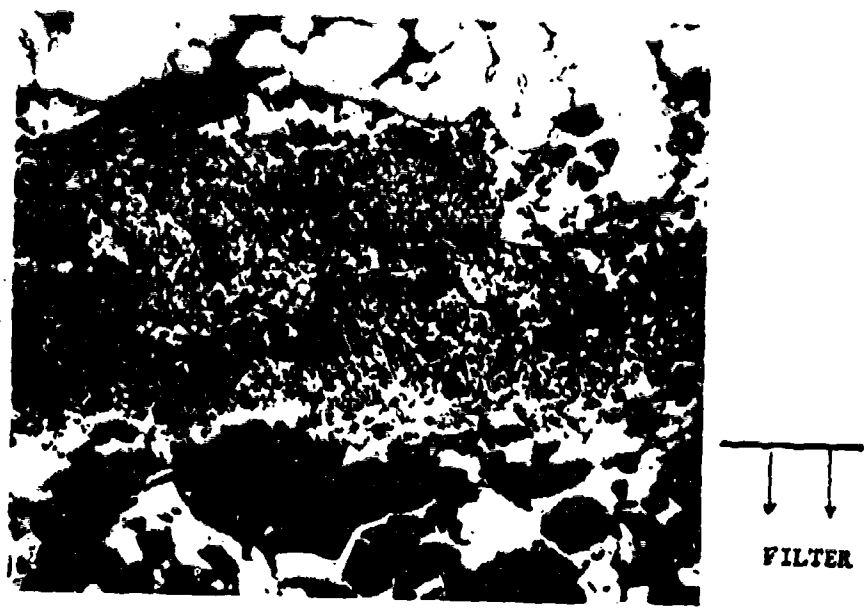

Figure 5. Photomicrograph showing filtration of aluminum oxide from a 7075 aluminum alloy melt.

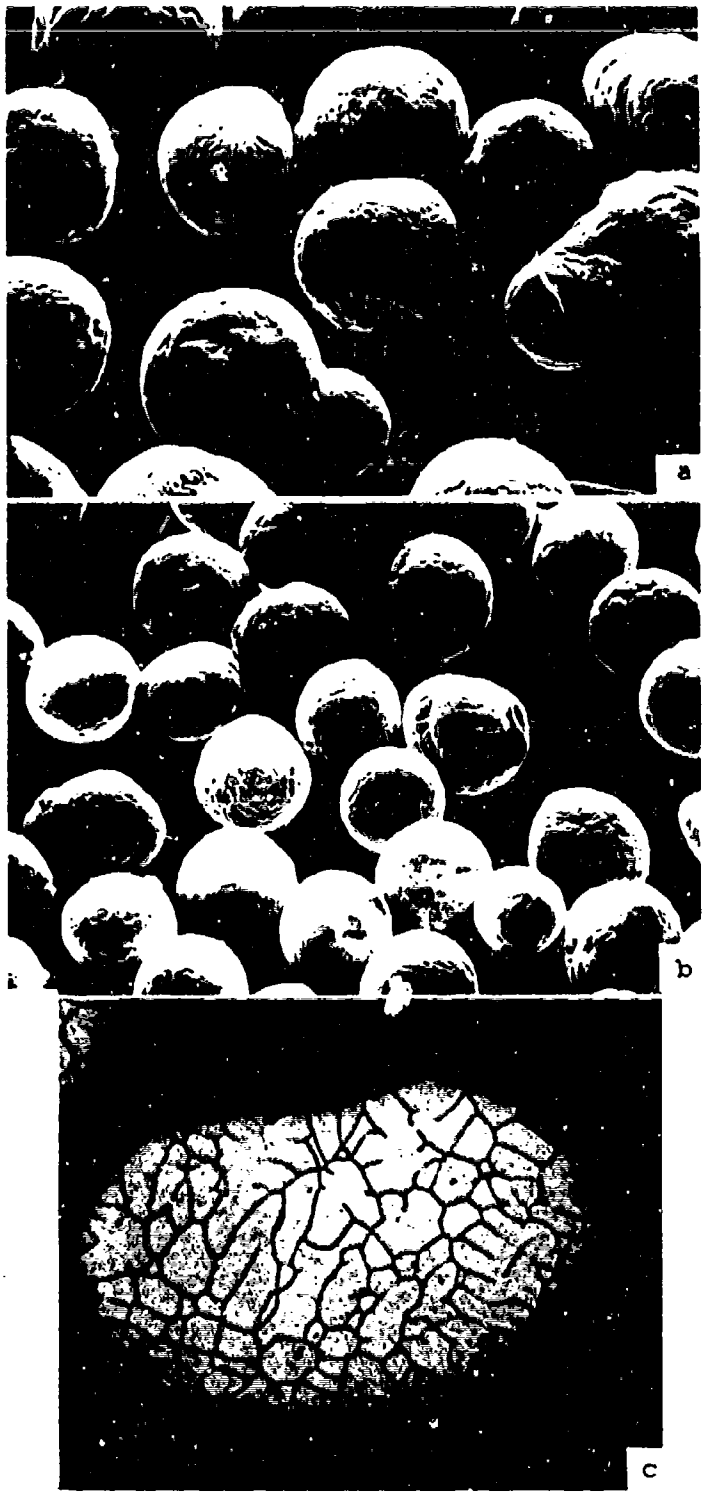

Figure 6. Structures of atomized pure aluminum powders made in Run #1; (a) and (b) are SEM views of different size powders at 50X, (c) is a representative microstructure of the powders.

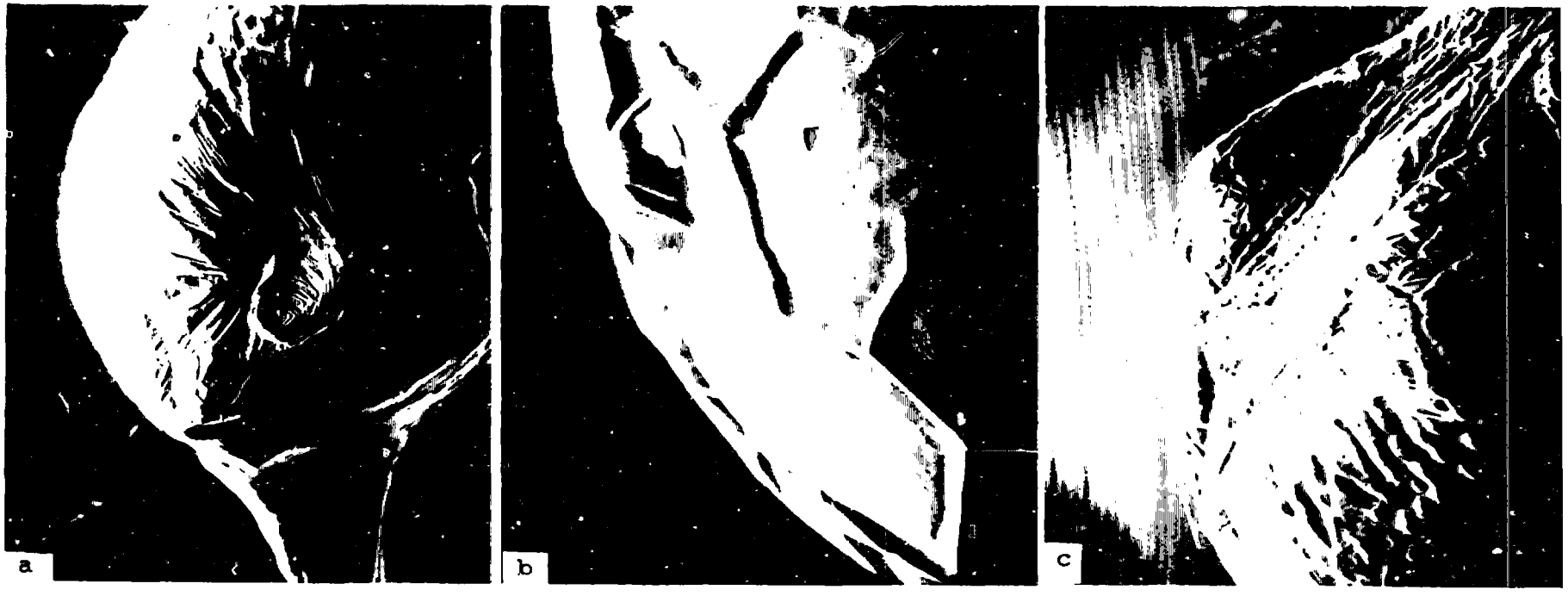

Figure 7. Surface irregularities of atomized pure aluminum powders; (a) Run #1, 590X, (b) Run #15, 500X, (c) Run #16, 590X.

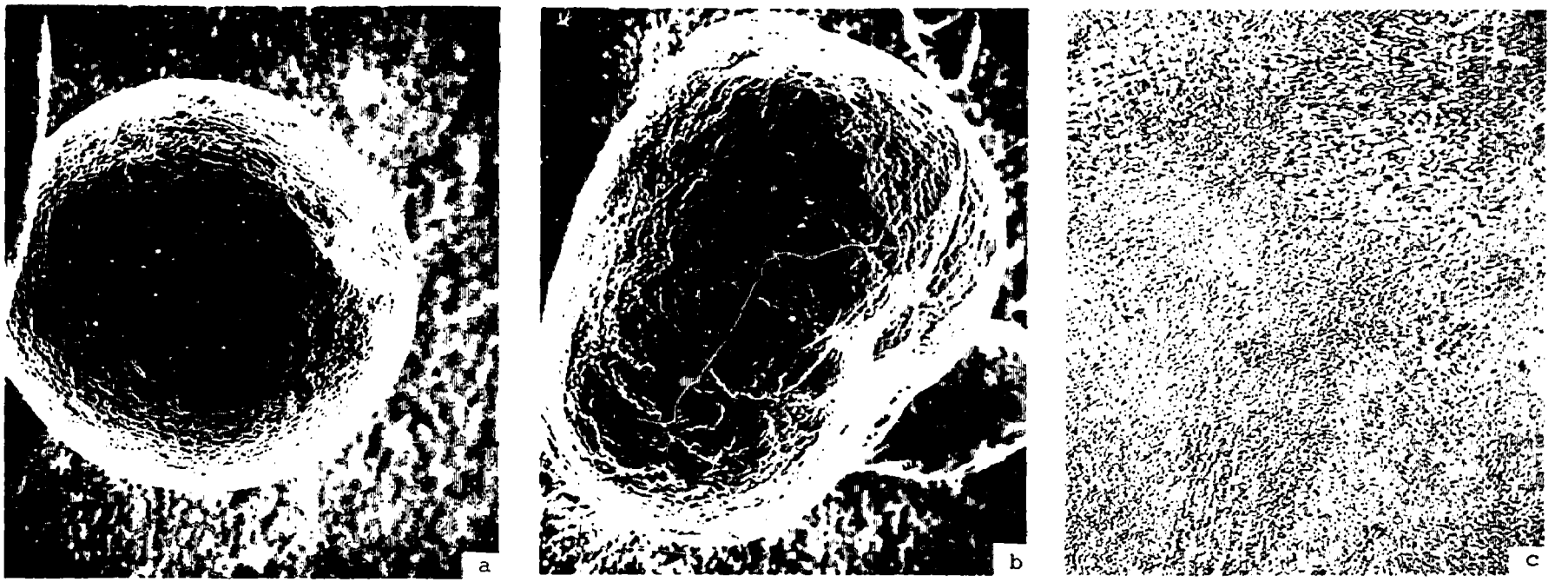

Figure 8. Atomized powder of 7075 aluminum alloy from Run #14; (a) and (b) are SEM views at 110X and 200X, respectively, (c) is a photomicrograph of a polished and etched cross-section at 100X.

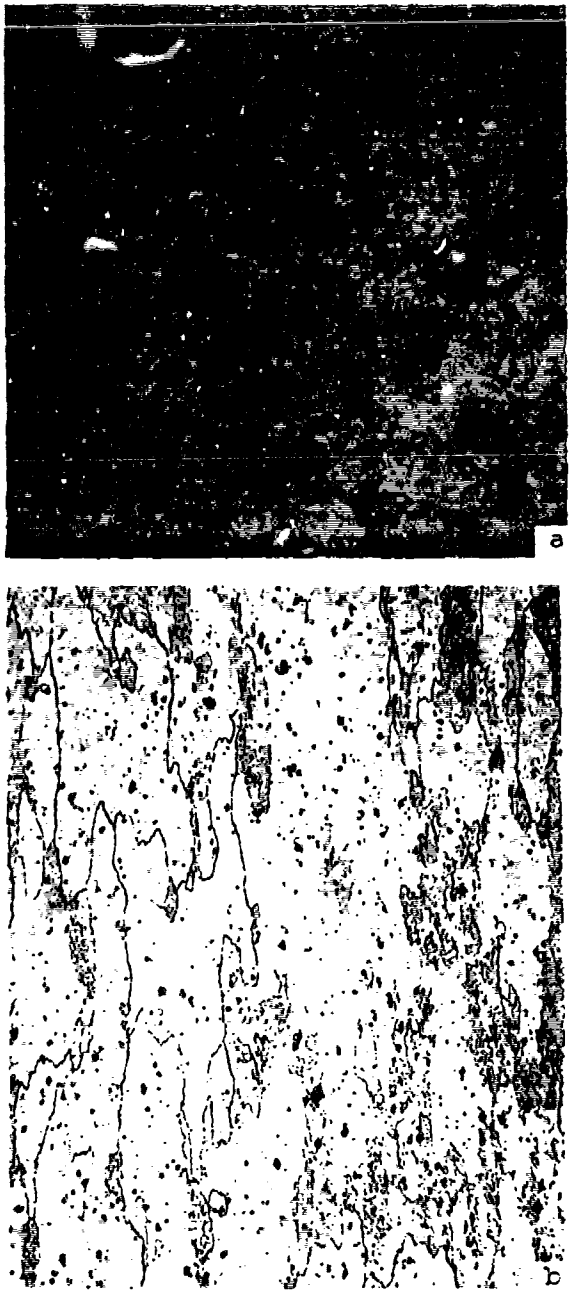

Figure 9. Microstructure of 7075-T6 extrusion made from atomized spherical powders, 100X; (a) and (b) are transverse and longitudinal cross-sections, respectively.

PART III

REFINING BY PARTIAL SOLIDIFICATION

A major technical difficulty in refining processes which employ partial solidification when solidification is dendritic, is that the segregated liquid is interspersed on such a fine scale in interdendritic spaces that it is difficult to remove from the dendritic solid. In this note we describe two refining processes which employ the basic finding that metal alloys behave as a highly fluid slurry when they are as much as half solid, provided they are vigorously agitated during solidification (1). The solid particles that form during solidification are, or approach, small spheroids. The fine dendritic structure is absent and the segregated liquid can be easily and efficiently separated from the solid.

The technical and patent literature describes various processes for refining metal alloys which employ partial solidification followed by separation of liquid and solid phases. When the volume fraction solid is small and it is in particulate form, for example, oxides and nonmetallics in

aluminum or Fe-Sn intermetallic in molten tin, separation can be accomplished by filtration techniques[2-4]. In usual solidification processes, however, at volume fractions solid greater than 0.20 a dendritic network forms and the interdendritic liquid is made to flow out of this network by centrifugation or other techniques. The United States Bureau of Mines has applied centrifugal separation to the refining of tin and zinc alloys[5,6]. Singleton and Robinson[7] have described a process in which an aluminum-silicon melt is partially solidified in a centrifuge and the interdendritic liquid is made to flow radially outward. In other proposed processes, a local portion of a melt is partly solidified while the bulk remains liquid. This liquid is then stirred with the effect that some of the interdendritic enriched liquid is washed out from the partially solidified region into the bulk liquid[8-11].

In both processes described here the metal is partially solidified while it is vigorously agitated by one or more rotating blades, Figure 1. As distinct from some of the processes listed above,[8-11] it is not simply the bulk liquid that is agitated, but the entire liquid-solid mixture. The combination of the vigorous agitation and relatively slow rate of heat removal from the solidifying slurry causes it to be essentially isothermal and to have a uniform distribution of primary solid particles in the segregated liquid. In one case, the particulate solid is separated from the liquid by

atomization of the liquid-solid slurry. In the other case, this separation is achieved by preferential draining of the liquid from the slurry.

In the first process, shown in Figure 1a, a propeller located at the bottom of the mixer blades, forces both the solid and the liquid through the bottom hole of the crucible. The stream of the liquid-solid alloy is struck by jets of air or inert gas. The portion of the stream that is liquid is atomized to very fine droplets. The portion that is solid remains at its size when struck by the jets. Refining is now accomplished by simple size fractionation of the resulting particulate alloy. Figure 2 shows graphically results of one test on a Sn-15% Pb alloy. Note the smaller particles are significantly enriched in alloy element.

In the second process, shown in Figure 1b, the thixotropic behavior of the slurry is used so the metal alloy "filters" itself. Due to the thixotropic nature of the liquid-solid slurry,[1] the primary solid particles weld and wedge together in locations where the slurry is not subjected to high rates of shear. Hence, the bath in the immediate vicinity of an orifice is not agitated, or is only gently agitated. Here, the solid forms an interconnecting network and acts as a filter, letting liquid pass but holding back solid. The stream passing out is now highly segregated liquid. Gravity is ample pressure required to make this

process work because the bulk of the material present behaves as a fluid slurry. Surface tension does not impede removal of the liquid since surface is not being created during its removal, as it would be if the liquid were being drained from interdendritic spaces. Table I summarizes some experiments on the hyper-eutectic aluminum-silicon alloy containing iron and titanium demonstrating the feasibility of this process. This alloy was that employed by Singleton and Robinson (7) in their refining experiments using a centrifugal separation technique. The drained liquid is significantly lowered in all solute elements present, and its composition is in good agreement with that previously reported (7). In the general case, the liquid removed will be either enriched or depleted in alloy elements, depending on the nature of the phase diagram of the alloy.

While the two refining processes described in this note are batch type, improved economics could be obtained by developing similar processes that operate continuously.

ACKNOWLEDGMENT

The authors acknowledge financial support by the Advanced Research Projects agency of this research program.

REFERENCES

1. D. B. Spencer, R. Mehrabian, M. C. Flemings, Met. Trans., 1972, Vol. 3, pp. 1925.

2. G. Reinacher, Metal Industry, 1949, Vol. 75, pp. 183.

3. E. L. Jones, A. Tunaes, Canad. Inst. Min. and Metal, 1944, Vol. 47, pp. 35.

4. H. W. St. Clair, U.S. Bureau of Mines Report of Investigations (4614), 1949.

5. A. K. Schellinger and M. P. Spendlove, ibid., (5007), 1953.

6. S. A. Ruppert and P. M. Sullivan, ibid., (6417), 1964; (6889), 1967.

7. O. R. Singleton and G. C. Robinson, Jr. J. Inst. of Metals, 1971, Vol. 99, pp. 155.

8. B. M. Larsen, U. S. Patent No. 2,087,347, July 20, 1937.

9. A. Reynor, U. S. Patent No. 2,471,899, May 31, 1949.

10. O. C. Aamot, U. S. Patent No. 3,249,425, May 3, 1966.

11. S. L. Dewez, J. Metals, 1965, pp. 940.

TABLE I

Refining of an Aluminum Alloy By Gravity Draining of the Aluminum-Rich Liquid

	Silicon (wt pct)	Iron (wt pct)	Titanium (wt pct)
Initial Composition	30	6	1
Drained Liquid Composition at 750°C	22.6	4.65	0.43
Drained Liquid Composition at 600°C	13.1	1.77	0.15

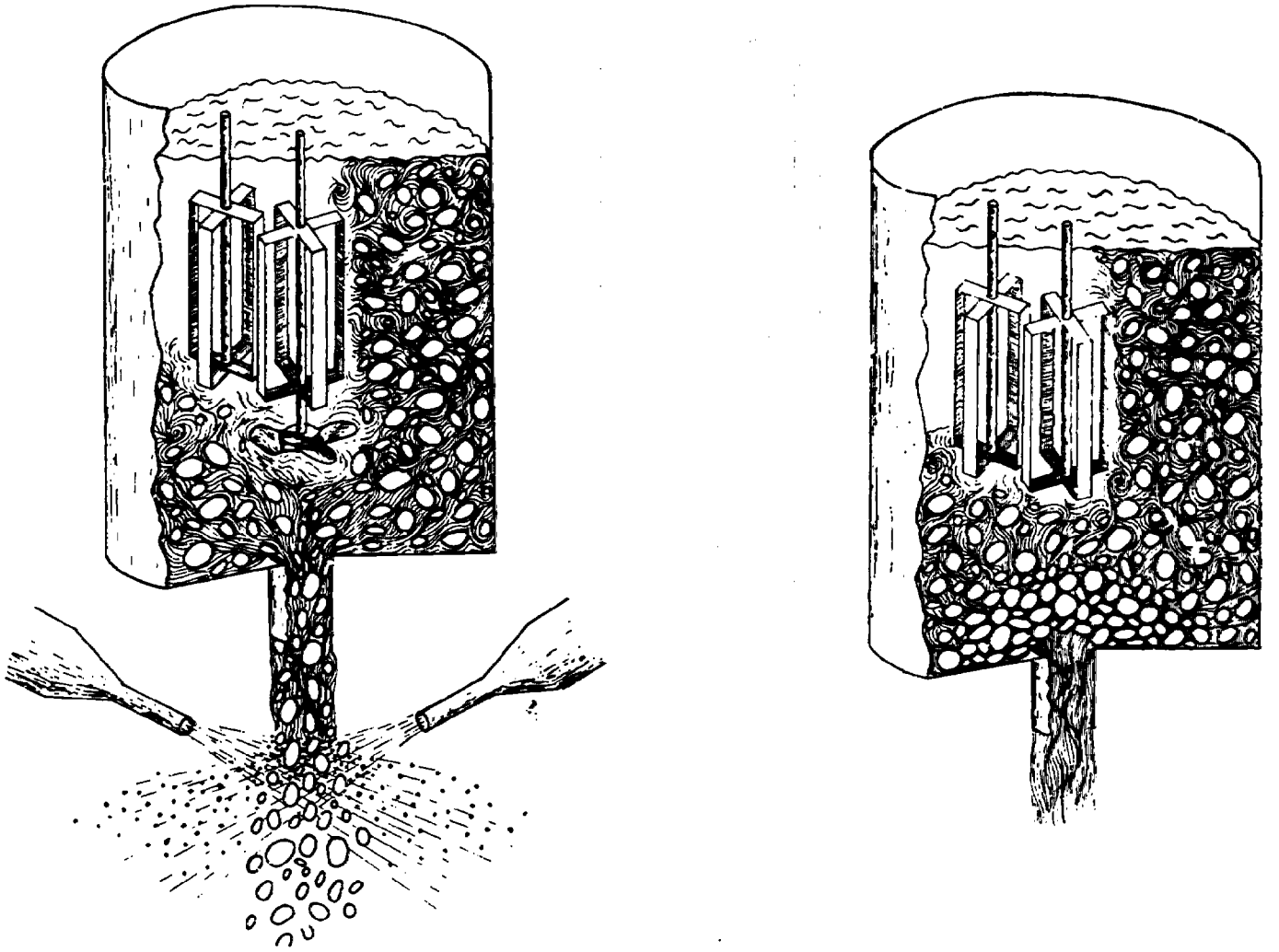

(a) (b)

Figure 1. Schematic illustration of two Rheorefining processes. In both processes, partial solidification is accompanied by vigorous agitation. Separation of solid from liquid in the slurry is achieved by: (a) atomization, (b) preferential draining of the liquid.

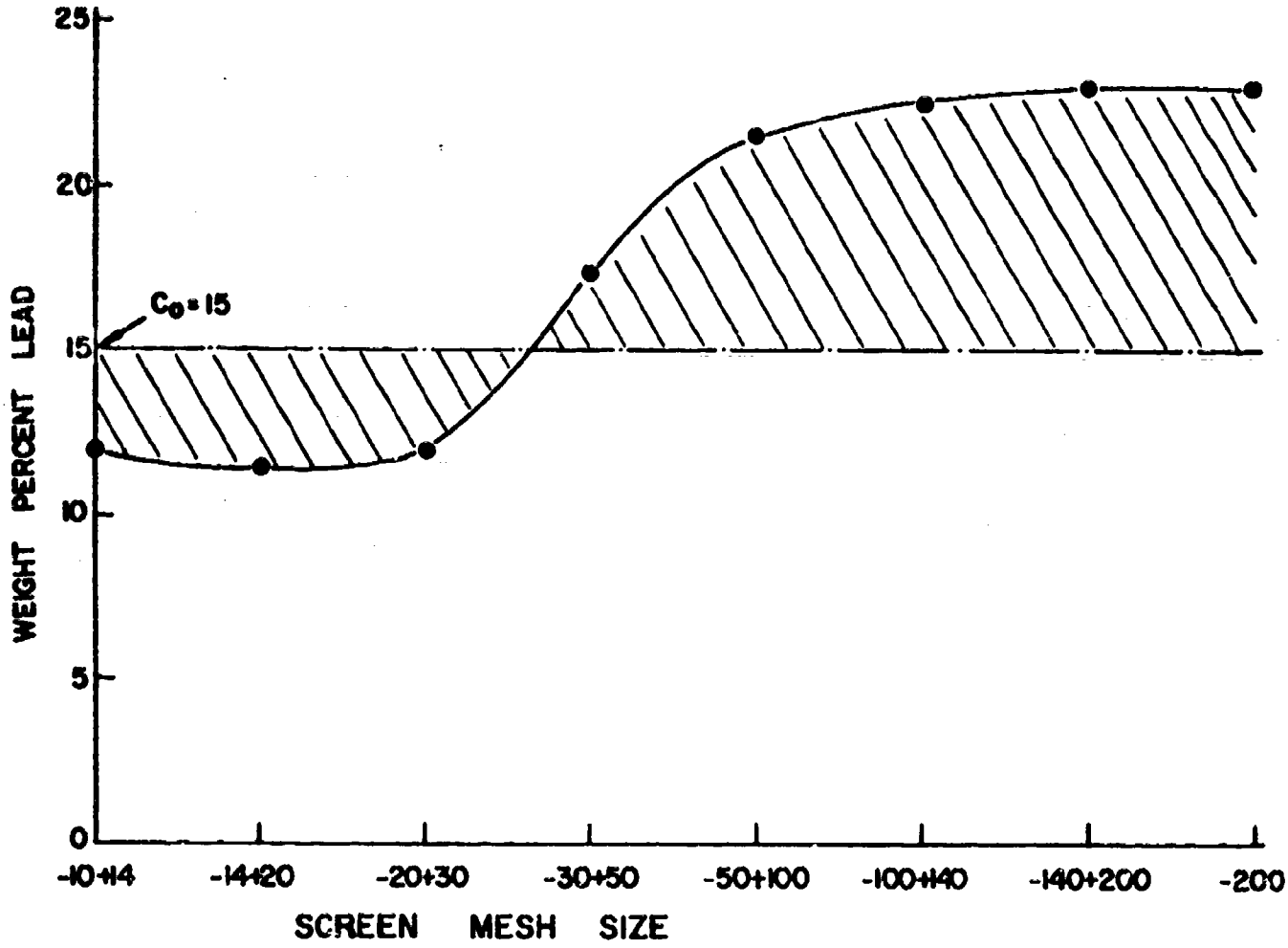

Figure 2. Composition versus powder mesh size of Sn-15% Pb alloy Rheorefined by atomization at 0.4 fraction solid.

TASKS III AND IV

THERMOMECHANICAL TREATMENT, MICROSTRUCTURE AND MECHANICAL PROPERTIES

L.N. Moskowitz
L.F.P. Van Swam
S. Wastberg
S.J. Berman
J. Im
R. Safoglu
A. Needleman
R.M. Pelloux
A.S. Argon
N.J. Grant

LIQUID METAL ATOMIZATION FOR HOT WORKING PREFORMS

N.J. Grant and R.M. Pelloux

Abstract

Rapid quenching of a liquid metal by atomization or splat cooling overcomes the major limitation of most solidification processes; namely, the segregation of alloying elements, impurities and constituent phases. The cooling rates of different atomizing processes are related to the dendrite arm spacings and to the microstructure of the atomized powders. The increased solubility limits and the formation of metastable compounds in splat cooled alloys are discussed. Consolidation of the powders by hot isostatic compaction, hot extrusion or hot forging and rolling processes yield billets with properties equivalent or better than the wrought alloys. The application of this powder processing technology to high performance alloys is reviewed.

I. Introduction

Today powder metallurgy is taking on a new meaning: the demand is for fully dense materials in low, intermediate or high alloy classes, fully heat treated with hot or cold worked structures. The requirements for higher tonnages of powders has encouraged a multitude of atomization processes, some of which offer real promise for production of high quality powders at costs which can be competitive with the similar alloys produced by ingot technology.

A list of the different atomization processes includes:

a) high pressure air and water atomization

b) low pressure steam atomization for coarse powders

c) inert gas atomization by argon or helium or nitrogen

d) rotating electrode atomization of high alloy materials in an inert gas atmosphere

e) soluble gas (usually hydrogen) atomization in a vacuum

f) ultrasonic atomization

g) magnetic atomization

h) splat cooling or rapid quenching of small liquid metal droplets against a high conductivity metallic substrate

Emerging from the list of atomization techniques is the awareness of an important feature of the process; namely, the relatively rapid to extremely rapid cooling rates of the liquid metal. These high cooling rates diminish or overcome the major faults of most solidification processes; namely, the segregation of alloying elements, impurities, and all excess phases, and they prevent the formation of a very coarse dendrite and grain structure which is difficult to hot work, or to work at all.

II. Cooling Rates and Solidification Structures

Figure 1 shows the effect of cooling rate on dendrite arm spacing (DAS) for aluminum[1], and the degree of structure control which is attainable through various atomization methods. The similar curve for copper is steeper, but less well defined[2]. For highly alloyed materials, the curve can be expected to flatten because of the lower thermal conductivity of the liquid metal.

At the one extreme, ingot cooling rates lead to coarse grain size and large dendrite arm spacing, coarse inclusions and second phase particles; furthermore, large ingots always show significant porosity and a severe three-dimensional segregation pattern. With inexpensive, relatively plastic alloys these faults can be tolerated and largely corrected by working and homogenization of the end product.

Before looking at some of the improvements in the control of the structure and properties of actual alloy systems, it is worthwhile to consider rapid quenching of liquid metals somewhat more broadly.

It was only about ten years ago that Professor Pol Duwez[3-6] and co-workers re-examined and significantly advanced the state of the art and potential of splat cooling. Shortly thereafter, Predecki, Mullendore and Grant[7] found experimentally that the cooling rates attainable in splat cooling, were 10^7 to 10^8 °C/sec. These measurements were supported by calculations and by a calibration of cooling rate data suggested by Dean[8]. Matyja, et.al.[1] confirmed the extrapolated cooling rate data shown in Figure 1. A similar curve has now been measured for Cu base alloys[2] and further calculations have confirmed the approximate maximum cooling rates attainable[9-12].

At cooling rates greater than about 10^6 °C/sec it is possible to change the solute solubility limit by an order of magnitude[13,14] (see Giessen[15]) and to form metastable compounds[15]. The size of non-equilibrium phases and of inclusion particles are also refined by order of magnitude. Cooling rates as high as 10^7 to 10^9 °C/sec can result in grain sizes of less than 0.01 microns[16-18], or in amorphous structures[19-23].

In the ultimate case of amorphous structures retained from the liquid phase, all segregation is essentially prevented. Unfortunately, to achieve these cooling rates, the resultant splats are only 0.1 to 10 microns thick; the foils are irregular, difficult to process and to consolidate, and they will react with the ambiant atmosphere. The finished product would be expensive to say the least.

Consider, however, the central portion of Figure 1, where practical, feasible cooling rates are attainable for commercial atomized powders.

The cooling rate and DAS areas for each class of atomization depend on the powder diameter, conductivity of the atomized metal, and quench capacity of the coolant. For finely atomized powders gas atomization will result in DAS values of about 10 microns in the case of aluminum. Water (or steam) atomization offers further structure refinements. By quenching against a metallic substrate, coarse flakes 50 microns thick by several millimeters in diameter can be produced with DAS values as small as one micron. This atomization against a cold metallic substrate is relatively new, but successful trials have been reported using rotating discs, or copper rolls[2,11,24] as the substrate.

III. Powder Cleanliness

The contamination of the atomized powders will be critical since large surface areas are generated in most of the atomization processes. The inert gas methods, assuming suitable control of gas purity, result in only small increases in oxygen content. In the case of argon atomization of superalloys, the oxygen content increases from that of the vacuum master melt, which is typically 30 to 75 ppm, to a final content of 50 to 125 ppm depending upon the leak rate of the atomizing system.

The rotating electrode atomization method[25] results in an increase of less than 25 ppm oxygen over that of the electrode material because the alloy is in the molten state for a very short time.

In splat cooling coarse powders in air, the oxygen content increases by several hundred ppm in spite of the relatively short exposure times in the oxidizing atmosphere. Because of the large surfaces produced by splat cooling methods, inert gas atmospheres will be required.

The water and steam atomization of superalloys to produce coarse powders (0.4 to 4 mm diameter) result in extensive oxidation with oxygen content of 3000 to 4000 ppm. Nevertheless, if the resultant particles are spherical in nature, without folds or creases, this oxygen content, which is largely on the surface, can be lowered to 200 to 300 ppm by chemical cleaning of the powders. For instance, cobalt base superalloys strengthened by high carbon content, and high alloy iron base materials (tool steels, high speed tool steels, stainless steels), are successfully steam

atomized provided they are free of significant amounts of Al, Ti, and Zr. The powders can then be mechanically and chemically cleaned to achieve oxygen contents of less than about 300 ppm.

The obvious advantage of water or steam atomization, wherever it can be used, is in the large cost savings. Finally, since all or most atomized materials are re-exposed to the ambiant atmosphere during storage, handling, and processing the oxygen content will increase to the detriment of the final product. A vacuum degassing of the powders in a temperature range from 500 to 1000°F prior to consolidation appears to be a general processing requirement.

IV. Powder Consolidation

The powders must be consolidated into fully dense bodies to achieve strength, toughness, and ductility. The higher the quench rates utilized to produce the powders, especially at rates greater than about 10^5 °C/sec (see Figure 1), the greater is the tendency for structural changes to take place during consolidation and processing of the compact or bloom. In the case of splat cooled powders these changes may call for selection of hot pressing temperatures and extrusion or rolling temperatures which will produce the desired structures and properties.

In general, the pattern of processes which is emerging for consolidation and densification are the following:

a) Forging and rolling preforms - These may be prepared by cold pressing and sintering, hot mechanical pressing, and to a lesser extent by hot isostatic pressing; the preform is generally not fully dense. This process looks attractive for iron and steel powder parts for the large market areas of automotive parts, household appliances, and general hardware.

b) Hot isostatic pressing (HIP) - Growing in parallel with developments in high alloy powder atomization, this excellent densification method should be able to provide suitably large ingots to compete on a commercial basis with ingot practice for forging. The powder must be sheathed in an evacuated container for compaction by HIP. Maximum pressures are about 30,000 psi (2000 atmospheres) at temperatures as high as 1425°C. The working volume for this temperature and pressure level is a chamber about 14 inches in

diameter by about 40 inches high. Larger pressing units are technologically feasible and can be made as soon as there is a demand; cost per pound of material in such large units is attractive for high alloy materials. Billet compacts, preforms, dies, vanes and blades for jet engines can be manufactured by this process.

c) Hot extrusion and other hot working processes - Powders may also be packed into containers without cold or hot pressing, evacuated, sealed and then hot extruded at some nominal extrusion ratio (from 6 to 1 to 20 to 1) to achieve full densification. Hot extrusion is preferred to forging or rolling of canned powders, but it is usually limited by the minimum extrusion ratio and by the capacity of the extrusion press. On the average, lower temperatures can be used for hot extrusion of powders than is necessary for extrusion of solid compacts or ingot or bloom sections, thus the microstructure refinements can be more easily retained.

V. Structure and Properties of Alloys Processed from Quenched Powders

In the discussion which follows, the structures and properties of several commercial, semi-commercial, or experimental powder alloy products made of powders solidified at rates from 10^2 to 10^6 °C/sec will be examined. These cooling rates encompass rates achieved by gas atomization, steam atomization, and metal substrate atomization.

A. Aluminum Alloys

Binary aluminum alloys, splat cooled to achieve cooling rates of about 10^6 °C/sec show large increases in solid solubility. Table I shows the increase for 7 binary alloys[13,26]. Suppression of precipitation during solidification beyond the maximum solubility limit in each of these systems opens the possibility of the development of precipitation hardening; in the case of the Al-Cu system, one gains the possibility of increasing the amount of finely dispersed ageing phase by a factor of 2 to 7.

1. Al-Si Alloy - The potential of this class of alloy was demonstrated by splat quenching up to 1000 gram melts against a rotating copper disc of an Al-7% Si alloy[16]. The DAS indicated a quench rate of 10^4 to 10^5 °C/sec, with the silicon content precipitated as submicron particles. The foils, measuring about 50 microns in thickness by 10 mm in the other

dimensions, were canned, evacuated and hot extruded at only 300°C. Table II compares the properties of this binary alloy against those of a commercial 5% Si alloy (No. 43) in 3 cast conditions. In addition to an increase in yield strength, the ductility of the cast alloy is 3 to 6 times greater than that for the cast commercial material.

Significant coarsening of the silicon precipitate did not occur at temperatures less than 400°C, thus showing that the structure is resistant to overaging.

2. Aluminum alloy 2024 - The properties of this commercial high strength alloy (4.5% Cu, 1.45% Mg, 0.57% Mn, 0.28% Fe, 0.10% Si, bal. Al) were compared for three different processing histories: bar form from a full-scale ingot, air atomized coarse powder, and as splat cooled (rotating copper disc) coarse flake powder[16]. The powders were canned, evacuated and hot extruded at 300°C at an extrusion ratio of 12 to 1. All three products were of the same composition, and were given identical heat treatments prior to testing (495°C solution treatment plus room temperature ageing: T4 condition).

Table III compares the structural characteristics of the three products in the hot worked or hot extruded condition. Figure 2 compares the hot worked structures of the ingot product and the splat powder product.

It has been demonstrated that alloy 2024 contains coarse non-equilibrium constituent particles, which are cracked or serve as crack initiation sites during fatigue[27,28]. Improvements in fatigue life can be expected from the structure refinement. Table IV shows the results of tension and fatigue tests (axial, zero mean stress). The final grain sizes of all three products were approximately equal in T4 condition.

Splat cooling suppressed completely the formation of the brittle, complex (CuMgFeAl) intermetallic phase and only the $CuMgAl_2$ phase was observed. This phase did not coarsen during the 495°C solution treatment. In no case was there evidence of cracking or debonding of the micron sized intermetallic phases during fatigue testing.

At 205°C, the splat atomized product did not show intergranular creep fracture in creep tests of at least 400 hours, whereas the ingot product

showed the intergraunular fracture at about 80 hours; the net effect was an increase in stress for 1000 hours rupture life from 8600 to 12,500 psi (6.1 to 8.9 Kg/mm^2).

B. IN-100

IN-100 is one of the strongest nickel base alloys, available as a cast material; it is not forgeable. A typical composition, in weight percent, is:

10.5 Cr, 15.4 Co, 3.02 Mo, 5.55 Al, 4.72 Ti, 0.16 C, 0.015 B, 0.06 Zr, 1.05 V, 0.94 Fe, <0.10 Mn, <0.1 Si, 0.007 S, balance Ni.

Powders from three sources showed the following oxygen content in ppm.

	Powder Source	Remelt Stock	Powder
a.	Argon atomization	108	158
b.	Soluble gas atomization	50	53
c.	Rotating electrode	74	79

The cooling rate of the powders was about 10^2 °C/sec, yielding a DAS of about 5 microns, compared to a DAS of about 70 microns for the precision cast structure. The latter had a grain size range of 1500 to 3000 microns. After hot extrusion of the powders, the final grain size of the alloy ranged from 6 to 8 microns.

Figure 2 compares the dendritic patterns of a powder particle and a precision casting. Note the relatively coarse carbide particles in the precision cast dendritic structure[29].

One of the problems encountered with HIP compacts of IN-100 is the presence of a carbide network (TiC) along prior powder particle boundaries, as shown in Figure 3. This carbide distribution makes subsequent recrystallization for grain coarsening much more difficult and it also decreases the ductility of the alloy. During extrusion of the alloy, the preferential carbide and oxide patterns are broken up but the formation of stringers can be quite detrimental[30].

Table V compares room temperature properties for the as-cast, HIP, extruded, and extruded plus grain coarsened states. In the HIP condition, there is a small increase in ultimate strength associated with the increased

ductility over the as-cast condition. By contrast, the extruded structures show large increases in yield, ultimate tensile strength and ductility compared to the cast product. Even after recrystallizing to a grain size of about 100 microns (from 8 microns), the ultimate tensile strength remains considerably higher than that of the casting due to the higher ductility.

These highly attractive low temperature properties which continue to be superior to those of the casting to about 750-800°C do not, unfortunately, give the best creep strength at 900 to 1000°C where a coarse grain size stabilized by coarse carbides appears to be superior. In the HIP condition, the fracture path follows the inter-powder-particle boundaries where carbides and oxide films lead to a lower strength (Figure 4a). By comparison, in a similar test at 1150°C, IN-100 in the extruded condition undergoes normal intergranular cracking. The presence of carbides and oxide films is a major problem in considering the possibility of using this class of alloy in the HIP condition[29].

Table VI compares the stress for a 100-hour rupture life at 982°C (1800°F) for the as-cast condition and various grain sizes of extruded material.

Grain coarsening beyond about 500 microns is difficult, especially when the stable coarse carbides network is present.

Perhaps one of the most interesting applications made possible by the powder approach is that of utilizing the ultra-fine grain to achieve superplasticity for easy forming and then to heat treat the structure to achieve the grain size desired for the particular application. Figure 5 shows the presence of the superplastic state for IN-100 in tests performed on the as-extruded condition (g.s. equals 8 microns) at 1038°C (1900°F).

C. MAR-M-509 and a Hafnium Modification

These cobalt base alloys are of particular interest because of a possibility of utilizing steam or water atomization to produce coarse powders (0.4 to 4 mm) which can be cleaned to a level of oxygen content of about 250 ppm[30]. The water quench, being faster than the inert gas quench, yields a DAS of about 5 microns with a much larger diameter of the powders. The compositions of these alloys are, in weight percent:

	C	Ni	Cr	W	Ta	Zr	Hf	Co
MAR-M-509	0.6	10	22	7	3.5	.7	-	bal.
Hf. Mod. Co	.2 - .75	10	22	7 Mo	-	-	2-9	bal.

Once cleaned, the powders were canned, evacuated, sealed, and consolidated by HIP. In addition, powders consolidated by HIP were subsequently extruded or hot rolled.

The powder approach to making preforms or final shapes depends on one's ability to bond the powders by sintering, HIP, or hot mechanical pressing. The presence of films or hard phases at powder surfaces interferes with bonding, as shown in Figure 4 for IN-100. In the case of MAR-M-509, coarse powders were processed by HIP at 28,000 psi (2000 atm.) and at temperatures of 1093, 1178, and 1260°C (2000, 2150, and 2300°F). The dependence of the microstructure upon the HIP temperature can be summarized as follows:

a) with increasing HIP temperatures, the number of inter-powder particle fractures decreases,

b) the dendritic pattern gives way to a partially recrystallized grain pattern at 1178°C, however, the dendritic structure is still prominent. Figure 6 shows the longitudinal microstructure near the fracture of a room temperature tensile test[31] of the material compacted at 1178°C.

c) at 1260°C, a fully recrystallized structure appears.

Figure 7 shows the fine, uniform grain structure after hot extrusion (grain size equals 4-6 microns). The same structure re-exposed to HIP at 1260°C coarsens as shown in Figure 7. In these alloys, the stable carbide dispersion makes uniform coarsening difficult to achieve. Figure 8 shows the rate of coarsening for the MAR-M-509 alloy.

Results of tension tests at room temperature are shown in Table VII for MAR-M-509[31].

Again, significant improvements are observed in yield and tensile strength for the extruded condition, along with large increases in ductility. The HIP product, as noted above, shows low ductility and relatively low tensile strength.

In stress rupture tests at 982°C (1800°F), as with the IN-100 alloy,

the best results are shown by the cast alloy and the poorest by the highly ductile, essentially superplastic, fine grained extruded alloy. Grain coarsening attempts have been successful in improving the high temperature properties, as shown in Table VIII[31].

VI. DISCUSSION

It is evident that the proper use of atomized and quenched powders can lead to an excellent control of the microstructure of an alloy. Cooling rates from 10^1 to 10^6 °C/sec should result in the control of grain size, inclusion and second phase particle size and distribution. In some special applications higher cooling rates may be desired to achieve increases in solubility of solutes, to produce metastable intermetallic compounds, and even to produce amorphous structures. Such structures would then be converted to stable phases but with particle sizes, shapes, and distributions which are not otherwise attainable.

The improvement in ductility and hot plasticity, of complex and highly alloyed material should encourage use of the powder approach, to higher alloy contents. For instance, increases in Al + Ti in the IN-100 alloy and of carbon and carbide former elements in the MAR-M-509 alloy, are feasible.

A number of other fruitful research areas are worth mentioning:

1. Improvements in atomization are still necessary, both to control the powder size and distribution, but also to limit the retained or trapped argon in inert gas atomization, or hydrogen in the soluble gas-vacuum method. Cost improvements are definitively required.
2. Control of the powder surface films is needed when the hot pressed condition is desired as the final processing step.
3. A better understanding of the influence of the HIP parameters on the properties of the HIP billet is required.
4. Optimum hot working conditions to shape a billet and to control the grain size.
5. Thermomechanical treatments to take advantage of the high ductility and the superplastic potential, of the totally new structures. Solution and precipitation processes have to be adapted because of the metastability of compositions and structures of the rapidly quenched materials.

6. Alloy development to take advantage of the increased ductility and hot plasticity. In this respect, alloy chemistries may be modified for the HIP state and for the hot worked product.

In summary, there are a number of interesting technological developments which make the processing of high performance alloys from quenched powders look feasible and attractive. The long range opportunities are great and these new processes should not be looked at as mere laboratory curiosities.

VII. ACKNOWLEDGEMENTS

The authors are indebted not only to their students and associates for the data in this presentation, but to NASA, ARPA and INCRA for support of various phases of the research.

VIII. REFERENCES

1. H. Matyja, B.C. Giessen, and N.J. Grant, J. Inst. Metals, 96, (1968), 30.
2. V.K. Sarin and N.J. Grant, Met. Trans., 3, (1972), 757.
3. P. Duwez, R.H. Willens, and W. Klement,Jr., J. Appl. Phys., 31, (1960), 1136.
4. P. Duwez and R.H. Willens, Trans. Met. Soc. AIME, 227, (1963), 362.
5. W. Klement,Jr., R.H. Willens, and P. Duwez, Nature (London), 187, (1960), 2267.
6. P. Duwez, R.H. Willens, and R.C. Crewdson, J. Appl. Phys., 35, (1965), 2267.
7. P. Predecki, A.W. Mullendore, and N.J. Grant, Trans. Met. Soc. AIME, 233, (1965), 1581.
8. W.A. Dean and R.E. Spear, Proc. 12th Army Mats. Res. Conf., 268, (1966), Syracuse University Press, Syracuse, New York.
9. R.C. Ruhl, Mats. Sci. and Eng., 1, (1967), 313.
10. R.C. Ruhl and M. Cohen, Trans. TMS-AIME, 245, (1969), 241.
11. T.R. Anantharaman and C. Suryanarayana, J. Mats. Sci., 6, (1971), 111 and 7, (1972), 351.
12. M.H. Burden and J. Jones, J. Inst. Metals, 98, (1970), 249.
13. C.H. Jansen, "Splat Cooled Aluminum-Rich Transition Metal Alloys: Supersaturation, Annealing Behavior, and Atmospheric Corrosion", Ph.D. Thesis, Department of Metallurgy and Materials Science, MIT, (1971).
14. R.C. Ruhl, B.C. Biessen, M. Cohen and N.J. Grant, Mats. Sci. and Eng., 2, (1967), 314.

15. B.C. Giessen; "Constitution of Non-Equilibrium Alloys After Rapid Quenching from the Melt", Developments in the Structural Chemistry of Alloy Phases, B.C. Giessen, Ed., Plenium Press, New York (1969).

16. M.R. Lebo, "Structure Refinement and Property Control in Aluminum Alloys Through Rapid Quenching of the Melt", Ph.D. Thesis, Department of Metallurgy and Materials Science, MIT, (1971).

17. R.C. Ruhl, B.C. Giessen, M. Cohen and N.J. Grant, Acta Met., 15, (Nov., 1967), 1693.

18. P.K. Srivastava, B.C. Giessen, and N.J. Grant, Met. Trans., 3, (1972), 977.

19. P. Duwez and C.H. Lin, J. Appl. Phys., 38, (1967), 4096.

20. P.K. Rastogi and P. Duwez, J. Non-Crystal. Sol., 5, (1970).

21. H.S. Chen and D. Turnbull, J. Appl. Phys., 38, (1967), 3646.

22. R. Ray, B.C. Giessen and N.J. Grant, Scripta Met., 2, (1968), 357.

23. A. Revcolevschi and N.J. Grant, "Study of a Splat-Cooled Cu-Zr-Non-Crystalline Phase", Met. Trans., 3, (1972), 1545.

24. Proc. of the Intl. Conf. on Metastable Metallic Alloys, Ed. M. Paic, Fizika, 2, Suppl. 2, (1970), (Brela).

25. N.J. Grant, "Special Powder Atomization Production Techniques", Powder Metallurgy, 17th Sagamore Army Mats, Res. Conf., Burke, Reed and Weiss, Eds., Syracuse University Press, (1971).

26. M. Itagaki, B.C. Giessen, and N.J. Grant, Trans. ASM, 61 (1968), 330.

27. K. Erhardt and N.J. Grant, Fracture 1969 - Proc. of the 2nd Intl. Conf. on Fracture (Brighton, England), Chapman and Hall, Ltd., (April, 1969).

28. R.M. Pelloux, K. Erhardt, and N.J. Grant, "Applications of the Scanning Electron Microscope to Electron Fractography", Scanning Electron Microscopy - 1970, Proc. 3rd Annual SEM Symposium, IIT Research Institute, pp. 281-87, (Chicago, Illinois), (1970).

29. L.N. Moskowitz, "Properties of a Nickel Base Superalloy Processed by Powder Metallurgy", S.M. Thesis, Department of Metallurgy and Materials Science, MIT, (1972).

30. R.W. Widmer, "Steam Atomization of Superalloys", Powder Metallurgy, 17th Sagamore Army Mats. Res. Conf., Burke, Reed and Weiss, Eds., Syracuse University Press, (1971).

31. R.K. Robinson, private communication.

TABLE I

Maximum Metastable Solubilities Observed at Cooling Rate of ≈ 10^6 °C/second

System	Max. Equil. Sol. (a/o)	Max. Extrap. Metastable Sol. a/o	Equil. Eutect. Comp. a/o	Solubil. Increase
Al-Pd	nil	7.5	7.5	
Al-Cu	2.5	18.	17.3	7X
Al-Mn	0.7	9.	1.0	13X
Al-Fe	0.025	4.	0.9	160X
Al-Co	0.02	0.5	0.45	25X
Al-Ni	0.023	1.2	2.7	50X
Al-Si	1.59	11.	11.3	7X

TABLE II

Al-Si Alloys Tested at 20°C

		0.2% Y.S.		U.T.S.		El.	R.A.
Alloy	Condition	psi	Kg/mm²	psi	Kg/mm²	%	%
Al-7% Si	Air atom. As extrud.	17,300	12.3	27,600	19.6	26	41
Alloy 43	Die cast	13,000	9.2	27,000	19.1	4	-
(5% Si)	Sand cast	9,000	6.4	18,000	12.8	6	-
	Perm. mold	10,000	7.1	22,000	15.6	8	-

TABLE III

Structural Characteristics of 2024 Alloy

Product	Quench Rate °C/sec	Dendrite Size (microns)	Constituent Particle Size, (microns)
Ingot bar	10^{-1}	60	10-20
Air atomized	10^2	7	4-6
Splat atomized	10^5	1-2	0.5-1

TABLE IV

Room Temperature Properties of Al Alloy 2024-T4

Product	0.2% Y.S. Ksi	0.2% Y.S. Kg/mm²	U.T.S. Ksi	U.T.S. Kg/mm²	El. %	R.A. %	Fatigue life, cyl. at 30,000 psi (21.2 Kg/mm²)
Ingot bar	40.2	28.5	67.2	48.7	23	37	100,000
Air atomized	42	29.7	70	49.5	25	33	300,000
Splat atomized	47	33.3	76	54	24	34	700,000

TABLE V

Room Temperature Properties of IN-100

Condition	0.2% Y.S. Ksi	0.2% Y.S. Kg/mm²	U.T.S. Ksi	U.T.S. Kg/mm²	El. %	R.A. %
As cast (1500μ)	136	96	143	101	4	8
As HIP	137	97	163	116	8	10
As Extrd. (8μ)	175	124	244	172	20	16
Extrd., Recryst.	171	121	238	168	21	17
100μ grain coarsened	137	97	188	133	14	7

TABLE VI

Stress Rupture Data at 982°C for IN-100

Condition	Stress for 100-Hour Life Ksi	Stress for 100-Hour Life Kg/mm²	El., %
As Cast	22	15.6	10
As extrd. (8 g.s.)	2	2	43
Extrd., Recryst. (100 g.s.)	12	8.5	5
Extrd., Recryst. (500 g.s.)	17	12.1	4

TABLE VII

Room Temperature and 982°C Properties of MAR-M-509

Condition	0.2% Y.S. Ksi	0.2% Y.S. Kg/mm²	U.T.S. Ksi	U.T.S. Kg/mm²	El. %	R.A. %
As cast (4000μ g.s.)	80	56.7	115	81.8	2.5	-
As Extrd. (3-4μ g.s.)	130	92.6	192	136.0	14.	12
Extrd. Recryst. (10-20μ g.s.)	94	66.6	166	117.5	11.	8
HIP (5-6μ g.s.)	81	57.3	108	76.5	1.1	0.4

TABLE VIII

Stress Rupture Properties at 982°C for MAR-M-509

Condition	Stress for 100-Hour Life Ksi	Kg/mm²	%
As cast (4000μ g.s.)	17	12	8-10
As extrd. (5μ g.s.)	2.5	1.77	40-120
Extrd., Recryst. (4 and 500μ mixed g.s.)	7.5*	5.32	10

* at 1010°C (1850°F)

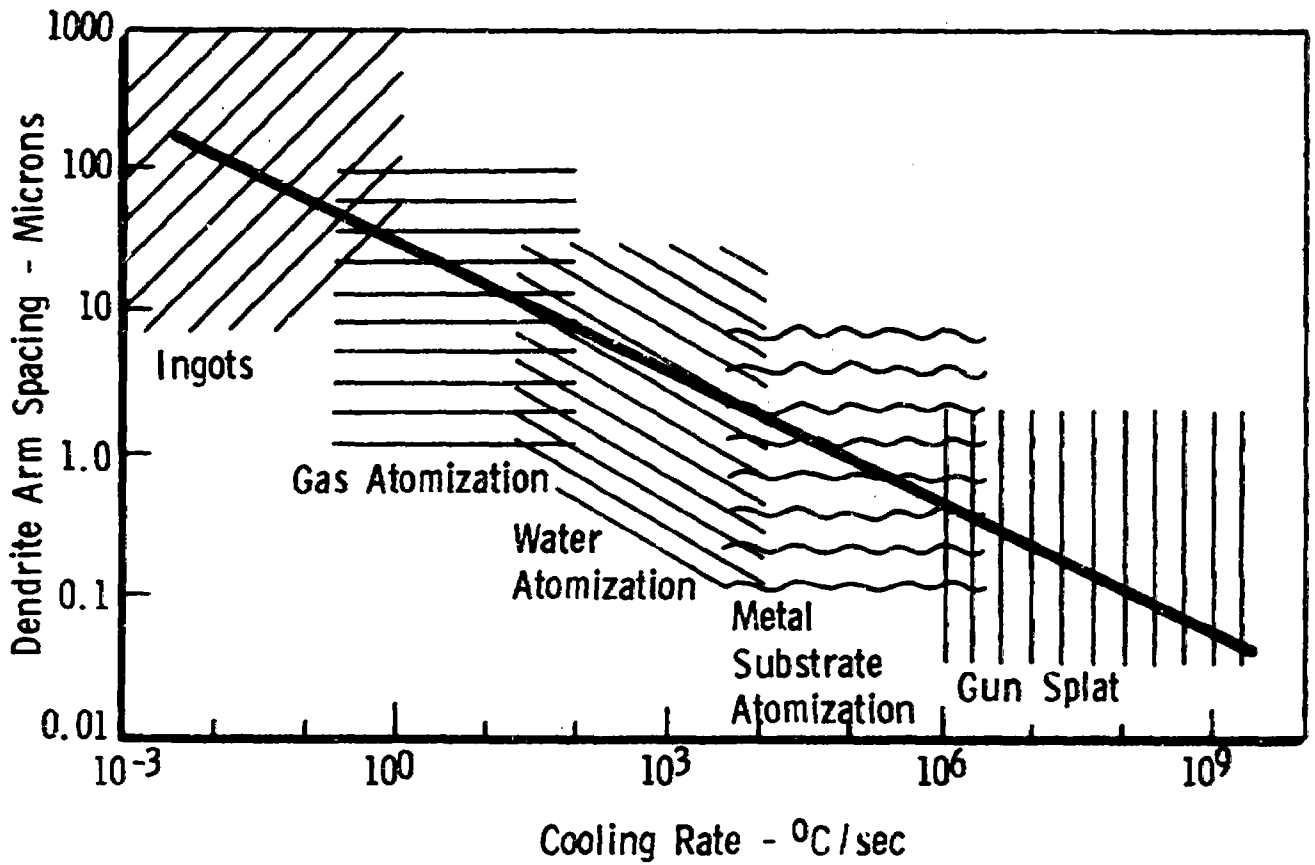

Figure 1 - Dendrite arm structure as a function of cooling rate for aluminum and aluminum alloys.

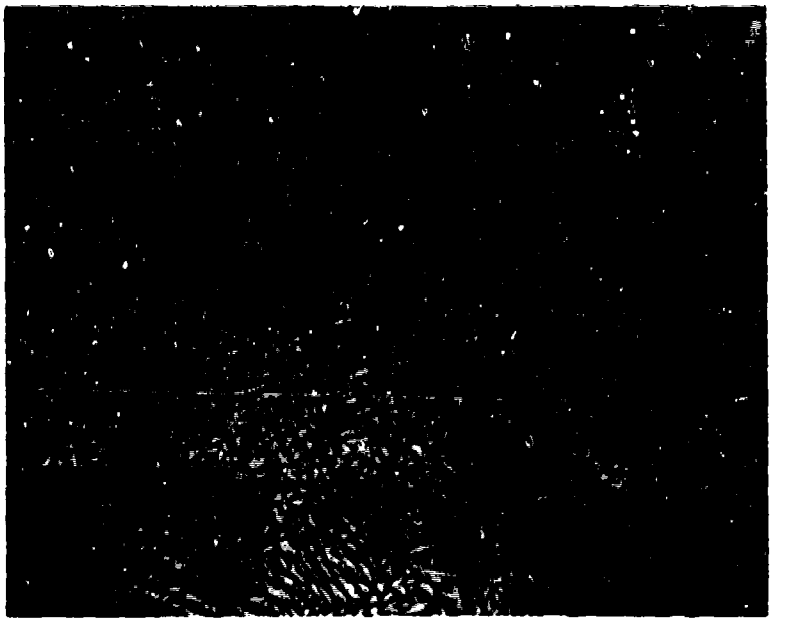

(a)

(b)

Figure 2 - Polished and etched sections of IN-100 showing dendritic patterns (a) powder particle by rotating electrode process, 200X; (b) precision cast tensile bar, 100X.

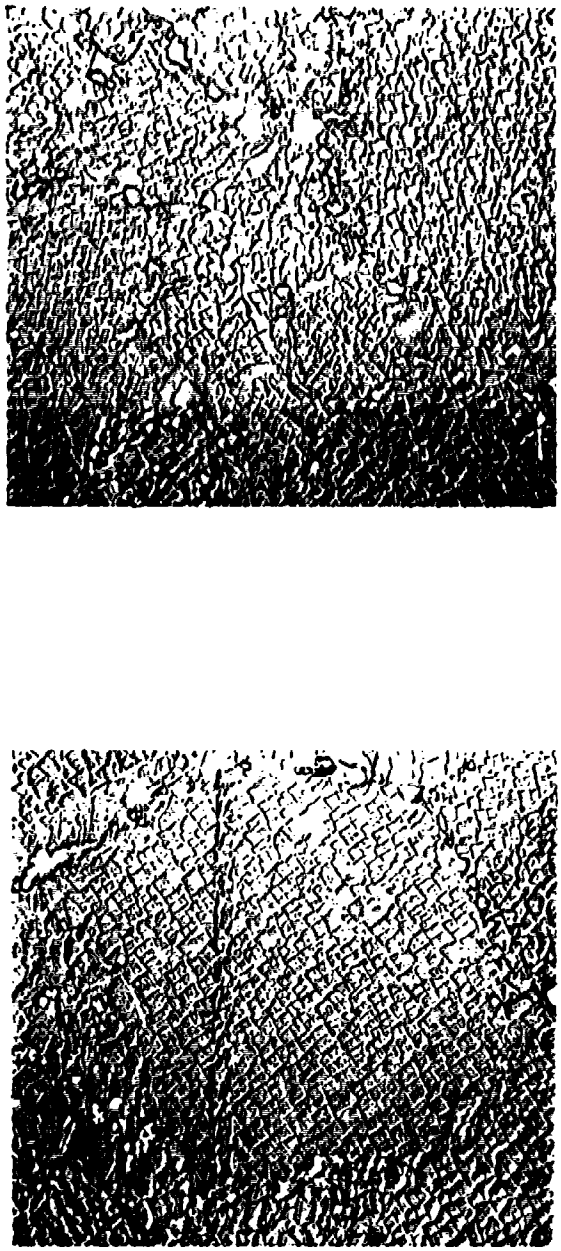

Figure 3 - Replica electron micrographs of as-HIP FM powder showing extensive carbide phase surrounding prior particle boundaries, 4000X.

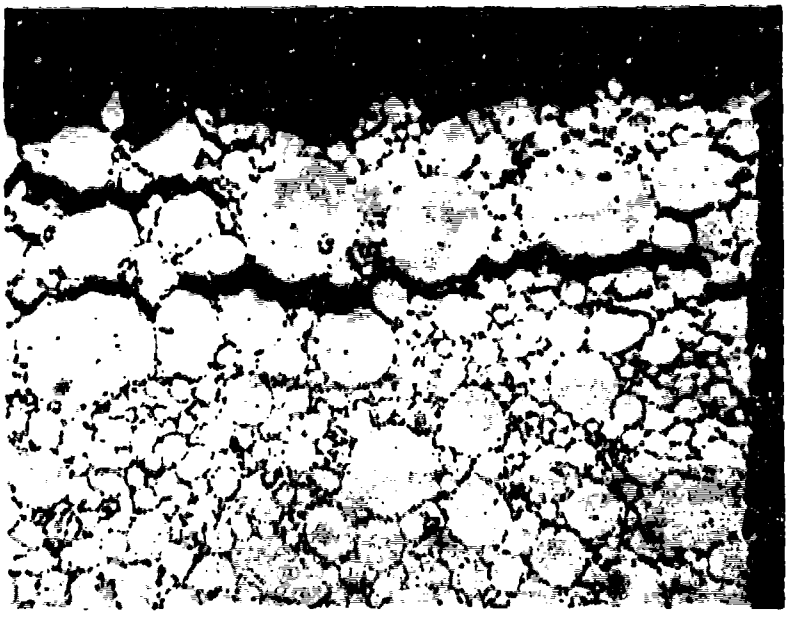

(a)

(b)

Figure 4 - High strain rate tests of IN-100 at 1150°C (2100°F). (a) HIP condition, (b) hot extruded condition, 200X.

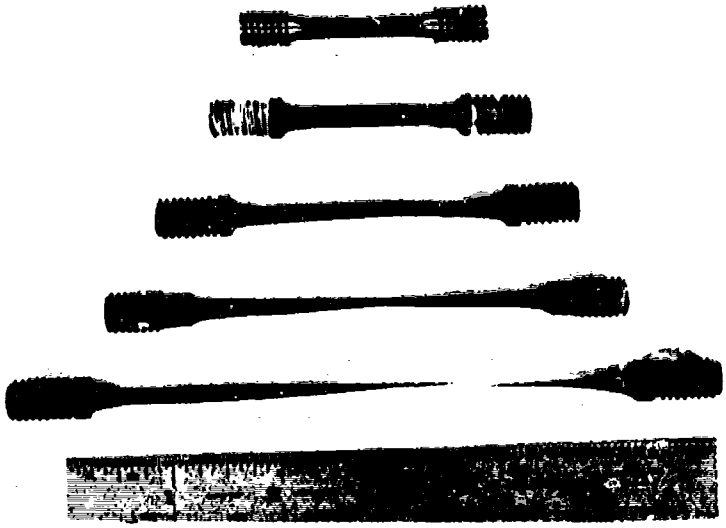

Figure 5 - As-extruded test bars superplastically deformed at 1038°C (1900°F) at strain rates from 0.5 to 0.01 min^{-1}. Bar at top is size of undeformed tensile specimen.

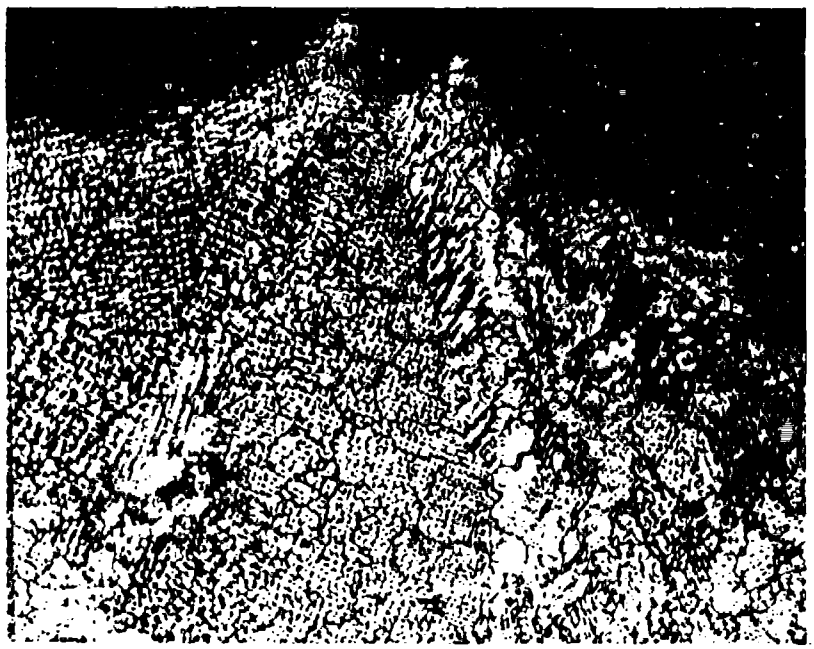

Figure 6 - MAR-M-509 at 1178°C (2150°F) and 2000 atmospheres (28 ksi) for 2 hours. Tension test at 20°C. (a) cross section (b) longitudinal section at fracture.

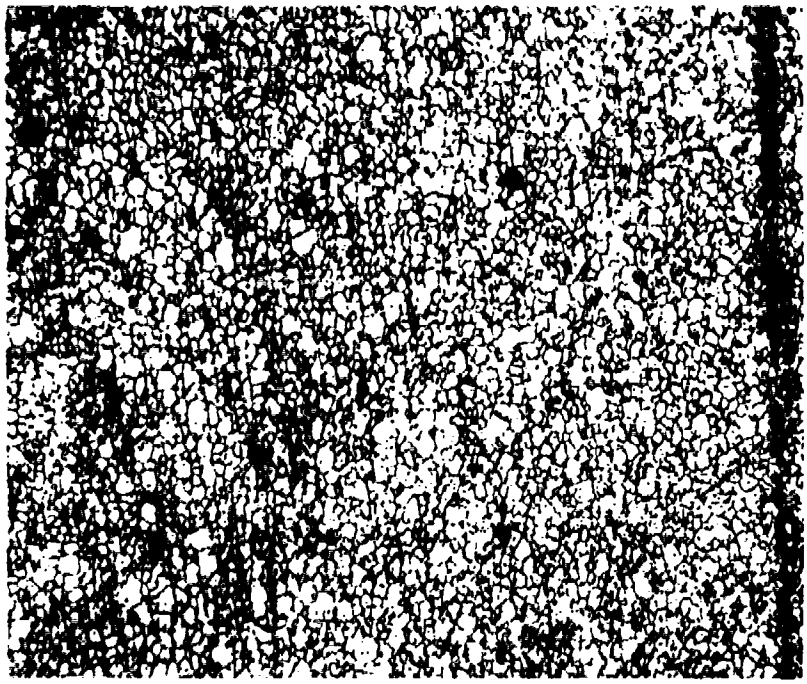

(a)

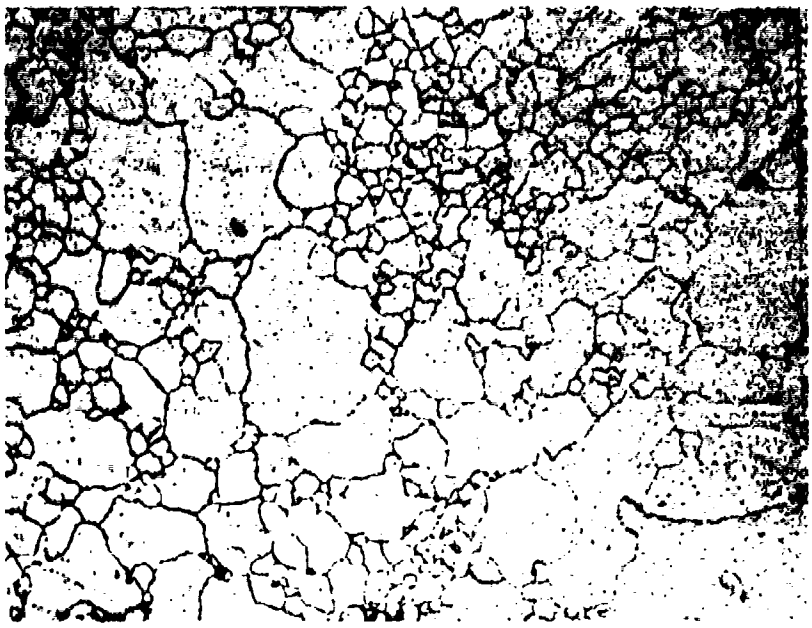

(b)

Figure 7 - Cobalt-1 atom percent HfC P/M alloy comparing (a) HIP + extruded structures with (b) same material re-HIP at 1260°C (2300°F) for 1 hour.

PROPERTIES OF IN-100 PROCESSED BY POWDER METALLURGY

by

L.N. Moskowitz, R.M. Pelloux and N.J. Grant
Department of Metallurgy and Materials Science
Massachusetts Institute of Technology
Cambridge, Massachusetts

ABSTRACT

A powder metallurgy approach to the production of IN-100 has been shown to result in a fully dense, homogeneous alloy with excellent hot-workability. Small billets were prepared by compacting metal powders processed by inert-gas atomization, by vacuum-atomization, and by the rotating electrode process. The different powders are characterized by scanning electron microscopy, and size distributions as well as dendrite arm spacings are presented. Compaction of the powders was done by hot isostatic pressing followed by hot extrusion. The mechanical properties of different billets are compared to the cast IN-100 as a function of the processing variables. Characterization of the hot workability of the powder processed IN-100 is first done by high strain rate testing, and finally by an investigation of the superplastic behavior at low strain rates in the temperature range from 1800°F to 2100°F. The rate of grain coarsening at 2270°F is shown to depend upon the size and amount of titanium carbide phase at the prior particle boundaries.

The excellent low temperature properties of IN-100 processed by powder metallurgy are related to the refinement of the grain size and microstructure and break-down of powder particle films obtained during atomization and hot extrusion. The stress-rupture properties at 1800°F, which are strongly dependent upon the grain size obtained during the 2270°F coarsening heat treatment, are slightly inferior to the properties of the cast alloy.

PROPERTIES OF IN-100 PROCESSED BY POWDER METALLURGY

by

L.N. Moskowitz, R.M. Pelloux and N.J. Grant

I. INTRODUCTION

The main goal of this work was to investigate the properties of a nickel-base superalloy processed by powder metallurgy. This material will be referred to as a P/M alloy as opposed to a cast alloy. Nickel base superalloys, widely used as components of modern gas turbines, consist of a solid-solution hardened nickel-chromium matrix strengthened by an ordered gamma-prime ($Ni_3(Al, Ti)$) dispersed precipitate, and by some complex metal carbides. The metallurgy of these alloys has been reviewed by Decker[1] and Sims[2]. The complexity of the alloy chemistry is such that severe segregation is always present in small as well as in large castings. Although the precipitated gamma prime phase goes into solution above about 2000°F, the carbide phases and the primary gamma prime do not re-solution until incipient melting has taken place at about 2300°F. Therefore, the hot plasticity of the cast alloys is severely limited even above 2100°F.

Since a prealloyed powder particle is an extremely small casting, segregation is restricted to each particle of powder. Cooling from the molten state is much faster for a powder particle

(10^3 °C/sec) than for a sand casting (10^0 - 10^{-2} °C/sec). As a consequence, the dendrite arm spacing and the volume fraction of large second phase particles are quite small, which will facilitate homogenization of the alloy. The mode of compaction of the powders can be selected from a wide variety of processes, such as sintering, hot isostatic compression, hot extrusion, etc., which can be tailored to optimize the size and shape of the finished part. The fine grained structure, achieved by the powder process, insures good ductility even for the brittle and hard-to-work alloy compositions.

Allen et.al.[3] made one of the first attempts to produce P/M ingots of Astroloy. To eliminate oxidation of individual powder particles, an "all-inert" method of powder production, collection and densification in an argon atmosphere was developed. Densification was performed by hydraulic pressing in a heated die, under a range of temperatures and pressures. Subsequent forgings of full scale discs yielded a structurally uniform product; however, the mechanical properties were inferior to those of conventional Astroloy forgings. The microstructure of the P/M alloy showed recrystallized grains and a network of small, discrete precipitates, identified as titanium carbide (TiC), along the prior particle boundaries.

Reichman et.al.[4] conducted a program to process superalloys from argon atomized powders with a low interstitial content. The two alloys studied were IN-100 and U-700, used respectively for cast turbine blades and wrought turbine discs. The consolidation

techniques evaluated were vacuum hot pressing, forging, extrusion, hot isostatic pressing and spark sintering. Direct hot extrusion was found to be the best compaction process due to the rapidity of densification and the reproducibility of the processing variables. Hot isostatic pressing, while producing limited amounts of plastic deformation, was considered important for the fabrication of large forging or extrusion preforms. These processes will be discussed in more detail later. An evaluation of the final extruded product showed an ultrafine grain structure exhibiting superplastic behavior at high temperatures and low strain rates. An extremely large grain size structure was also achieved following some undisclosed thermomechanical treatment. This material exhibited stress-rupture properties superior to those of the cast and wrought alloys. The grain growth behavior leading to grain sizes larger than the original powder particles was attributed to the low contamination of the powder surface and low oxygen content of the densified product.

In a further investigation into the superplasticity of the extruded IN-100 powder, Reichman et.al.[5] showed that grain growth can also be achieved subsequent to superplastic deformation without an intermediate thermomechanical treatment. In order to obtain a very fine grain size (on the order of a few microns) which will lead to superplastic deformation, the powder compacts were extruded below the recrystallization temperature of the alloy. Adiabatic heating during extrusion leads to recrystallization and a fine-grained structure.

A practical method for fabricating high temperature alloys to close tolerances, utilizing the low strength and high ductility offered by the superplastic behavior of the alloys, was patented in 1970 under the name of "gatorizing"[6]. It is claimed to apply to alloys in the cast condition, as well as to powder products. The process consists of working the alloy initially in compression at a temperature below, but approaching the recrystallization temperature and producing a very fine recrystallized grain size. Forging is done in hot dies, in an inert atmosphere, at an appropriately slow deformation rate. The part is then recrystallized and grain coarsening restores the high temperature strength. Production of full-scale compressor and turbine discs by the gatorizing process from IN-100 powder billets is described by Athey et.al.[7].

The mechanism of grain coarsening in the P/M alloy to the grain sizes of the cast alloy was studied more recently by Reichman et.al.[8]. A series of alloys were designed and tested with very low carbon contents, thereby eliminating the presence of carbides at grain boundaries and allowing easy grain growth. It was suggested that a final carburizing treatment can be easily accomplished to precipitate some carbides for grain boundary stability.

IN-100 was selected for our work since it is one of the highest strength cast-nickel base superalloys, very difficult to fabricate, with a high volume percent of gamma prime. Powders obtained by three different atomizing techniques were investigated: inert-

gas atomization, vacuum atomization, and the rotating electrode process. The microstructure, grain growth, hot plasticity, and mechanical properties of billets compacted by hot isostatic pressing and hot extrusion were investigated and compared to the cast alloy.

II. CHARACTERIZATION OF METAL POWDERS

Three types of prealloyed IN-100 powders were evaluated. They will be referred to as FM powder (inert-gas atomization), HM powder (vacuum atomization), and NM powder (rotating electrode process). In inert-gas atomization, a pre-alloyed vacuum cast ingot is vacuum remelted, and atomized by a stream of high purity argon gas. The size of the spherically solidifying particles is controlled by the atomizing parameters. In vacuum atomization, a vacuum remelted alloy is pressurized and saturated with a soluble gas such as hydrogen. Atomization is obtained by dissociation of the liquid metal-gas mixture in a vacuum chamber. As the metal rises, the stream is exploded by the gas escaping the liquid metal, and a coarse powder is produced. The rotating electrode process[9] uses a consumable rotating electrode of the alloy which is continually melted by an arc from a stationary tungsten electrode. Powder production takes place in a chamber filled with high purity helium, in which fine spherical droplets are flung off by centrifugal force. The powder particle size is controlled by varying the electrode diameter and the electrode rotating speed. The principles behind the production and control of powder particles have been reviewed by Orr[10].

Coarse, spherical IN-100 powders could not be produced by steam atomization due to the high titanium and aluminum content of the alloy. The coarse powder obtained was sharp and flaky with a thin, adherent oxide film. The shapes of these powders are

unfavorable for processing since they present many reentrant cavities and folds in cleaning, and have a very low packing density in hot isostatic pressing or extrusion cans.

Chemistries, size ranges and screen analyses of the three powders used are presented in Tables I and II. With the exception of FM powder, all contain less than 100 ppm of oxygen and show little oxygen pick-up during powder production. Typical powder particles viewed by scanning electron microscopy are shown in Figures 1, 2 and 3. FM powders are predominantly spherical in shape with many fine particles attached to coarser particles. The dendritic structure can be seen in relief only on the surface of the larger particles. HM powders are much more irregular in shape, and consist of flakes as well as droplets. Some surfaces contain protrusions, and the dendritic structure can be identified. NM powders are much smoother and well-rounded, and more uniform in size. The surface appearance indicates a much cleaner powder. Polished and etched cross-sections of powder particles of each type are presented in Figures 4, 5 and 6. The average secondary dendrite arm spacing in FM powder is 2 microns, in HM is 6 microns and in NM is 3 microns, and varies little in each heat. For a discussion of the variation in dendrite arm spacing with cooling rate, see Ref. 13. A semi-qualitative analysis of the surface and interior of the particles was done with a non-dispersive X-ray attachment to the SEM. There was no marked difference in chemistry between the core and the outside surface of the powders.

III. POWDER CONSOLIDATION

Hot isostatic pressing (HIP) is a consolidation process involving the application of a hydrostatic pressure by a gas (usually agron or helium) at elevated temperatures to evacuated, canned powders. With the advent of modern high-pressure equipment, large diameter parts with complex geometries can be fabricated[11]. It has been shown that full density can be achieved by HIP processing,[12,13,14] with good control over microstructure and chemistry. While the final structure is isotropic, only limited amounts of plastic deformation can be achieved during pressing. The basic requirement of the canning material is high plasticity at the forming temperature. Thin gauge low alloy carbon steel is often used and contamination of the core is negligible[14].

Direct powder extrusion, in evacuated cans, offers both hot consolidation and hot mechanical working to yield a fully dense wrought material. Interparticle shearing promotes a break-up of prior particle boundaries as well as enhancing bonding. Hot extrusion of superalloy powders has been carried out over a wide range of temperatures and extrusion ratios[4,15]. The parameters involved in the selection of the correct temperatures, reduction ratios, canning material and heat treatment are discussed by Bufferd[15]. In general, the canning material must be as strong as the powder at the extrusion temperature, and it should be easy to remove after processing.

In this study, small billets of IN-100 were prepared by the above consolidation techniques, as listed below:

1) Hot isostatically pressed FM powders, 1" x 1-1/2" x 20". Pressed at 2320°F and 25,000 psi for one hour.

2) Hot isostatically pressed HM powders, extruded to 3/4" diameter rod. Pressed at 2300°F and 15,000 psi for one hour; extruded at 2000°F with a 12:1 reduction.

3) Direct extruded FM and NM powders (2 bars), 1/2" diameter x 7' in length. Extruded at 2150°F with a 20:1 reduction.

IV. RESULTS AND DISCUSSION

Microstructure

All metallographic samples were polished to 0.05 micron alumina in distilled water. The different etching solutions given in Table III attack gamma prime, leaving the carbides in relief and gamma prime depressed relative to the gamma matrix. Etchant no. 1 gave the best overall structural definition, while etchant no. 4 was used to delineate the dendritic structure. All were applied by immersion and the etching times are indicated.

Two-stage carbon-chromium replicas were prepared from cellulose acetate first stage replicas. The shadowing angle was approximately 30°.

In order to compare the structures and properties of the powder product to the cast alloy, an investment casting of IN-100 was made into 24 3/8-inch diameter thread tensile bars. The casting was made from a vacuum cast ingot of IN-100 (see Table I for the chemical analysis). The bar was remelted under an argon atomsphere, and cast at 2730°F into a mold at 1500°F. The average grain size in the cast bars is 1500 microns, with about five grains per diameter.

The average secondary dendrite arm spacing in the cast IN-100 tensile bars is 28 microns, as seen in Figure 7, and the typical cast nickel-base superalloy structure is evident in Figure 8. The average size of the matrix gamma prime particles is about 1.5

microns.

Figure 9 shows the structure of the hot isostatically pressed bar of FM powder. Recrystallization has taken place within the particle boundaries, but there is no sign of plastic deformation in individual powder particles. An almost continuous film of second phase precipitates surrounds each particle. This, as well as the gamma prime morphology and size (about 0.7 microns), can be seen more readily in the replica electron micrographs of Figure 10. Nondispersive X-ray analysis showed the surrounding phase to be rich in titanium, a strong carbide forming element, and to contain a much smaller concentration of aluminum. In order to make a positive identification, carbon extraction replicas were prepared. A 10% bromine in alcohol solution was used to dissolve the matrix after direct evaporation of a carbon film on the polished and well-etched sample. Electron diffraction of the extracted replicas, using a 200 kv electron beam, showed the phase to be titanium carbide. The presence of aluminum in the carbides is most likely related to an oxide phase identified by Moyer in similar work on U-700[16].

Upon examination of the bar of HM powder which had been hot isostatically pressed and then extruded, the entire length was found to contain numerous holes and cavities. This porosity is attributed to the presence of some residual hydrogen, remaining in the powders after vacuum atomizing, and vacuum degassing prior to hot pressing.

The microstructure of the as-extruded bars is shown in Figures 11 (FM powder) and 12 (NM powder). The particles have been well deformed, and a recrystallized grain size of about 8 microns is evident in both bars. Large carbides within the particle boundaries can be seen in the bar extruded from NM powders. These carbides were present in the original powders. The prior particle boundaries of the FM powder extrusion are still delineated by a second phase, although not to the extent that it was in the HIP material. In the NM powder bar, this effect is even smaller. The average gamma prime particle size after extrusion is about 0.2 microns in each alloy.

Grain Coarsening

In order to see if significant grain growth could easily occur past the prior particle boundaries, a series of grain coarsening experiments were run. Tests initially performed at 2300°F showed evidence of incipient melting, and 2270°F was selected as an optimum coarsening temperature. The samples from the FM powder extrusion showed substantially less grain growth than those from the NM powder, indicating that the surrounding carbide phase can slow down grain growth markedly. In both alloys, however, grain boundaries were able to grow past the prior particle boundaries. For the FM powder extrusion, the average grain size was about 50 microns after 24 hours at 2270°F, with grains as large as 100 microns. For the NM extrusion, after the same treatment, an average grain size of about 100 microns was measured, with grains

as large as 200 microns (Figure 13).

Mechanical Properties

- Room Temperature Properties: The room temperature tensile properties and Rockwell C hardness values for the different materials are presented in Table 4. The excellent room temperature tensile properties of the as-extruded material are attributed to the refinement of the microstructure during atomization and the break-down of powder particle films during hot extrusion. There is no difference between transverse and longitudinal hardness, but the high hardness values correlate well with the high tensile properties. The tensile ductilities of all the P/M alloys are excellent considering the strength levels and compared to the ductility of the cast alloy.

- Hot Plasticity Tests: Characterization of the hot workability of the powder processed IN-100 was first done by high strain rate testing and finally by an investigation of the superplastic behavior at low strain rates. The high speed tensile testing was performed in a Nemlab high strain rate machine which has a stroke of 2-1/2 inches, and is capable of reaching a maximum load of 5000 pounds within 20 milliseconds, with maximum deformation rates on the order of 20 sec^{-1}. It has been used successfully as a means of simulating hot working operations, to find the optimum conditions of strain rate and temperature to forge high strength materials[17,18,19]. A complete discussion of the operation and calibration of the machine can be found in the work of Cederblad[17].

An 11-inch radiant split furnace was used to reach a maximum temperature of 2200°F in five minutes. Thermocouples were spot welded directly on the specimens. Tests were conducted on the as-cast, as-HIP, and as-extruded materials at 1900°F, 2000°F, 2100°F and 2200°F, the temperature range of conventional superalloy forging. The holding time at temperature was less than five minutes in all cases so as to limit structural changes and make the tests more reproducible.

The stress versus rupture time and stress versus average deformation rate showed suitable linear relationships on log-log plots. Typical curves for the as-extruded powders are shown in Figures 14 and 15. The ductility, measured as elongation after fracture, is presented for each test. The most noticeable difference in the behavior of the three materials tested is the sharp change in slope exhibited by the extruded product at rates below about 10^{-1} sec^{-1}. This break in the slope, indicating a change in structure, deformation or fracture mode, was not exhibited by either the cast or HIP alloy.

Poor ductility (<5% elongation) was exhibited at all temperatures by the cast and HIP bars. The ductility of the extruded material, however, is seen to increase markedly at slower deformation rates, especially at 2100°F. Total elongations as a function of deformation rate are plotted in Figure 16.

This behavior is identical to that shown by the work of Greene[20] and Cederblad[17] on cast Udimet 700 and Nimonic 115, respectively. It was found that the ductility of these nickel-base

superalloys increases as the strain rate decreases at all test temperatures, but ductility is maximized at 2100°F at all strain rates. The increase in ductility as the temperature is raised to 2100°F is due to the increased amounts of gamma prime going into the gamma solid solution. The decrease in ductility at temperatures greater than 2100°F is due to a structural change brought about by recrystallization.

A typical fracture cross-section of the hot isostatically pressed FM powder is shown in Figure 17. The bar failed by interparticle separation, explaining the low ductility of this material. The influence of the surrounding titanium carbide and oxide phases in initiating fracture at the powder particle boundaries was obviously great. A cross-section of an extruded FM powder test bar is shown in Figure 18. The material exhibits extensive intergranular cracking, accounting for part of its higher ductility.

A comparison of the high strain rate stress levels showed the extruded material to be stronger or as strong as the cast material, with the hot pressed material the weakest of the three. At deformation rates below about 10^{-1} sec^{-1}, however, the stress levels in the extruded product fall rapidly below both of the other materials, an effect most pronounced at 2100°F.

- Superplastic Deformation of As-Extruded Alloys: This extreme sensitivity of the deformation stress and ductility on temperature, strain rate and structure led to a series of low strain rate tensile tests, to investigate the superplastic behavior of the extruded material which had been reported by Reichman et.al.[5]. High

temperature tensile tests were performed on the as-extruded alloys over a range of strain rates from .005 to .5 $min.^{-1}$ at 1800°F, 1900°F, 2000°F and 2100°F.

Figure 19 shows the total elongation that can be obtained at different strain rates at 1900°F, as compared to an undeformed tensile bar of a one inch gauge length. The results are plotted on log-log coordinates as true flow stress vs. strain rate in Figure 20. It was found that the initial holding time at temperature had a marked effect on the tensile behavior, especially at the lower temperatures. For this reason, soaking times of 30 minutes at temperature were used before beginning each test. The slopes of the curves in Figure 20 are approximately the same and equal to 0.5 below about 10^{-1} $min.^{-1}$. This value of the slope was taken as the strain rate sensitivity exponent, m, in $\sigma = K\dot{\varepsilon}^m$, where σ = flow stress, K = constant, and $\dot{\varepsilon}$ = strain rate. The activation energy for the deformation process was determined from an Arrhenius plot at two stress levels. A constant activation energy of approximately 98 kcal/mole was found. These results are in agreement with the work of Reichman et.al.[5].

The microstructure of a superplastically deformed tensile bar is shown in Figure 21. The most noticeable change exhibited is the extreme growth of the gamma prime particles, from about 0.2 micron to an average size of one micron.

- Creep Testing: 1800°F stress-rupture tests were conducted on the extruded material from FM and NM powders, and the grain-coarsened (24 hours at 2270°F - air cooled) NM powder material.

To optimize the creep strength, the as-extruded material was over-aged at 1800°F for 24 hours, and the grain-coarsened material at 1825°F for 20 hours. The stress-rupture results are compared to stress-rupture properties of fine and coarse-grained cast IN-100[21] in Figure 22. The total elongations are presented for each test. The extruded material (average grain size of 8 microns) exhibits stress-rupture properties far inferior to that of the cast material, as a result of the fine grain size. The 100 micron grain-coarsened material shows stress-rupture properties beginning to approach those of the cast material. The total elongations observed in the material, however, are below those of the cast alloy. The difference in stress-rupture strength should be compensated for by improved fatigue properties due to the finer grain size and size of the second phase particles in the P/M alloy.

Some current work with low-carbon (.02%) P/M IN-100 alloys has shown that easy grain growth to cast grain sizes is possible. A hot isostatic pressing of these powders at 2300°F and 27,700 psi for one hour yielded a recrystallized grain size of about 500 microns with good 1800°F stress-rupture properties in the as-HIP condition. It is hoped that through proper processing of these low carbon P/M alloys, the creep and fatigue properties will prove to be superior to those of the cast alloy.

V. CONCLUSIONS

1. A powder metallurgy approach to the production of a highly alloyed, cast nickel-base superalloy results in a fully dense, homogeneous alloy with excellent hot-workability. The control over dendrite arm spacing, phase distribution and grain size is made possible by proper choice of prealloyed powder particles, consolidation methods and parameters.

2. The extruded P/M alloys show much better mechanical properties than do the hot isostatically pressed alloys. This is a result of the extensive interparticle shearing during hot extrusion, which promotes the break-up of prior particle boundaries and enhances bonding. The prior particle boundaries in the HIP product are delineated by an almost continuous film of titanium carbide and oxides, which retards grain growth and results in poor high temperature properties.

3. Inert-gas atomized powders and rotating electrode process powders show roughly equal properties after extrusion. Grain growth at 2270°F occurs more easily in the R.E.P. powder extrusion, which contains less surrounding carbide phase, than in the inert-gas atomized powder extrusion. In both materials, however, grain boundaries were able to grow past the prior particle boundaries.

4. The excellent room-temperature tensile properties of the as-extruded material are attributed to the refinement of the grain size and microstructure and break-down of the powder particle films during atomization and hot extrusion.

5. The ultra-fine grain structure resulting after extrusion and recrystallization, enables low strain rate, superplastic deformation of the P/M alloy to be employed as a close-tolerance fabrication procedure.

6. The stress-rupture properties at 1800°F are strongly dependent upon the grain size. Through use of a low-carbon P/M alloy of IN-100, easy grain growth is possible to typical cast grain sizes, and high-temperature stress-rupture properties should greatly improve.

REFERENCES

1. R.F. Decker: "Strengthening Mechanisms in Nickel-Base Superalloys", Market Development Department, International Nickel Company.

2. C.T. Sims: "A Contemporary View of Nickel-Base Superalloys", J. of Metals, Oct., 1966.

3. M.M. Allen, R.L. Athey, J.B. Moore: "Application of Powder Metallurgy to Superalloy Forgings", Metals Engineering Quarterly, Feb., 1969, p. 20.

4. S.H. Reichman, B.W. Castledine, J.W. Smythe: "Superalloy P/M Components for Elevated Temperature Applications", SAE Congress, Detroit, Michigan, Jan., 1970.

5. S.H. Reichman and J.W. Smythe: "Superplasticity in P/M IN-100 Alloy", Int. J. of Powder Met., 6, 1970, p. 65.

6. J.B. Moore, J. Tequesta, R.L. Athey: "Fabrication Method for the High Temperature Alloys", U.S. Patent 3,519,503, July 7, 1970.

7. R.L. Athey and J.B. Moore: "Development of IN-100 Powder Metallurgy Discs for Advanced Jet Engine Application", 18th Sagamore Army Materials Research Conference, August, 1971.

8. S.H. Reichman and J.W. Smythe: "New Developments in Superalloy Powders", Modern Developments in Powder Metallurgy, Hausner, ed., Vol. 5, Plenum Press, 1970, p. 73.

9. A.R. Kaufman: "Method and Apparatus for Making Powder", U.S. Patent 3,099,041, July 30, 1963.

10. C. Orr: Particulate Technology, Macmillan, New York, 1966.

11. H.D. Hanes: "Hot Isostatic Pressing of High Performance Materials", 18th Sagamore Army Materials Research Conference, August, 1971.

12. Semi-Annual Technical Report No. 1, ARPA, Contract No.: DAHC15 70 C 0283, January, 1971.

13. Semi-Annual Technical Report No. 2, ARPA, Contract No.: DAHC15 70 C 0283, June, 1971.

14. Semi-Annual Technical Report No. 3, ARPA, Contract No.: DAHC15 70 C 0283, January, 1972.

15. A.S. Bufferd: "Complex Superalloy Shapes", 18th Sagamore Army Materials Research Conference, August, 1971.

16. K.H. Moyer: "A Correlation of Mechanical Properties of Sintered U-700 Powder with Particle Boundary Morphology", Modern Developments in Powder Metallurgy, Hausner, ed., Vol. 5, Plenum Press, 1970, p. 85.

17. N. Cederblad: "Hot Deformation of Nimonic 115 at High Strain Rates", S.M. Thesis, MIT, August, 1971.

18. J. Dhosi, L. Morsing, N.J. Grant: "The Effect of Bismuth on the Hot Plasticity of Two Stainless Steels at High Temperatures and High Strain Rates", Eighth Mechanical Working and Steel Processing Conf., AIME, N.Y., 1967.

19. R.H. Kane and N.J. Grant: "Recrystallization and Grain Refinement", Ultrafine-Grain Metals, J. Burke and V. Weiss, ed., Syracuse University Press, 1970, p. 163-179.

20. B.N. Greene: "High Strain Rate Deformation of Udimet 700", S.M. Thesis, MIT, January, 1966.

21. "Engineering Properties of IN-100", International Nickel Company.

Table I - IN-100 Chemistries (w/o)

	Ni	Cr	Co	Mo	Al	Ti	C	B	Zr	V	Fe	Mn	Si	S	Oxygen (ppm)	
															Ingot	Powder
As-Cast	Bal.	10.5	15.4	3.02	5.55	4.72	.16	.015	.06	1.05	.94	<.10	.05	.007		
FM Powder	Bal.	9.54	13.97	3.70	5.65	4.82	.17	.014	--	--	--	--	--	--	108	158
HM Powder	Bal.	10.5	15.4	3.02	5.55	4.72	.16	.015	.06	1.05	.94	<.10	.05	.007	50	53
NM Powder	Bal.	9.40	15.18	3.08	5.81	4.82	.178	.016	.06	.99	<.01	<.10	<.10	.001	74	79

Table II - Size Range and Screen Analysis (% retained) of the Powders as Received from the Manufacturers

	FM POWDER	HM POWDER	NM POWDER
Size Range (microns):	-250+44	-707+74	-500+44
Mesh:			
-25+35	0.0	4.6	0.0
-35+60	0.5	43.0	4.3
-60+100	1.3	24.0	58.0
-100+200	43.3	28.4	29.5
-200+325	23.3	0.0	6.6
-325	31.6	0.0	1.6

Table III - Etchants

1. 92 HCl
   5 HNO_3
   3 H_2SO_4 - add last
   immersion (~30 sec)
   good for IN-100 microstructure and $Ni_3(Al, Ti)$
2. 60 glycerine
   30 HCl
   15 HNO_3
   immersion (~120 sec)
3. good for IN-100 microstructure and $Ni_3(Al,Ti)$
3. Kalling's etch
   5g $CuCl_2 \cdot 2H_2O$
   100 ml C_2H_5OH
   100 ml HCl
   immersion (~200 sec)
   good for IN-100 microstructure and grain structure
4. 70 HCl
   10 H_2O_2 (30%)
   HF (activator)
   immersion (~20 sec)
   good for IN-100 dendrite structure

Table IV - IN-100 Room Temperature Properties

Material	Hardness (R_c)	.2% YS (ksi)	UTS (ksi)	% elong.	% RA
As-Cast	32	136	143	4	8
As-HIP + EXTR (HM)	41	-	-	-	-
As-HIP (FM)	49	137	163	8	10
As-EXTR (FM)	43	175	244	20	16
As-EXTR (NM)	43	171	238	21	17
As-Grain Coarsened (NM)	33	137	188	14	7

(a)

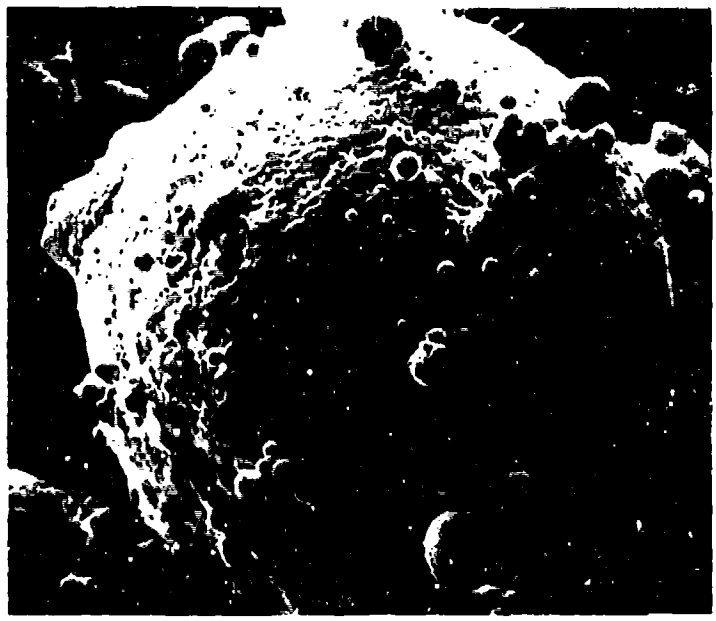

(b)

Figure 1 - As-received FM powders as viewed in SEM: (a) 138X, (b) 680X.

(a)

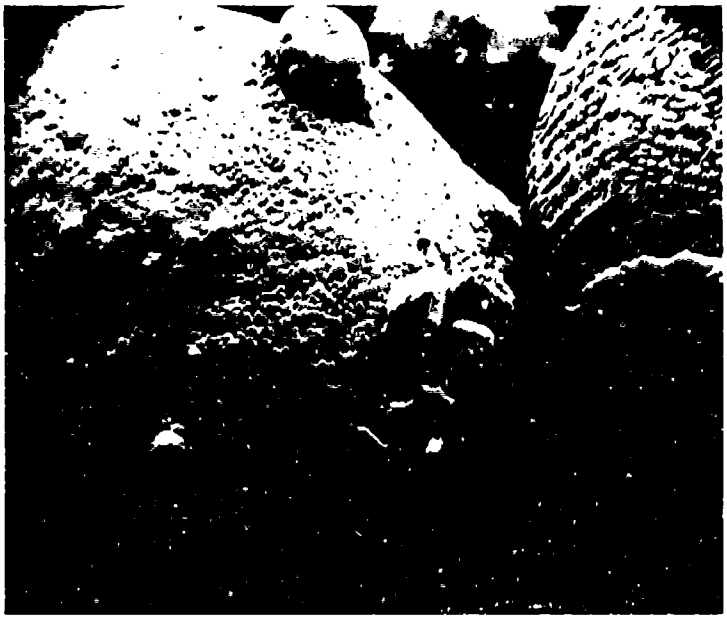

(b)

Figure 2 - As-received HM powders as viewed in SEM: (a) 24X, (b) 245X.

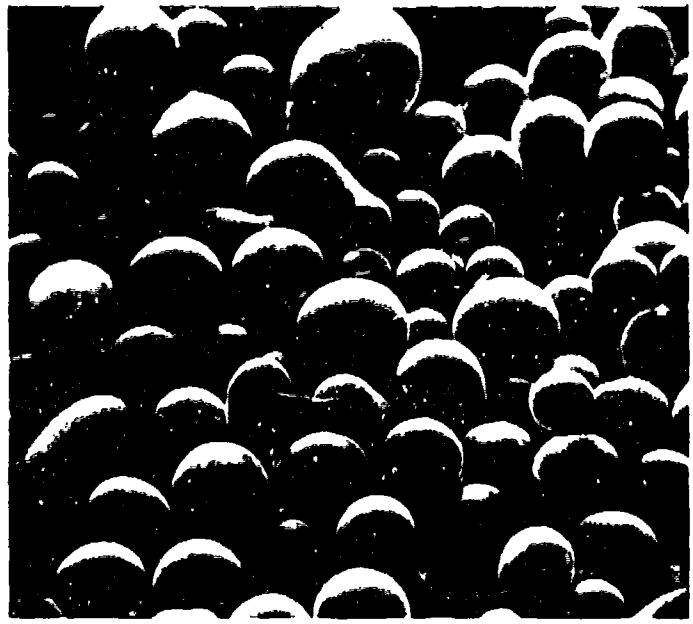

(a)

(b)

Figure 3 - As-received NM powders as viewed in SEM: (a) 63X, (b) 253X.

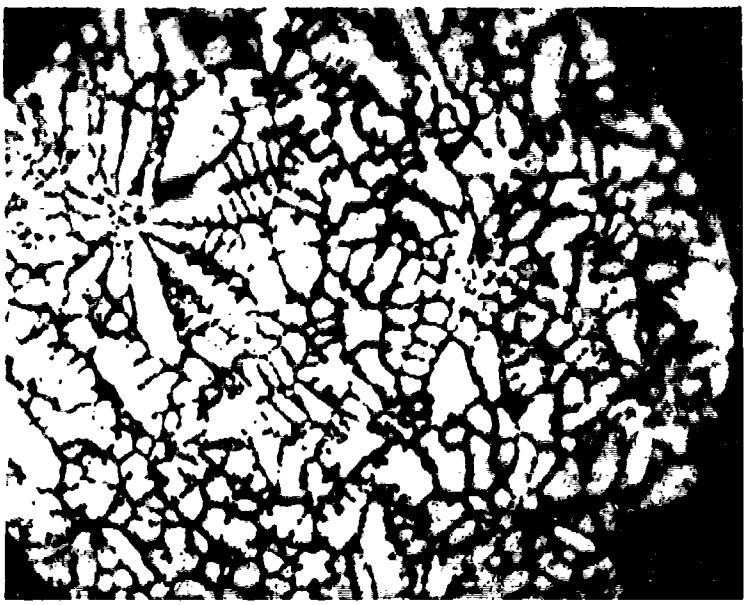

Figure 4 - Polished and etched section of as-received FM powders showing dendritic structure. 500X.

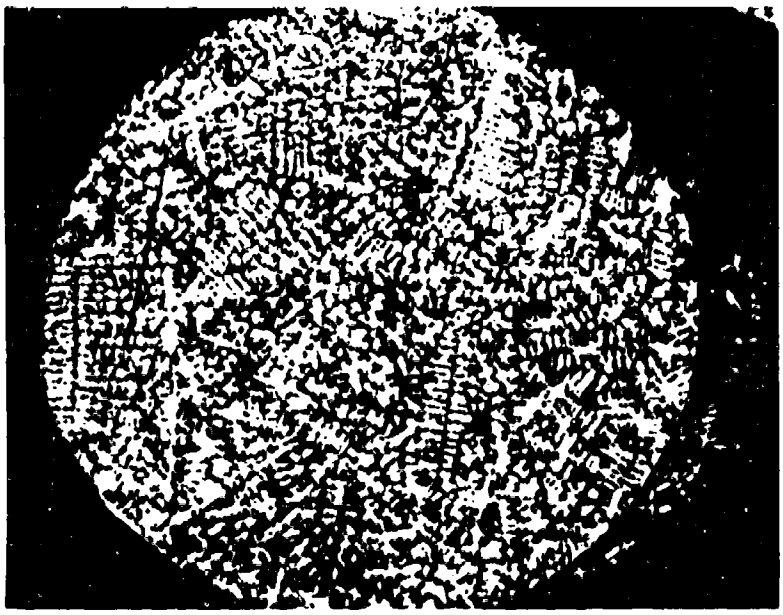

Figure 5 - Polished and etched section of as-received HM powders showing dendritic structure. 50X.

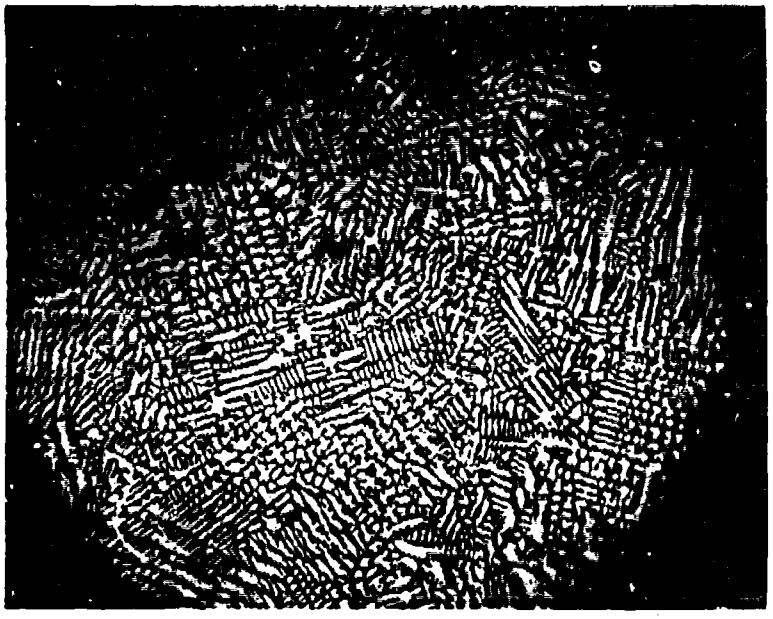

Figure 6 - Polished and etched section of as-received NM powders showing dendritic structure. 200X.

Figure 7 - Polished and etched cross-section of as-cast tensile bar showing dendritic structure. 100X.

Figure 8 - As-cast IN-100 microstructure. 1000X.

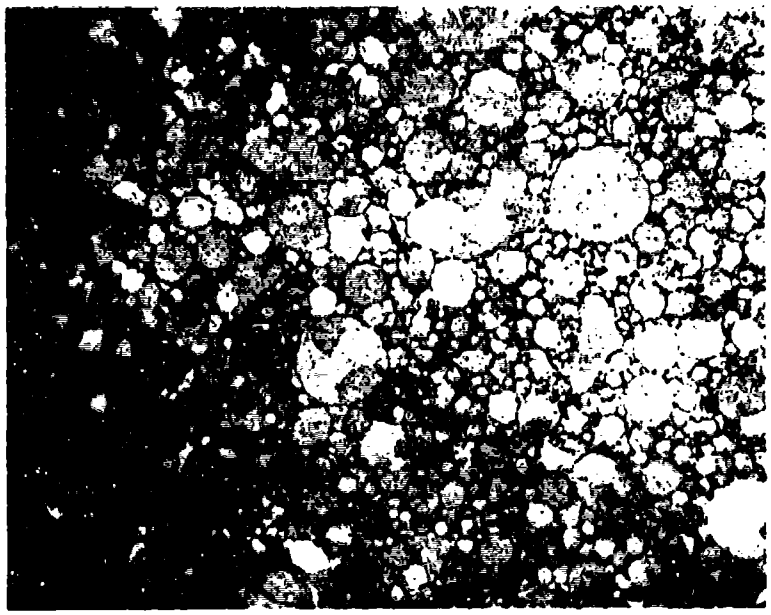

Figure 9 - As-HIP FM powder. 100X.

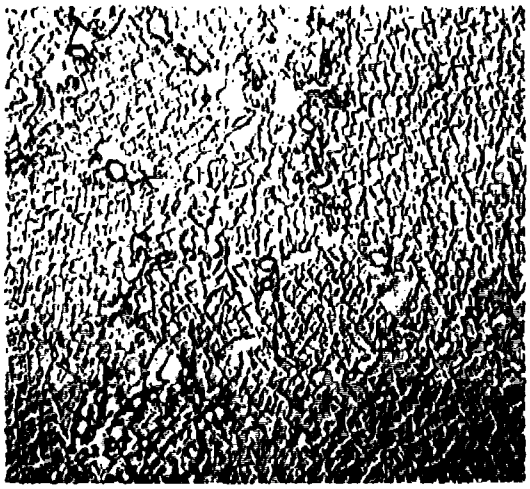

(a)

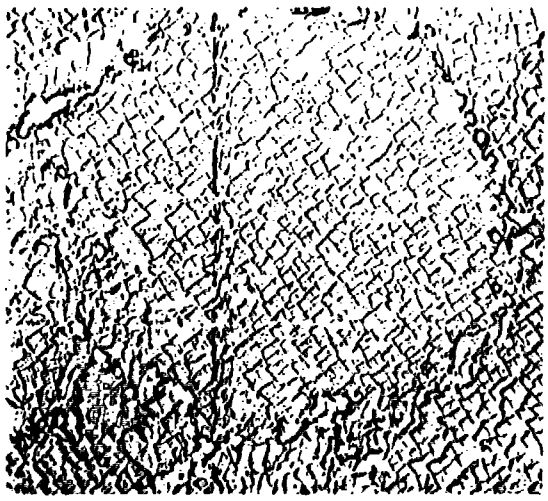

(b)

Figure 10 - Replica electron micrographs of as-HIP FM powder showing extensive carbide phase surrounding prior particle boundaries. (a) 4000X, (b) 5000X.

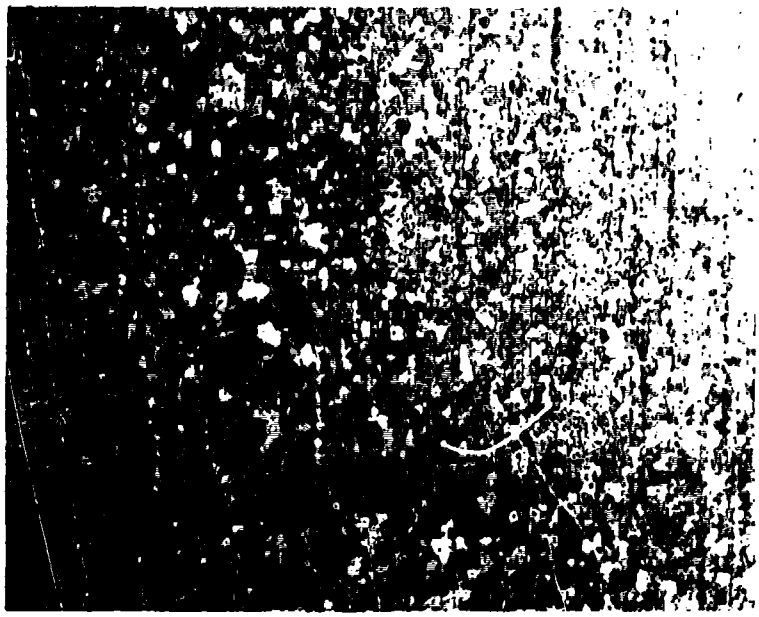

Figure 11 - Longitudinal section of as-extruded FM powder. 200X.

Figure 12 - Longitudinal section of as-extruded NM powder. 200X.

Figure 13 - Grain-coarsened NM powder extrusion. 24 hours at 2270°F. 500X.

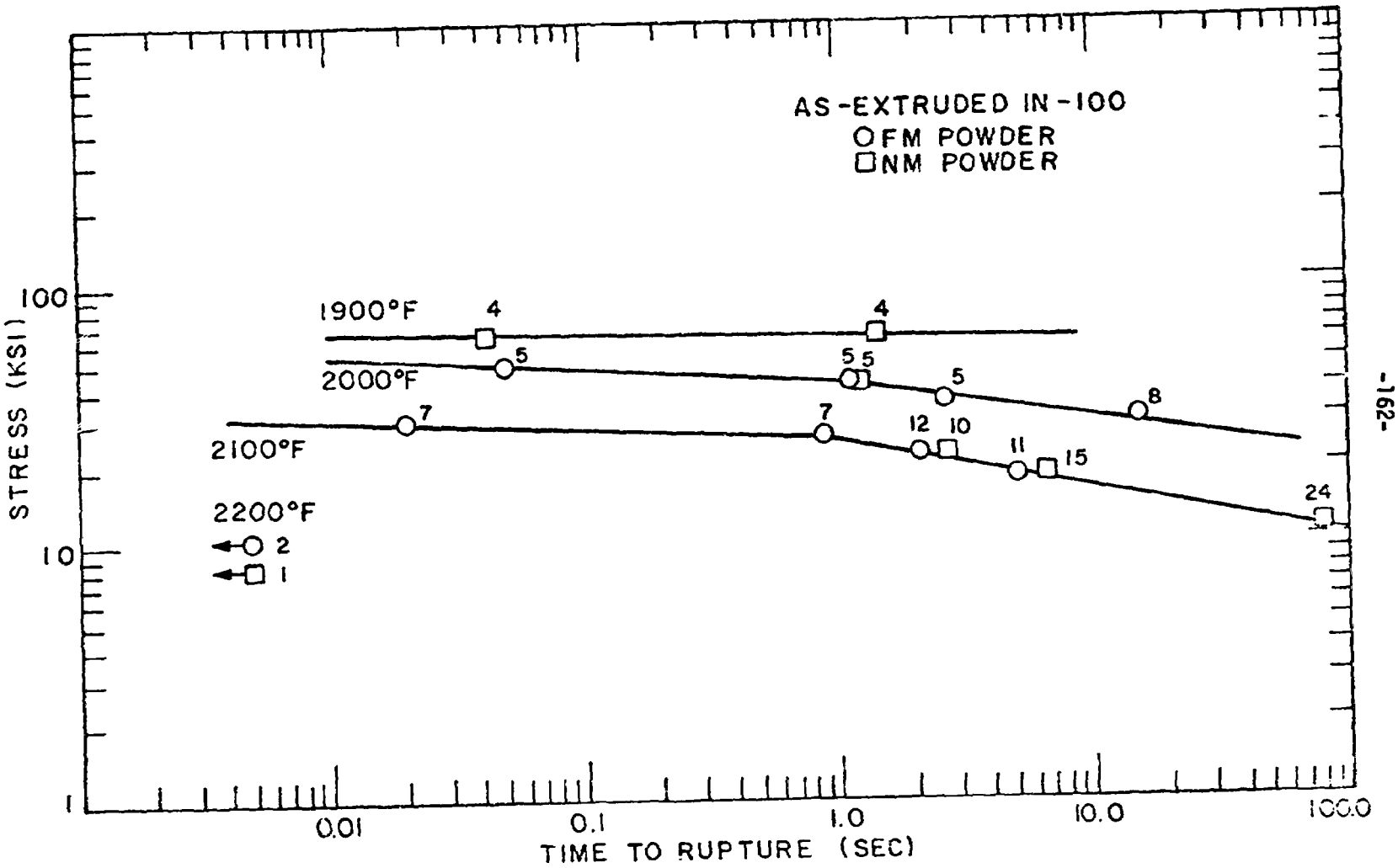

Figure 14 - High strain rate log stress vs. log rupture time at various temperatures for as-extruded IN-100.

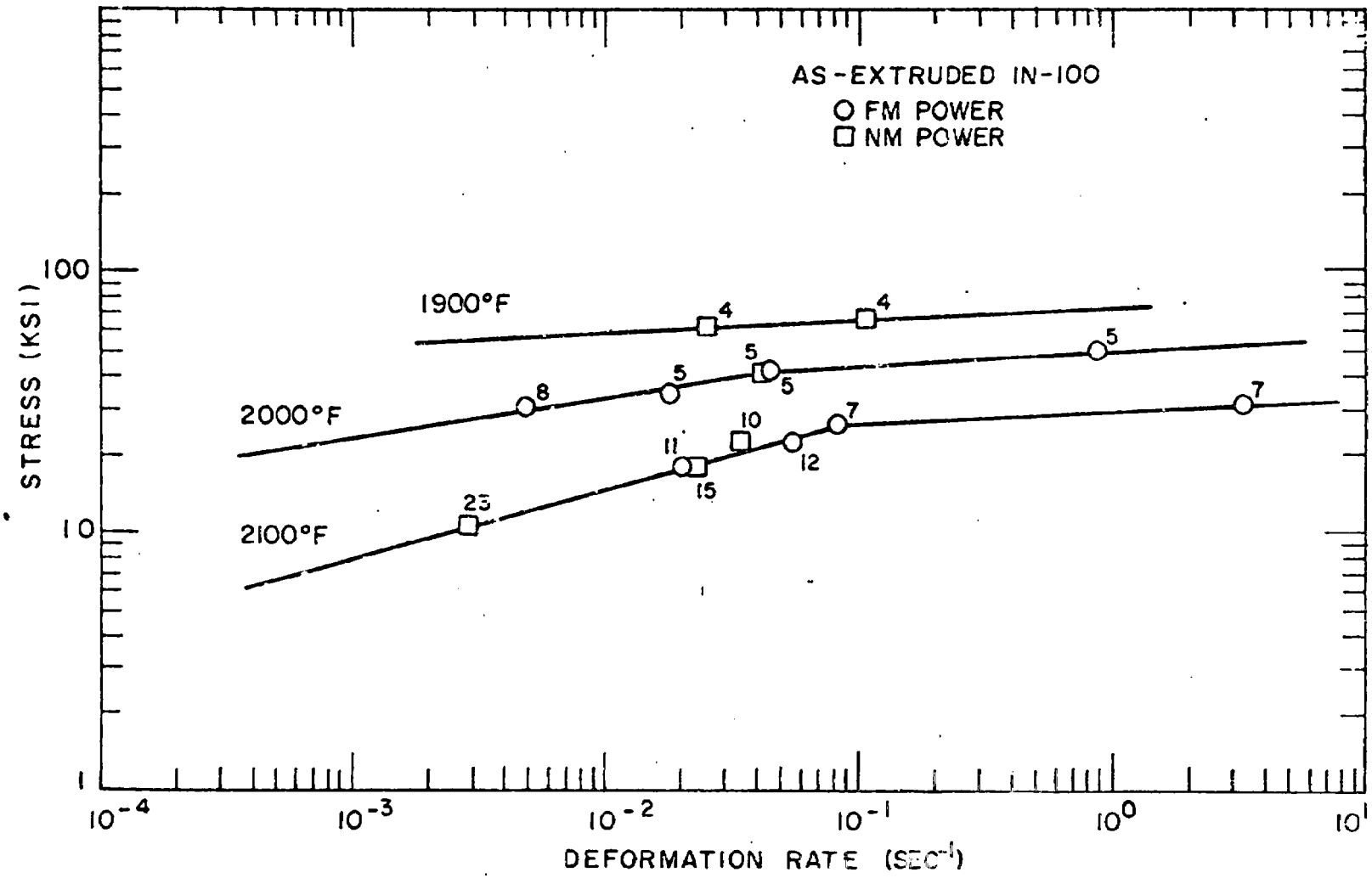

Figure 15 - High strain rate log stress vs. log deformation rate at various temperatures for as-extruded IN-100.

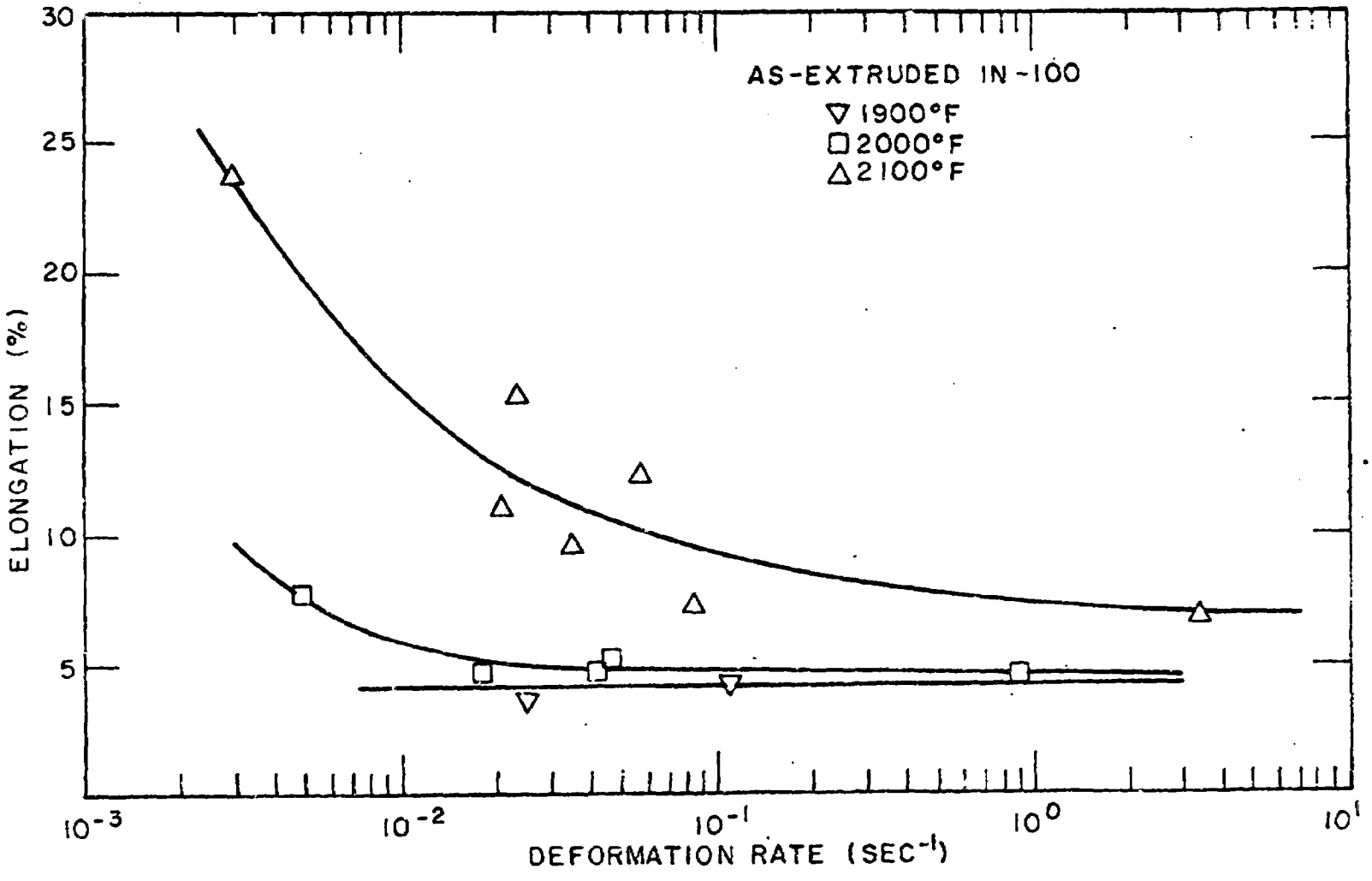

Figure 16 - High strain rate effect of deformation rate on elongation at various temperatures for as-extruded IN-100.

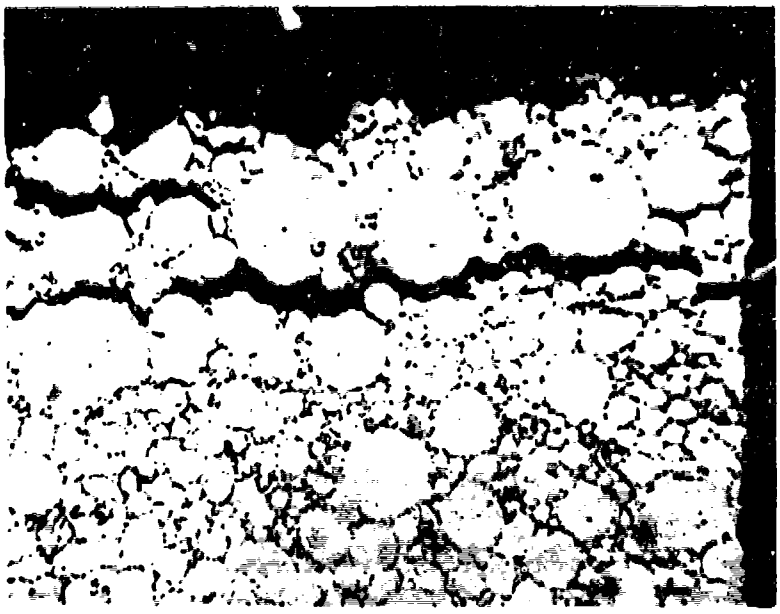

Figure 17 - High strain rate fracture cross-section of HIP FM powder test bar at 2100°F. Polished. 200X.

Figure 18 - High strain rate fracture cross-section of extruded NM powder test bar pulled at 2100°F. Polished and etched. 200X.

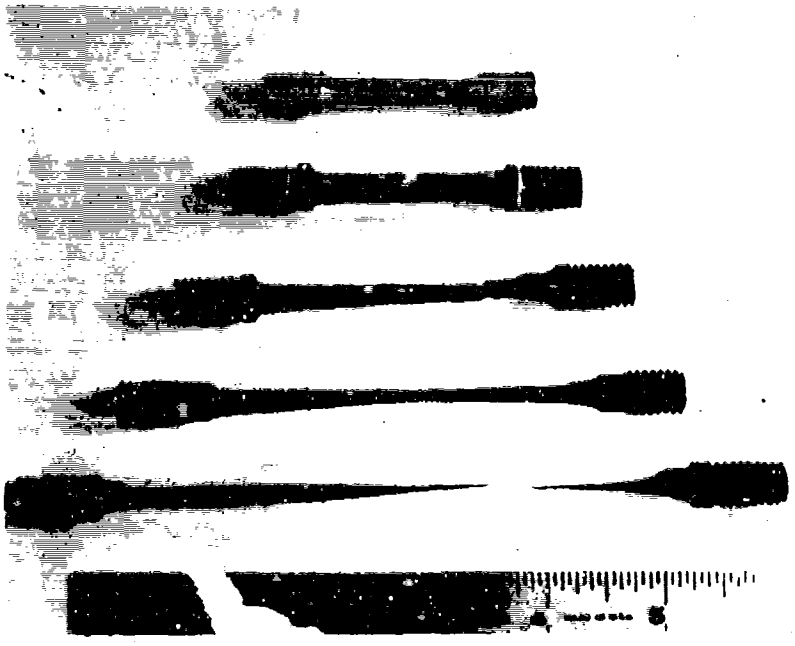

Figure 19 - As-extruded test bars superplastically deformed at 1900°F at strain rates from 0.5 min^{-1} to 0.01 min^{-1}. Bar at top is size of undeformed tensile specimen.

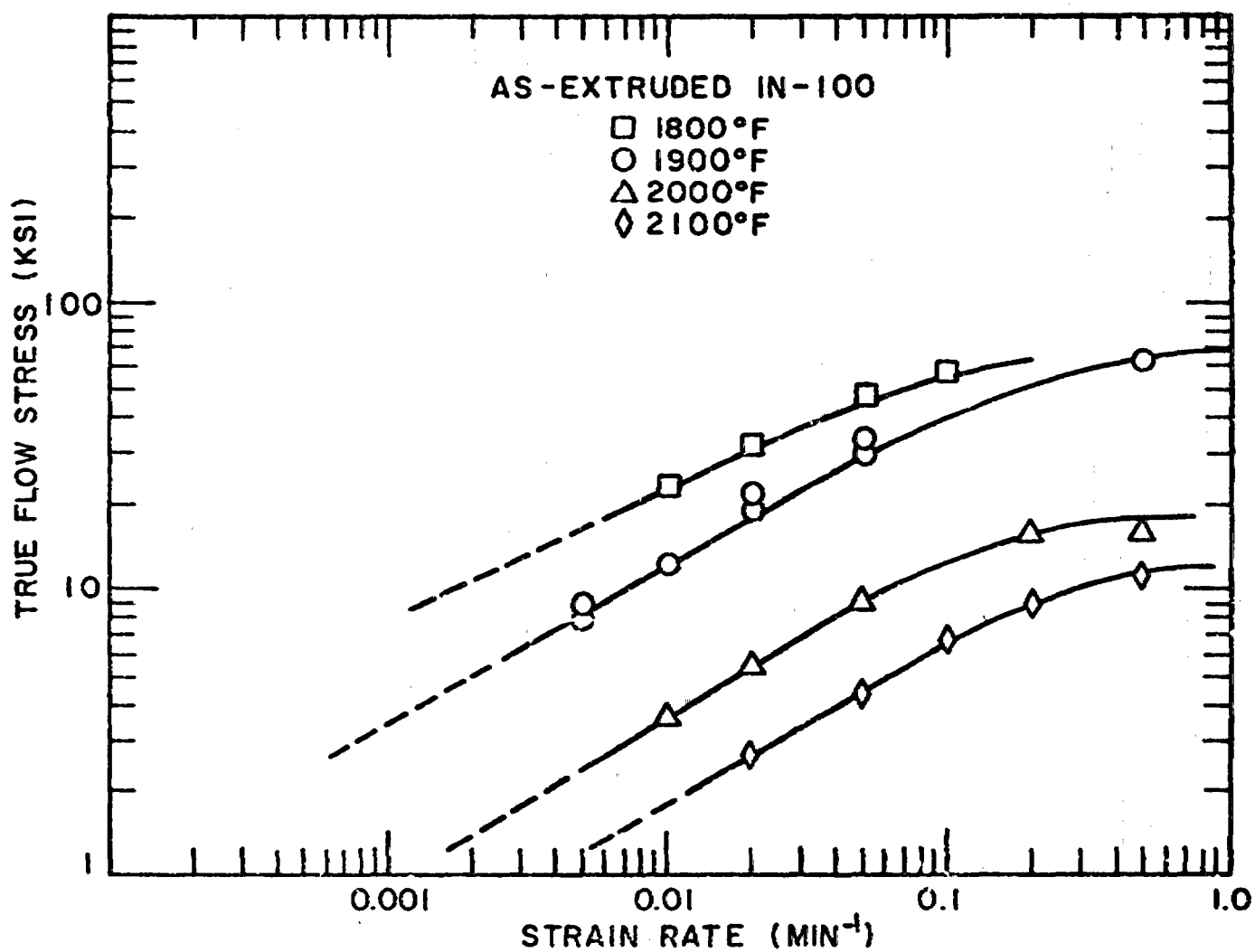

Figure 20 - Superplastic deformation of as-extruded IN-100 at various temperatures plotted as log tr flow stress vs. log strain rate.

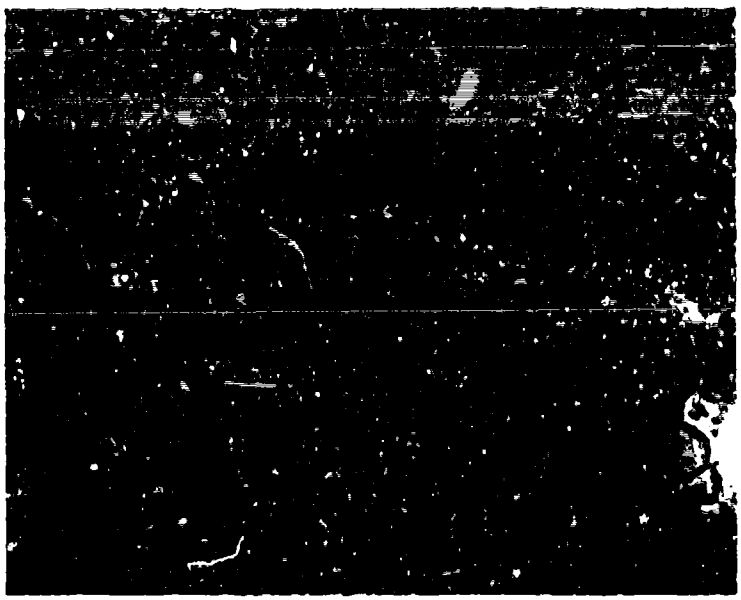

Figure 21 - Microstructure of superplastically deformed as-extruded material pulled at 1900°F. 1000X.

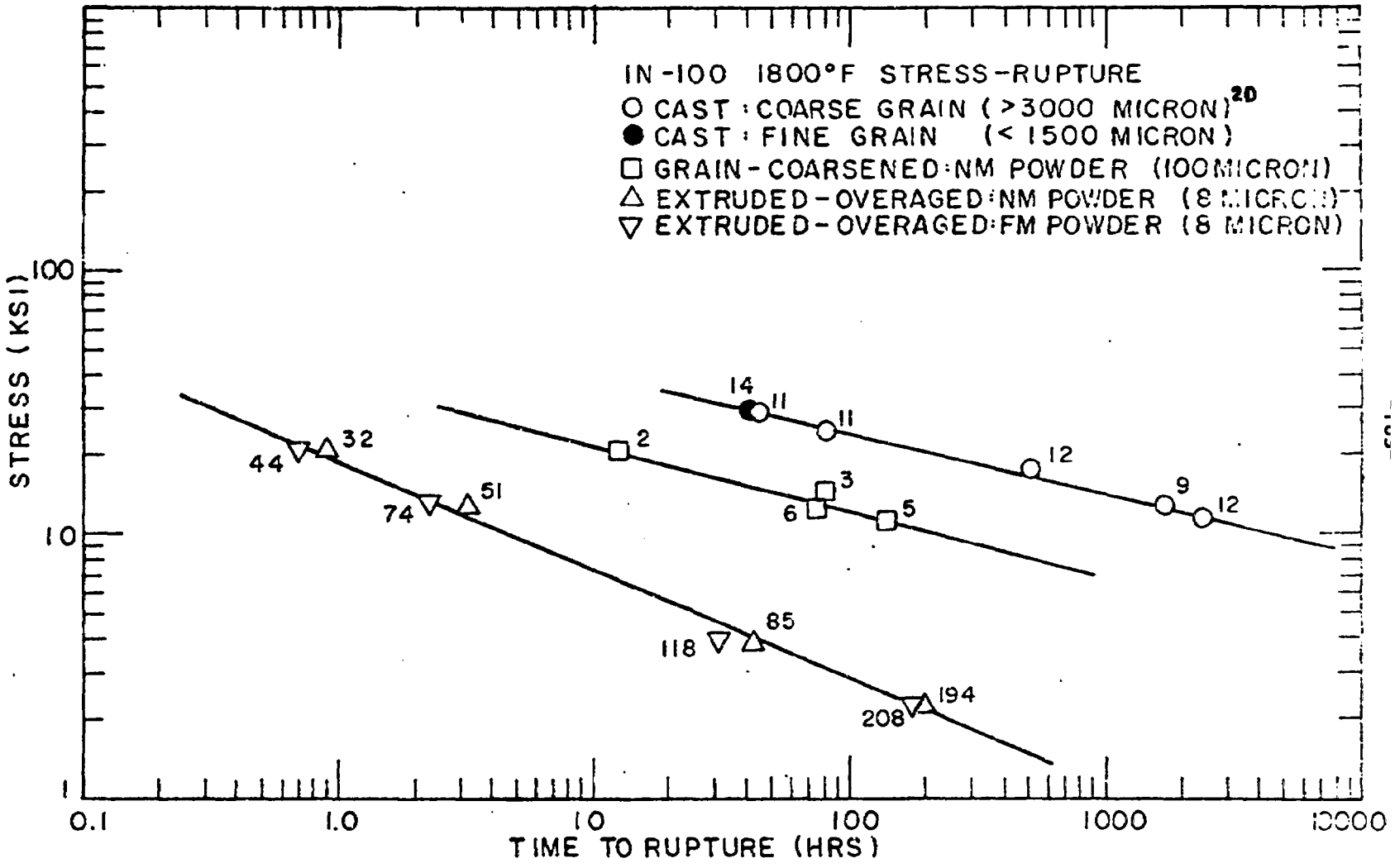

Figure 22 - 1800°F stress-rupture properties for various grain sizes of cast IN-100 and extruded IN-100 powders.

PROPERTIES OF MARAGING STEEL 300 PRODUCED BY POWDER METALLURGY

by

L.F. Van Swam, R.M. Pelloux and N.J. Grant

ABSTRACT

Powders of 300 grade maraging steel were produced by two different atomizing processes and consolidated either by hot isostatic pressing, extrusion and hot rolling or by a combination of these methods. The tensile properties of the PM alloys were equivalent or superior to the properties of the conventionally cast and forged alloys, while there was no improvement in the fatigue and fracture toughness properties. Fine grain size materials (1-5 microns) were obtained by hot rolling conventionally processed and PM bars of maraging steel 300 at 760, 820 and 870°C and cooling in air. In all cases, the tensile properties and the fracture toughness were improved by the grain size refinement.

I. INTRODUCTION

Maraging steels are a class of high strength, high alloy steels with a carbon content below 0.03%. The 200, 250 and 300 grade maraging steels contain 18% nickel plus different amounts of cobalt, molybdenum and titanium[1]. The different grade numbers refer to the tensile strength level in ksi, which can be achieved by the precipitation of a fine dispersion of Ni_3Mo phase during aging. Cobalt lowers the solubility of molybdenum in the iron-nickel matrix and thereby increases the amount of Ni_3Mo precipitated[2,3]. Titanium is both a hardening and refining addition which ties up the residual carbon and nitrogen[1]. Very small amounts of boron and zirconium are also added to prevent carbide precipitation at grain boundaries and to react with residual oxygen.

Segregation of alloying elements during solidification of the ingot is a recurring problem in these highly alloyed steels because this segregation persists throughout reduction to the final mill form, although it can be decreased but not entirely eliminated by working and homogenization at 1250°C[4]. The segregation shows up as a banded structure in the etched microstructure of the alloys[4].

Banding has been shown to cause a wide scatter in the tensile strength and fracture toughness properties of these steels[4]. Concurrently, the development of higher strength steels of this type with higher alloy content is limited by the increased segregation problems.

These problems due to macro- and microsegregation can be eliminated by processing the alloys from rapidly quenched powders which have typical secondary dendrite arm spacings of the order of 4 to 10 microns[5]. The

powder metallurgy route also offers the possibility of producing semi finished parts with great savings in forging and machining operations.

In this study, we report on the mechanical properties (tensile strength, fracture toughness and fatigue strength) of very fine grain size maraging steels and of maraging 300 grade steels produced by powder metallurgy. Three different atomization processes were used to produce rapidly quenched powders. The powders were consolidated either by hot isostatic pressing, extrusion, hot rolling or a combination of these methods. The influence of different microstructures on the mechanical properties was evaluated; the properties were compared to those of the conventionally cast and forged alloys.

II. MATERIALS

Consumable vacuum arc melted 300 grade maraging steel was received in the annealed condition (one hour at 820°C, followed by cooling in still air) from Vasco in the form of 100 mm wide X 32 mm thick (4 X 1-1/4 in) bars. The composition of this material is given in Table I. The mechanical properties were measured in the as-received annealed condition and after aging 3 hours at 480°C, followed by cooling in still air. These properties serve as a basis of comparison for the properties of the alloys produced by powder metallurgy, and for the fine grain size steels.

Powders were produced by steam atomization and by the rotating electrode process (REP). Steam atomized powders (SA), produced by Industrial Materials Technology, Inc., were obtained by disintegrating a 9 mm diameter stream of molten metal with low pressure steam. The metal droplets are collected in a water-filled tank placed under the nozzle. The process is capable of producing large diameter (5 mm (4 mesh) to .4 mm (35 mesh))

spherical particles[5].

The steam atomized powders were covered with an oxide skin which was removed by chemical cleaning with acid followed by hydrogen reduction. This process is attractive because of its high production rate, low cost, and the high cooling rates obtained. The cooling rates of 100°C/sec for medium sized particles and of 1000°C/sec for small (<1 mm) particles, result in secondary dendrite arm spacings of about 12 and 4 microns, respectively[5].

The rotating electrode process (REP) used by Nuclear Metals, Inc. produces essentially uncontaminated spherical powders of 0.4 mm (35 mesh) to 0.8 mm (20 mesh) with a secondary dendrite arm spacing of approximately 6 microns[5]. REP powders are expensive due to low production rates and the cost of preparing the bars for atomization.

The powders were consolidated by hot isostatic pressing (HIP), extrusion, hot rolling or a combination of these methods. In each case, the powders were handpacked in steel cans which were sealed by welding. The cans were degassed at 400°C, evacuated to a pressure of 10^{-3} torr, and purged with argon three times before final closure under vacuum.

Hot isostatic pressings for 1 to 3 hours were carried out between 1100 and 1250°C and at 100-200 N/mm^2 (14,500-28,000 psi). The different HIP variables for the various runs are given in Table II.

A number of rectangular HIP pressed cans were hot rolled between 1100 and 1000°C in 10% reduction passes. The resulting flat stock was used primarily for fracture toughness testing. Table II gives the detailed parameters of extrusions of HIP compacts and direct powder extrusions.

Chemical analyses of the maraging steels used to produce steam atomized

and rotating electrode powders are listed in Table I. By comparing these analyses to the analysis of an extrusion of steam atomized powder, it can be seen that the extruded steel contains large volume fractions of metallic oxides, and a lower content of titanium and aluminum alloying elements. Thus, a few mechanical tests were sufficient to confirm the limited mechanical properties of this alloy. On the other hand, the oxygen level of the alloy processed from REP powder is only slightly higher than for the commercial grade level (Table I). Compacts made from REP powder have undergone extensive mechanical testing.

In a further attempt to improve the tensile and fracture toughness properties of 300 grade maraging steel, fine grain size Vascomax 300 was produced by hot rolling in 10% reduction passes at 760, 820 and 870°C. This rolling procedure produced steels with grain sizes from 1 to 5 microns compared to the 25 to 50 micron grain size of the commercially available steel.

III. EXPERIMENTAL PROCEDURES AND RESULTS

The tensile bars had a 25.4 mm (1 inch) gauge length and a 4.06 mm (0.160 inch) gauge diameter. Reduction in area, U.T.S. and 0.2% offset yield values are reported for annealed and aged material (3 hours at 480°C followed by cooling in still air), and are summarized in Table III.

The fracture toughness of aged maraging steel was measured by following the ASTM method E 399 70T. Compact tensile specimens were fatigue precracked at a frequency of 20 Hz. The final 1.0 mm of the fatigue crack was always propagated at a load of less than half the final fracture load.

The fatigue precracked specimens were loaded at a constant strain rate

which was kept well within the recommended limits. Load and crack opening displacement were recorded on an X-Y recorder. All the alloys tested showed a distinct "pop-in" at the onset of fracture. The fracture toughness indices were measured in planes parallel and perpendicular to the rolling direction.

The test results are given in Table IVa and IVb. The load, K_f, and the number of cycles, N, to give the final 1.0 mm of fatigue crack, crack length measurements, a, and the fracture load, P, are also reported.

Fatigue tests of smooth bars in tension-compression with a zero mean load were performed on a Baldwin SF-1 machine under constant load amplitude. The cylindrical specimens with a 3.8 mm (0.15 inch) diameter and 7.6 mm (0.3 inch) long gauge section, were aged for 3 hours at 480°C and polished with 600 grit carbide paper and 1 micron diamond paste. Any polishing scratches were at 45° angles to the tensile axis. The results of 14 tests of commercial material in the aged condition and of 16 tests of extruded rotating electrode powder material tested in air, together with 13 tests of commercial steel tested in dry argon (dewpoint -50°C) are given in Table V and are plotted on a S-N curve in Figure 4.

IV. DISCUSSION

A. Tensile Properties

The low tensile strength and the limited reduction of area of the alloys produced from the steam atomized powders in both the annealed and aged condition is attributed to the high oxide content of this alloy. Large metal oxide inclusions of complex chemistry were observed by metallography. The presence of oxide inclusions on the fracture surfaces of

tensile bars was confirmed by scanning electron microscopy. Fracture in these alloys was always initiated at the oxide-inclusions.

PM alloys made from high purity rotating electrode powders were free of large (1 micron or more) oxide inclusions, although Ti(C,N) and Ti_2S inclusions are normally found in maraging steels[6]. The size (up to 10 microns) and distribution of Ti(C,N) inclusions in the PM Alloys were equivalent to those found in commercial steel. In general, the PM alloys had notably fewer Ti_2S inclusions than the commercial alloy.

In the following comparison of the tensile properties of commercially available Vascomax 300 with rotating electrode PM alloys, only the properties of the aged alloys will be discussed since they are the most interesting alloys in practice.

Hot isostatic pressing of REP powder at 1200°C and 100 N/mm^2 for 1 hour produced a fully dense alloy. The tensile reduction of area of annealed RH specimens was however only 22% and aged RH specimens broke before any large scale yielding took place. Fracture in this alloy was by separation along prior powder particle boundaries. The low interparticle bond strength is thought to be due to thin adherent oxide films which are not broken down during hot isostatic pressing

The powder particle oxide films can be broken down by extruding either a lightly compacted powder or a HIP powder billet at a sufficiently high extrusion ratio. Alloys RE and REH which were extruded with a ratio of 11.5. had slightly higher (about 5%) yield and ultimate tensile strengths than the commercial alloy. A significant difference in tensile reduction of area was found between alloy RE and REH. Alloy REH had a tensile

reduction of area of 62% compared to 48% RA for alloy RE and 49% RA for Vascomax 300. The powder particles in these two PM alloys were completely bonded together and no delamination was observed on the fracture surfaces of the tensile bars.

Five cm thick rectangular HIP powder billets were hot rolled at 1000°C to produce alloys with tensile properties which depended on the amount of reduction of area received during the hot rolling operation. The yield strength, U.T.S. and reduction of area of alloy HR69 are lower than those of Vascomax 300. The lower tensile properties of alloy HR69 were attributed to particle oxide-films which remained unbroken after the limited reduction of area given during hot rolling this alloy. Higher reductions of area during rolling (alloys HR83 and HR91) increased the yield strength, U.T.S., and reduction of area to values slightly higher than those of Vascomax 300.

In summary we can state that high strength maraging steel alloys with superior tensile properties can be made by powder metallurgy by either extrusion or hot rolling of high purity powders. The extrusion ratio or the hot rolling reduction must be high enough to insure the complete breakdown of the oxide film and the bonding of powder particles.

Maraging steels are conventionally hot rolled at 1000°C and the grain size in the final mill product range from 25 to 50 microns. Hot rolling of Vascomax 300 and of extruded REP powder bars at 760, 820 and 870°C produced steels with a grain size from 1 to 5 microns. The fine grain size Vascomax 300 and PM alloys were tested in the air cooled hot rolled condition and after an aging treatment of 3 hours at 480°C. The U.T.S. and the 0.2% offset yield strengths of the aged VM and ER alloys were 5 to 10%

higher than for the commercial Vascomax 300. Reductions of area of the fine grain alloys were equal to or better than the RA of commercial stock, but no systematic improvements in ductility were observed.

Fine grain size Vascomax 300 was furthermore given an intermediate 1 hour anneal at 820°C after the hot rolling operation to duplicate the typical commercial process. The intermediate anneal improved the tensile reduction of area from 49% to an average of 63%; the U.T.S. and yield strength of this alloy were approximately 5% higher than those of commercial Vascomax 300.

8. Fracture Toughness Properties

If we were to evaluate only the results of the tensile tests, we could conclude that the PM alloys are better than the conventional alloys. However, the fracture toughness tests showed a marked difference between the two types of alloys. The HIP plus hot rolled PM bars have a fracture toughness index K_{IC} which is 20-30% lower than the K_{IC} value of the commercial alloy. The fracture surfaces of the PM alloy specimens show extensive longitudinal delamination along powder particle boundaries. The delamination planes are parallel to the rolling plane. Delamination is due to a low interface bond strength between powder particles resulting from thin powder particle oxide films which are not broken down during hot rolling. Interparticle delamination is enhanced in plane strain fracture toughness testing due to the high transverse stress in the area immediately ahead of the advancing crack front. The fracture surfaces of Vascomax 300, HR69, HR83 and HR91 fracture toughness specimens are shown in Figures 1 through 3. These figures clearly show that the amount of delamination decreases

with increasing reductions of area during rolling. The high degree of delamination in alloy HR69 was expected from the limited tensile reduction of area of this alloy which was attributed to the presence of continuous oxide films. It was surprising to find that failure by delamination was still observed after 83% reduction of area by hot rolling but it was apparently eliminated after 91% reduction. The lower fracture toughness of all the PM alloys as compared to the commercial alloy is attributed to the presence of interstitial elements. As would be expected the fracture toughness value increased with increasing amounts of delamination.

It is interesting to note that the failure by delamination was not always observed on the fracture surfaces of tensile bars. Thus the plane strain fracture toughness test is a critical test which demonstrates clearly the quality of the interparticle bond strength.

The plane strain fracture toughness of maraging steel 300 was improved by hot rolling the commercial alloy at 760, 820 or 870°C. Alloys hot rolled at these temperatures and given an intermediate anneal showed a substantial increase in their K_{IC} values. The best combination of tensile strength and fracture toughness was obtained by hot rolling at 870°C.

The PM alloy bars made by extrusion and hot rolling at 760, 820 and 870°C were unfortunately not thick enough to permit a valid determination of their K_{IC} values.

C. Fatigue Properties

The S-N curves of Vascomax 300 tested in air and in argon (dewpoint -50°C) and of hot isostatically pressed and extruded rotating electrode powder are given in Figure 4. It is observed that specimens tested in dry

argon show a much higher fatigue limit and much less scatter in the data than similar specimens tested in air. The lower fatigue strength and the higher scatterband obtained by testing in air are due to the corrosive effect of water vapor in the air. The fatigue strength of commercial Vascomax 300 and the PM alloy are about the same. Thus the presence of banding and of structural inhomogeneities in the commercial alloys cannot alone account for the poor fatigue properties of maraging steels. The authors have shown in another paper[7] that the poor fatigue behavior of the maraging steels is related to the local cyclic softening of the alloy.

V. CONCLUSIONS

1. A high strength maraging 300, high alloy steel was produced by powder metallurgy with tensile properties equivalent or superior to the conventionally cast and forged alloys.

2. The fatigue and fracture toughness properties of maraging steel 300 are not improved by the powder metallurgy process.

3. A plane strain fracture toughness test is an ideal test to measure qualitatively the interparticle bond strength of a PM alloy because of the high triaxial state of stress present at the tip of the crack.

4. The tensile and fracture toughness properties of 300 grade maraging steel were improved by hot rolling the alloy at 760, 820 and 870°C.

ACKNOWLEDGEMENTS

The authors gratefully acknowledge the support of ARPA grant DAHC15-70-C-0283 during the course of this investigation. We would also like to thank Dr. E.P. Abrahamson, III (AMMRC, Watertown, Massachusetts) for providing some of the materials.

REFERENCES

1. S. Floreen, "The Physical Metallurgy of Maraging Steel", Met. Rev., Review 126, 115 (1968).

2. G.P. Miller and W.I. Mitchell, "Structure of Nickel-Cobalt-Molybdenum Maraging Steels in the Air-Cooled Condition", J. Iron and Steel Inst., 203, 895 (1965).

3. S. Floreen and G.R. Speich, "Some Observations on the Strength and Toughness of Maraging Steels", Trans. ASM, 57, 714 (1964).

4. A.M. Hull and C.J. Slunder, "The Metallurgy, Behavior and Application of the 18 Percent Nickel Maraging Steels", NASA SP 5051 (1968).

5. "Structure and Property Control Through Rapid Quenching of Liquid Metals", ARPA Contract DACH15-70-C-0283, Semi-Annual Technical Report #2, July, 1971.

6. T. Boniszewski and E. Boniszewski, "Inclusions in 18 Ni-Co-Mo Maraging Steel", J. Iron and Steel Institute, 204, 360 (1966).

7. L. Van Swam, R.M. Pelloux and N.J. Grant, "Fatigue Behavior of Maraging Steel 300", in preparation.

TABLE I

Chemical Composition of the Maraging Steels 300 Used in This Work

	Vascomax 300 (100 X 32 mm bar)	Steam Atomized Powder		Rotating Electrode Powder	
		Before Atomization	After Extrusion	Before Atomization	After Rolling
C	.014	.020	.012	.009	
Al	.09	.11	.02	.11	
Ti	.66	.66	.06	.64	
Ni	18.26	18.50		18.33	
Co	8.82	9.07		9.04	
Mo	4.81	4.98		4.88	
Si	.02	.04		.01	
Mn	.05	.05		.02	
S	.004	.005		.006	
P	.005	.009		.004	
O	<20 ppm	<20 ppm	1400	<20 ppm	43 ppm

TABLE II

Processing Variables of the Materials

Material Designation	Processing Designation
Vascomax 300	Commercially available 300 grade maraging steel.
SAE	Steam atomized powder, extruded 1120°C: extrusion ratio 10.5.
RH	Rotating electrode powder, HIP 1200°C, 100 N/mm² (14,500 psi) 1 hour.
RE	Rotating electrode powder extruded at 1100°C: extrusion ratio 11.5.
REH	Rotating electrode powder, HIP 1200°C, 100 N/mm² (14,500 psi) 1 hour, afterwards extruded at 1100°C: extrusion ratio 11.5.
HR69 HR83 HR91	Rotating electrode powder, HIP 1200°C, 200 N/mm² (28,000 psi), 1 hour and hot rolled in 10% reduction passes at 1000°C to total reduction of 69, 83 and 91% respectively.
VM76 VM82 VM87	Vascomax 300, hot rolled at 760, 820 and 870°C, respectively, to obtain fine grain size, and tested in as-received and aged conditions.
VM76A VM82A VM87A	Same as above, but with an intermediate 1 hour 820°C anneal. Materials were tested in the as annealed and in the annealed plus aged condition.
ER76 ER82 ER87	Rotating electrode powder, extruded at 1100°C: extrusion ratio 10, and hot rolled at 760, 820, and 870°C

TABLE III

Tensile Properties of 300 Grade Maraging Steels

	Annealed			Aged		
	U.T.S. N/mm²	.2% Yield N/mm²	R.A. %	U.T.S. N/mm²	.2% Yield N/mm²	R.A. %
Vascomax 300	1000	850	73	1905	1870	49
SAE	1125	690	46	1700	1620	12
RH	1015	850	22	specimen broke before yielding		
RE	1055	860	68	2000	1970	48
REH	1040	860	65	2010	1970	62
HR69	1020	770	62	1870	1815	39
HR83	1010	770	70	1980	1930	53
HR91	1010	790	74	1960	1910	55
VM76	1055	830	72	2100	2075	57
VM82	1070	830	64	2085	2050	49
VM87	980	780	65	1990	1960	53
VM76A	1020	800	74	1985	1940	65
VM82A	940	760	75	1970	1930	63
VM87A	970	760	72	1990	1960	61
ER76	1150	830	69	1920	1905	49
ER82	1105	840	67	2020	2000	31
ER87	1020	790	60	2015	2000	46

TABLE IV(a)

Fracture Toughness Measurements of
300 Grade Maraging Steels

Crack Parallel to the R.D.

	K_f N	N_c X100	a mm	P N	K_{IC} $MNm^{-3/2}$	Average K_{IC} $MNm^{-3/2}$
Vascomax 300	2800	60	13.05	6950	68.4	68.2
	2800	55	12.95	7120	69.0	
	3100	40	13.80	7040	67.2	
VM76	2200	180	13.28	6230	62.9	62.5
	2200	160	13.13	6230	61.9	
	2200	170	12.72	6630	62.6	
VM82	2200	170	12.85	7020	67.1	68.8
	2200	160	12.88	7120	68.5	
	2200	90	12.88	7400	70.9	
VM87	2200	150	12.50	8570	78.7	78.5
	2200	160	12.70	8280	77.9	
	2200	160	13.18	8240	81.8	
	2800	60	13.08	7790	76.5	
	2800	40	13.31	7900	79.8	
	2800	50	13.74	7120	76.3	
VM76A	2200	187	12.75	8350	79.0	79.0
VM82A	2200	143	12.83	8420	80.5	81.2
	2200	125	12.85	8550	81.9	
VM87A	2200	237	12.75	8820	83.4	83.0
	2200	147	12.77	8900	84.5	
	2200	175	12.77	8520	81.0	
HR69	7800	340	26.02	15600	53.7	55.7
(1/2"	6700	355	25.69	16900	57.2	
specimen)	6700	400	25.73	16500	56.0	
HR83	2800	240	13.39	5740	58.7	59.7
	2800	200	13.56	5600	58.5	
	2800	215	13.46	6010	62.0	
HR91	2200	90	13.69	4230	45.0	43.6
	1800	300	12.98	4450	43.3	
	2000	255	13.26	4230	42.6	

TABLE IV(b)

Fracture Toughness Measurements of
300 Grade Maraging Steels

Crack Perpendicular to R.D.

	K_f N	N_c X100	a mm	P N	K_{IC} $MNm^{-3/2}$	Average K_{IC} $MNm^{-3/2}$
Vascomax 300	8900	480	26.11	22200	77.4	77.4
HR69	6700	340	26.29	19350	67.9	68.5
	6700	405	25.80	21500	73.0	
	6700	385	25.65	19100	64.7	
HR83	2800	245	13.05	7010	69.2	71.2
	2800	195	12.15	8460	74.9	
	2800	215	13.36	6810	69.5	

TABLE V

Life (number of cycles to failure X1000) of Fatigue Specimens Tested In Tension-Compression at the Stress Amplitude Levels Indicated

Stress N/mm² (ksi)	1380 (200)	1030 (150)	900 (130)	830 (120)	760 (110)	690 (100)	620 (90)	550 (80)	480 (70)
Vascomax 300	1.5	20		41		80	72	116	1053
							218	423	5330*
							274	498	
							2273	937	
Rotating electrode powder extruded		8		21		89	87	98	267
						885	109	334	514
							343	416	662
							1907	5060*	5860*
Vascomax 300 tested in argon		50	64	255	623	4180			
			109	487	753	8269			
				529	997				
					1184				

* Specimen did not break

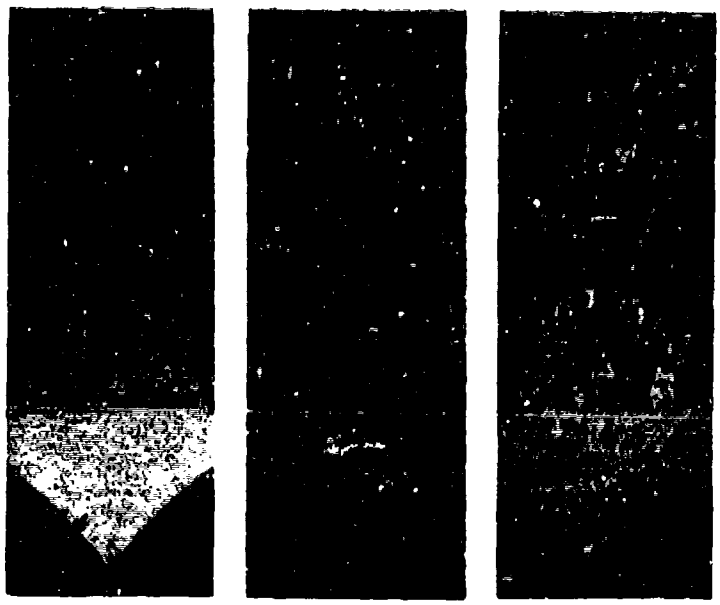

Figure 1. Fracture surface of fracture toughness specimens. From left to right: Vascomax 300, fracture plane parallel to the rolling direction, HR69 fracture plane parallel and perpendicular to the rolling direction, respectively. Specimen thickness 1.27 cm (0.5 inch).

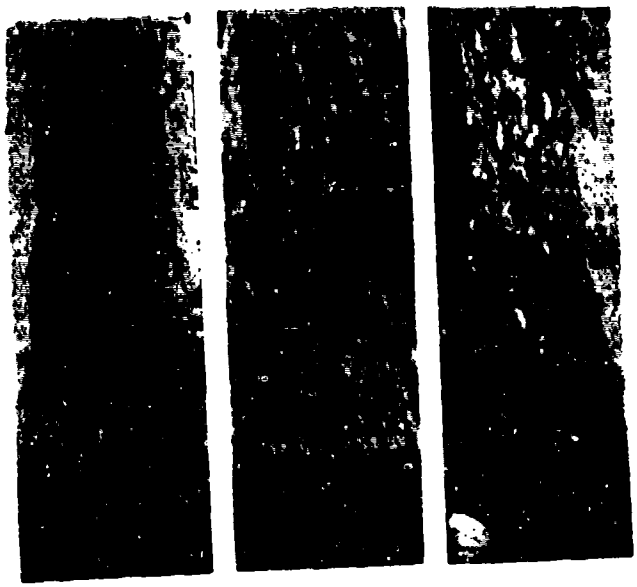

Figure 2. Fracture surface of fracture toughness specimens. From left to right: Vascomax 300 fracture plane perpendicular to the rolling direction HR83 fracture plane parallel and perpendicular to the rolling direction, respectively. Specimen thickness .625 cm (0.25 inch).

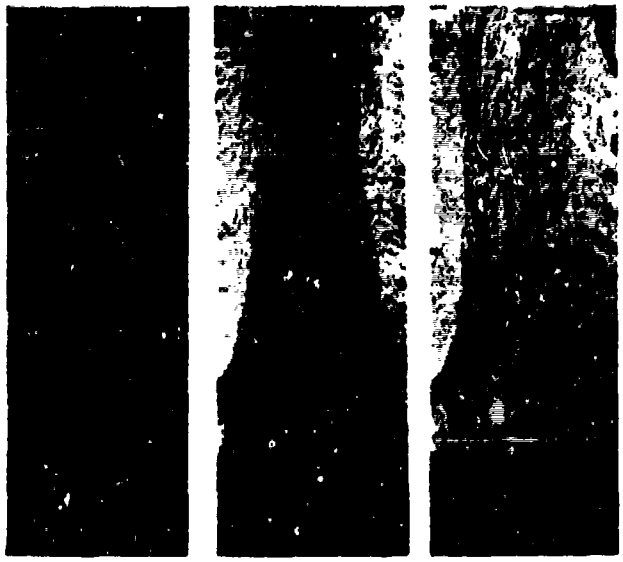

Figure 3. Fracture surface of fracture toughness specimens. From left to right: HR91, VM82 and VM82A, fracture plane parallel to the rolling direction in each specimen. Specimen thickness .635 cm (.25 inch).

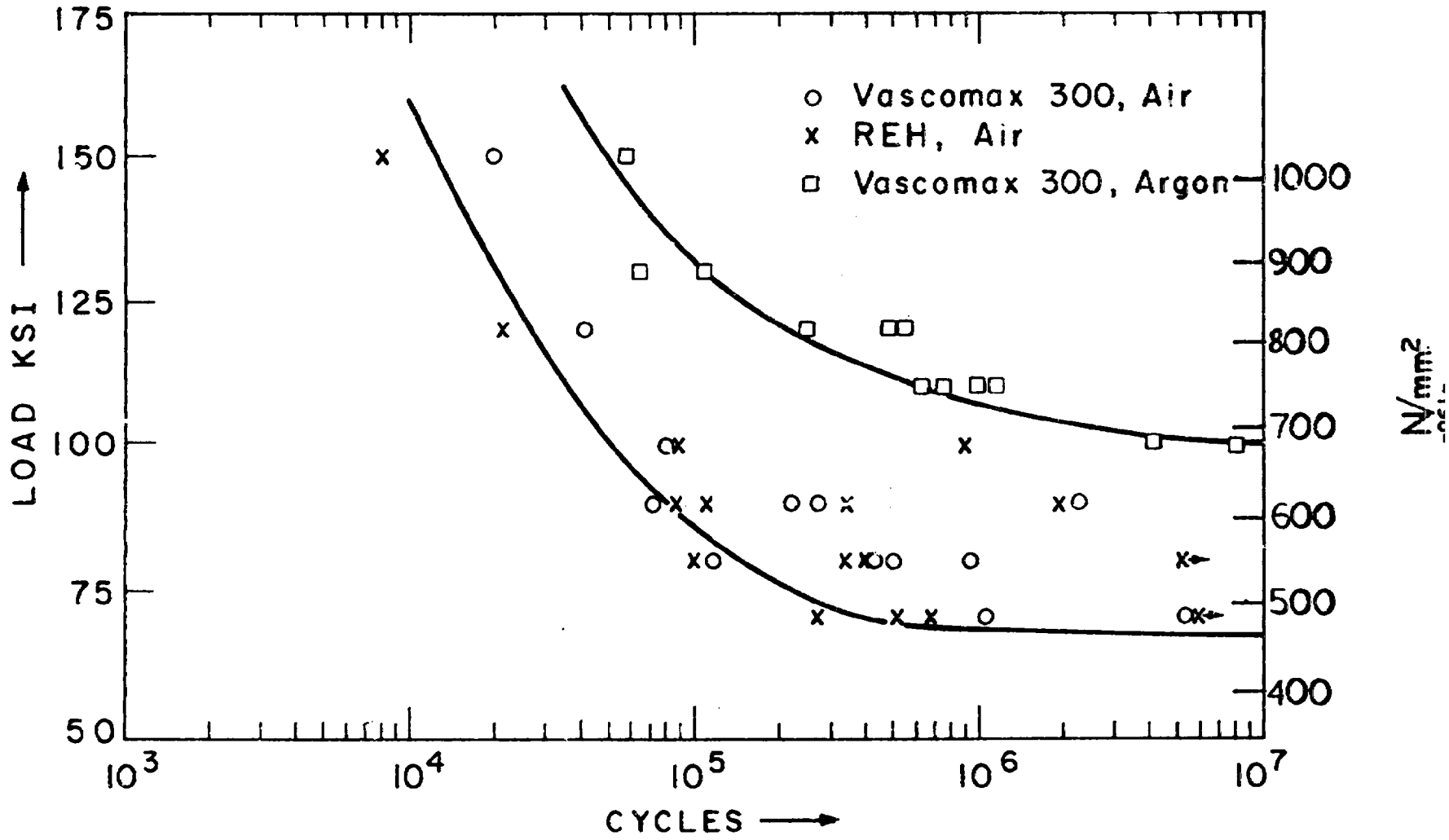

Figure 4. S-N curves of Vascomax 300 and of a powder metallurgy product produced by hot isostatic pressingand extrusion.

FRACTURE TOUGHNESS AND FATIGUE CRACK GROWTH RATES OF IN-100 PROCESSED BY POWDER METALLURGY

by S. Wästberg, R.M. Pelloux and N.J. Grant

I. INTRODUCTION

The main goal of this work was to investigate the fracture properties of a nickel base superalloy processed by powder metallurgy. This material will be referred to as a P/M alloy by opposition to a cast alloy.

The P/M alloy is made from pre-alloyed powder particles with very small dendrite arm spacings and low volume fraction of large second phase particles. Thus, we can expect a high degree of homogenization and an isotropic structure in the compacted ingots. These microstructure features should result in marked improvements in the fracture properties over the properties of the coarse grained cast alloys. The properties investigated were fracture toughness and fatigue crack growth rates at room temperature and at 1400°F.

II. MATERIALS AND TEST PROCEDURES

A. Materials

The chemical analyses of the cast IN-100 and the P/M IN-100 are given in Table I. The two chemical analyses are very close and, if anything, the impurity content of the P/M alloy is lower than the casting. Table II gives the detailed gas analysis of three different P/M ingots near the center and at the edges of the ingots.

B. Processing

IN-100 billets were processed by three different processing techniques which were:

a) as cast ingot (2 ingots 2.5 inches diameter X 2 inches long)

b) as cast ingot - hot isostatically pressed (HIP) for 5 hours at 2150°F (1195°C) under 15,000 psi of argon (three ingots 2.5 inches diameter X 2 inches long)

The average grain size of the cast alloy was about 2000 microns with a well defined dendritic structure. Figures 1 and 2 show, respectively, the microstructure of the as-cast alloy and the heat treated alloy. Figures 3 and 4 show the same for the cast and HIP alloy. The heat treatment cycle is given in Table IV. The HIP cycle was used to close any pore or interdendritic cavities which would affect the fracture properties of the cast alloy.

c) P/M forgings made from REP powder. The REP powder particle size was 35 mesh (<500 microns) with two or more grains per powder particle. Figures 5 and 6 show respectively, an overall view of a typical powder particle and the microstructure of the as-atomized powder. The powders were compacted in cans (8 inch diameter X 4 inches high) which shrank by 11% in the HIP cycle. The HIP conditions are given in Table III.

The three HIP ingots were forged by Wyman Gordon (Worcester, Mass.) and the forging conditions were not reported because they are of a proprietary nature. Figure 7 shows a typical forged pancake. Microsections of the forged pancakes showed that two of the three pancakes contained a fair amount of residual porosity at the particle interfaces. The forging designated 2H20 appeared to have a minimum of porosity and thus it was used as the source of the material for all the fracture tests.

Gas analysis of the three forgings showed a good correlation between

gas content and porosity. It appears that during the HIP cycle argon can diffuse through the can material and lead to pore formation at or near the surface of the forging. The higher content of oxygen in the center of the billet seems to indicate an incomplete or imperfect heating-outgassing cycle prior to sealing of the can.

C. Microstructure

Figures 8 and 9 show the typical microstructure billet 2H20. The average grain size is 400μ as measured along the length of the grain. The aspect ratio is about 3. The original powder particle size can be easily identified, each particle containing two or three grains. A very small amount of primary γ' appears at particle or grain boundary triple points.

Figure 10 shows that near the edge of the forging the interparticle porosity is extensive. This porosity could be the result of hot cracking during forging and/or of poor interparticle bonding due to the high argon gas content, or oxide film at the particle surfaces.

Following the heat treatment cycle described in Table IV, the microstructure of the HIP-forged alloy changes markedly. There is a well-defined coarsening of γ' particles along he prior particle boundaries with the formation of a coarser interparticle zone averaging 6μ in width. Figures 11 and 12 show the typical structure of the HIP-forged-heat treated alloy.

D. Mechanical Properties

Hardness and room temperature tensile properties (2 tests) are given in Table V for the different alloy conditions tested.

The tensile bars of the PM alloy had a diameter of .160 inch which would include an average of 130 grains per cross section which is large

enough to give a meaningful result.

E. Fracture Toughness (K_{IC}) Tests

Compact tension specimens with B = 0.25 inch and W = 0.80 inch (see Figure 13) were used for fracture toughness measurements. The material was tested in the as received condition. The tests were performed on a MTS fatigue machine in air at room temperature according to ASTM Specification E399-70T. The results are given in Table VI. Two tests were run for each alloy.

In all of the K_{IC} tests the ratio $B/(K_{IC}/YS)^2$ was smaller than 2.5, that is, too small to give a valid K_{IC} value according to ASTM E399-70T. The specimen thickness however is typical of the thickness of a turbine blade, so the measured values of K_{IC} are considered useful for real life applications.

The K_{IC} value for a crack running in the through thickness direction (see Figure 14) is larger than the K_{IC} in a radial direction. This difference is attributed to the grain anisotropy. The grain size width being smaller in the through thickness direction than in the radial direction. In the radial direction the tips of the elongated particles appears to serve as a stress concentration site which can account for rapid crack initiation and propagation along the particle boundaries.

The difference in fracture toughness from one specimen to the next is probably due to the distribution of pores in the material (see Figure 10).

The cast plus HIP material has a lower fracture toughness (40-49 ksi $\sqrt{\text{inch}}$) than the cast (52-69 ksi $\sqrt{\text{inch}}$). An examination of the fracture surface of the cast alloy shows that the crack follows the interdendritic

shrinkage cavities (see Figure 15) resulting in crack branching and a higher toughness. In the cast plus HIP alloy the fracture surface is planar in each grain (see Figure 16) and there is no sign of interdendritic fracture. The scatter of the fracture toughness data is due to the large grain size of the cast alloys which is such that there are only 3-5 grains per cross section of the fracture toughness specimen.

III. FATIGUE CRACK PROPAGATION (da/dn vs. ΔK)

Single edge crack specimens with B = 0.20 inch and W = 0.50 inch and L = 1.50 inch (see Figure 17) were used for these measurements. The material was tested in the as received condition. The fatigue crack was initiated from a 0.125 inch notch which was machined by Electrode Discharge Machining. The crack path was always in the through thickness direction (see Figure 14). The crack length was measured with a traveling microscope with a resolution of 5×10^{-4} inch. The tests were run on an Instron fatigue machine in room air at room temperature and at 1400°F. The P/M-HIP material was fatigued at a frequency of 10 cycles/second and the two cast alloys at a frequency of 15 cycles/second at room temperature and at a frequency of 10 cycles/second at 1400°F. All the test results are summarized in Figure 18. All the values are the mean value of at least two tests. There was a large scatter band for the data of the two cast structures because of the anisotropy resulting from the large grain size (3-5 grains over the width of the specimen) and the coarse dendritic structure (see Figures 1 and 3). It was found that crack growth was discontinuous in the cast and cast plus HIP alloy with long crack arrest periods at grain boundaries. In the P/M alloy the fatigue fracture proceeded more uniformly.

Figure 18 shows that at low stress intensity factor (ΔK) the crack propagation rate in the P/M-HIP material is markedly slower than in the cast alloys. However, there is a reversal at higher stress intensity factors where the growth rate in the PM alloy is higher than in the cast alloy. This reversal is due to the high slope of the $dl/dn/\Delta K$ curve for the P/M alloy. This high slope is unaccounted for at this time. It could be related to residual stresses present in the forging or to a high work hardening rate in the plastic zone at the crack tip. Further tests will be required to measure the difference in the threshold stress intensity factor ΔK_{th} for non-propagating cracks. So far, the test results show that the difference could be significant and that fatigue cracks will be harder to initiate in the P/M alloy.

In the cast alloy there is extensive branching of the fatigue cracks along grain boundaries or within the dendrites. This crack branching appears to be due to the coarse microstructure. As a result of crack branching the imposed crack tip opening displacement is spread over many crack fronts leading a relatively slow growth rate at each separate front. On the other hand the uniform microstructure of the P/M-HIP alloy is such that there is only a single fatigue crack with a well defined front and a higher crack growth rate.

At 1400°F there is no marked difference between the fatigue crack growth rates of the PM alloy and the cast alloy. In the cast alloy there is a minimum of crack branching by contrast to the room temperature behavior. The higher growth rates at 1400°F can be easily accounted for on the basis of a CTOD crack extension model: The growth rate increases as E and Y decrease with increasing temperature. Furthermore, the well known

ductility trough of the superalloys between 1300 and 1400°F could lead to a faster growth rate. Finally, the corrosive influence of oxidation at the crack tip may account for a large part of the higher growth rate at 1400°F. SEM fractography shows that fatigue striations could not be resolved because of a thick oxide film following the 1400°F tests.

IV. CONCLUSIONS

1. The room temperature fracture toughness indices K_Q of P/M-HIP-forged IN-100 alloys were measured and compared to K_Q values for cast and cast-HIP IN-100 alloys. The P/M alloy shows an increase in toughness over the cast alloy from 20 to 50% depending upon the test direction.

2. The fatigue crack growth rates in the cast and cast-HIP IN-100 alloy show a large scatterband at room temperature. This scatter is due to crack branching and crack arrest associated with the coarse grain and dendritic cast structure.

3. The fatigue crack growth rates in the P/M alloy at room temperature are very uniform at a given ΔK level. The threshold for non-propagating fatigue cracks is higher for the PM alloy than for the cast alloy.

4. At 1400°F there is no marked difference in fatigue crack growth rates between the P/M and the cast alloys.

TABLE I

CHEMICAL COMPOSITION OF IN-100

	Ni	Cr	Co	Mo	Al	Ti	C	B	Zr	V	Fe	Mn	Si	S
P/M	Bal.	9.20	14.9	2.92	5.65	4.68	.02	.014	.07	.94	.46	<.10	<.10	.006
CAST	Bal.	9.10	14.6	2.93	5.64	4.88	.02	.016	.059	1.04	.37	<.10	<.10	.007

TABLE II

GAS ANALYSIS IN ppm BY WEIGHT

	2H19 Edge	2H19 Cent.	2H20 E	2H20 C	2H21 E	2H21 C
N	ND 10	14	ND 10	ND 10	45	51
O	31	375	125	750	84	116
H	6.5	67	27	37	4.9	4.6
Ar	62	4.5	2.6	1.1	54	21
He	ND<2	ND<2	ND<2	ND<2	ND<2	ND<2

ND = none detected, less than

TABLE III

HIP (pressure-temperature-time) PROCESSING PARAMETERS

Identification	HIP-ing Temp.	Time	Pressure
2H19	2200°F	5 hours	14,600 psi
2H20	2250°F	5 hours	14,900 psi
2H21	2150°F	5 hours	14,400 psi

TABLE IV

HEAT TREATMENT FOR IN-100

2050 ± 15°F	2 hours	oil quenched
1600	40 minutes	air cooled
1800	45 minutes	air cooled
1200	24 hours	air cooled
1400	4 hours	air cooled

TABLE V

MECHANICAL PROPERTIES OF IN-100

	Hardness (R_c)	YS (Ksi)	UTS (Ksi)	Elong. (%)	R.A.
P/M HIP + Forged	40	130,149	155,183	4,9	4,12
Cast	39	136*	143*	4*	8*
Cast + HIP	36		132		

* from L.N. Moskowitz
° estimated from hardness test

TABLE VI

FRACTURE TOUGHNESS PROPERTIES OF IN-100

	K_{IQ} (Ksi $\sqrt{inch}$)	$B/(K_{IQ}/YS)^2$	$R_Y = HR_X$ (inch)	Ligament R_X
P/M HIP + Forged				
Through Thickness	85,99	.43,.78	.050,.090	$\geq$ 17
Radial	59,73	.80,1.60	.020,.050	$\geq$ 32
Cast	52,68	1.0,1.74	.023,.040	$\geq$ 40
Cast + HIP	40,49	1.63,2.5	.016,.024	$\geq$ 67

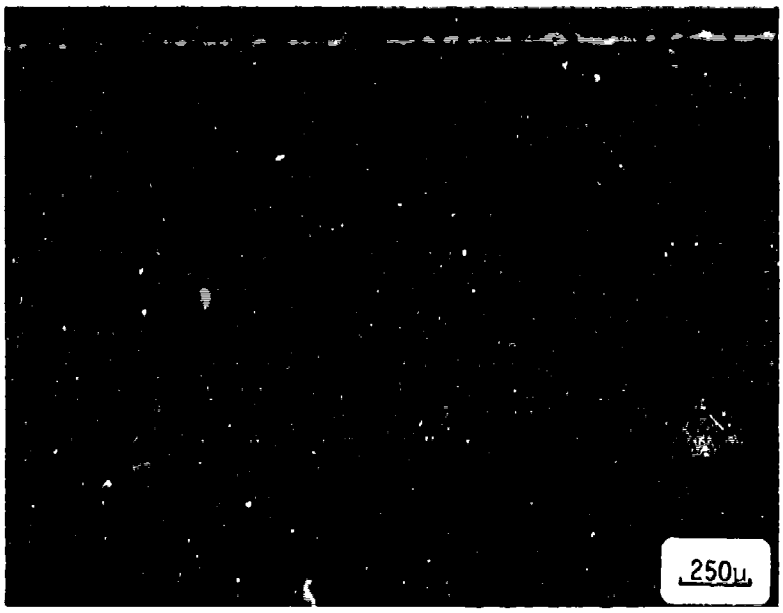

Figure 1. Microstructure of as-received cast IN-100 (40X).

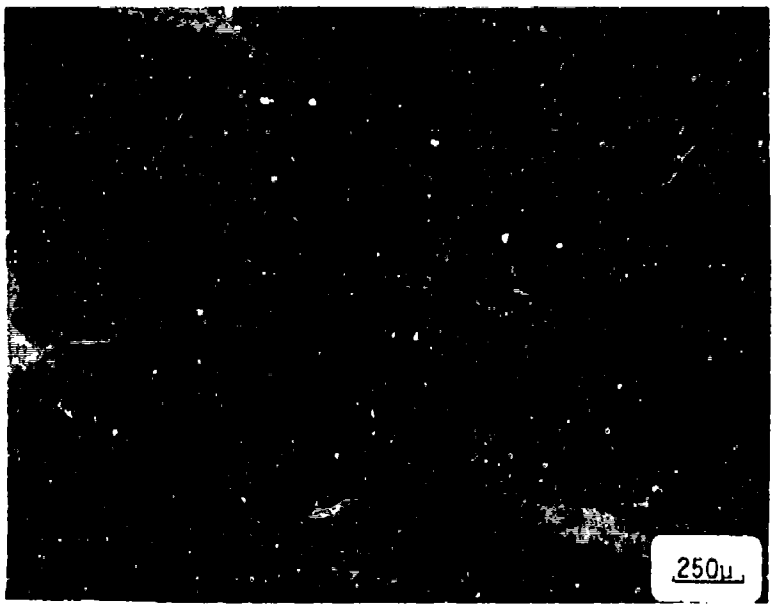

Figure 2. Microstructure of heat treated cast IN-100 (40X).

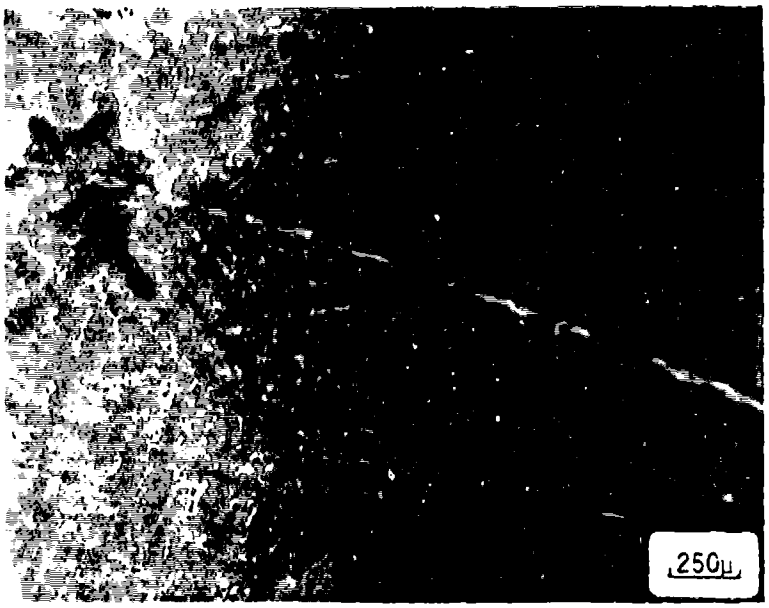

Figure 3. Microstructure of as-received cast plus HIP IN-100 (40X).

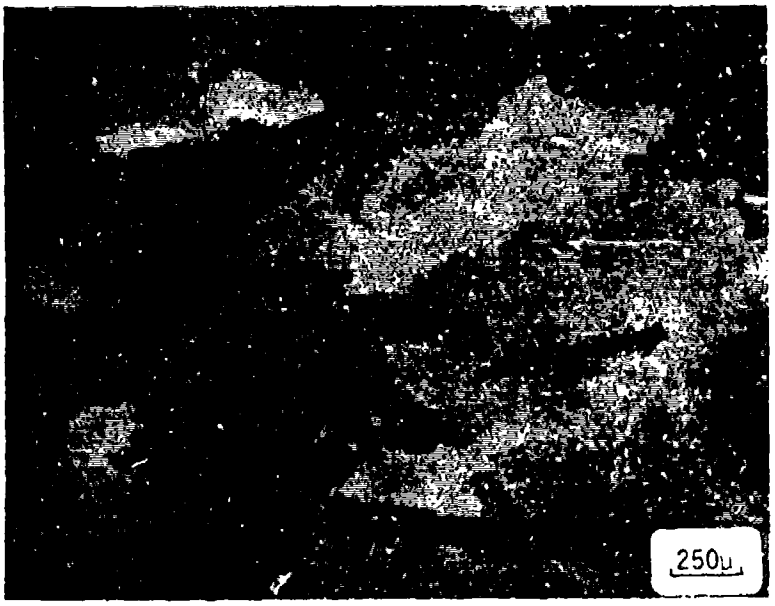

Figure 4. Microstructure of heat treated cast plus HIP IN-100 (40X).

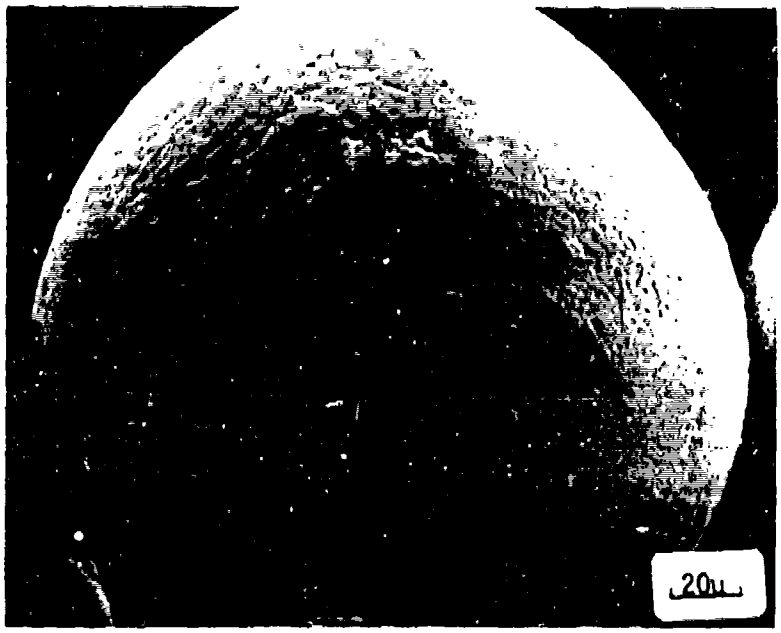

Figure 5. Overall view of typical IN-100 powder processed by REP™ technique (500X).

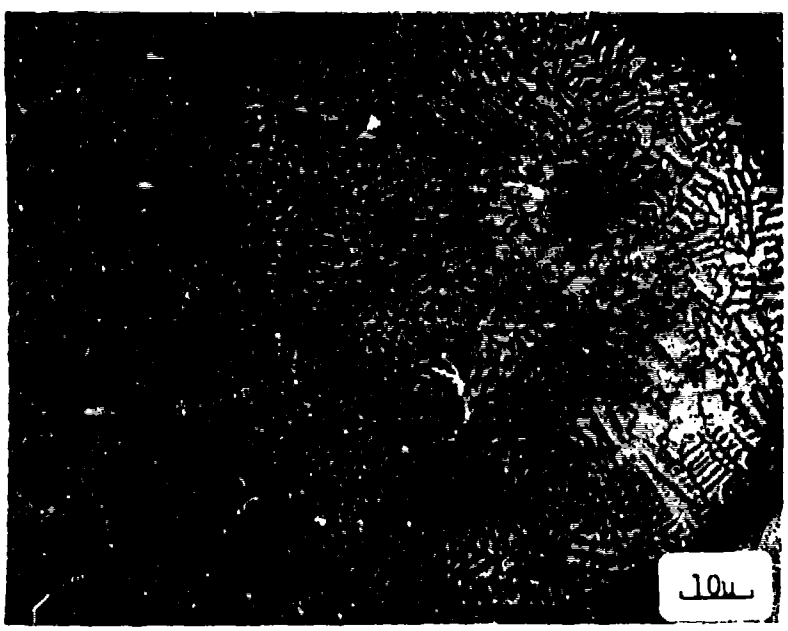

Figure 6. Microstructure of typical IN-100 powder processed by REP™ technique (1000X).

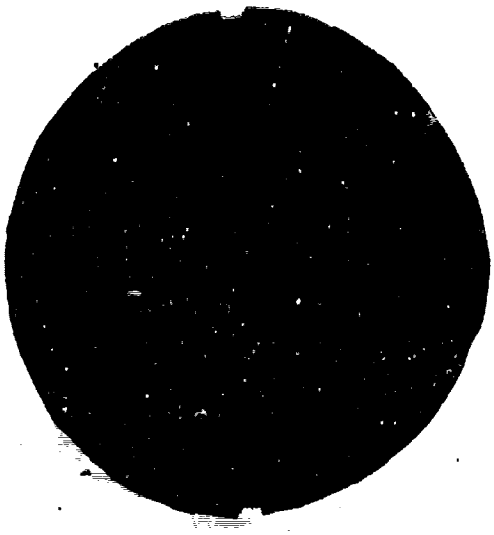

Figure 7. IN-100 billet processed by powder metallurgy and HIP and forged.

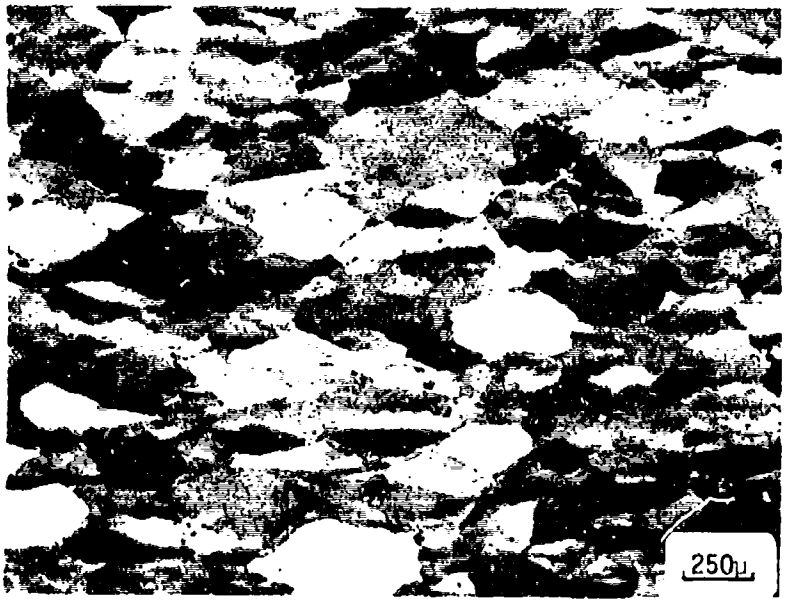

Figure 8. Microstructure of as received P/M plus HIP and forged IN-100 (40X).

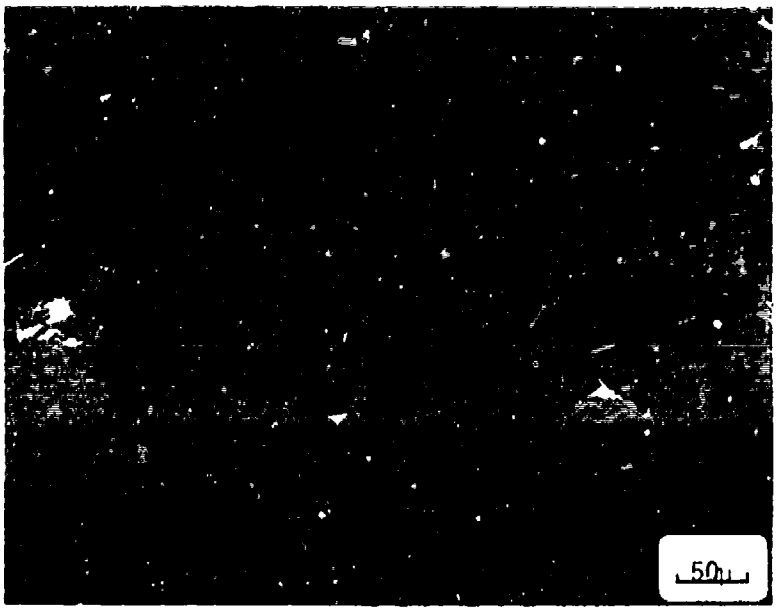

Figure 9. Microstructure of as received P/M plus HIP and forged IN-100 (200X).

Figure 10. Pores in P/M plus HIP and forged IN-100 (200X).

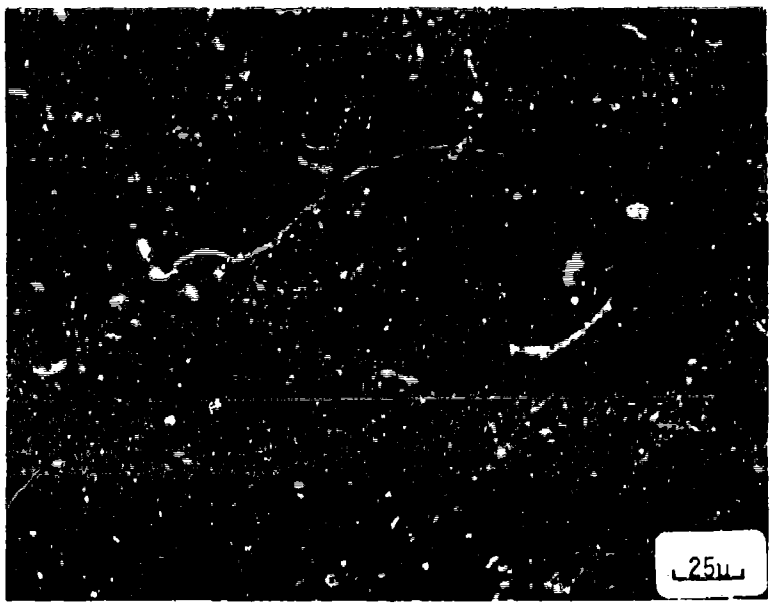

Figure 11. Microstructure of heat treated P/M plus HIP and forged IN-100. (400X)

Figure 12. Microstructure of heat treated P/M plus HIP and forged IN-100 (1000X).

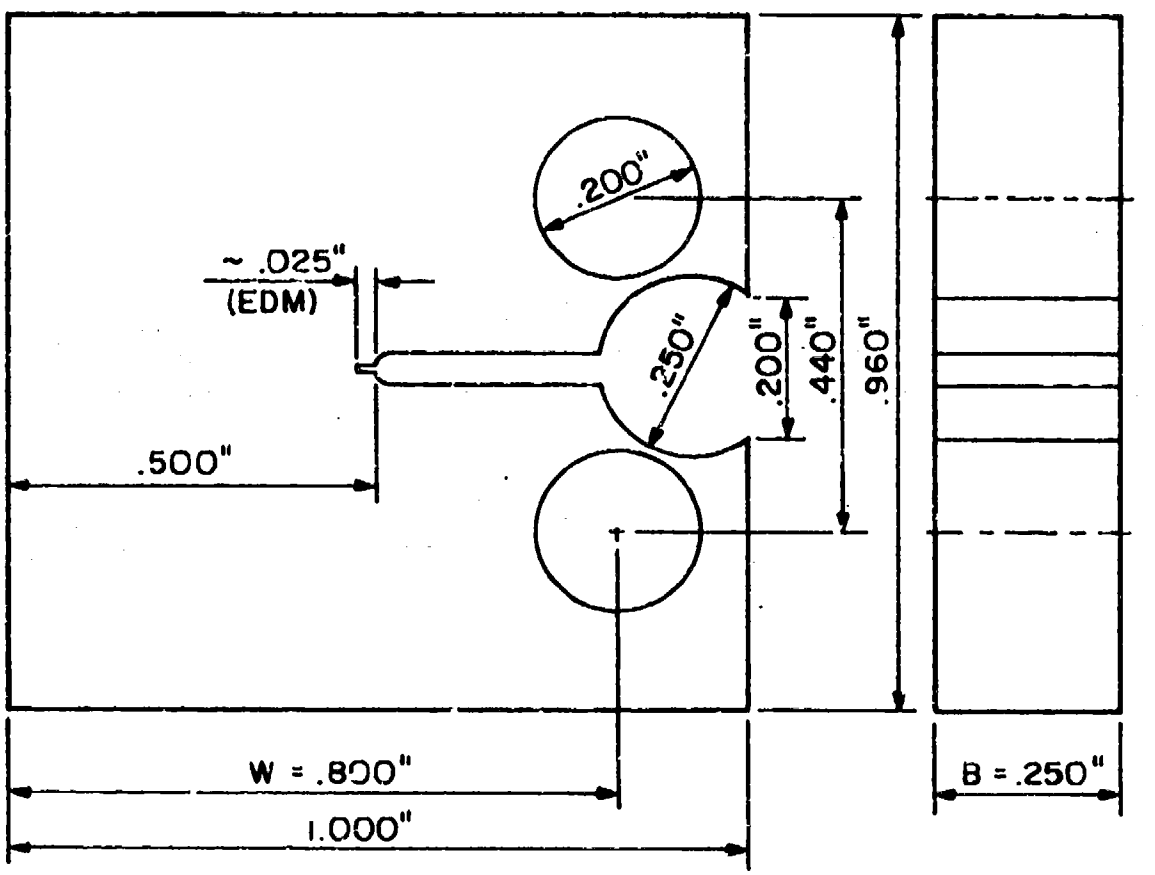

Figure 13. Compact-tension specimen used for fracture toughness testing.

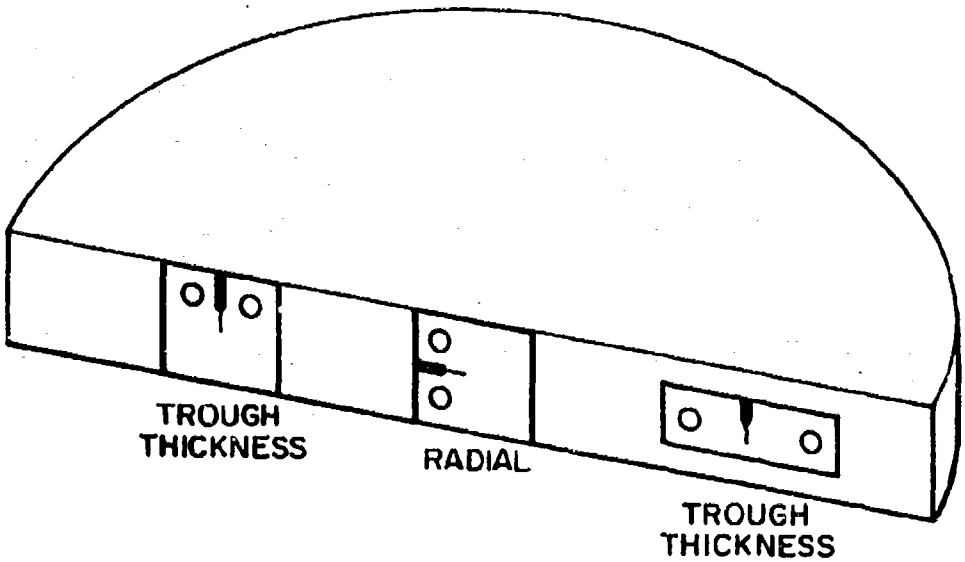

Figure 14 - Orientation of fracture toughness and fatigue specimens in forged P/M billet of IN-100.

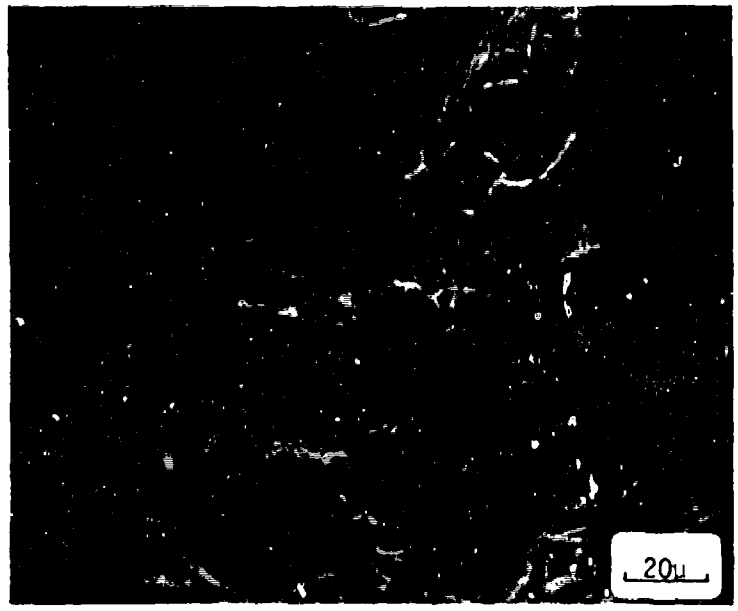

Figure 15. Fracture surface of cast IN-100 (630X).

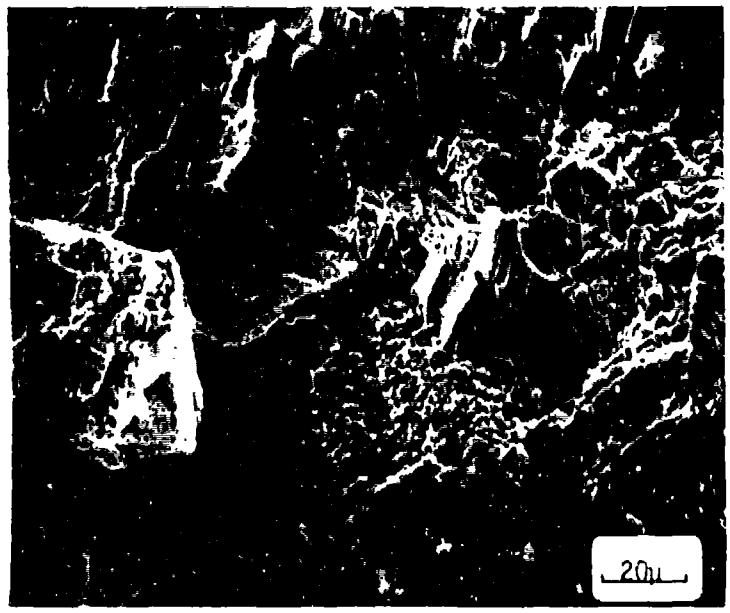

Figure 16. Fracture surface of cast plus HIP IN-100 (600X).

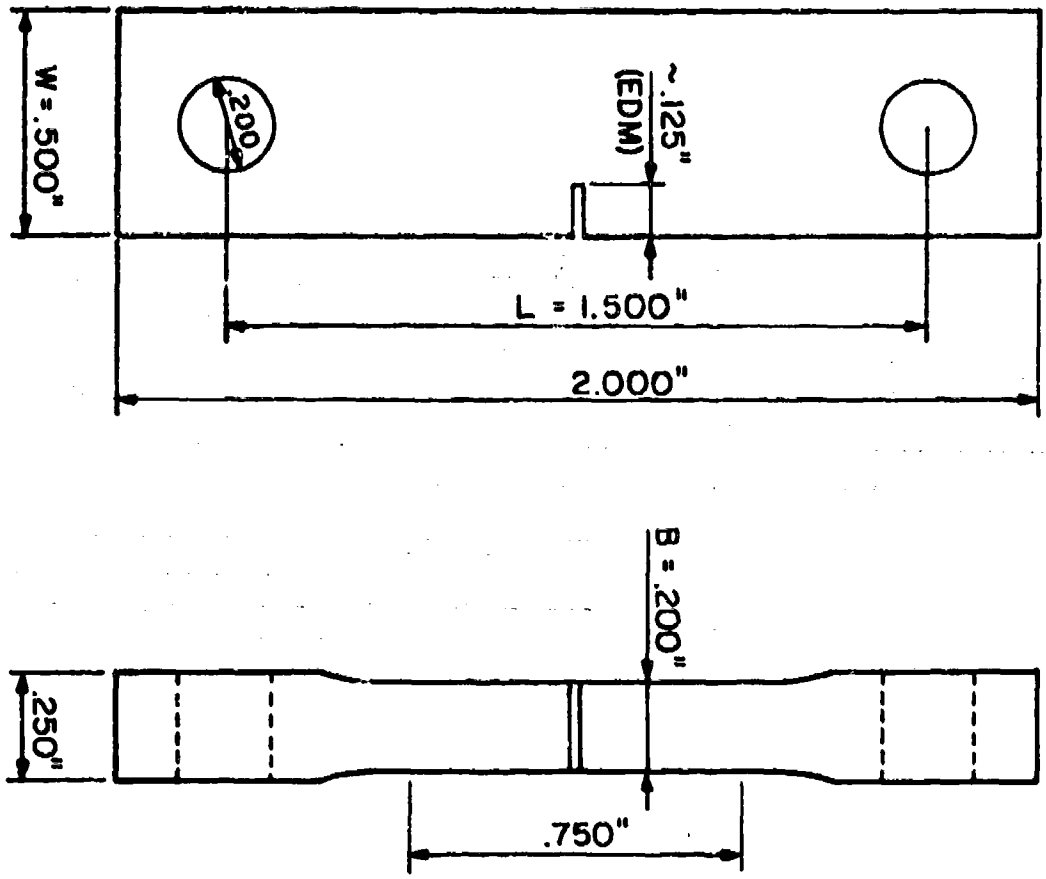

Figure 17. Single-edge-crack specimen used for fatigue crack propagation testing.

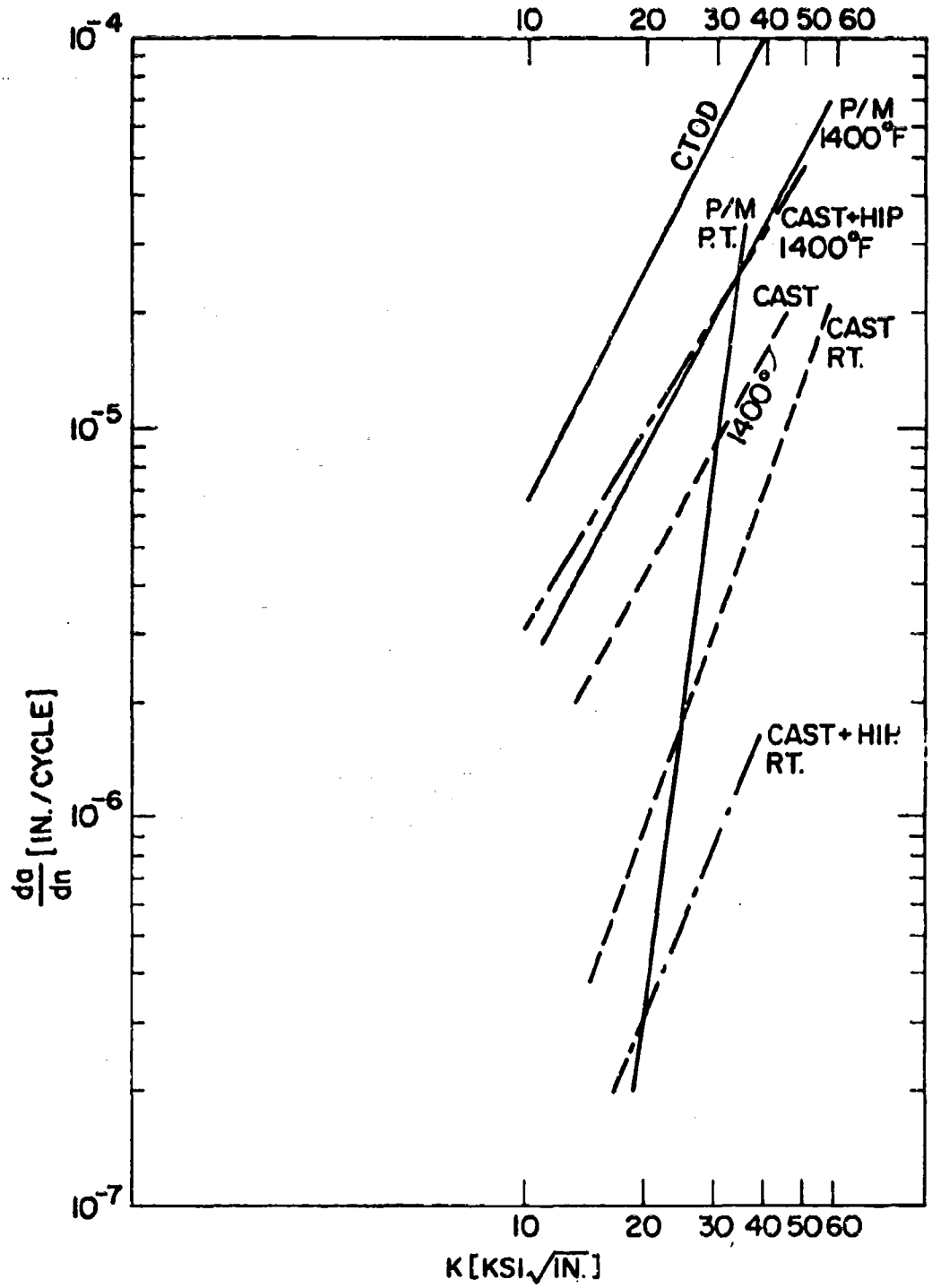

Figure 18. Fatigue crack propagation in P/M, cast and cast plus HIP IN-100 at room temperature at 1400°F.

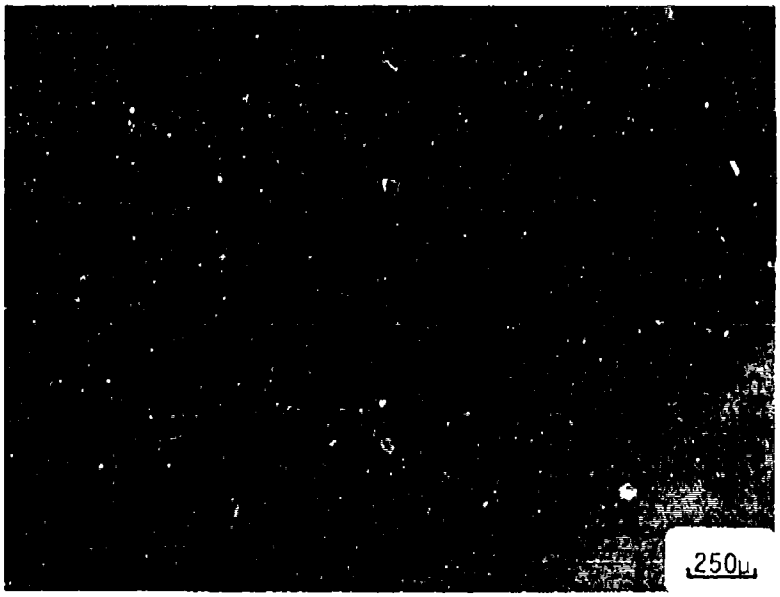

Figure 19. Branching of the fatigue crack in cast IN-100 (40X).

THE DEFORMATION OF HOT ISOSTATICALLY PRESSED IN-100 AT HIGH TEMPERATURES AND HIGH STRAIN RATES

by S.J. Berman and N.J. Grant

The hot workability of hot isostatically pressed IN-100 powders was studied within the temperature range 1800 to 2000°F (982 to 1093°C), at strain rates of about 10^{-6} to 10^{-1} sec^{-1}. These ranges cover the temperatures and strain rates of commercial interest in industrial hot working operations. The program was initiated to obtain increased knowledge of the interdependence of stress, strain, strain-rate, and temperature during hot working of a HIP product, and to optimize the hot isostatic pressing parameters of temperature, time, and pressure for a given alloy powder.

It was found that the optimum HIP conditions were a pressing temperature of either 2150°F (1195°C) or 2200°F (1220°C) and a 2 to 3 hour pressing time. The 2 hour hot isostatically pressed material was observed to exhibit properties equal to or superior to those of the 5 hour HIP material at the high operating temperatures (i.e. 2000°F (1093°C)), arguing against the benefits of a long HIP cycle.

The optimum hot working temperature was about 1900°F (1038°C); the optimum deformation rates were between 10^{-3} and 10^{-4} sec^{-1}.

I. Introduction

High temperature tests were conducted to evaluate the hot plasticity of hot isostatically pressed (to be referred to as HIP) IN-100 powder products. The hot plasticity test variables were chosen to approximate hot working operations. The purpose of the program was to evaluate several HIP

parameters (i.e. temperature, time and pressure) and to indicate preferred HIP conditions for large scale production of HIP IN-100 powder compacts.

II. Materials and Powder Consolidation

The processing of superalloys from atomized powders compacted by sintering; by hot pressing and forging; by hot extursion; or by hot isostatic pressing has resulted in a marked improvement in the homogeniety of the alloys, and in higher mechanical properties at room and at intermediate temperatures. This improvement of mechanical properties is due in part to the elimination of casting defects such as shrinkage cavities, variable grain sizes, and coarse, brittle interdendritic phases.

The superalloy chosen for this investigation was IN-100, which is a commonly used, cast nickel-base superalloy, with one of the best strength to weight ratios[1,2]. IN-100 consists of a solid-solution nickel-chromium-cobalt matrix strengthened by an ordered gamma prime [$Ni_3(Al,Ti)$] precipitate and by several complex metal carbides (i.e. M_6C, $M_{23}C_6$). The physical metallurgy of IN-100 has been reviewed by Decker and Sims[3]. A typical composition of IN-100 is given in Table I, combined with the gas analysis of the "Rotating Electrode Process" (REP) powder used in this investigation. The low carbon, IN-100 prealloyed powders were supplied by the Nuclear Metals Division of Whittaker, Inc. A powder of low carbon content (about 0.018%C) was used in order to eliminate the formation of complex metal carbides (i.e. M_6C, $M_{23}C_6$), which inhibit grain growth in P/M products[5]. A typical size distribution and screen analysis of the REP powder is given in Table II.

Figure 1a is a scanning electron microscope (SEM) photomicrograph of

a typical powder particle produced by REP. Note that the powder particles are quite spherical in geometry and show a distinct dendritic surface structure. The powder particle surface is free of oxide scale, however, this does not preclude the presence of a thin, continuous oxide film. Figure 1b is a polished and etched cross-section; it clearly illustrates the dendritic structure of the powder. The average dendrite arm spacing was calculated to be about 3 microns, and did not vary signficantly from heat to heat.

III. Experimental Procedure

The powders were consolidated by hot isostatic pressing[6-8] at IMT (Industrial Materials Technology, Inc.). The powders were packed in low alloy carbon steel cans 12 inches (304.8 mm) in length with an outer diameter of 3/8 inch (9.5 mm) and a bore size of 5/16 inch (7.9 mm). The approximate weight of the powder packed in each can was 7/10 pound (.32 kg). The packing density within the can was approximately 65% theoretical density. After packing, the cans were evacuated at 600°C (1138°C) to a pressure of 10^{-3} torr while purged with argon several times, and sealed under vacuum by welding. The sealed cans were heated to HIP temperatures of 2050, 2100, 2150, 2200 and 2250°F (1140, 1170, 1195, 1220 and 1250°C) at a constant heating rate of 1000°F (538°C) per hour, the final 50°F (10°C) at a rate of 1°F (.555°C) per minute. The cans were kept at the maximum temperature and pressed under a pressure of 103.4 N/mm^2 (15 ksi) for either 2 or 5 hours. After pressing, the cans were cooled under pressure at a rate of 20°F (6.7°C) per minute. The HIP temperatures, times, and pressures chosen for this investigation were typical of those of commercial HIP conditions. Ten different conditions were selected for evaluation.

Figure 2a is a photomicrograph of the typical microstructure of IN-100 powders HIP at a lower HIP temperature, 2050°F (1140°C) for 5 hours and Figure 2b is the microstructure of the higher HIP temperature material; 2250°F (1250°C) for 5 hours.

The HIP bars (5/8 inch (15.9 mm) in diameter and 12 inches (304.8 mm) in length) were sectioned, metallographically examined, and machined into ASTM standard high temperature tensile bar specimens. The tensile bars each had 1 inch (25.4 mm) gauge lengths and .250 inch (6.35 mm) guage diameters, with 3/8-16 (UNC-1A) threaded sections. The hot workability of the as-HIP specimens was evaluated by constant load, high strain-rate, tensile tests. High strain-rate torsional tests could have been used, but it was decided that the tensile test would offer a more accurate approximation of the failure conditions during hot working of a HIP material.

The high speed, high temperature tensile tests were performed on a pneumatic high strain-rate machine. The machine has a 2-1/2 inch (63.5 mm) piston throw and is capable of reaching a maximum load of 5000 pounds (approximately 100 ksi in a .250 inch (6.35 mm) gauge diameter) within 20 milliseconds, and a maximum deformation rate of 30 inches per inch per second (seconds^{-1}). The load is applied by means of differential pressure, air piston action (subsequent to a small preload on the specimen train to remove slack); the rupture time (t_R) is measured by an electric chronometer (accuracy of 0.01 seconds) which is automatically activated by the application of the load and is stopped at fracture by means of an electric microswitch. The applied load is taken from the pressure dial gauge on the machine, or from the output signal of a temperature compensated, strain

gauge load cell, recorded on a X-Y recorder.

The specimens were brought to the test temperatures in less than 4 minutes by means of a dual elliptical reflector, radiant infrared, split jacket furnace using type T-3 tubular quartz-tungsten filament high intensity lamps. Thus furnace enables even heating along its entire 11 inch (279.4 mm) length. The test temperatures were monitored and were controlled during testing by a chromel-alumel thermocouple spot welded to the center portion of the specimen surface, and a Leeds-Northrup potentiometer. The control accuracy of this set-up was ±3°F (1.7°C). The tensile specimens were held at temperature for 3 minutes before testing to insure uniform temperature. After fracture, the bars were air cooled to room temperature, measured for total elongation and reduction in cross-sectional area, and prepared for metallographic and SEM inspection.

IV. Results and Discussion

A. Short Time Stress Rupture Behavior

The results of the hot plasticity tests are presented in Tables III (1800°F (982°C) test data), IV (1900°F (1038°C) test data) and V (2000°F (1093°C) test data); the specimen designations and HIP variables are also included in the tables. Note that within this report the use of the term "stress" denotes a true rupture stress; the term "strain" denotes a true strain; and an average deformation rate has been used in place of a true strain-rate or a minimum creep rate (MCR) since only the load and not the strain can be controlled using the above mentioned apparatus.

Log-log plots of stress versus average deformation rate are given in Figures 3 to 7. The stress necessary for the rupture of the material

decreases with an increase in test temperature for all HIP conditions. Stress versus time to rupture plots (not shown) exhibited a similar relationship. The slopes of these rupture stress curves are typical of those for conventional superalloys tested at elevated temperatures. From the figure a comparison of the rupture strength for the 2 and 5 hour HIP materials, for different pressures and test temperatures, yields a distinct pattern of behavior, illustrated in Table VI.

From the table, one observes that in 1800°F (982°C) stress rupture tests the material HIP for 5 hours has rupture strengths superior to those of the material HIP for 2 hours for all HIP temperatures. This may be related to the coarser grain size of the 5 hour material as well as to the presence of a coarser gamma prime precipitate morphology. In 1900°F (1038°C) tests, for the lower HIP temperatures of 2050°F (1140°C) and 2100°F (1170°C), the strength performance is mixed, with the 2 hour HIP material performing better than the 5 hour material in slow deformation rate tests. However, at the highest HIP temperatures of 2150, 2200 and 2250°F (1195, 1220 and 1250°C), the 5 hour HIP material maintains dominance in performance.

In tests at 2000°F (1093°C) the materials which were HIP at the lower temperatures of 2050°F (1140°C) and 2100°F (1170°C) exhibit a mixed performance with regard to the rupture strength. The 2 hour HIP material generally performed better than the 5 hour HIP material; the three higher HIP temperature materials exhibited superior performance in the 2 hour material compared to the 5 hour HIP material. This "reversal" in behavior can possibly be explained by an extended dissolution of the coarser gamma prime

in the 5 hour material to a point greater in extent than that in the 2 hour material, a plausible argument since the gamma prime solvus is reported to be around 2000°F (1093°C)[3,9]. However, the limited scope of this investigation prohibits any firmer statement of possible causes relating morphology or energistic differences to rupture strength behavior.

B. High Temperature Fracture

Whatever these morphology or energistic differences may be, they are not illustrated by fracture behavior for the different HIP conditions; Figures 8 to 10 illustrate the fractures of the material HIP at 2250°F (1250°C) for 2 and 5 hours and tested at the three test temperatures at varying strain rates. Note the intergranular (also interpowder particle) cracking in each case, however the majority of cracks have propagated along powder particle boundaries. These fractures cannot easily be differentiated from the fractures of material HIP at 2200, 2150, and 2050°F (1220, 1195, and 1140°C) (Figures 11, 12, and 13, respectively) except that at these lower HIP temperatures there is greater retention of shape by the large powder particles. Even though it is apparent that a greater degree of recrystallization occurs as the HIP temperature increases, the fractures remain largely along powder particle boundaries; only for the 2250°F (1250°C) HIP product is there some evidence of pure intercrystalline cracking (Figures 8 and 9).

The fracture surface itself is more easily judged from Figures 14 and 15, based on tests at 1900°F (1038°C) for material HIP at 2200°F (1220°C) and 2150°F (1195°C), respectively. The granular surfaces demonstrate the intermittent bond across powder particles, interspersed with fine oxide

film fragments from the original powders. While the structures look quite brittle, there is good to excellent ductility in cold and hot tension tests, equivalent to or greater than that for the cast alloy (see below). Strength levels at 1800 to 2000°F (982 to 1093°C) (Figures 3 to 7) are also excellent and not indicative of a brittle structure.

Figure 16 demonstrates the irregular path of the interpowder particle fracture as the fracture path weaves into the structure on both sides of the particle boundary.

The spheroidization or solution (partial) of the oxide films would improve both strength and ductility, perhaps to a degree that would yield comparable properties to those of the wrought powder alloy.

C. Rupture Life Versus Deformation Rate

Turning to another aspect of this investigation, if the average deformation rates obtained for testing are plotted against rupture times, a curve yielding a Monkman-Grant[13] type relationship is obtained (Figure 17). The average curve is drawn at 45 degrees in the traditional manner, with the 2-sigma confidence limits shown. The scatter is surprisingly small and supports the contention that these HIP materials are behaving in a predictable manner, free of important defects.

One problem in high strain rate testing to obtain hot plasticity data is that the strain rate figures are difficult to measure (rupture time on the other hand is easily and accurately measured). Figure 17, permits one to interpolate strain rate values from the measured rupture life once a few points can be obtained to obtain this plot.

D. Ductility

Total elongations of all tests are given in Tables III, IV, and V, and range from a low value of 1.5% at high strain rates (short rupture times) to a high value of about 25% at low strain rates (long rupture times), depending on the test temperatures and HIP conditions.

Curves of rupture stress versus elongation for the extreme HIP conditions are given in Figures 18 to 23. Figure 18 is a plot of the data from the 1800°F (982°C) tests for the 2050°F (1140°C) HIP material. The plot illustrates that the material which has been HIP at 2050°F (1140°C) for 5 hours shows higher elongation values for a given stress than does the 2 hour HIP material. Figure 18 is a plot of the 1800°F (982°C) test data for the 2250°F (1250°C) HIP material. Here it can be seen that the elongation for a given stress level does not vary significantly with HIP time as it did in Figure 16.

In plots of 1900°F (1038°C) test data shown in Figures 20 and 21, the 2 hour HIP material is superior to the 5 hour material for a HIP temperature of 2050°F (1140°C) and is only superior at lower stress levels for a HIP temperature of 2250°F (1250°C); elongations of up to 25.5% were obtained at these lower levels of stress (lower strain rates). In the plots of the 2000°F (1094°C) test data shown in Figures 22 and 23, at the lower HIP temperature the 2 hour material is superior in behavior; however, for the 2250°F (1250°C) HIP the performance is almost equal, with the 5 hour material slightly better.

Figures 24 to 28 are plots of elongation versus the rupture time for 1900°F (1038°C) tests of different HIP conditions. These curves

indicate a tendency of the material towards superplastic behavior[14]. In all the curves, the 2 hour HIP condition offers equal or better elongation values at slow strain rates (long time to rupture) than does the 5 hour material. These excellent ductility values are maximized for the middle range of HIP temperatures. A HIP temperature of 2150 to 2200°F (1195 to 1220°C) is optimum because the resultant structures achieve their highest ductility values at fracture at the highest strain rates (short deformation times), which would simplify hot rolling or forging operations.

Thus, from comparisons of the test data, the test or hot working temperature offering the highest values of ductility and hot plasticity is 1900°F (1038°C); from additional comparisons, the optimum HIP parameters are a temperature of 3150°F (1195°C) or 2200°F (1220°C), and a pressing time of 2 or 3 hours.

Recapitulating, the curves described in the previous paragraphs illustrate that HIP IN-100 has a behavior typical of wrought or cast nickel-base superalloys; these curves describe a behavior which is considered to be encouraging. The ductility or hot plasticity of the HIP product was found to be an improvement over that of the cast alloy, but only fair in relation to the extruded material. For example, the elongation of a typical cast IN-100 product at 1900°F (1038°C) is approximately 6%[15], the elongation of a P/M HIP IN-100 product at 1900°F (1038°C) was found in this investigation to be 25% (maximum), however Moskowitz[14] reported that extruded P/M IN-100 exhibited elongations at 1900°F (1038°C) of 100 to 150%. This manyfold superiority of the extruded product can be attributed to the elimination of the detrimental effects of fine oxide films originally residing on powder particle surfaces. Any further increase in the ductility of the HIP

material must come from the dissolution or break-up of these boundary films.

V. Conclusions

The hot workability of HIP IN-100 powders was studied within the temperature range 1800 to 2000°F (982 to 1093°C), at strain rates of about 10^{-6} to 10^{-1} sec^{-1}. The ranges cover the temperatures and strain-rates of commercial interest in industrial hot working operations. From the tests run and the data evaluated the following conclusions were drawn:

1) The HIP IN-100 powders which were HIP for a period of 2 hours generally exhibited mechanical properties and behavior equal or superior to those of the material HIP for 5 hours. It would be desirable to avoid use of longer HIP cycles for obvious cost reasons.

2) The optimum HIP parameter conditions were temperatures of 2150°F (1195°C) or 2200°F (1220°C), and a pressing time of 2 to 3 hours, with the possibility of improvement with increased HIP pressures.

3) The optimum temperature for hot pressing (in terms of resultant ductility) was found to be 1900°F.

4) The optimum deformation rates at this temperature (in terms of ductility) were found to be 10^{-3} to 10^{-4} $seconds^{-1}$.

5) At elevated temperature, the HIP material exhibits tensile mechanical properties superior to those reported for the cast material.

6) The presence of powder particle oxide films prevents perfect bonding of the powder particles during the HIP cycle.

7) Low strain rate (10^{-2} to 10^{-4} per sec), tensile type testing at intermediate to high temperatures offers a good approximation of hot working operations.

REFERENCES

1. "Engineering Properties of IN-100", Huntington Alloys, International Nickel Corporation, 1971.

2. R.W. Fawley, "Superalloy Progress", The Superalloys, eds, C.T. Sims, and W.C. Hagel, Wiley Press, New York, New York, 1972, p. 3.

3. R.F. Decker and C.T. Sims; "Metallurgy of Nickel-Base Alloys", The Superalloys, eds. C.T. Sims and W.C. Hagel, Wiley Press, New York, New York, 1972, p. 33.

4. J.K. Friedman and G.S. Ansell, "Powder Metallurgy", The Superalloys, eds., C.T. Sims and W.C. Hagel, Wiley Press, New York, New York, 1972, p. 427.

5. S.E. Rogers, Powder Metallurgy, 12, (1963), 122.

6. S.J. Paprocki, E.S. Hodge, "The Compaction of Powders by Isostatic Pressure", Mechanical Behavior of Materials Under Pressure, Elsevier Material Science Series, American Elsevier Publishing Co., New York, New York, 1970, p. 591.

7. P.R. Sahn, Powder Met. International, 3, No. 1, (Feb., 1971), 74, Part I, and Powder Met. International, 3, No. 2, (May, 1971), 26, Part II.

8. Semi-Annual Technical Report No. 3, ARPA Contract NO. DAHC15-70-C-0283, January, 1972.

9. W. Wallace, W. Wiebe, E.P. Whelan, R.V. Dainty, and T. Terada, Powder Metallurgy, 16. No. 32, (1973), 416.

10. K.H. Moyer, Tech. Report AFML-TR-69-21, 1969, Wright-Patterson AFB, Ohio.

11. M.M. Allen, R.L. Athey, and J.B. Moore, Metals Eng. Quarterly, 10, (1970), 20.

12. N.J. Grant, private communication, 1973.

13. F.C. Monkman and N.J. Grant, An Empirical Relationship Between Rupture Life and Minimum Creep Rate in Creep-Rupture Tests, Deformation and Fracture at Elevated Temperatures, eds., N.J. Grant and A.W. Mullendore, MIT Press, Cambridge, Massachusetts, 1965, p. 91.

14. L.N. Moskowitz, R.M. Pelloux, and N.J. Grant, "Properties of IN-100 Processed by Powder Metallurgy", Superalloys-Processing, Proc. of the Second Int'l Conf., IMD High Temperature Alloys Committee, AIME, MCIC 72-10.

15. S. Wästberg, private communication, 1973.

TABLE I

IN-100 Composition

Element*	As-Cast	Low C Powder**	Normal C Powder**
Ni	Bal.	Bal.	Bal.
Cr	10.5	9.20	9.52
Co	15.4	14.90	15.01
Mo	3.02	2.92	3.07
Al	5.55	5.65	5.73
Ti	4.72	4.68	4.71
C	0.16	0.018	0.178
B	0.015	0.014	0.018
Zr	0.06	0.07	0.05
V	1.05	0.94	0.98
Fe	0.94	0.46	0.01
Mn	0.10	0.10	0.01
Si	0.05	0.10	0.02
S	0.007	0.006	-

Gas Analysis

Low Carbon - REP Argon Atomized (used in HIP)

O_2	130 ppm
H_2	7.5 ppm
Ar	16. ppm
He	none

TABLE II

Size Range and Screen Analysis

Size Range: -500 + 48 Mesh -20 to +295 μm

Screen Analysis:

Mesh	μm	%
-25 + 35	-620 to +417	0.0
-35 + 60	-417 to +230	4.5
-60 + 100	-230 to +149	41.5
-100 + 200	-149 to +74	41.4
-200 + 325	-74 to +44	11.3
-325 +	-44 to +20	1.3

TABLE III

Results of 1800°F (982°C) Testing

Specimen Number	HIP* Temp. °F (°C)	HIP* Time hrs.	Rupture Time secs.	Rupture Stress ksi	Rupture Stress N/mm²	Strain in/in	Elong. %	R.A. %	Ave. Def. Rate sec^{-1}
3A56-1	2050	2	4643	153	105.52	.079	8.2	7.1	1.8×10^{-5}
-2	(1140)		277	236	162.70	.034	3.5	2.4	1.3×10^{-4}
-3			1663	194	133.77	.047	4.8	4.0	2.9×10^{-5}
-4			232	279	192.32	.024	2.4	1.6	1.6×10^{-4}
-5			43	324	223.40	.016	1.6	0.8	3.7×10^{-4}
3A59-1	2050	5	9846	160	110.33	.089	9.3	10.9	9.5×10^{-6}
-2	(1140)		661	242	166.82	.043	4.4	4.7	6.7×10^{-5}
-3			240	281	193.69	.033	3.4	2.4	1.4×10^{-4}
-4			41	324	223.40	.024	2.4	0.8	5.9×10^{-4}
-5			3381	203	139.95	.058	6.0	8.6	1.8×10^{-5}
3A65-1	2100	2	2381	195	134.45	.052	5.3	4.7	2.5×10^{-5}
-2	(1170)		3544	157	108.27	.074	7.7	10.1	2.2×10^{-5}
-3			294	281	193.69	.027	2.7	2.4	9.2×10^{-5}
-4			149	324	223.40	.020	2.0	1.6	1.3×10^{-4}
-5			818	240	165.46	.039	4.2	4.0	5.8×10^{-5}
3A68-1	2100	5	686	281	193.69	.032	3.3	2.4	4.8×10^{-5}
-2	(1170)		99	367	253.02	.024	2.4	1.6	2.4×10^{-4}
-3			3318	197	135.83	.052	5.3	3.2	1.6×10^{-5}
-4			62	410	282.64	.014	1.4	0.8	2.3×10^{-4}
-5			1155	238	164.07	.042	4.3	3.2	2.2×10^{-5}
2K03-1	2150	2	3907	198	136.51	.054	5.5	6.3	1.4×10^{-5}
-2	(1195)		221	285	196.53	.029	2.9	4.0	1.3×10^{-4}
-3			95	424	292.35	.023	2.3	2.4	2.4×10^{-4}
-4			344	246	169.56	.033	3.3	4.8	9.6×10^{-5}
-5			144	332	228.90	.025	2.5	3.2	1.7×10^{-4}

Specimen Number	HIP* Temp. °F (°C)	HIP* Time hrs.	Rupture Time secs.	Rupture Stress ksi	Rupture Stress N/mm²	Strain in/in	Elong. %	R.A. %	Ave. Def. Rate sec^{-1}
2K09-1	2150	5	7428	200	137.89	.077	8.0	7.0	1.1×10^{-5}
-2	(1195)		339	285	196.53	.037	3.8	4.0	1.1×10^{-4}
-3			179	427	294.41	.033	3.4	3.2	1.9×10^{-4}
-4			479	248	170.94	.036	3.7	5.5	9.8×10^{-5}
-5			204	335	230.96	.033	3.3	4.0	1.6×10^{-4}
2L53-1	2200	2	2849	198	136.51	.055	5.6	3.2	2.0×10^{-5}
-2	(1220)		579	285	196.53	.033	3.3	4.0	5.5×10^{-5}
-3			79	431	297.15	.016	1.6	2.4	2.9×10^{-4}
-4			780	242	166.82	.052	4.6	4.7	4.6×10^{-5}
-5			148	333	229.58	.025	2.5	4.0	1.7×10^{-4}
2L51-1	2200	5	12038	198	136.51	.079	8.3	6.3	6.9×10^{-6}
-2	(1220)		758	285	196.53	.042	4.3	4.0	5.7×10^{-5}
-3			133	417	287.54	.027	2.7	3.2	2.0×10^{-4}
-4			901	242	166.82	.055	5.0	4.7	5.0×10^{-5}
-5			222	335	230.96	.033	3.3	4.0	1.5×10^{-4}
2L45-1	2250	2	4925	244	168.19	.043	5.2	3.2	1.1×10^{-5}
-2	(1250)		1383	288	198.59	.036	3.7	4.0	2.7×10^{-5}
-3			137	417	287.54	.024	2.0	2.4	1.5×10^{-4}
-4			97	457	315.10	.014	1.4	2.4	1.8×10^{-4}
-5			592	329	226.84	.029	2.9	3.2	5.0×10^{-5}
2L46-1	2250	5	9108	248	170.94	.041	4.2	5.5	4.6×10^{-6}
-2	(1250)		825	283	195.16	.032	3.3	2.4	4.0×10^{-5}
-3			225	420	289.60	.015	1.9	4.0	8.5×10^{-5}
-4			538	332	228.90	.025	2.5	2.4	5.1×10^{-5}
-5			119	450	310.29	.013	1.3	0.8	1.1×10^{-4}

* All HIP'ed at 15000 psi (103.4 N/mm²)

TABLE IV

Results of 1900°F (1038°C) Testing

Specimen Number	HIP* Temp. °F (°C)	HIP* Time hrs.	Rupture Time secs.	Rupture Stress ksi	Rupture Stress N/mm²	Strain in/in	Elong. %	R.A. %	Ave. Def. Rate sec⁻¹
3A55-1	2050	2	281	147	101.31	.039	4.0	4.0	1.4×10^{-4}
-2	(1140)		5197	115	79.24	.134	14.3	15.7	2.8×10^{-5}
-3			125	197	135.83	.026	2.6	5.5	2.1×10^{-4}
-4			696	134	92.38	.068	6.8	9.5	9.8×10^{-5}
-5			7894	119	82.09	.120	12.8	17.7	3.3×10^{-5}
-6			3562	123	84.83	.114	12.1	14.6	3.4×10^{-5}
3A53-1	2050	5	240	198	136.51	.028	2.8	4.8	1.2×10^{-4}
-2	(1140)		528	149	102.78	.041	4.2	4.8	8.0×10^{-5}
-3			8	232	159.95	.015	1.5	0.8	2.0×10^{-3}
-4			1327	108	74.44	.075	7.8	10.9	6.0×10^{-5}
-5			1101	130	89.64	.067	6.9	7.8	6.3×10^{-5}
3A54-1	2100	2	221	210	144.75	.033	3.5	1.6	1.6×10^{-4}
-2	(1170)		1043	153	105.52	.065	6.7	9.3	6.4×10^{-5}
-3			695	194	133.77	.040	4.1	3.2	6.5×10^{-5}
-4			31	236	162.70	.020	2.0	2.4	6.4×10^{-4}
-5			2125	111	76.50	.128	13.6	13.2	5.7×10^{-5}
-6			921	178	122.69	.057	5.9	7.1	6.4×10^{-5}
3A67-1	2100	5	5918	119	82.09	.156	16.9	19.0	2.9×10^{-5}
-2	(1170)		1099	152	104.84	.068	7.0	6.3	5.6×10^{-5}
-3			405	173	119.25	.044	4.5	4.8	1.2×10^{-4}
-4			169	194	133.77	.025	2.5	3.2	2.0×10^{-4}
-5			98	234	161.33	.021	2.1	1.6	2.5×10^{-4}
2K12-1	2150	2	4528	119	82.09	.133	14.2	17.7	3.1×10^{-5}
-2	(1195)		779	147	101.31	.054	5.5	3.2	7.1×10^{-5}
-3			4097	133	91.70	.130	13.9	13.9	3.4×10^{-5}
-4			75	189	130.34	.020	2.0	0.0	2.7×10^{-4}
-5			92	194	133.77	.023	2.3	2.4	2.5×10^{-4}
-6			1921	137	94.44	.064	6.6	3.2	3.8×10^{-5}
-7			357	156	107.58	.048	4.9	4.0	1.4×10^{-4}
-8			52	234	161.33	.017	1.7	0.8	3.3×10^{-4}

Specimen Number	HIP* Temp. °F (°C)	HIP* Time hrs.	Rupture Time secs.	Rupture Stress ksi	Rupture Stress N/mm²	Strain in/in	Elong. %	R.A. %	Ave. Def. Rate sec^{-1}
2K07-1	2150	5	3289	148	101.99	.070	7.2	4.7	2.2×10^{-5}
-2	(1195)		125	189	130.34	.022	2.2	1.6	1.8×10^{-4}
-3			98	236	162.70	.017	1.7	0.8	1.9×10^{-4}
-4			18789	138	95.13	.123	13.1	13.2	1.5×10^{-5}
-5			1204	170	117.19	.052	5.3	3.8	4.4×10^{-5}
2K05-1	2200	2	320	194	133.77	.051	5.2	4.0	1.6×10^{-4}
-2	(1220)		69	234	161.33	.023	2.3	1.6	3.3×10^{-4}
-3			1132	161	111.02	.058	10.6	12.4	9.4×10^{-5}
-4			4736	121	83.46	.213	23.7	20.4	5.0×10^{-5}
-5			409	170	117.19	.055	5.6	3.8	1.4×10^{-4}
2L42-1	2200	5	490	219	151.03	.040	4.1	4.7	8.4×10^{-5}
-2	(1220)		3473	148	111.80	.077	8.0	9.2	2.3×10^{-5}
-3			82	283	195.16	.015	1.5	3.2	1.8×10^{-4}
-4			543	195	134.45	.044	4.5	4.7	8.3×10^{-5}
-5			280	240	165.44	.024	2.4	4.1	9.6×10^{-5}
2L44-1	2250	2	3736	152	104.84	.056	9.3	7.1	2.5×10^{-5}
-2	(1250)		1019	197	135.83	.044	4.5	5.5	4.4×10^{-5}
-3			206	240	165.44	.026	2.6	3.2	1.3×10^{-4}
-4			7973	142	97.87	.124	13.2	15.4	1.7×10^{-5}
-5			16109	121	83.46	.226	25.3	20.4	1.3×10^{-5}
2L43-1	2250	5	7881	157	108.27	.086	9.0	9.4	1.1×10^{-5}
-2	(1250)		72	335	230.96	.022	2.2	4.0	3.1×10^{-4}
-3			642	245	168.88	.025	3.3	3.2	6.0×10^{-5}
-4			1110	202	139.26	.054	5.5	7.1	5.0×10^{-5}
-5			21600	110	75.81	.124	13.2	12.4	6.1×10^{-6}

* All HIP'ed at 15,000 psi (103.4 N/mm²)

TABLE V

Results of 2000°F (1093°C) Testing

Specimen Number	HIP* Temp. °F(°C)	HIP* Time hrs.	Rupture Time secs.	Rupture Stress ksi	Rupture Stress N/mm²	Strain in/in	Elong. %	R.A. %	Ave. Def. Rate sec^{-1}
3A57-1	2050	2	76	151	104.15	.032	3.2	4.0	4.2×10^{-4}
-2	(1140)		420	102	70.32	.059	6.1	6.0	1.5×10^{-4}
-3			935	57	39.33	.102	10.7	12.4	1.0×10^{-4}
-4			18	194	133.77	.024	2.4	3.2	1.3×10^{-3}
-5			209	125	86.20	.038	3.9	4.7	1.9×10^{-4}
3A60-1	2050	5	21	144	99.25	.020	2.0	1.6	9.5×10^{-4}
-2	(1140)		116	100	68.94	.033	3.3	3.2	3.9×10^{-4}
-3			1136	57	39.33	.096	10.1	10.2	8.9×10^{-5}
-4			62	172	118.57	.027	1.7	0.8	1.7×10^{-3}
-5			6	192	132.39	.019	1.9	2.4	2.1×10^{-3}
3A66-1	2100	2	76	140	91.60	.033	3.4	1.6	4.5×10^{-4}
-2	(1170)		252	104	71.69	.053	5.4	6.3	2.2×10^{-4}
-3			1727	69	47.56	.108	11.4	15.4	6.6×10^{-5}
-4			18	190	131.02	.020	2.0	1.6	1.1×10^{-3}
-5			158	124	85.52	.042	4.1	4.0	2.6×10^{-4}
3A70-1	2100	2	13	143	98.56	.023	2.3	0.8	1.0×10^{-3}
-2	(1170)		305	105	72.38	.036	3.7	5.6	1.2×10^{-4}
-3			699	55	37.95	.060	6.2	7.8	8.9×10^{-5}
-4			12	194	133.77	.023	2.3	1.6	1.2×10^{-3}
-5			142	123	84.83	.030	3.0	3.1	2.1×10^{-4}
2K04-1	2150	2	27	143	98.56	.030	2.8	1.6	1.0×10^{-3}
-2	(1195)		160	103	71.00	.045	4.6	6.3	2.9×10^{-4}
-3			2618	59	40.70	.127	13.5	15.3	5.6×10^{-5}
-4			16	189	130.34	.024	2.4	1.6	1.5×10^{-3}
-5			62	125	86.20	.036	3.7	4.7	6.0×10^{-4}

Specimen Number	HIP* Temp. °F(°C)	HIP* Time hrs.	Rupture Time secs.	Rupture Stress ksi	Rupture Stress N/mm²	Strain in/in	Elong. %	R.A. %	Ave. Def. Rate sec⁻¹
2K08-1	2150	5	10	144	99.25	.020	2.0	2.4	2.0×10^{-3}
-2	(1195)		83	102	70.32	.032	3.2	5.5	3.9×10^{-4}
-3			1367	58	40.01	.101	10.6	9.1	7.8×10^{-5}
-4			6	190	131.02	.018	1.8	1.6	3.0×10^{-3}
-5			60	124	85.52	.026	2.6	4.0	4.3×10^{-4}
2K11-1	2200	2	42	146	100.6	.036	3.7	0.8	8.8×10^{-4}
-2	(1220)		460	103	71.0	.064	6.6	5.6	1.4×10^{-4}
-3			3934	58	40.0	.166	18.1	12.4	6.9×10^{-5}
-4			24	190	131.0	.030	3.0	2.4	1.3×10^{-3}
-5			189	123	84.8	.041	4.4	3.1	2.3×10^{-4}
2L52-1	2200	5	114	147	101.3	.037	4.2	4.0	3.7×10^{-4}
-2	(1220)		245	100	68.9	.062	6.4	2.4	1.8×10^{-4}
-3			22	197	135.8	.035	3.6	3.2	1.4×10^{-3}
-4			535	80	55.1	.080	8.3	4.8	1.4×10^{-4}
-5			147	123	84.8	.044	4.5	3.1	3.1×10^{-4}
2L49-1	2250	2	230	147	101.31	.037	3.8	1.6	1.7×10^{-4}
-2	(1250)		2829	106	73.1	.072	7.5	8.6	5.7×10^{-5}
-3			123	192	132.4	.030	3.0	1.6	2.4×10^{-4}
-4			9	238	164.1	.022	2.2	1.6	2.5×10^{-3}
-5			197	166	114.5	.033	3.4	1.6	1.8×10^{-4}
2L50-1	2250	5	347	149	102.7	.039	4.0	3.2	1.2×10^{-4}
-2	(1250)		3073	110	75.8	.071	7.4	10.2	5.4×10^{-3}
-3			126	194	133.8	.038	3.9	1.6	2.1×10^{-4}
-4			34	240	165.4	.023	2.3	1.6	6.8×10^{-5}
-5			235	169	116.5	.038	3.9	1.6	1.5×10^{-4}

* All HIP'ed at 15,000 psi (103.4 N/mm²).

TABLE VI

Comparison of Rupture Strength Superiority with HIP Time

	HIP Time Exhibiting Superior Stress Rupture
1800°F Tests	
HIP Temperature	
2050	5 hours
2100	5 hours
2150	5 hours
2200	5 hours
2250	5 hours
1900°F Tests	
HIP Temperature	
2050	Mixed
2100	Mixed
2150	5 hours
2200	5 hours
2250	5 hours
2000°F Tests	
HIP Temperature	
2050	Mixed
2100	Mixed
2150	2 hours
2200	2 hours
2250	Mixed

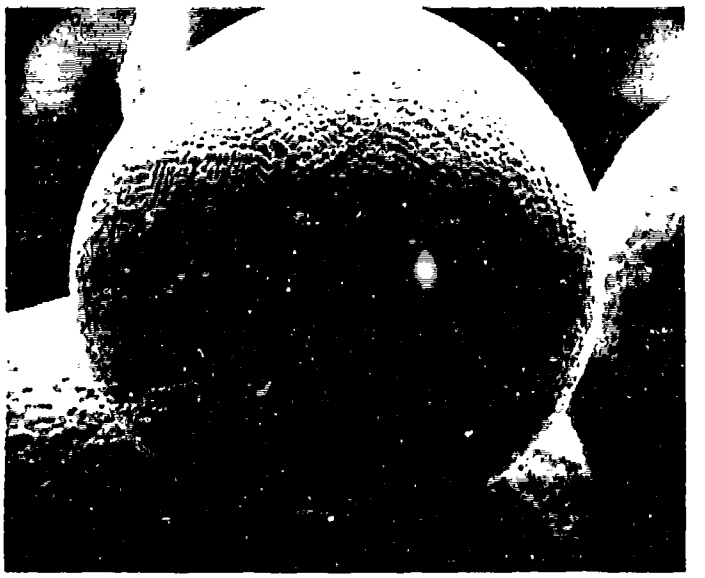

Figure 1a. Typical REP™ IN-100 powder particle (500X).

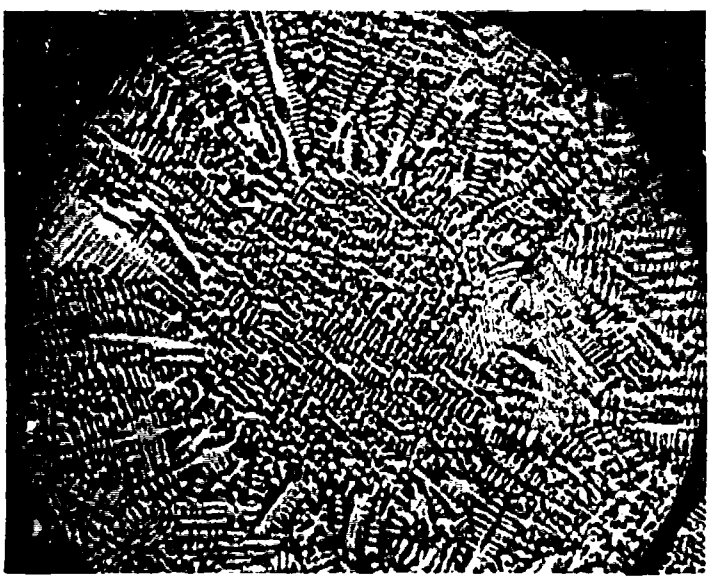

Figure 1b. Dendrite structure in REP IN-100 powder (300X).

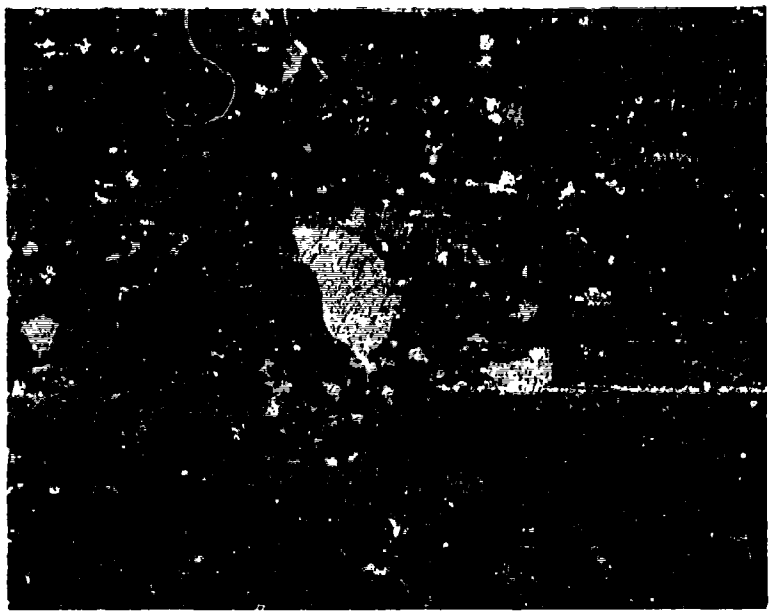

Figure 2a. Typical microstructure of IN-100 HIP at 2100°F (1170°C) for 2 hours at 15 ksi (103.4 N/mm²). Designation: (3A68-2) (200X).

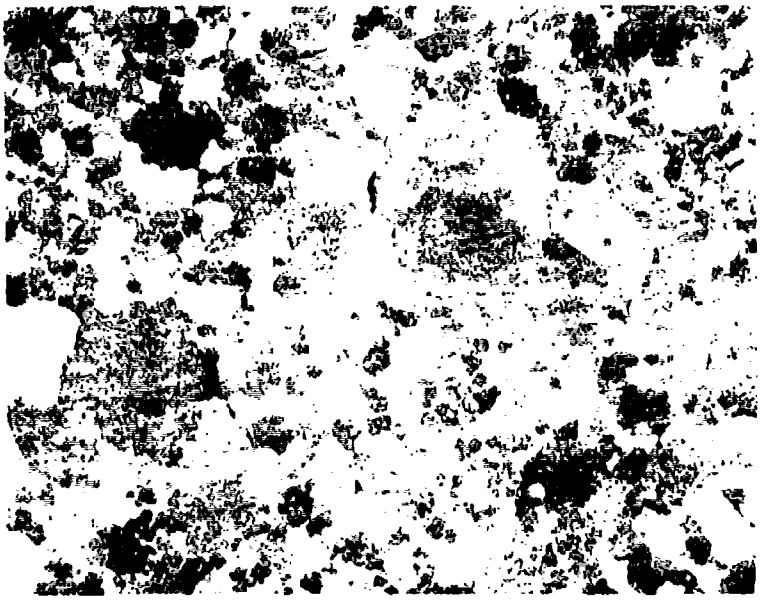

Figure 2b. Typical microstructure of IN-100 HIP at 2250°F (1250°C) for 5 hours at 15 ksi (103.4 N/mm²). Designation: (2L43-1) (200X) Taken after testing.

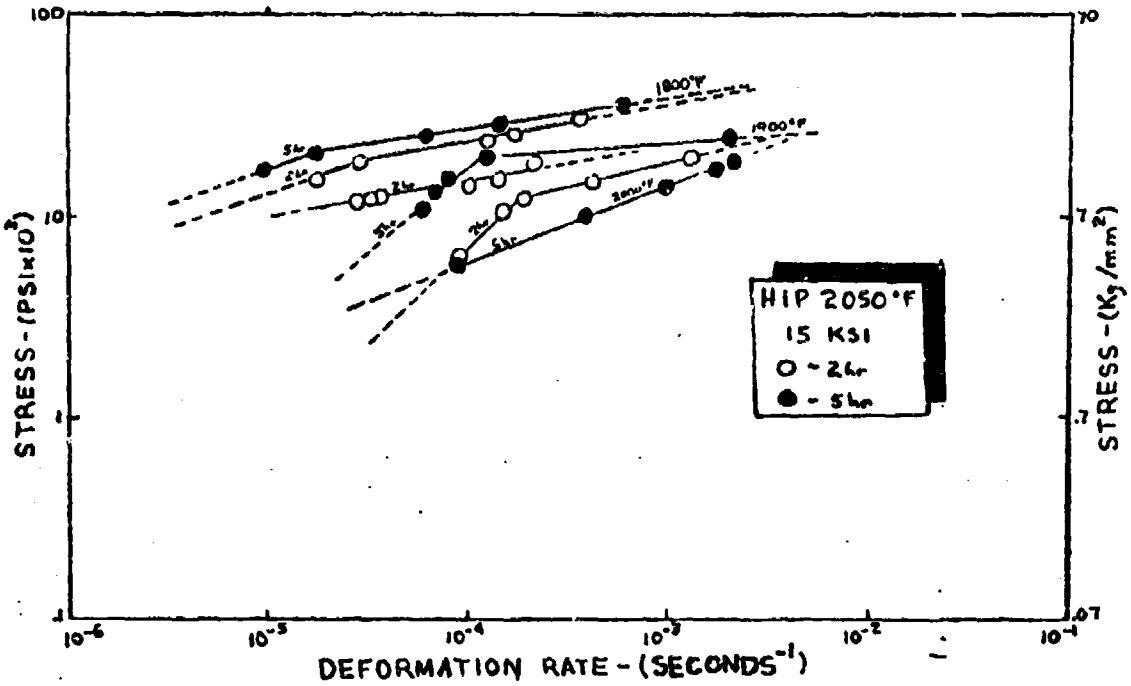

Figure 3. Stress vs. deformation rate plot for IN-100 HIP at 2050°F (1140°C) for 2 and 5 hours.

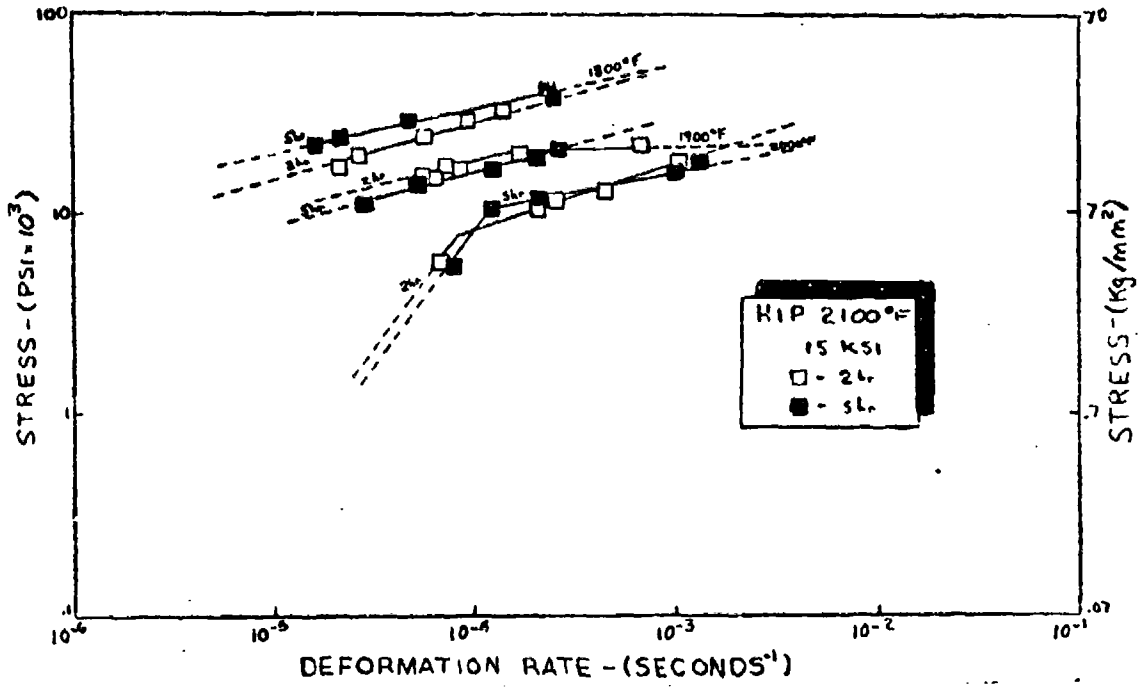

Figure 4. Stress vs. deformation rate plot for IN-100 HIP at 2100°F (1170°C) for 2 and 5 hours.

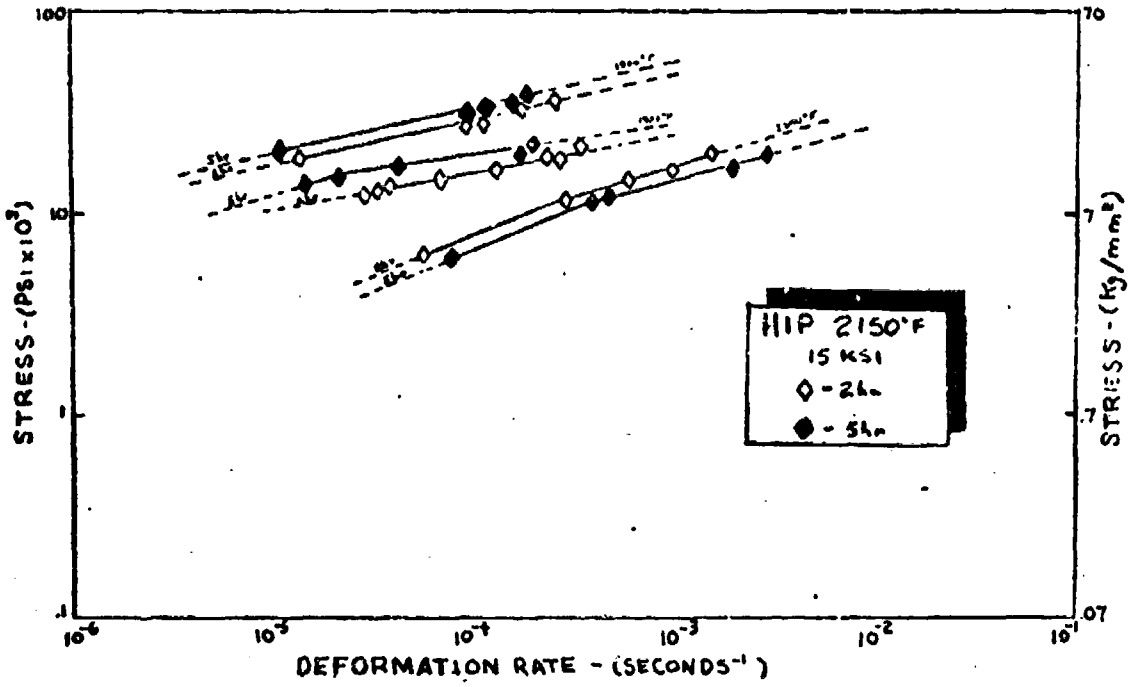

Figure 5. Stress vs. deformation rate plot for IN-100 HIP at 2150°F (1195°C) for 2 and 5 hours.

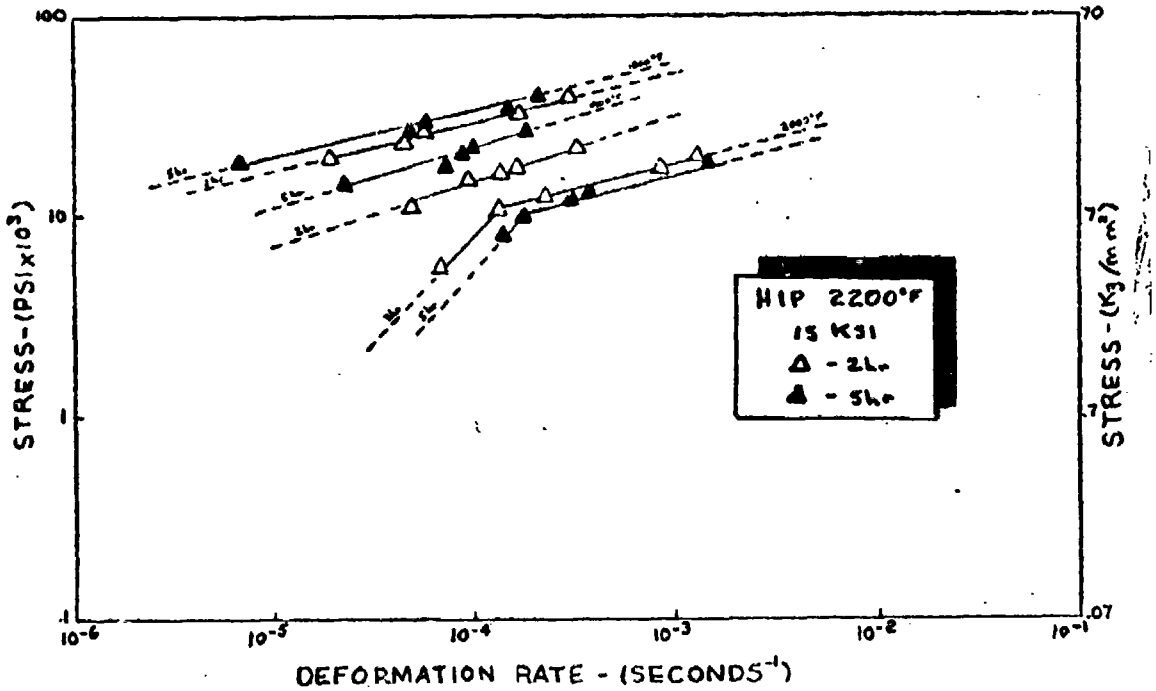

Figure 6. Stress vs. deformation rate plot for IN-100 HIP at 2200°F (1220°C) for 2 and 5 hours.

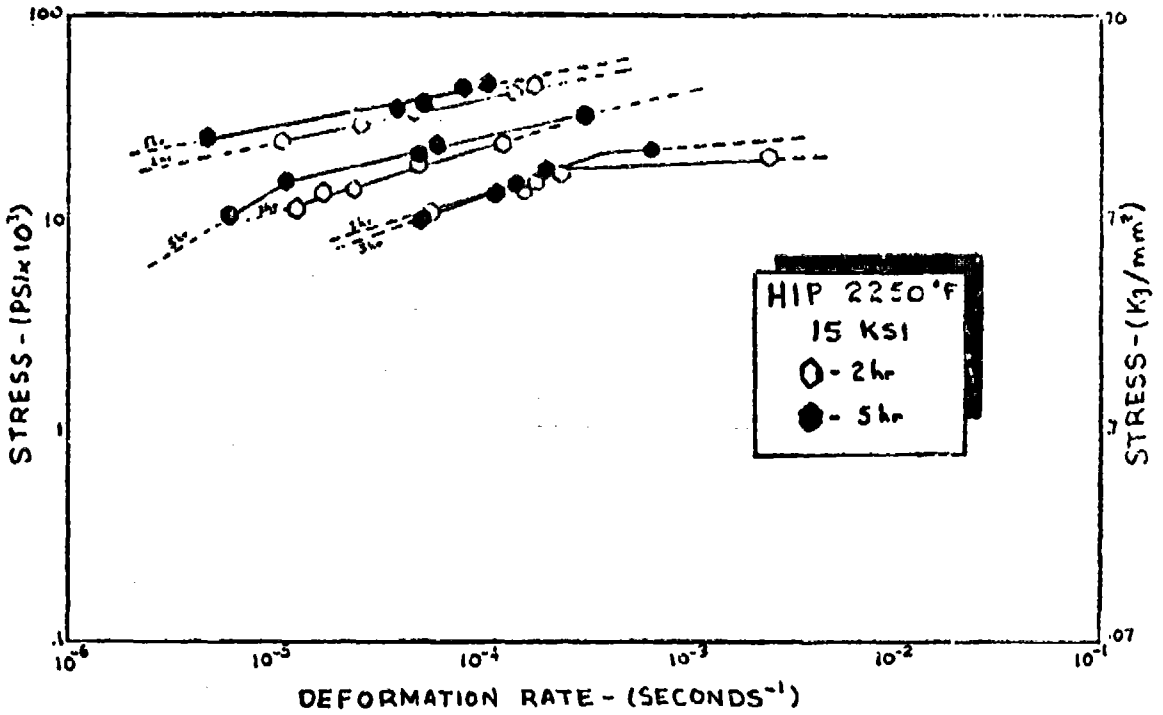

Figure 7. Stress vs. deformation rate plot for IN-100 HIP at 2250°F (1250°C) for 2 and 5 hours.

Figure 8. Typical post-test photomicrograph of IN-100 HIP at 2250°F (1250°C) for 2 hours; designation (2L49-2); tested at 2000°F (1093°C); 106 ksi (73.1 N/mm^2). Deformation rate: 5.7 X 10^{-5} sec^{-1} (400X).

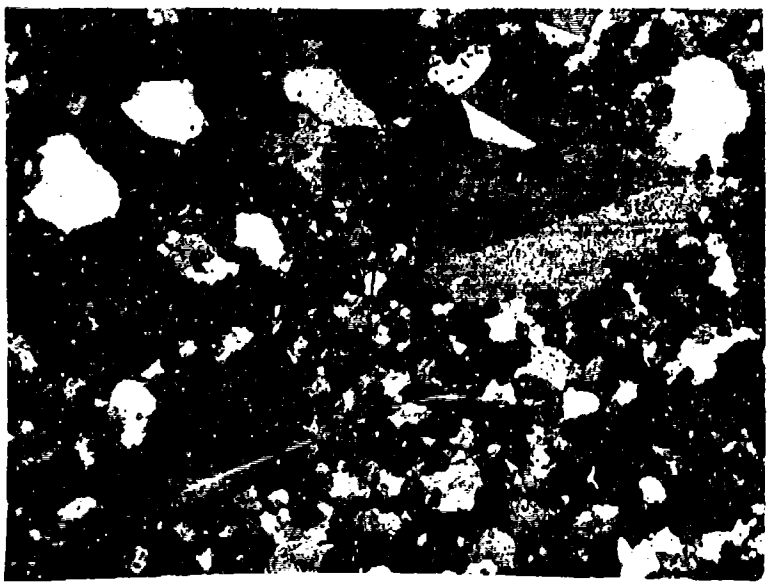

Figure 9. Typical post-test photomicrograph of IN-100 HIP at 2250°F (1250°C) for 2 hours; designation (2L43-2); tested at 1900°F (1038°C); 335 ksi (231 N/mm^2). Deformation rate: 3.1 X 10^{-4} sec^{-1}. (200X).

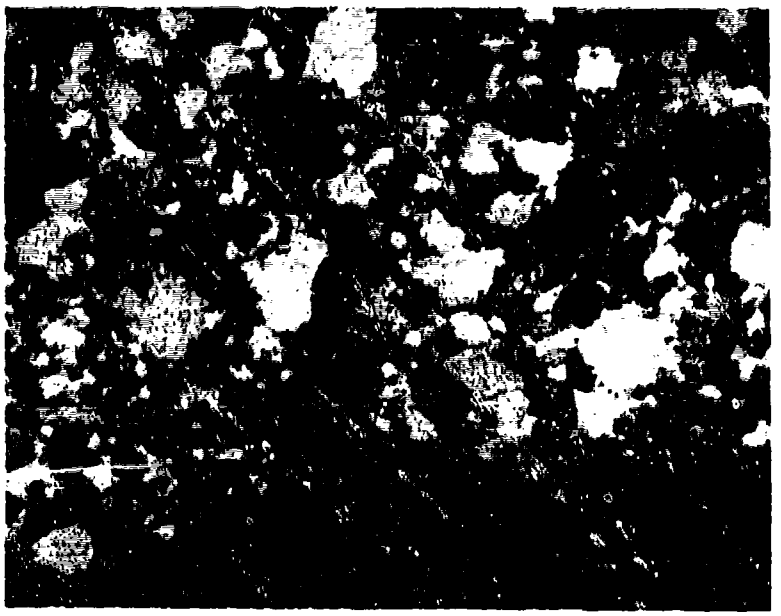

Figure 10. Typical post-test photomicrograph of IN-100 HIP at 2250°F (1250°C) for 5 hours; designation (2L46-1); tested at 1800°F (982°C); 248 ksi (170.9 N/mm^2). Deformation rate: 4.6×10^{-6} sec^{-1}. (200X)

Figure 11. Typical post-test photomicrograph of IN-100 HIP at 2200°F (1220°C) for 5 hours; designation (2L42-2); tested at 1900°F (1038°C); 148 ksi (111.8 N/mm^2). Deformation rate: 2.3×10^{-5} sec^{-1}. (200X)

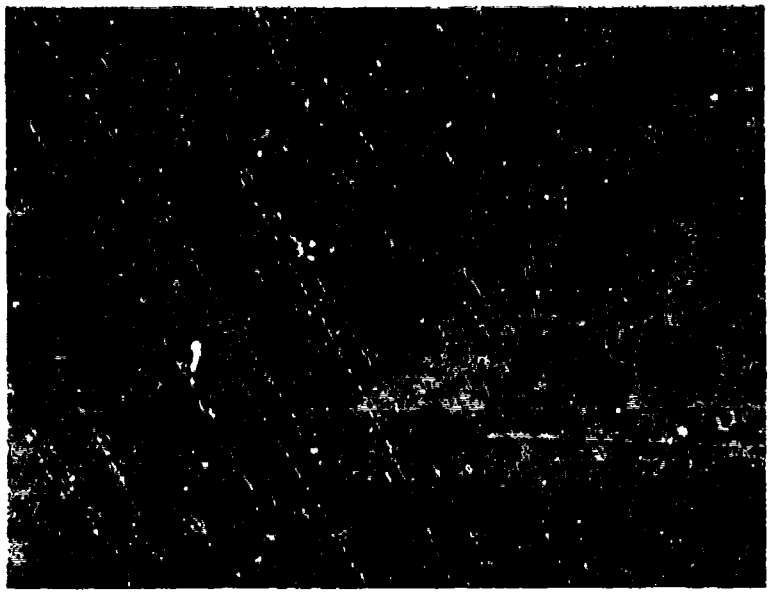

Figure 12. Typical post-test photomicrograph of IN-100 HIP at 2150°F (1195°C) for 2 hours; designation (2K12-4); tested at 1900°F (1038°C); 189 ksi (130.3 N/mm^2). Deformation rate: 2.7×10^{-4} sec^{-1}. (200X).

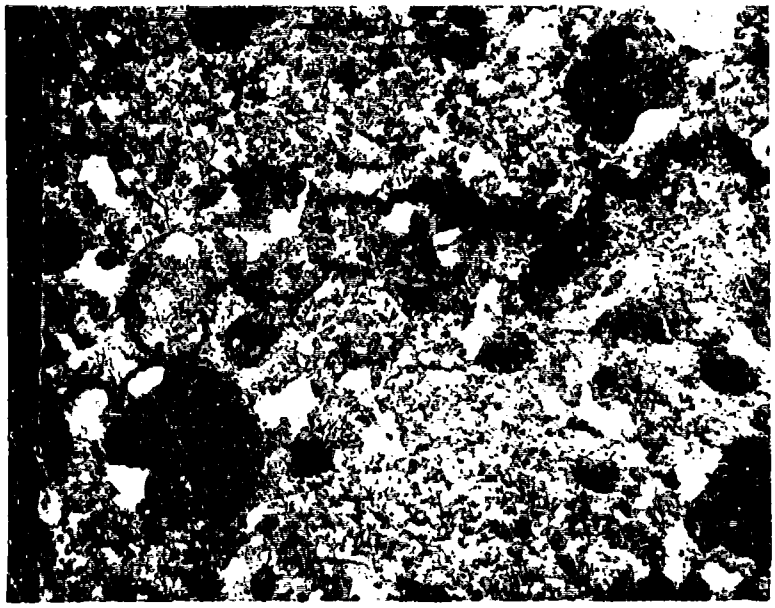

Figure 13. Typical post-test photomicrograph of IN-100 HIP at 2050°F (1140°C) for 5 hours; designation (3A53-3); tested at 1900°F (1038°C); 232 ksi (160 N/mm^2). Deformation rate: 2.0×10^{-3} sec^{-1}. (200X).

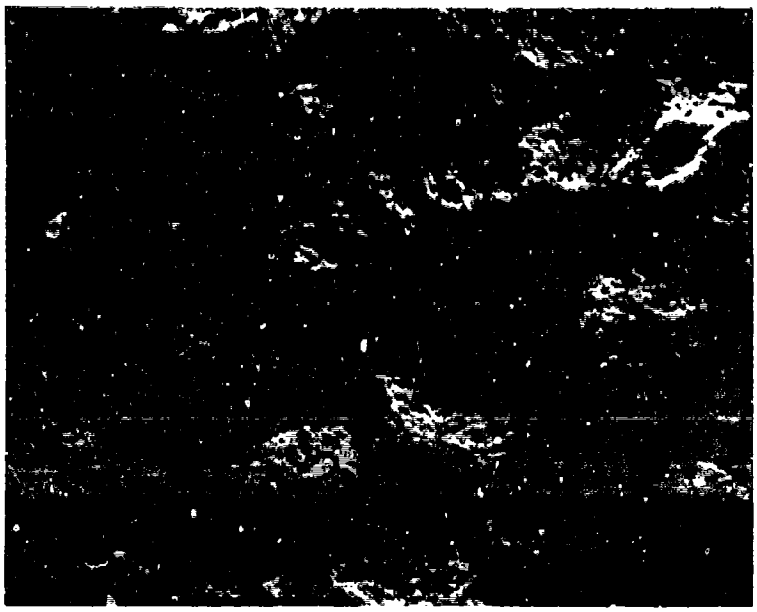

Figure 14. Typical SEM fractograph of IN-100 HIP at 2200°F (1220°C) for 5 hours; designation (2L52-4); tested at 2000°F (1093°C); 80 ksi (55 N/mm^2). Deformation rate: 1.4 X 10^{-4} sec^{-1}. (130X).

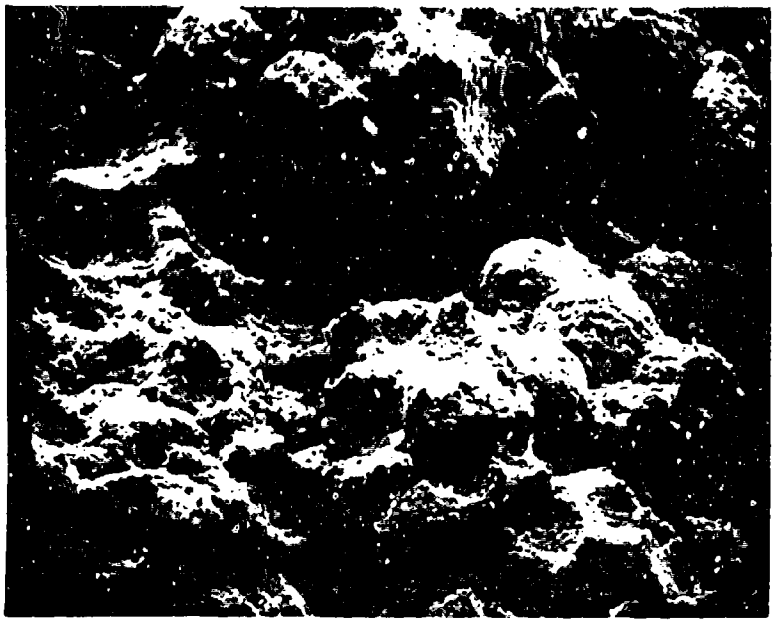

Figure 15. Typical SEM fractograph of IN-100 HIP at 2150°F (1195°C) for 2 hours; designation (2K12-4); tested at 1900°F (1038°C); 189 ksi (130.3 N/mm^2). Deformation rate: 2.7 X 10^{-4} sec^{-1}. (119X).

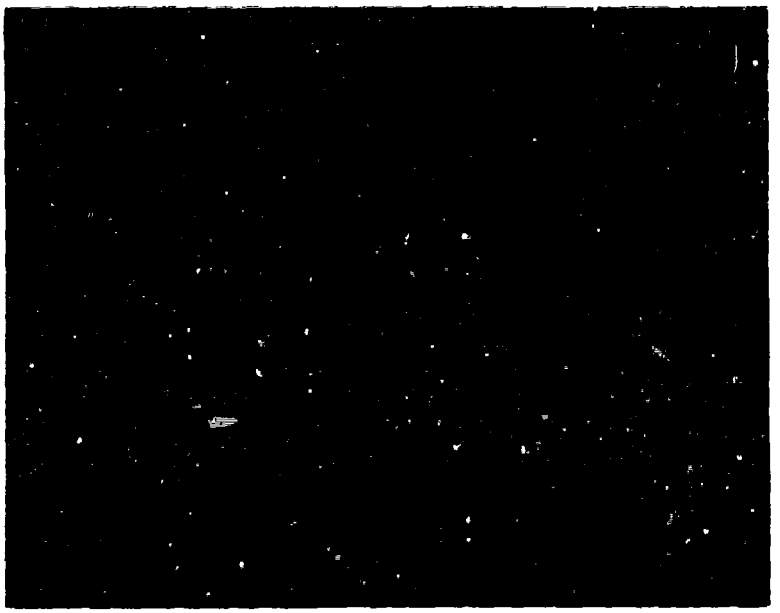

Figure 16. Typical post-test photomicrograph of IN-100 HIP at 2150°F (1195°C) for 2 hours; designation (2K12-4); tested at 1900°F (1038°C); 189 ksi (130.3 N/mm²). Deformation rate: 2.7 X 10^{-4} sec^{-1}. (1000X).

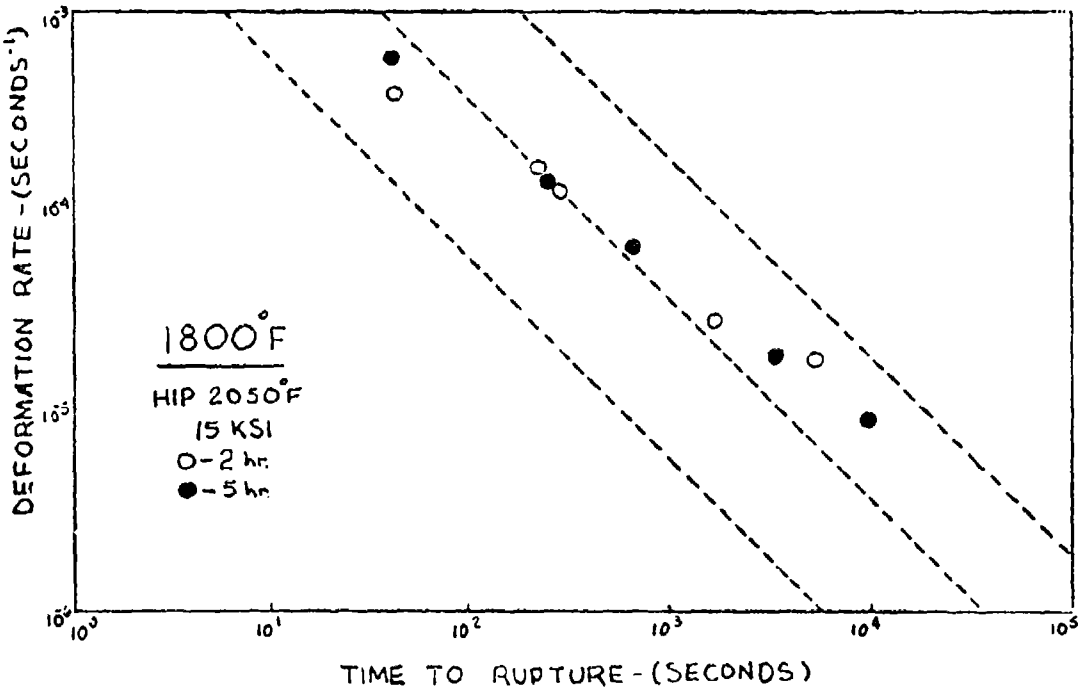

Figure 17. Typical rupture time vs. deformation rate plot (Monkman-Grant) for material HIP at 2050°F (1140°C) for 2 and 5 hours. Tested at 1800°F (982°C).

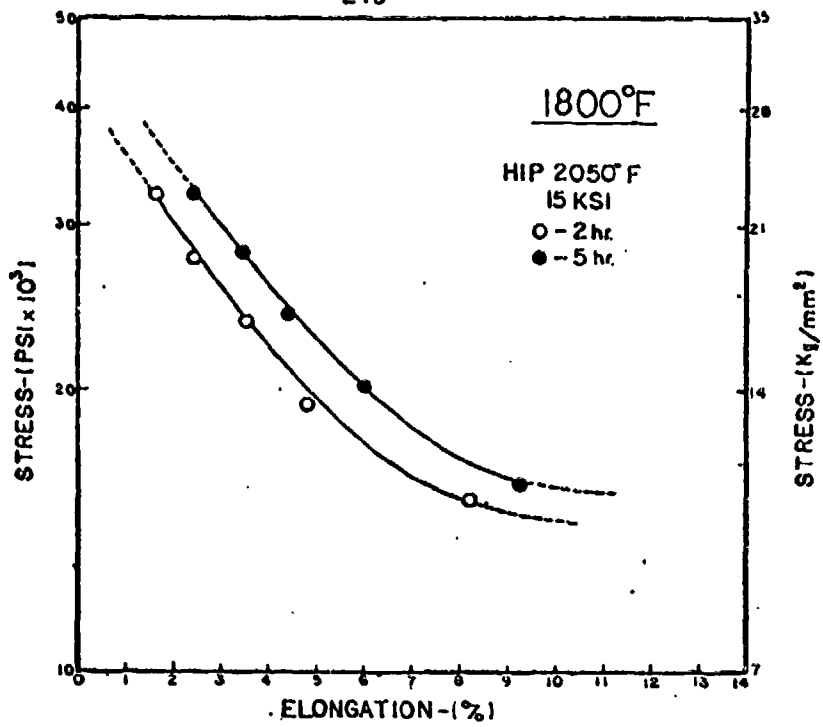

Figure 18. Stress vs. elongation curve for IN-100 HIP at 2050°F (1140°C) tested at 1800°F (982°C).

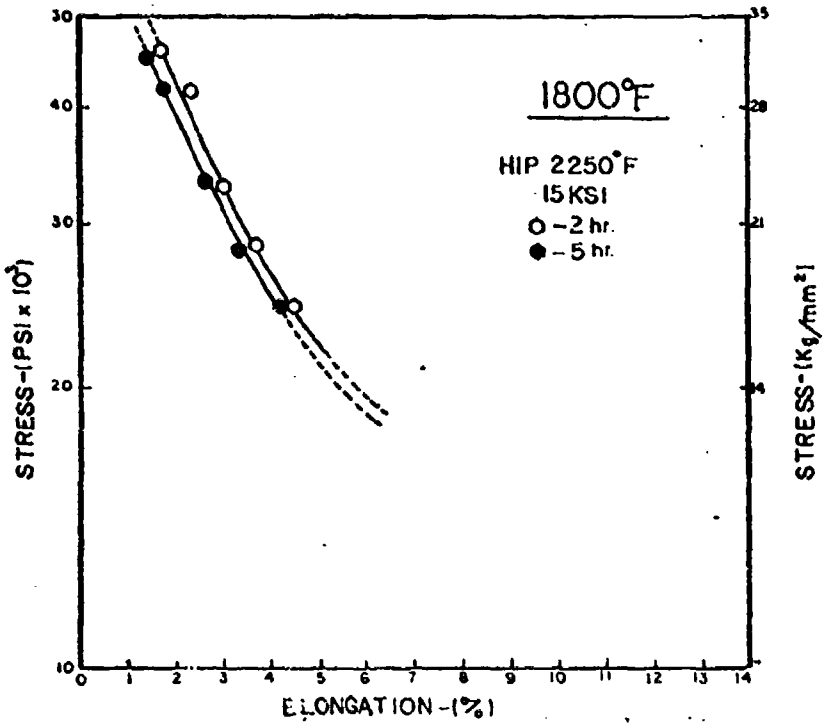

Figure 19. Stress vs. elongation curve for IN-100 HIP at 2250°F (1250°C) tested at 1800°F (982°C).

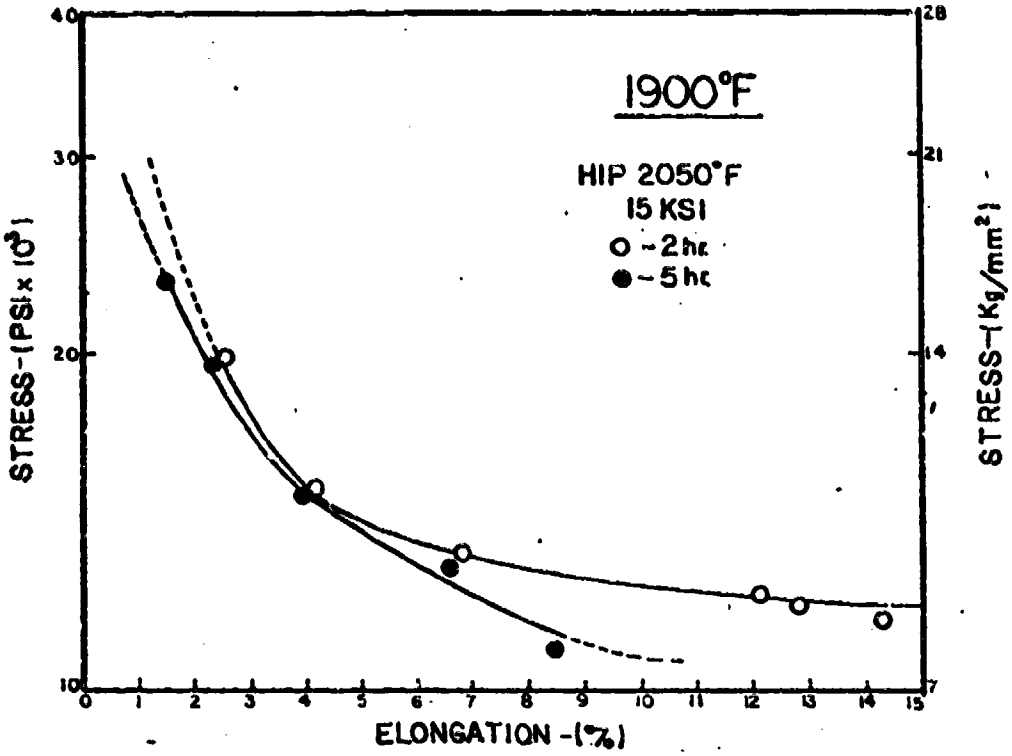

Figure 20. Stress vs. elongation curve for IN-100 HIP at 2050°F (1140°C) tested at 1900°F (1038°C).

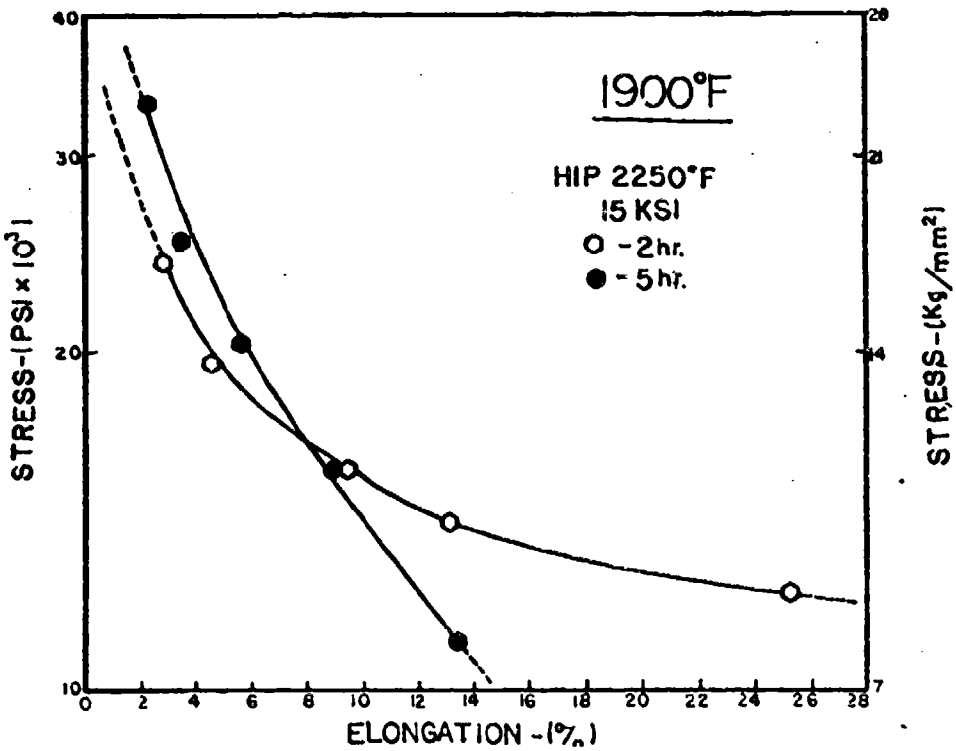

Figure 21. Stress vs. elongation curve for IN-100 HIP at 2250°F (1250°C) tested at 1900°F (1038°C).

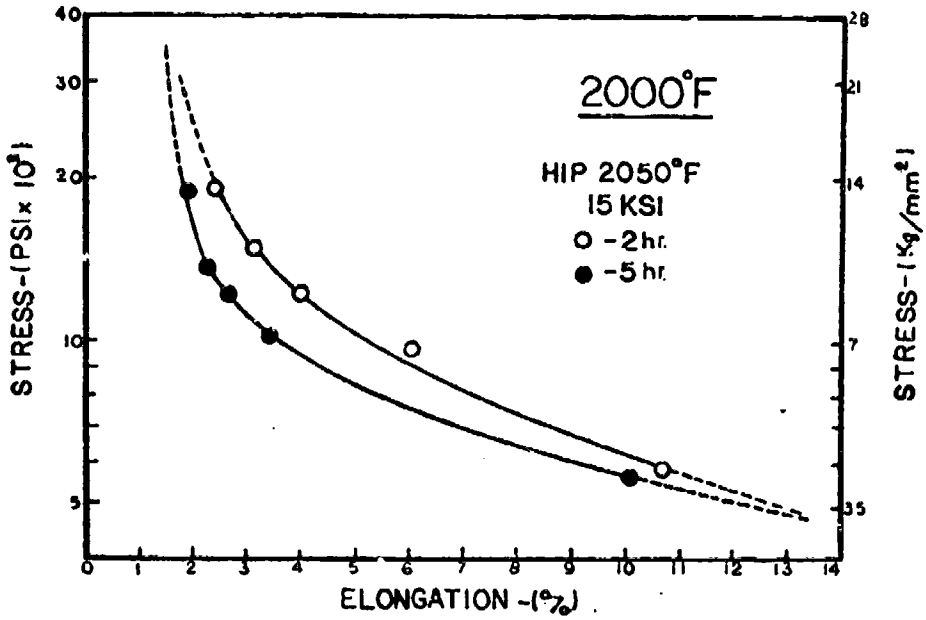

Figure 22. Stress vs. elongation curve for IN-100 HIP at 2050°F (1140°C) tested at 2000°F (1093°C).

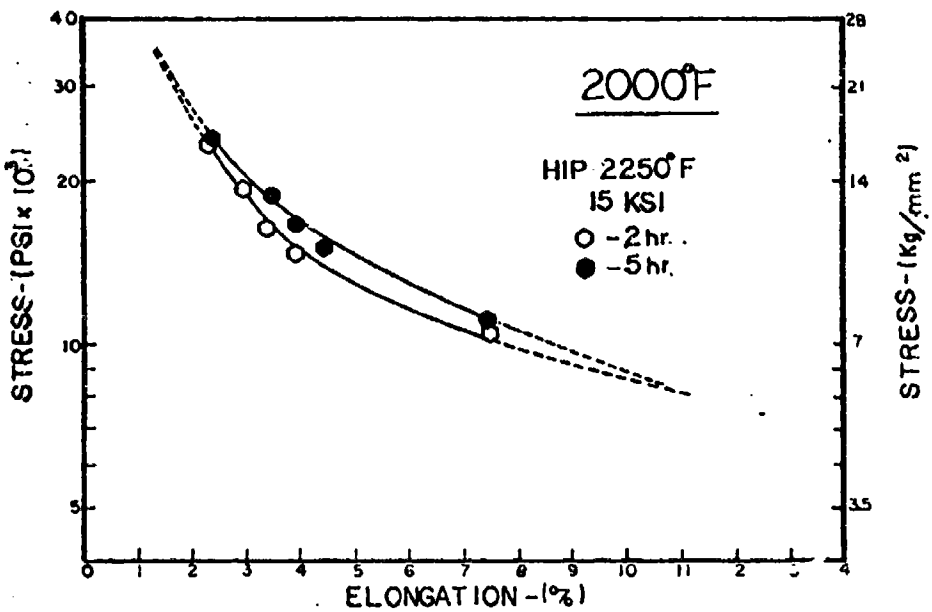

Figure 23. Stress vs. elongation curve for IN-100 HIP at 2250°F (1250°C) tested at 2000°F (1093°C).

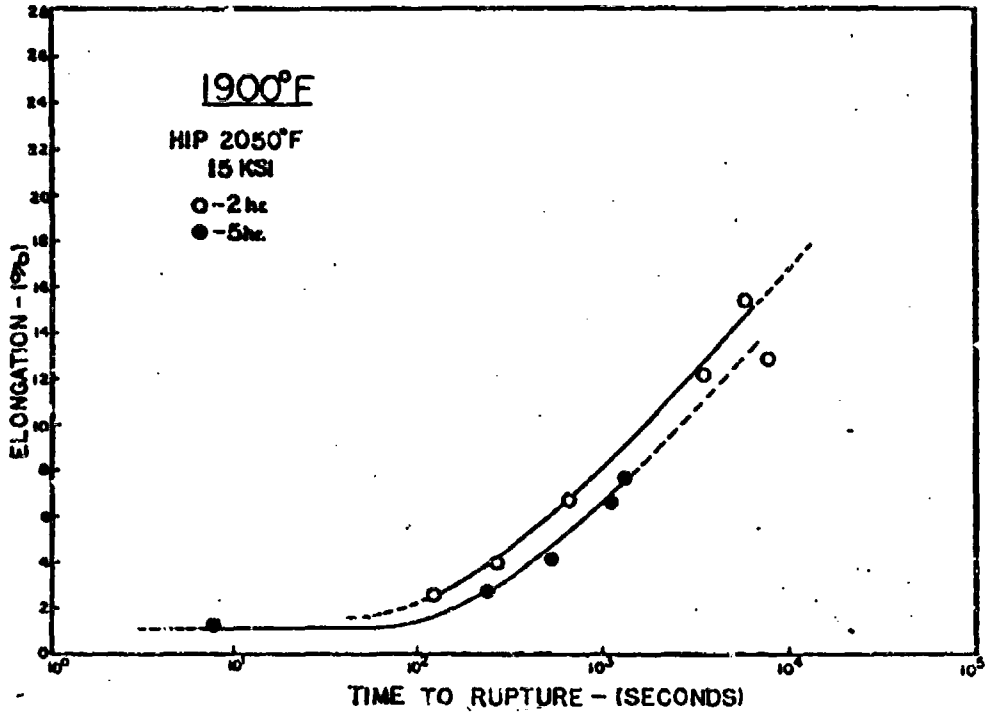

Figure 24. Elongation vs. rupture time curves for IN-100 HIP at 2050°F (1140°C) tested at 1900°F (1038°C).

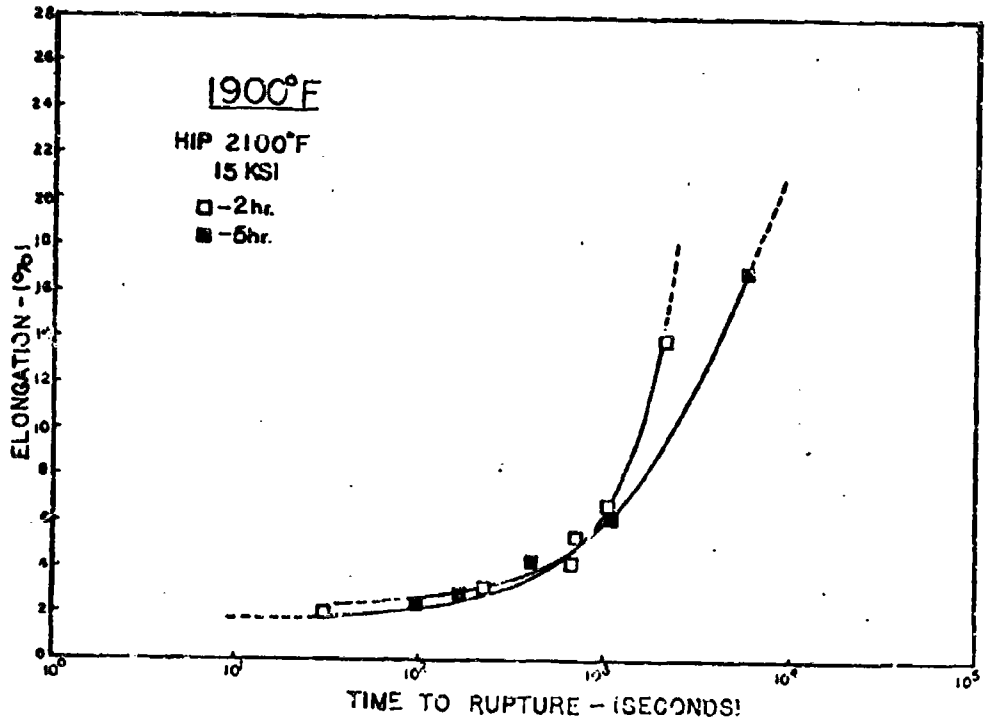

Figure 25. Elongation vs. rupture time curves for IN-100 HIP at 2100°F (1170°C) tested at 1900°F (1038°C).

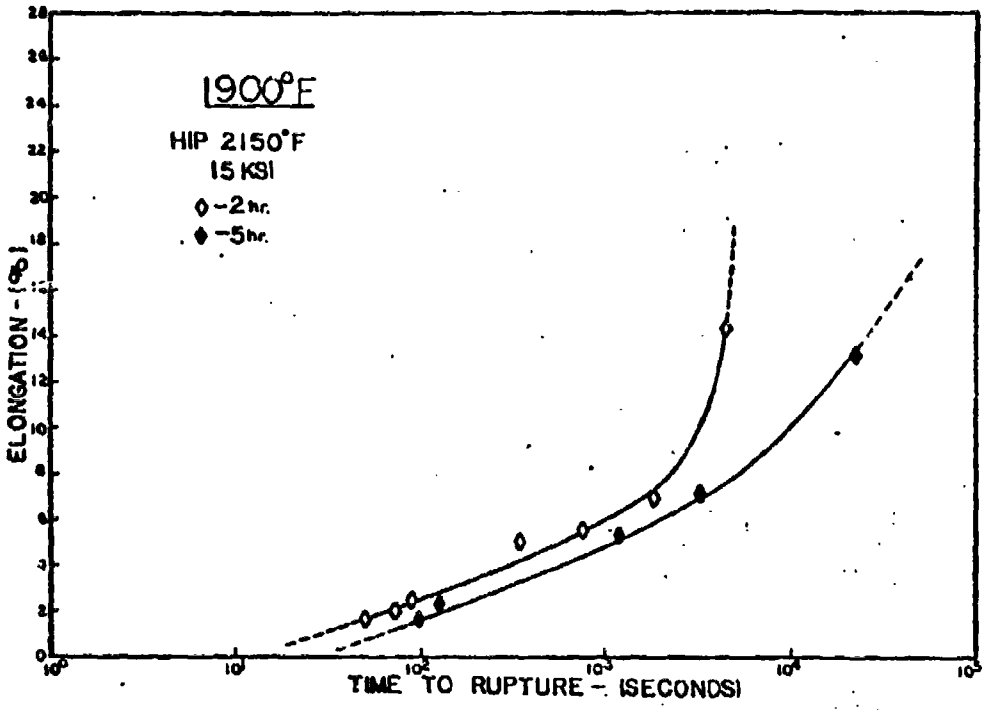

Figure 26. Elongation vs. rupture time curve for IN-100 HIP at 2150°F (1195°C)tested at 1900°F (1038°C).

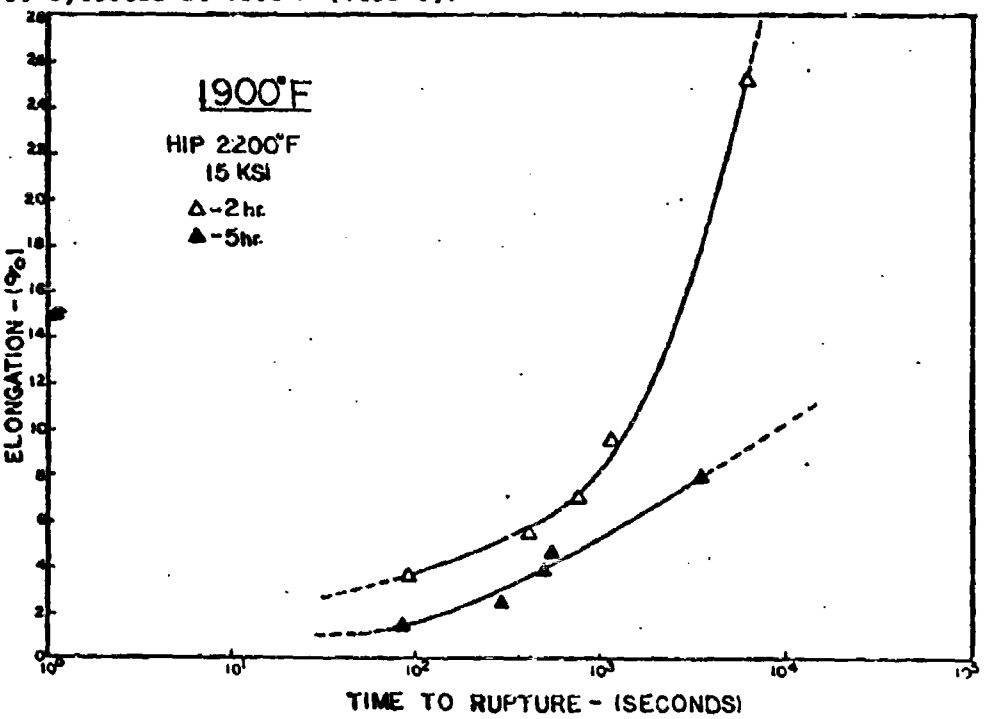

Figure 27. Elongation vs. rupture time curve for IN-100 HIP at 2200°F (1220°C) tested at 1900°F (1038°C).

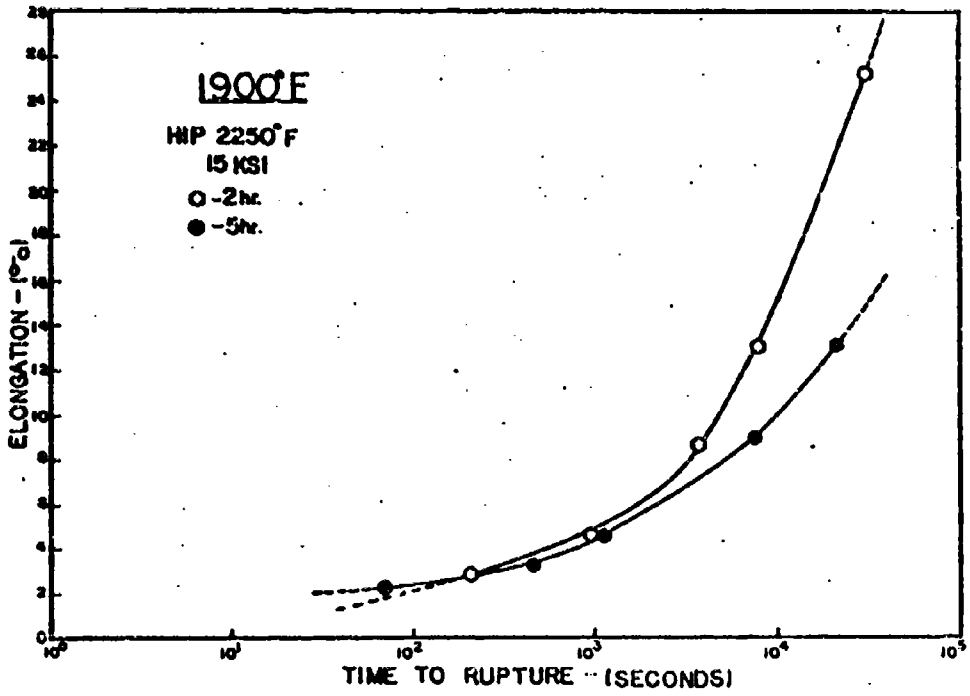

Figure 28. Elongation vs. rupture time curve for IN-100 HIP at 2250°F (1250°C) tested at 1900°F (1038°C).

Distribution of Plastic Strain and Triaxial Tensile Stress in Necked Steel and Copper Bars

A. S. Argon,(*) J. Im,(*) and A. Needleman(**)
Massachusetts Institute of Technology, Cambridge, Mass.

Abstract

The distributions of plastic strain and triaxial tensile stress have been computed by both an approximate method based on an extension of the Bridgman development and by a finite element analysis in inhomogeneously deforming bars after necking. The computations have been made for both initially smooth bars as well as bars having machined initial natural neck profiles, for two types of stress-strain behavior, modelling a spheroidized 1045 steel and a fully aged Cu-0.6% Cr alloy. The results of the finite element analysis show that the approximate method based on an extension of the Bridgman development is good only for slightly necked bars. In more acutely necked bars the Bridgman development is good only near the center of the neck. Some experimental results on strain distribution and on neck profiles are also presented.

(*) Department of Mechanical Engineering

(**) Department of Mathematics

I. *Introduction*

The distribution of stress and strain in a necked tensile bar has been of interest for some time not only for the purpose of obtaining true stress true strain curves for large plastic strains but also for the purpose of elucidating ductile fracture. In his pioneering study on the effect of pressure on fracture Bridgman[1] obtained an approximate solution for the distribution of stress and plastic strain across the plane of the neck, at the narrowest cross section for a given longitudinal profile radius of curvature of the neck in a round bar made of a non strain-hardening material. Experiments[1,2] have shown that the Bridgman solution is adequate for most applications in correcting stress strain curves in the post-necking range where the strain hardening rate has reached low values. The Bridgman solution has, however, also been used[2,3] for initially machined grooves in round bars with appreciable strain hardening rates. Clausing[4] has demonstrated that in such instances the axial plastic strain increments may no longer be uniform along the plane of the neck as is necessary for the Bridgman solution, making that solution no longer valid (for a discussion see McClintock[5]). There have been other solutions for plane strain configurations for non-hardening[1] and strain hardening materials[6] which, however, do not lend themselves as readily for experimental studies. Recently Chen[7] and Needleman[8] have independently obtained solutions for the necking of an initially round bar made of an elastic-plastic strain hardening material, from which it is possible to determine the changing shape of the neck with increasing extension of the bar as well as the current

stresses and strains throughout the bar. Of these two solutions that of Chen predicts radial stresses across the external boundary of the neck and is therefore, not fully reliable; on the other hand the solution of Needleman utilizing a finite element-numerical approach does not have such shortcomings.

As the accompanying paper[9] demonstrates, the necked region of a bar with its distribution of plastic strains (and therefore hardnesses) and triaxial tensile stresses, along the axis is a convenient plastic flow field for experimental studies of inclusion separation and plastic hole growth. It was therefore considered useful to obtain a number of solutions for the distribution of the plastic strain and triaxial tensile stress along the axis of a bar with a variety of initial neck contours and made of material having plastic stress strain curves of some common metals such as steel and copper. Here we describe the results of a set of such numerical computations using the approach of Needleman[8]. However, we develop first an approximate solution by extending the Bridgman development.

II. *Bounds for the Stress and Strain Distribution in the Neck Region of a Bar.*

Rhee and McClintock[10] have argued that useful bounds to the distribution of strains (and sometimes stresses) in a problem involving plastic flow of a strain hardening material can be obtained from two solutions for limiting behavior. In the first solution the material is modelled as a plastic rigid, non-hardening one with a yield stress resulting in the expansion of the same amount of plastic work as in the real stress strain curve over the range of plastic

strains of interest. In the second solution the material is modelled as a linearly hardening one with zero yield stress and a Poisson's ratio of 0.5 to simulate no change of volume. These solutions for the necked bar are readily obtainable for given neck dimensions and furnish bounds for cases in which the numerical solutions of the type to be presented below are unavailable.

A. *Non Strain Hardening, Rigid Plastic Material*

The distribution of the triaxial tensile stress along the axis of the bar in a non-hardening rigid plastic material with yield stress Y_0 is readily obtained by the method of Bridgman in which it is assumed that the surfaces of constant principal stress in the region of the neck have uniform curvature as shown in Fig. 1. The resulting distribution of triaxial stress σ_T, along the axis of the specimen a distance z away from the plane of the neck is then given by (see Appendix)

$$\frac{\sigma_T}{Y_0} = \frac{1}{3} + \ln\left(1 + \frac{a}{2R}\right) - \frac{z^2\left(2 + \ln\left(1 + \frac{a}{2R}\right)\right)}{a^2 + 2aR + z^2} \qquad (r = 0) \qquad [1]$$

where R is the minimum longitudinal (profile) radius of curvature at the neck and, a the radius of the narrowest portion of the neck. The expression given in Eq. [1] developed on the assumption that the principal stress surfaces are portions of spheres with decreasing radius of curvature going away from the plane of the neck will hold only over the region of the neck in which the curvature of the external profile remains concave outward. This will be at most only over one radius a along the axis. The distribution of the triaxial tensile stress along a radial line in the plane of the neck, as given

initially by Bridgman is

$$\frac{\sigma_T}{Y_o} = \frac{1}{3} + \ln\left(\frac{a^2 + 2aR - r^2}{2aR}\right) \qquad (z = 0) \qquad [2]$$

As is well known, the triaxial tensile stress in the Bridgman solution is maximum at the center of the neck and drops to lower values along both a radial line and an axial line away from the center.

A good measure for the local equivalent plastic strain increment along the axis in the neck region can be obtained from the reduction of net area of a principal strain surface as shown in Fig. 1. Point z_o along the axis and lying on a principal surface of radius of curvature R_o' moves after straining to a new point z_1 lying on another principal surface of radius of curvature R_1' obeying the constraint that the volume bounded between the plane of the neck and the principal strain surfaces before and after straining is constant. Then the equivalent plastic strain at the final point z_1 along the axis is given by

$$\varepsilon^p = \ln\left[\frac{(R_o')^2(1 - \cos\alpha_o)}{(R_1')^2(1 - \cos\alpha_1)}\right] \qquad [3]$$

where the angles α_1 and α_o obtained from the tangents to the external surface at the points of intersection of the final and initial principal strain surfaces can be readily obtained from a graphical construction, once the initial position z_o corresponding to a final position z_1 is found from the constraint of constant enclosed volume mentioned above. The same restriciton discussed above in connection with Eq. [1] also applies to Eq. [3].

B. *Linearly Hardening Material with Zero Yield Stress*

The distribution of triaxial tensile stress along the axis of the bar for a linearly hardening material can be obtained directly from the theory of stress concentrations in circumferentially grooved elastic bars given by Neuber[11] and is

$$\frac{\sigma_T}{\sigma_0} = \frac{C}{\sqrt{1+\left(\frac{z}{\bar{a}}\right)^2}} \qquad (r = 0) \qquad [4]$$

where

$$C = \frac{1 + \frac{a}{R} + \sqrt{1 + \frac{a}{R}}}{2\left(2 + \frac{a}{R} + \sqrt{1 + \frac{a}{R}}\right)} \qquad [5a]$$

$$\bar{a} = \frac{a\sqrt{1 + \frac{a}{R}}}{\sqrt{\frac{a}{R}}} \quad \text{, and} \qquad [5b]$$

$\sigma_0 = \frac{P}{\pi a^2}$ is the average ligament stress.

The distribution of triaxial tensile stress along a radial line in the plane of the neck, also given by Neuber[11] is

$$\frac{\sigma_T}{\sigma_0} = \frac{C}{\sqrt{1-\left(\frac{r}{\bar{a}}\right)^2}} \qquad (z = 0) \qquad [6]$$

Examination of Eqs. [4] and [6] shows that for a linear material the largest triaxial tensile stress occurs at the outer surface of the neck, drops along a diameter to a minimum at the center of the neck and continues to drop from this minimum value to still lower values along

the axis going away from the plane of the neck.

Comparing the linear material to the non-hardening material, it is found that the triaxiality (the ratio of the triaxial tensile stress to the flow stress or the average ligament stress) is normally somewhat higher for the linear material on the surface of the neck while in the center of the neck the non-hardening material develops the higher triaxiality.

In most ductile structural materials, the strain hardening rate at room temperature decreases rapidly with increasing plastic strain, making the bound based on the non-hardening material a closer representation of reality than that based on the linear material.

III. *Experiments on Neck Profiles*

As already mentioned above the Bridgman solution requires that the axial plastic strain increments are constant at every point on the plane of the neck. Clausing[4] recognized that in bars with an initially machined profile this need not be true. Norris[12] has demonstrated that a test for the uniformity of the axial strain through the plane of the neck is that the ratio of the increments of plastic strain at the surface of the neck must be

$$\frac{d\varepsilon^p_{zz}}{d\varepsilon^p_{\theta\theta}} = -2 . \qquad [7]$$

at all times. If the absolute value of this ratio is larger than 2 then the axial plastic strain increment in the interior is less than

that on the surface and vice-versa. Morris found that in bars with circumferential grooves with constant radius of curvature the absolute value of the ratio given in Eq. [7] at the start of straining was always larger than 2 and differed from 2 the more, the larger the inital a/R ratio (Fig. 1). Upon straining, the ratio asymptotically approached 2.

The departure from a condition of uniform axial strain in bars with initially machined longitudinal profiles is firstly a result of an initial uniform hardness and secondly a departure of the machined profile from the natural neck geometry. While nothing can be done about the uniform initial hardness, it is possible to start with a machined natural neck profile to eliminate the second cause. In a first step to test this possibility, a number of natural neck profiles were carefully measured on a very ductile necked copper bar. From such measurements it was determined that the natural neck profile can be described to a high degree of accuracy by an empirical equation of the form[13]:

$$r = a_0 \left[1 - V \left(\sqrt{1 + \frac{1}{\left(\frac{z}{a_0}\right)^2 + V^2}} - 1 \right) \right] \qquad [8]$$

with

$$V = \frac{\frac{a}{a_0}\left(2 - \frac{a}{a_0}\right)}{2\left(1 - \frac{a}{a_0}\right)} \qquad [9]$$

where a and a_o are the radius at the neck and the uniform radius of the shoulder at a great distance from the neck respectively.(*)

Two OFHC copper specimens were machined to an a/R ratio of

0.5 with natural neck profiles obtained according to Eq. [8]. They were then given a mechanical surface polish and were provided with a carefully inscribed square grid at the neck region, and were subsequently annealed in vaccuum. These specimens were then strained a number of steps further and the changing dimensions of the grid were photographically measured. Figure 2 shows these measurements plotted on logarithmic axes where they produce straight lines the slopes of which give the ratio of the plastic strain increments on the surface. Considering that the material is of uniformly low initial hardness and that it will undergo considerable strain hardening in the initial phases of deformation it can be concluded that the natural neck profile has reversed the trend discussed by Norris.[12] Thus, the Bridgman analysis applied to specimens with initial natural neck profiles should give the best approximate procedure for obtaining the distribution of stresses and strains in a ductile fracture study—short of obtaining a numerical solution of the type to be discussed below.

In the accompanying study on inclusion separation Argon and Im[9] have found it necessary to obtain the stress and strain distribution in necked bars at points along the axis, too far removed from the plane of the neck so that the stress and strain distributions given by Eqs. [1] and [3] become unreliable. It was necessary therefore to obtain more accurate numerical solutions by means of the analysis of Needleman.[8]

(*) In the preparation of the paper a different functional form for the neck profile due to Dondik [14], has come to our attention which gives equally good agreement for the profile as our form presented above. Since neither form has any basis in theory it is difficult to prefer one over another.

IV. *Numerical Computation of the Stress and Strain Distribution in Necked Bars of Steel and Copper*

A. *Stress Strain Curves for Steel and Copper*

In the numerical analysis of Needleman the stress strain curve of a metal is modelled as

$$\varepsilon = \begin{cases} \varepsilon_y\left(\frac{\sigma}{Y_0}\right) & (\sigma \leq Y_0) \\ \varepsilon_y\left(\frac{\sigma}{Y_0}\right)^n & (\sigma \geq Y_0) \end{cases} \qquad [10]$$

where $\underline{\varepsilon_y} = \underline{Y_0}/E$ is the elastic strain at yield and $\underline{Y_0}$ is the yield stress in tension. It is understood that stresses and strains given by Eq. [10] can stand for equivalent stress and equivalent strain in a $\underline{J_2}$ flow theory with isotropic strain hardening.

The experimentally obtained stress strain curves at room temperature for a spheroidized 1045 steel, and a copper - 0.6% chromium alloy are shown plotted on logarithmic coordinates in Figs. 3 and 4. The heat treatment procedure and state of microstructure is discussed in the accompanying paper by Argon and Im.[9] It is sufficient to point out here that in both materials the preciptate or inclusion spacing was so large (average particle spacing in excess of 5×10^{-4} cm) that these particles could not have contributed more than a maximum of 2% to the flow stress. Hence the stress strain curves in Figs. 3 and 4 are considered to be a good representation of the polycrystalline behavior of these materials in pure form.

Figures 3 and 4 show that the experimental stress strain curves for low carbon steel and copper do not completely fit the form of Eq. [10] over the entire range, but good fits over parts of the entire range can be obtained by appropriate choices for $\underline{\varepsilon_y}$ and $\underline{n}$ in Eq. [10]. Thus for steel a choice of $\underline{\varepsilon_y} = 0.0072$ and $\underline{n} = 8$ (used by Needleman[8])

appears best suited for the low strain range while a choice of $\varepsilon_y = 0.0094$ and $n = 4$ is best for intermediate and large strains. Correspondingly for copper while a choice of $\varepsilon_y = 0.0072$ and $n = 3$ is good for intermeidate strains, a choice of $\varepsilon_y = 0.00416$ and $n = 2.5$ is well suited over the entire range.(*)

B. *Numerical Results for Stress and STrain Distributions in Smooth Bars and Bars with an Initial Necking Profile*

The numerical, finite element technique used by Needleman[8] for initially smooth bars to compute the shape of the necked region and the stress and strain distribution in it after bifurcation (for the details of the original solution see Needleman[8]) was refined and generalized to deal with bars with arbitrary initial profiles. The refinement consisted of decreasing the grid size of the initial computation down to half its value while the generalization involved the use of the empirical profile curves given by Eqs. [8] and [9] to determine the nodal points in the finite element grid for two initial a/R ratios (Fig. 1) of 0.5 and 1.0. The two finite element grids obtained in this procedure for these two profiles are shown in Figs. [5a] and [5b]. The finite element grid was chosen long enough to make the deformations and stress distribution in the neck region insensitive to the details of the boundary conditions away from the neck. As found earlier by Needleman, this can be comfortably assured by a length to radius ratio of 4. The boundary conditions used in the computations were, uniform distribution of σ_{zz} away from the neck, zero radial displacement along the axis, zero axial displacement along the plane of the neck and zero σ_{rr} along the outer surface. In all

(*) It must be emphasized here that these yield strains are chosen for the best fit to a power law. The actual yield strains are different, they can be obtained from Tables I-IV by dividing the given yield stresses by the appropriate moduli.

computations the length dimensions were normalized with the inital radius a_o away from the neck, and all stresses were normalized with the yield stress in tension Y_o. For precision, each rectangular element shown in Fig. [5] was further divided into four triangles by connecting the nodes, ar the computations were continued for as long as proper convergence was possible.

Two sets of three computations were made for initial a/R ratios of 0, 0.5 and 1.0, for steel and copper.

1. *Results for Steel.*

The results of the finite element computations for steel for three initial a/R ratios are given in Tables I, II, and III where the distribution of equivalent plastic strain and triaxial tensile stress along the axis is tabulated for several stages of decreasing area ratio at the neck. These distributions are also shown graphically for several area ratios in Figs. 6-8. The broken curves have been obtained by graphical extrapolation. These figures show that the inhomogeneous distributions of st. and strain in the neck are quite localized. The dotted curves in F. labelled with primed numbers show the distribution of triaxial tensile stress computed by the extension of the Bridgman analysis according to Eq. [1] for a constant flow stress equal to the flow stress at the neck. Evidently when the necking is only slight the extended Bridgman analysis gives a good approximation of the actual distribution. When the neck gets more acute the extended Bridgman analysis overestimates the range of the zone of enhanced triaxial stress.

2. *Results for Copper*

The results of the finite element computations for copper for the same three inital a/R ratios are given in Tables IV, V, and VI

where again the distribution along the axis of equivalent plastic strain and triaxial tensile stress is tabulated for several stages of decreasing area ratio. These distributions of plastic strain and triaxial tensile stress along the axis are also shown in Figs. 9-11, which resemble closely the curves for steel.

V. *Discussion*

The extension of the Bridgman solution discussed in Sect. 2.1 where the material is modelled as non-hardening, and the linear hardening solution discussed in Sect. 2.2 where the material is assumed to have a negligible yield stress and linear hardening must now be compared with the finite element solution for a hardening material, presented in the last section. As argued by Rhee and McClintock[10] these two solutions will normally provide bounds for strain concentrations in materials with finite yield stress and non-linear strain hardening behavior. Although Rhee and McClintock furnished no proof for their assertion, all the examples which they cited in their work were in support of this rule. The developments in Sects 2.1 and 2.2 show that this rule which appears to hold for strain concentrations does not necessarily apply to stress concentrations in inhomogeneous plastic deformation, especially if the stresses have a strong component of triaxiality. Direct comparison of the extension of the Bridgman analysis for the distribution of triaxial stress along the axis with the results of the finite element computation demonstrates (see Fig. 6b) that this solution is rather good near the neck for not too acute neck profiles if the constant yield stress required in the solution is taken as the flow stress corresponding to the average

plastic strain across the plane of the neck. In comparison to the Bridgman solution the linear solution is rather poor and does not even parallel the actual triaxial stress distribution qualitatively.

Comparison of equivalent plastic strains at the center of the neck obtained by the finite element computation and shown in Figs. 6a-11a with the average plastic strain at the neck obtained from the area ratio shows that these computed strains are larger than the average strain for cases in which the bar was initially smooth ($(a/R)_i = 0$), (see Figs. 6a and 9a), and smaller than the average strain for cases in which the bar has an initial natural neck profile ($(a/R)_i > 0$) (See Figs. 7a, 8a, 10a, 11a). This difference is probably attributable to the initiation of yielding on the surface in the case of the bars with an initial profile. In all cases this difference which signifies a non-uniformity of strain across the neck is small and experimentally not readily observable (see Fig. 2), provided the bars have a natural neck profile.

The distribution of triaxial tensile stress along the axis as given in Figs. 6b - 11b shows this stress in units of the initial yield stress Y_o. Since the local flow stress has risen as a result of strain hardening this ratio does not represent the actual triaxiality, i.e the ratio of the local equivalent flow stress Y. The actual triaxiality for all six computed cases is shown plotted in Figs. 12a - 12f, together with the actual magnitudes of the local triaxial stress component and the local equivalent flow stress. These figures show that the triaxiality is accentuated to a value well above unity at the center of the neck for the cases where $(a/R)_i = 1$. It must be observed paranthetically here that the curves in Figs.

12a - 12f represent stages of additional extension of these initial geometries corresponding to a/a_1 ratios given in the figure captions. The triaxiality decreases steadily along the axis and near the shoulders drops below the level of average triaxiality existing in the smooth portions of the bar away from the neck.

The changing triaxiality along the axis of the necked bar is of interest in initiation of holes from inclusions and their subsequent growth leading to ductile fracture. This aspect of the distribution will be used in the accompanying study of Argon and Im[9] to test possible criteria for separation of non-deforming inclusions from the deforming ductile matrix.

Acknowledgement

This work was supported by both NSF under Grant GK 1875X and ARPA under Contract DAHC 15-70C-0283. During the course of this study we have had many profitable discussions with Professor F. A. McClintock.

References

1. P. W. Bridgman: Studies in Large Plastic Flow and Fracture, p.9, McGraw-Hill Book Company, New York, 1952.
2. E. R. Marshall and M. C. Shaw: Trans. ASM., 1952, vol. 44, p. 705.
3. H. E. Alpaugh, Jr.: Ivestigation of the Mechanisms of Failure in the Ductile Fracture of Mild Steel, SB Thesis, M.I.T., Dept. of Mech. Eng., 1965.
4. D. P. Clausing: The Tensile Fracture of Steel, Ph.D. Thesis Calif. Inst. Tech., 1966.

5. F. A. McClintock: in Fracture (H. Liebowitz, ed.) vol. 3, p. 106. Academic Press, New York, 1971.

6. J. E. Neimark: J. Appl. Mech., 1968, vol. 35, p. 111.

7. W. H. Chen: Int. J. Solids Structures, 1971, vol. 7, p. 685.

8. A. Needleman: J. Mech Phys. Solids, 1972, vol. 20, p. 111.

9. A. S. Argon, and J. Im: Met. Trans. this issue.

10. S. S. Rhee, and F. A. McClintock: in Proc. Fourth U.S. Nat. Cong. Appl. Mech., vol. 2, p. 1007, ASME, New York, 1962.

11. H. Neuber: Theory of Notch Stresses (English translation) p. 84, J. W. Edwards, Ann Arbor, Mich., 1946.

12. K. C. Norris: Strain in the Neck of a Tensile Specimen (also quoted in Ref- 5) S. M. Thesis, M.I.T. Dept. of Mech. Eng., 1967.

13. J. Im: Inclusion Separation in Plastic Deformation, S.M. Thesis, M.I.T., Dept. of Mech. Eng., 1971.

14. I. G. Dondik: Problemy Prochnosti, 1970, vol 8, p.54. (translation in Strength of Materials, March 1972, p937, Consultants Bureau).

Appendix

Extension of the Bridgman Solution for Triaxial Stress Distribution along the Axis of a Necked Bar

Referring to Fig. 1 and considering, after Bridgman, that the surfaces of constant principal stress are portions of spheres or rotationally symmetric surfaces having segments of circles as generators, the differential equation of equilibrium in the axial direction can be readily written as[13]

$$\frac{\partial \sigma_{zz}}{\partial z} + \frac{1}{R'}\left(2\sigma_{zz} - \sigma_{rr}\right) = 0 \qquad \text{[A1]}$$

where R' represents the radius of curvature of a principal stress

contour as shown in Fig. 1.

The Mises yield condition gives

$$\sigma_{rr} - \sigma_{zz} = \pm Y_o \qquad [A2]$$

Furthermore from the assumption of the shape of the principal stress surfaces, the curvature of the principal stress surface at any point z away from the plane of the neck, is by geometry

$$\frac{1}{R'} = \frac{2z}{z^2 + a(2R + a)} \qquad [A3]$$

where a is the radius of the neck at the plane of the neck and R the profile radius of curvature of the neck.

Since the axial stress σ_{zz} at the center of the neck is known from the original solution of Bridgman, the differential equation in Eq. [A1] can be directly integrated along the axis (r=o) after substitution of Eqs. [A2] and [A3]. The result is

$$\frac{\sigma_{zz}}{Y_o} = 1 + \ln\left(1 + \frac{a}{2R}\right) - \frac{z^2\left(2 + \ln\left(1 + \frac{a}{2R}\right)\right)}{\left(a^2 + 2aR + z^2\right)} \qquad [A4]$$

Noting that along the axis $\sigma_{rr} = \sigma_{\theta\theta}$ and that σ_{rr} is directly obtainable from Eq [A2] once σ_{zz} is known, the triaxial stress can be readily computed and is the expression given in Eq. [1].

As already mentioned in Sect. 2, this extension of the Bridgman solution is only good near the plane of the neck where surfaces of constant principal stress can be approximated by portions of spherical surfaces. Comparison of this solution with the finite element solution

shows (Fig. 6b) that although this is satisfied for necks with small a/R ratios, up to $z/a \approx 1$, for more acute necks with higher a/R ratios the solution begins to break down for $z/a \approx 0.25$.

Table I. Equivalent Plastic Strain and Triaxial Tensile Stress Distribution in a 1045 Steel Bar

$(a/R)_i = 0$, $n = 8$, $\varepsilon_y = 0.0072$, $Y_o = 68.6$ ksi.

I			II			III			IV			V		
$a/a_i = .8867$			$a/a_i = .8178$			$a/a_i = .7878$			$a/a_i = .7774$			$a/a_i = .7668$		
z/a_o	$\bar{\varepsilon}^p$	σ_T/Y_o	z/a_o	$\bar{\varepsilon}^p$	σ_T/Y_o	z/a_o	$\bar{\varepsilon}^p$	σ_T/Y_o	z/a_o	$\bar{\varepsilon}^p$	σ_T/Y_o	z/a_o	$\bar{\varepsilon}^p$	σ_T/Y_o
.059	.251	.678	.070	.429	.993	.076	.508	1.158	.078	.536	1.220	.080	.566	1.284
.170	.249	.672	.209	.419	.959	.225	.493	1.103	.232	.519	1.155	.238	.545	1.210
.292	.246	.661	.346	.402	.896	.372	.466	1.001	.382	.487	1.037	.392	.508	1.080
.408	.241	.644	.480	.378	.810	.515	.430	.867	.527	.446	.884	.540	.462	.900
.524	.235	.623	.611	.351	.710	.652	.388	.716	.666	.400	.713	.680	.411	.707
.638	.228	.598	.724	.321	.602	.783	.347	.558	.799	.355	.537	.814	.361	.508
.752	.220	.570	.853	.293	.507	.909	.309	.402	.926	.312	.362	.942	.315	.316
.865	.212	.540	.983	.265	.386	1.031	.274	.249	1.048	.275	.191	1.064	.277	.128
.977	.203	.510	1.100	.241	.284	1.149	.244	.106	1.166	.245	.035	1.182	.245	-.037
1.088	.194	.480	1.219	.219	.186	1.264	.221	-.015	1.280	.220	-.083	1.297	.220	-.141
1.198	.186	.451	1.326	.202	.100	1.376	.201	-.081	1.392	.201	-.126	1.409	.201	-.165
1.307	.178	.423	1.437	.186	.041	1.486	.186	-.084	1.503	.185	-.116	1.519	.185	-.144

Table II. Equivalent Plastic Strain and Triaxial Tensile Stress Distribution in a 1045 Steel Bar

$(a/R)_i = 0.5$, $n = 4$, $\varepsilon_y = 0.0094$, $Y_o = 50$ksi.

I $a/a_i = .8241$			II $a/a_i = .7754$			III $a/a_i = .7251$			IV $a/a_i = .6754$			V $a/a_i = .6473$		
a/z_o	$\bar{\varepsilon}^p$	σ_T/Y_o	z/a_o	$\bar{\varepsilon}^p$	σ_T/Y_o	z/a_o	$\bar{\varepsilon}^p$	σ_T/Y_o	z/a_o	$\bar{\varepsilon}^p$	σ_T/Y_o	z/a_o	$\bar{\varepsilon}^p$	σ_T/Y_o
.050	.355	2.079	.056	.463	2.525	.063	.580	3.021	.071	.702	3.520	.076	.773	3.948
.149	.332	1.961	.165	.426	2.327	.184	.520	2.710	.206	.612	3.082	.220	.664	3.351
.246	.293	1.741	.270	.363	1.981	.298	.427	2.199	.329	.480	2.384	.348	.509	2.484
.339	.245	1.467	.370	.291	1.575	.403	.327	1.634	.438	.353	1.646	.459	.364	1.650
.431	.196	1.175	.464	.223	1.169	.500	.239	1.092	.537	.248	.970	.559	.252	.903
.520	.150	.899	.556	.165	.798	.592	.169	.616	.629	.171	.409	.652	.172	.300
.608	.112	.653	.645	.116	.478	.682	.118	.241	.719	.117	.039	.741	.117	-.056
.696	.081	.450	.733	.082	.237	.770	.082	.044	.807	.080	-.102	.829	.079	-.173
.785	.058	.285	.822	.057	.107	.858	.055	-.030	.895	.054	-.137	.917	.053	-.189
.875	.040	.182	.911	.039	.057	.948	.038	-.041	.984	.036	-.119	1.006	.036	-.159
.967	.028	.132	1.003	.027	.044	1.039	.026	-.027	1.076	.024	-.085	1.098	.024	-.115
1.060	.020	.097	1.096	.019	.036	1.133	.017	-.016	1.169	.016	-.060	1.191	.015	-.083
1.156	.014	.084	1.192	.013	.040	1.228	.012	.002	1.265	.011	-.032	1.286	.011	-.051
1.255	.010	.082	1.291	.010	.051	1.327	.009	.021	1.363	.008	-.006	1.385	.008	-.021

Table III. Equivalent Plastic Strain and Triaxial Tensile Stress Distribution in a 1045 Steel Bar

$(a/R)_i = 1.0, \quad n = 4, \quad \varepsilon_y = 0.0094, \quad Y_o = 50\text{ksi}$

I			II			III			IV			V			VI			VII		
$a/a_i = .6401$			$a/a_i = .6512$			$a/a_i = .6628$			$a/a_i = .7111$			$a/a_i = .7741$			$a/a_i = .8116$			$a/a_i = .8478$		
z/a_o	$\bar{\varepsilon}^p$	σ_T/Y_o	z/a_o	$\bar{\varepsilon}^p$	σ_T/Y_o	z/a_o	$\bar{\varepsilon}^p$	σ_T/Y_o	z/a_o	$\bar{\varepsilon}^p$	σ_T/Y_o	z/a_o	$\bar{\varepsilon}^p$	σ_T/Y_o	z/a_o	$\bar{\varepsilon}^p$	σ_T/Y_o	z/a_o	$\bar{\varepsilon}^p$	σ_T/Y_o
.056	.719	4.815	.055	.693	4.558	.055	.658	4.413	.048	.553	3.728	.042	.414	3.030	.039	.340	2.637	.036	.271	2.278
.164	.606	4.008	.160	.586	3.867	.156	.566	3.752	.141	.485	3.310	.124	.377	2.784	.116	.313	2.467	.108	.251	2.154
.260	.448	2.928	.254	.439	2.887	.249	.429	2.843	.228	.383	2.657	.204	.314	2.362	.191	.267	2.157	.179	.219	1.941
.345	.308	2.022	.339	.304	2.013	.333	.300	2.007	.309	.280	1.976	.281	.247	1.884	.265	.213	1.787	.250	.180	1.664
.423	.202	1.246	.417	.200	1.258	.411	.199	1.249	.386	.192	1.349	.356	.173	1.411	.338	.160	1.404	.321	.135	1.361
.499	.128	.620	.492	.128	.643	.486	.128	.672	.461	.126	.808	.429	.121	.978	.411	.114	1.040	.393	.099	1.061
.578	.080	.190	.567	.080	.215	.561	.079	.243	.535	.080	.382	.504	.080	.604	.485	.078	.714	.466	.073	.784
.649	.049	-.029	.643	.049	-.010	.637	.050	.012	.611	.050	.116	.580	.050	.299	.561	.051	.429	.542	.049	.532
.723	.029	-.129	.722	.030	-.078	.715	.031	-.097	.690	.031	-.019	.659	.032	.112	.640	.032	.212	.621	.032	.320
.810	.017	-.184	.804	.017	-.172	.797	.018	-.160	.772	.019	-.102	.741	.020	-.007	.722	.021	.063	.704	.021	.144
.896	.010	-.183	.889	.010	-.175	.883	.010	-.165	.858	.011	-.122	.827	.013	-.853	.808	.013	-.004	.790	.014	.051
.985	.006	-.176	.979	.006	-.155	.973	.007	-.162	.948	.008	-.129	.917	.009	-.080	.898	.010	-.045	.880	.010	-.007

Table IV. Equivalent Plastic Strain and Triaxial Tensile Stress Distribution in a Cu-0.6% Cr. Jar

$(a/R)_i = 0$, $n = 3$, $\varepsilon_y = 0.0072$, $Y_o = 13$ ksi.

I			II			III			IV			V		
$a/a_i = .8001$			$a/a_i = .7566$			$a/a_i = .7043$			$a/a_i = .6462$			$a/a_i = .5880$		
z/a_o	$\bar{\varepsilon}^p$	σ_T/Y_o	z/a_o	$\bar{\varepsilon}^p$	σ_T/Y_o	z/a_o	$\bar{\varepsilon}^p$	σ_T/Y_o	z/a_o	$\bar{\varepsilon}^p$	σ_T/Y_o	z/a_o	$\bar{\varepsilon}^p$	σ_T/Y_o
.073	.460	1.539	.080	.580	1.920	.093	.733	2.477	.110	.900	3.187	.136	1.098	3.978
.215	.458	1.528	.245	.572	1.880	.280	.710	2.352	.329	.855	2.907	.394	1.013	3.479
.360	.452	1.509	.400	.559	1.800	.462	.670	2.140	.539	.783	2.425	.627	.877	2.670
.503	.444	1.483	.500	.534	1.693	.634	.627	1.844	.730	.700	1.850	.828	.742	1.740
.645	.439	1.450	.713	.515	1.570	.802	.580	1.527	.908	.616	1.255	1.010	.630	.808
.785	.432	1.412	.866	.495	1.440	.960	.537	1.233	1.066	.546	.712	1.170	.541	.072
.926	.422	1.369	1.010	.467	1.304	1.115	.492	.944	1.[illegible]20	.493	.300	1.328	.487	-.200
1.060	.416	1.326	1.151	.444	1.180	1.256	.457	.705	1.360	.452	.170	1.470	.452	-.148
1.200	.404	1.282	1.300	.424	1.068	1.400	.429	.557	1.507	.422	.216	1.612	.420	.008
1.317	.398	1.241	1.436	.408	.965	1.539	.408	.545	1.644	.401	.318	1.756	.400	.165
1.470	.386	1.202	1.571	.397	.886	1.676	.390	.588	1.785	.385	.430	1.892	.380	.312
1.603	.378	1.172	1.708	.379	.850	1.810	.375	.657	1.914	.370	.542	2.020	.365	.442
1.736	.370	1.140	1.840	.370	.859	1.940	.368	.728	2.017	.365	.640	2.154	.356	.555
1.866	.361	1.113	1.973	.362	.892	2.073	.362	.800	2.177	.360	.722	2.281	.350	.642

Table V. Equivalent Plastic Strain and Triaxial Tensile Stress Distribution in a Cu-0.6% Cr Bar

$(a/R)_i = 0.5, \quad n = 2.5, \quad \varepsilon_y = 0.00416, \quad Y_o = 8.2$ ksi

I			II			III			IV			V		
$a/a_i = .7294$			$a/a_i = .6600$			$a/a_i = .5966$			$a/a_i = .5439$			$a/a_i = .5082$		
z/a_o	$\bar{\varepsilon}^p$	σ_T/Y_o	z/a_o	$\bar{\varepsilon}^p$	σ_T/Y_o	z/a_o	$\bar{\varepsilon}^p$	σ_T/Y_o	z/a_o	$\bar{\varepsilon}^p$	σ_T/Y_o	z/a_o	$\bar{\varepsilon}^p$	σ_T/Y_o
.062	.570	5.871	.074	.748	7.396	.088	.925	8.734	.104	1.085	10.246	.116	1.202	12.174
.183	.529	5.408	.217	.670	6.600	.255	.799	7.688	.295	.912	8.750	.328	1.004	9.891
.300	.462	4.612	.347	.555	5.308	.400	.629	5.922	.453	.690	6.514	.500	.752	7.349
.409	.386	3.702	.465	.439	3.920	.524	.474	4.045	.584	.500	4.207	.638	.538	4.794
.513	.313	2.822	.573	.338	2.645	.635	.351	2.384	.697	.361	2.231	.754	.381	2.875
.613	.250	2.048	.675	.259	1.552	.737	.261	1.036	.799	.264	.685	.858	.274	1.311
.709	.197	1.398	.772	.198	.719	.834	.198	.164	.897	.197	-.230	.956	.202	-.093
.805	.155	.888	.867	.154	.309	.929	.152	-.084	.992	.151	-.376	1.051	.153	-.523
.900	.122	.585	.962	.120	.194	1.024	.119	-.086	1.086	.118	-.302	1.146	.118	-.392
.995	.098	.463	1.057	.096	.194	1.119	.094	-.008	1.181	.093	-.169	1.242	.091	-.190
1.092	.079	.422	1.154	.077	.234	1.216	.076	.086	1.277	.074	-.034	1.339	.074	-.071
1.190	.064	.431	1.252	.063	.298	1.314	.061	.187	1.375	.060	.094	1.437	.061	.051

Table VI. Equivalent Plastic Strain and Triaxial Tensile Stress Distribution in a Cu-0.6%Cr Bar

$(a/R)_i = 1.0$, $n = 2.5$, $\varepsilon_y = 0.00416$, $Y_o = 8.2$ ksi

I			II			III			IV			V			VI		
$a/a_i = .8381$			$a/a_i = .7614$			$a/a_i = .7000$			$a/a_i = .6407$			$a/a_i = .5877$			$a/a_i = .5434$		
z/a_o	$\bar{\varepsilon}^p$	σ_T/Y_o	z/a_o	$\bar{\varepsilon}^p$	σ_T/Y_o	z/a_o	$\bar{\varepsilon}^p$	σ_T/Y_o	z/a_o	$\bar{\varepsilon}^p$	σ_T/Y_o	z/a_o	$\bar{\varepsilon}^p$	σ_T/Y_o	z/a_o	$\bar{\varepsilon}^p$	σ_T/Y_o
.037	.284	4.510	.043	.440	6.240	.049	.580	7.749	.057	.728	9.188	.065	.870	10.331	.074	1.001	11.956
.109	.270	4.320	.127	.409	5.793	.145	.523	6.979	.166	.636	8.065	.188	.732	9.026	.211	.817	10.078
.182	.246	3.946	.210	.360	5.022	.236	.440	5.753	.265	.505	6.357	.296	.560	6.886	.327	.604	7.395
.255	.217	3.464	.291	.303	4.129	.322	.348	4.465	.356	.383	4.677	.391	.411	4.873	.425	.433	5.112
.329	.186	2.924	.370	.240	3.242	.405	.269	3.282	.441	.282	3.214	.477	.294	3.192	.513	.302	3.268
.404	.153	2.390	.448	.192	2.443	.485	.201	2.261	.522	.205	1.987	.559	.210	1.819	.596	.212	1.779
.481	.123	1.895	.528	.143	1.760	.565	.148	1.409	.602	.146	1.014	.639	.152	.748	.676	.151	.627
.561	.085	1.464	.608	.110	1.199	.646	.106	.761	.683	.110	.407	.720	.105	.152	.757	.107	-.039
.643	.073	1.106	.694	.100	.766	.729	.080	.411	.766	.075	.158	.803	.076	-.033	.840	.076	-.18
.729	.052	.823	.780	.059	.488	.815	.055	.251	.852	.050	.072	.889	.053	-.070	.926	.054	-.18
.818	.042	.613	.867	.045	.360	.904	.040	.200	.941	.039	.072	.978	.040	-.031	1.015	.039	-.11
.911	.035	.472	.959	.037	.285	.996	.038	.176	1.033	.030	.085	1.070	.029	.009	1.107	.030	-.05
1.007	.030	.376	1.055	.030	.239	1.092	.030	.161	1.128	.021	.095	1.165	.020	.038	1.202	.020	-.01

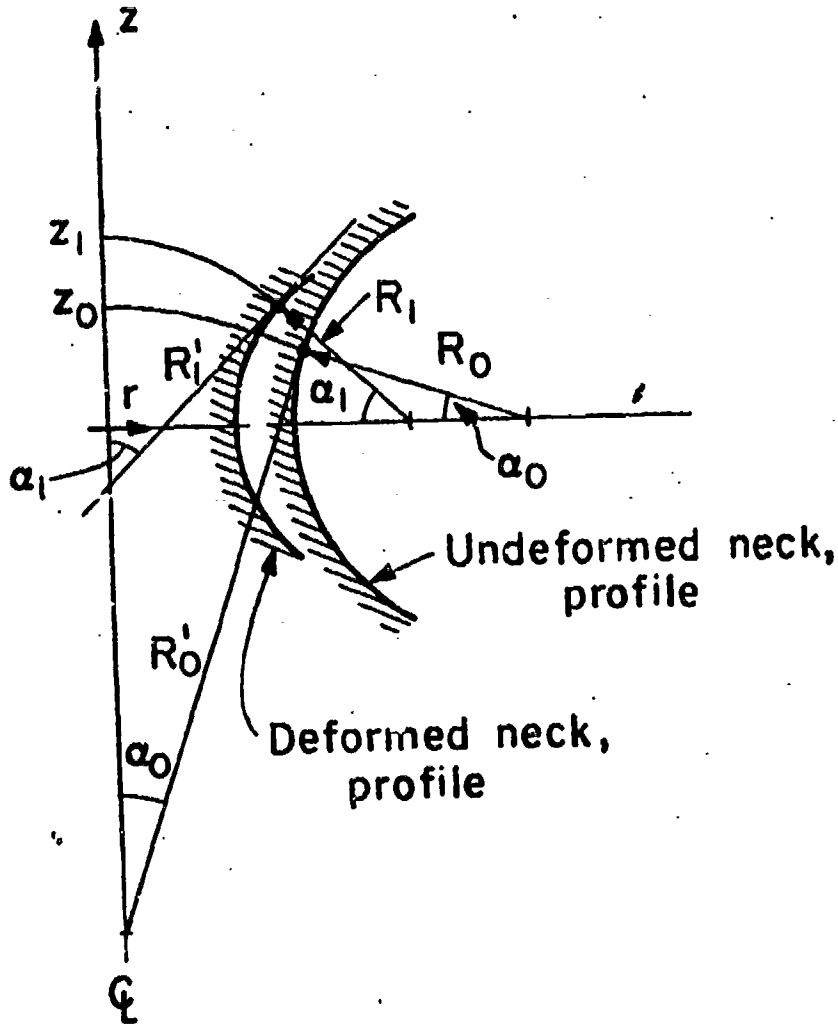

Fig. 1 Changes of neck profile with deformation in a tension specimen.

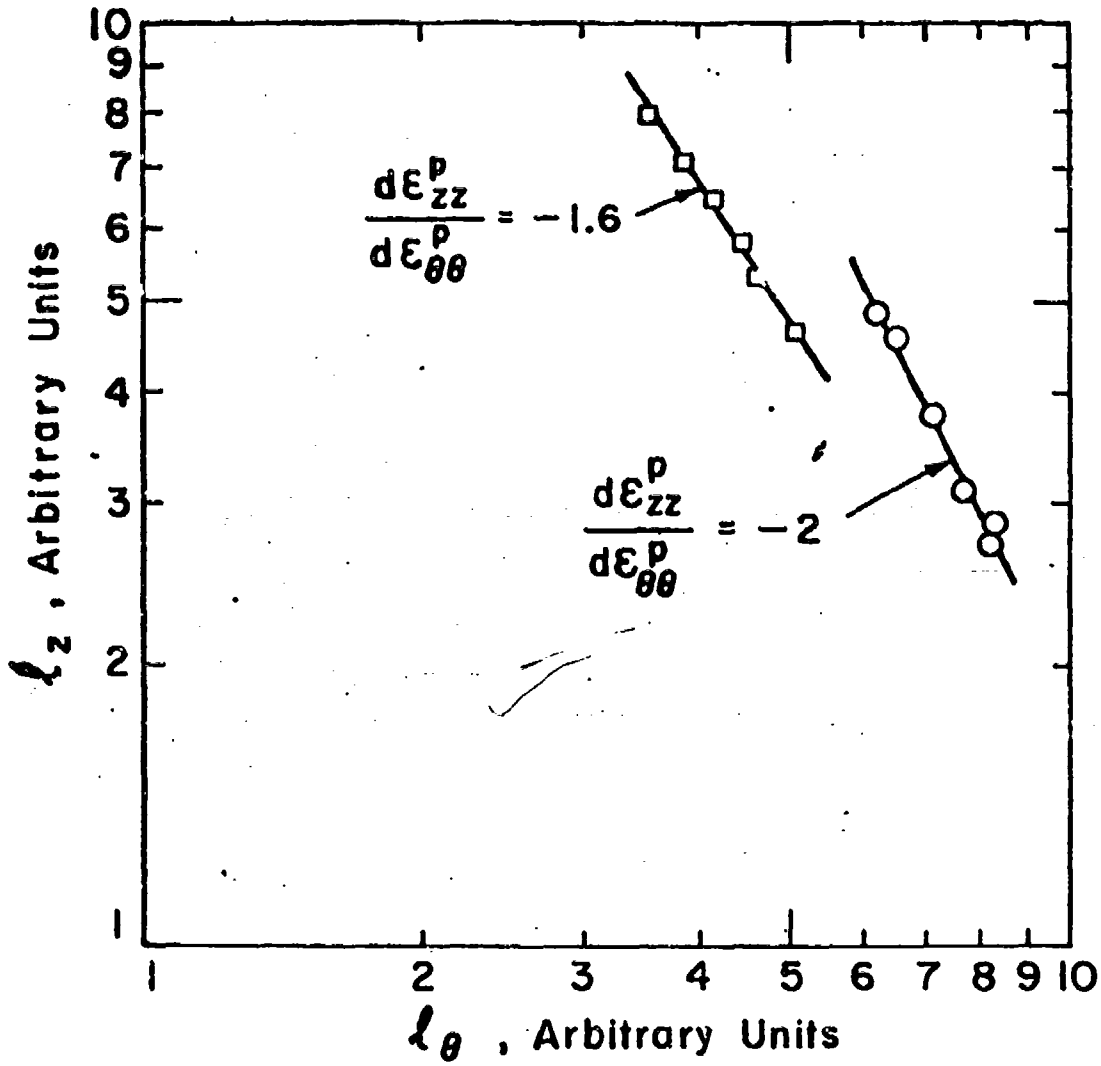

Fig. 2. Changes of shape of a grid inscribed on the surfaces of two specimens with initially machined natural neck profiles of $(a/R)_i = 0.5$.

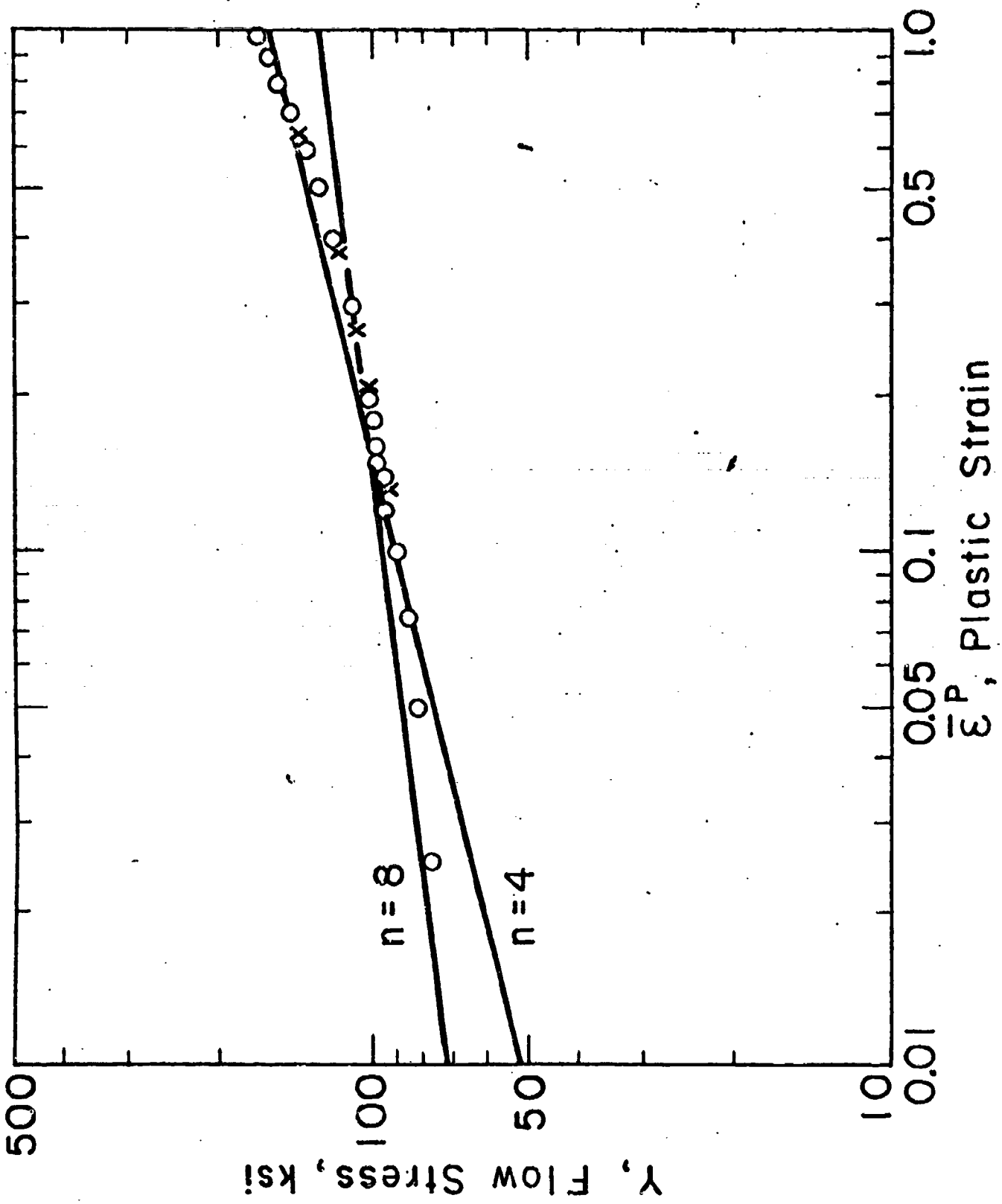

Fig. 3. True stress-true strain plot for two spheroidized 1045 steel specimens.

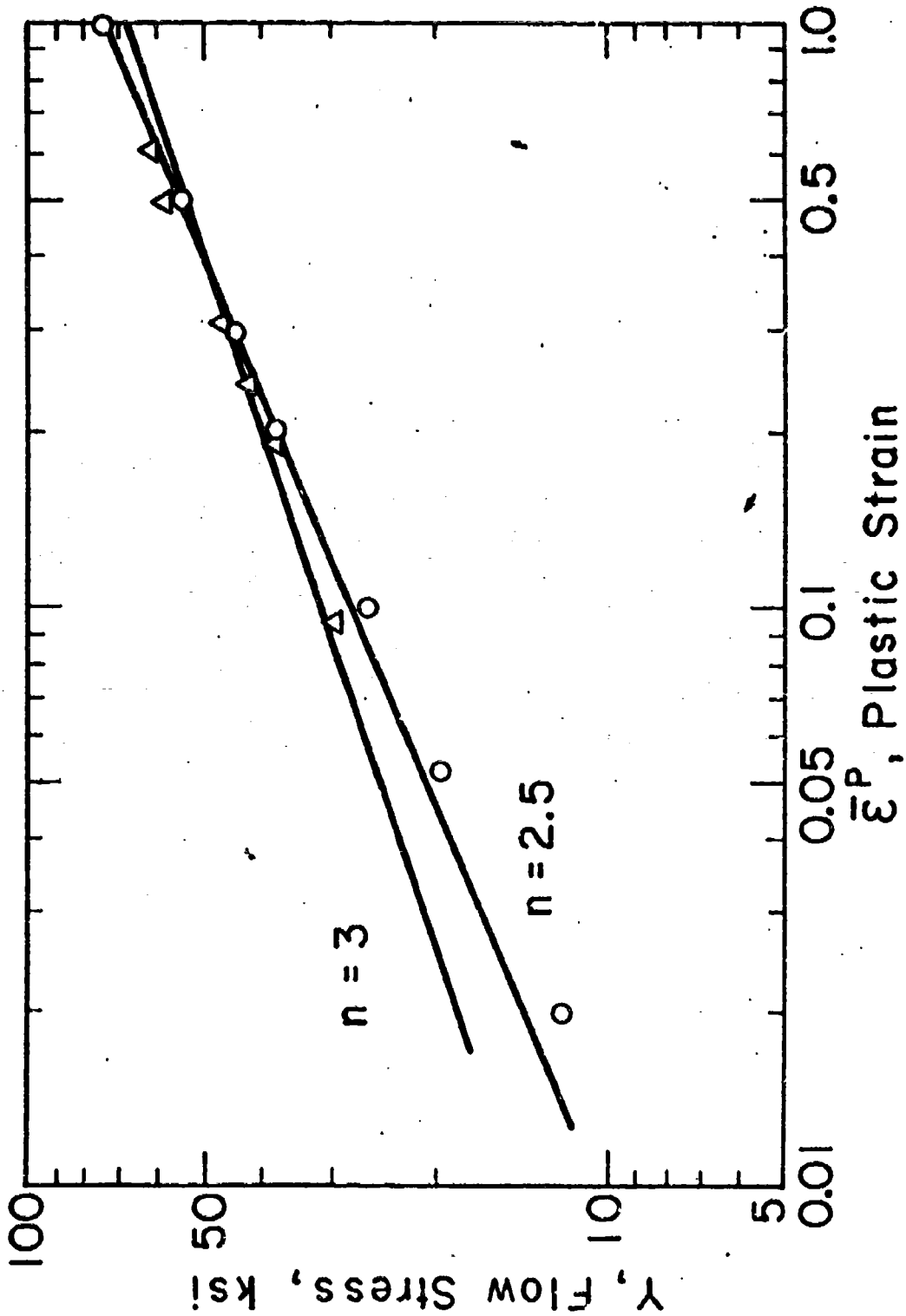

Fig. 4. True stress-true strain plot for two fully aged specimens of Cu - 0.6% Cr.

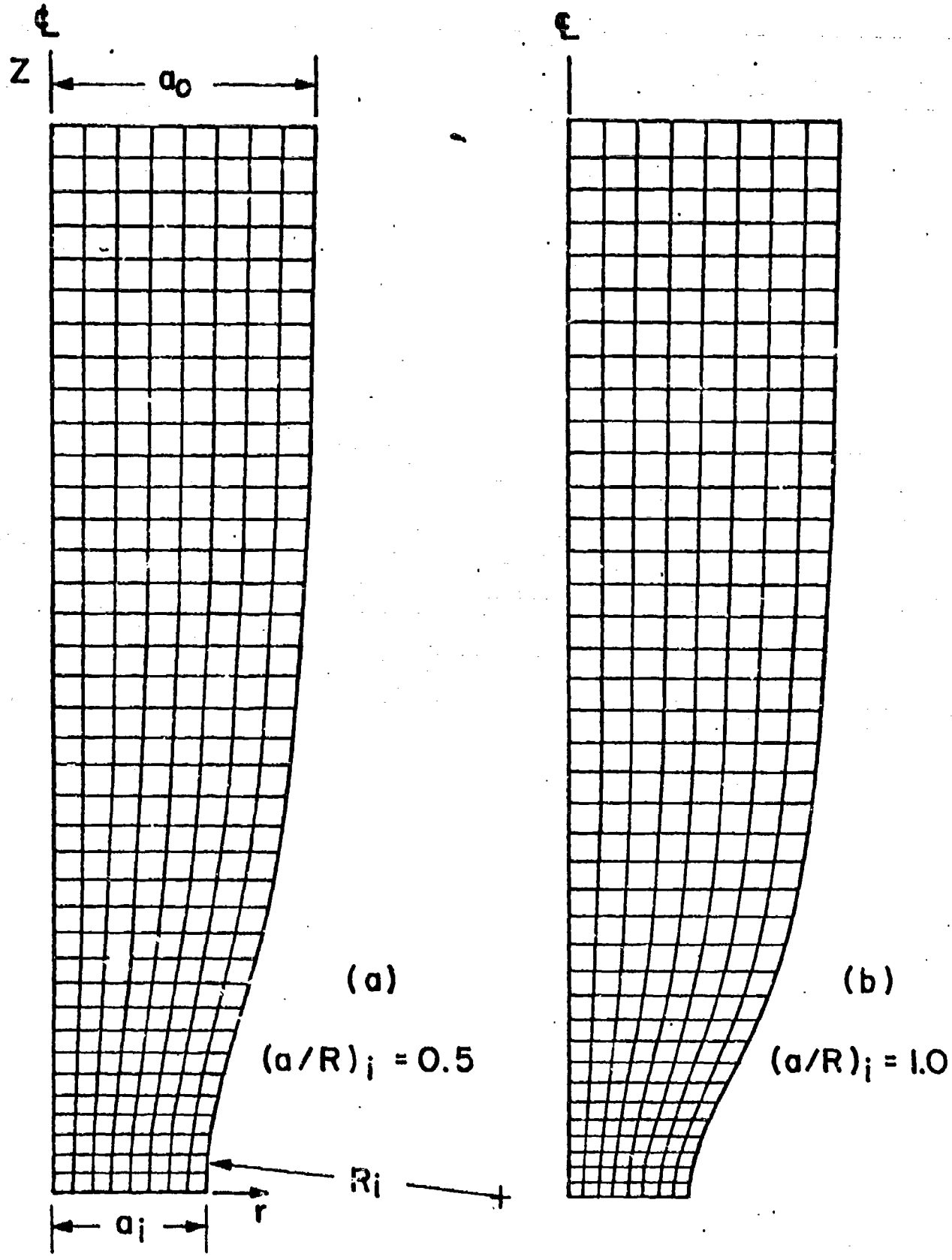

Fig. 5. Nodal points in finite element grids for bars with initally machined natural neck profiles, a) $(a/R)_i = 0.5$, b) $(a/R)_i = 1.0$.

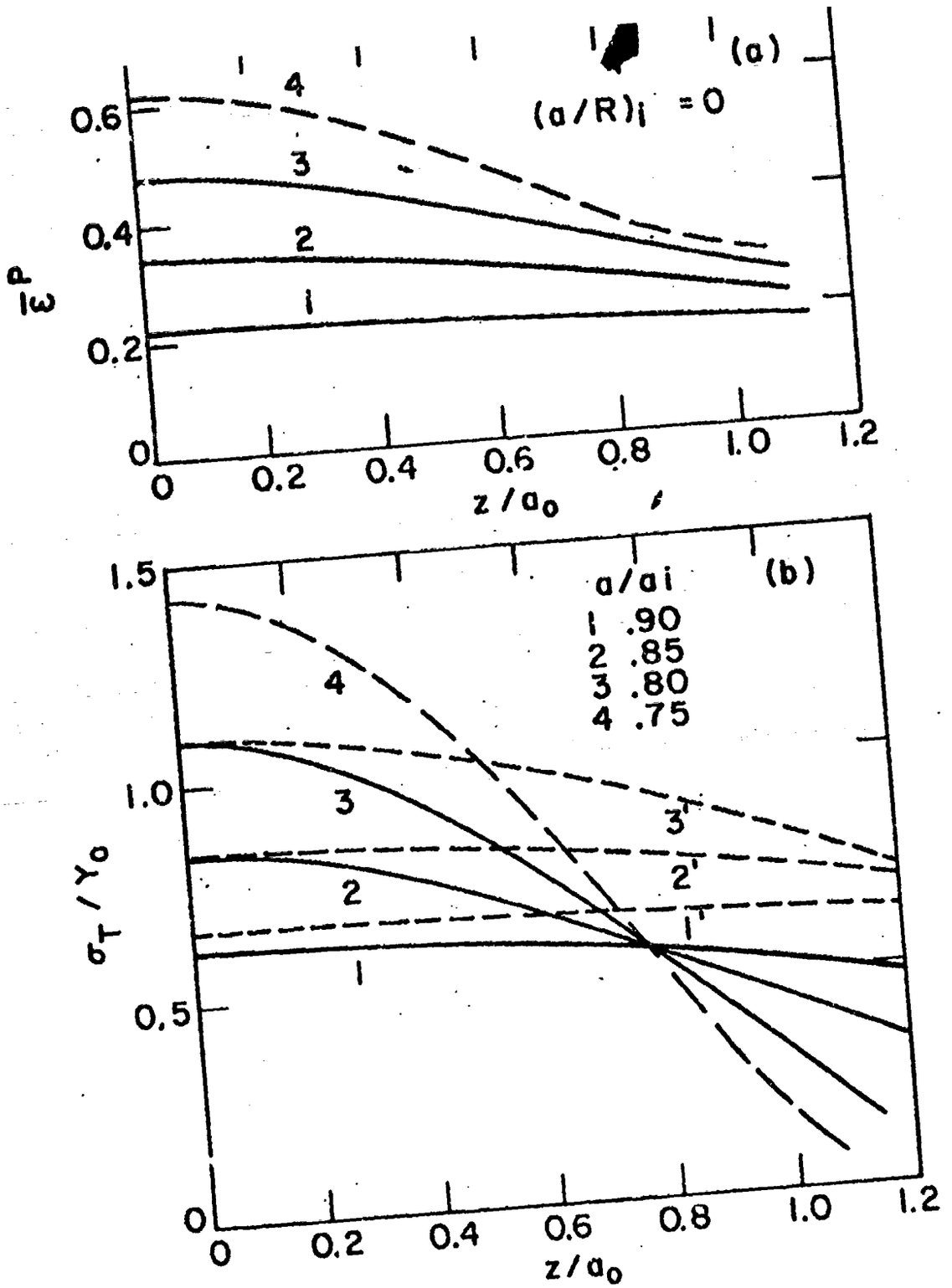

Fig. 6. Distribution of equivalent plastic strain (a), and triaxial tensile stress (b) for 1045 steel bar with $(a/R)_i = 0$, $(a/R)_f = 0.95$, $\varepsilon_y = 0.0072$, $n = 8$.

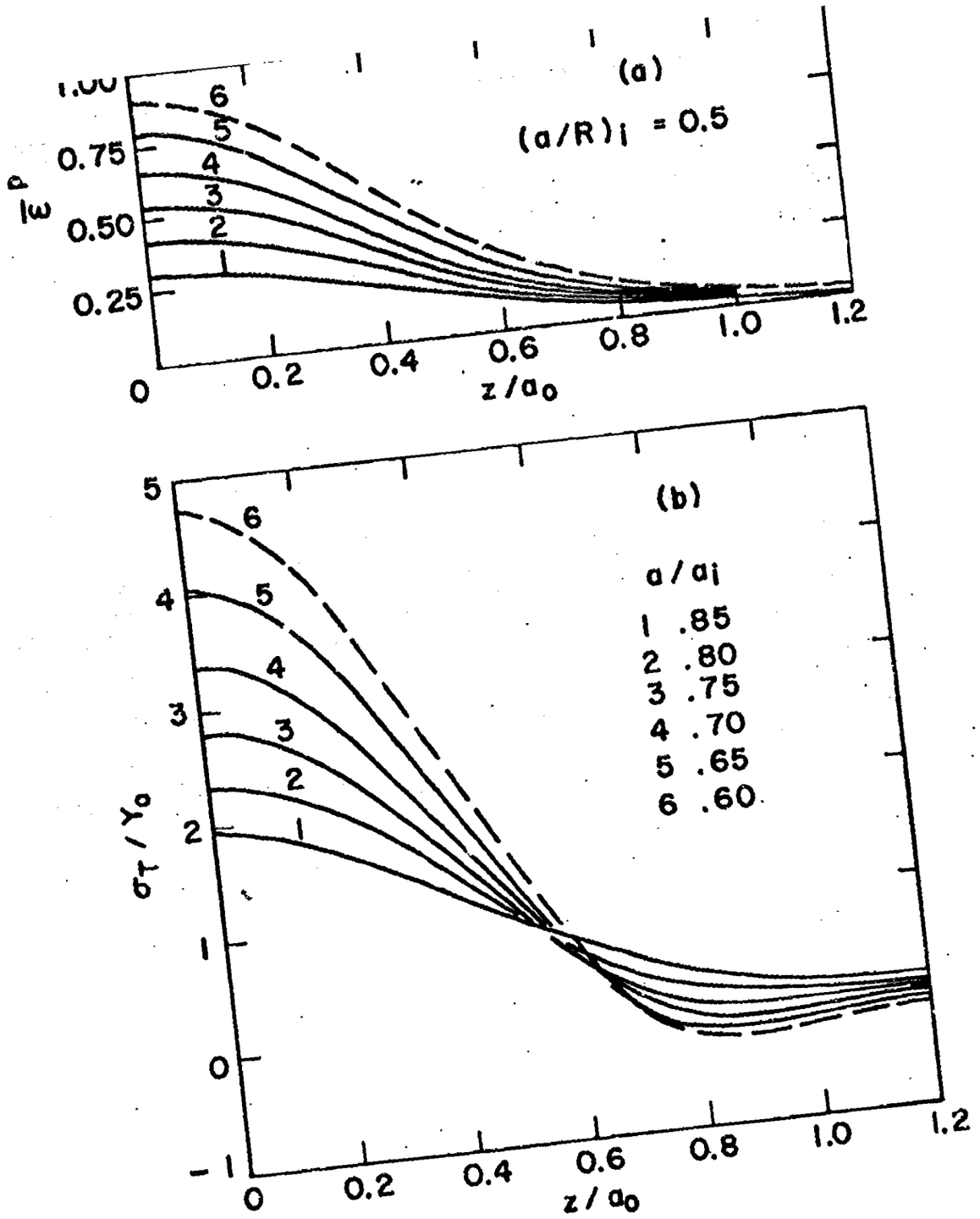

Fig. 7. Distribution of equivalent plastic strain (a), and triaxial tensile stress (b) for 1045 steel bar with $(a/R)_i = 0.5$, $(a/R)_f = 1.65$, $\varepsilon_y = 0.0094$, $n = 4$.

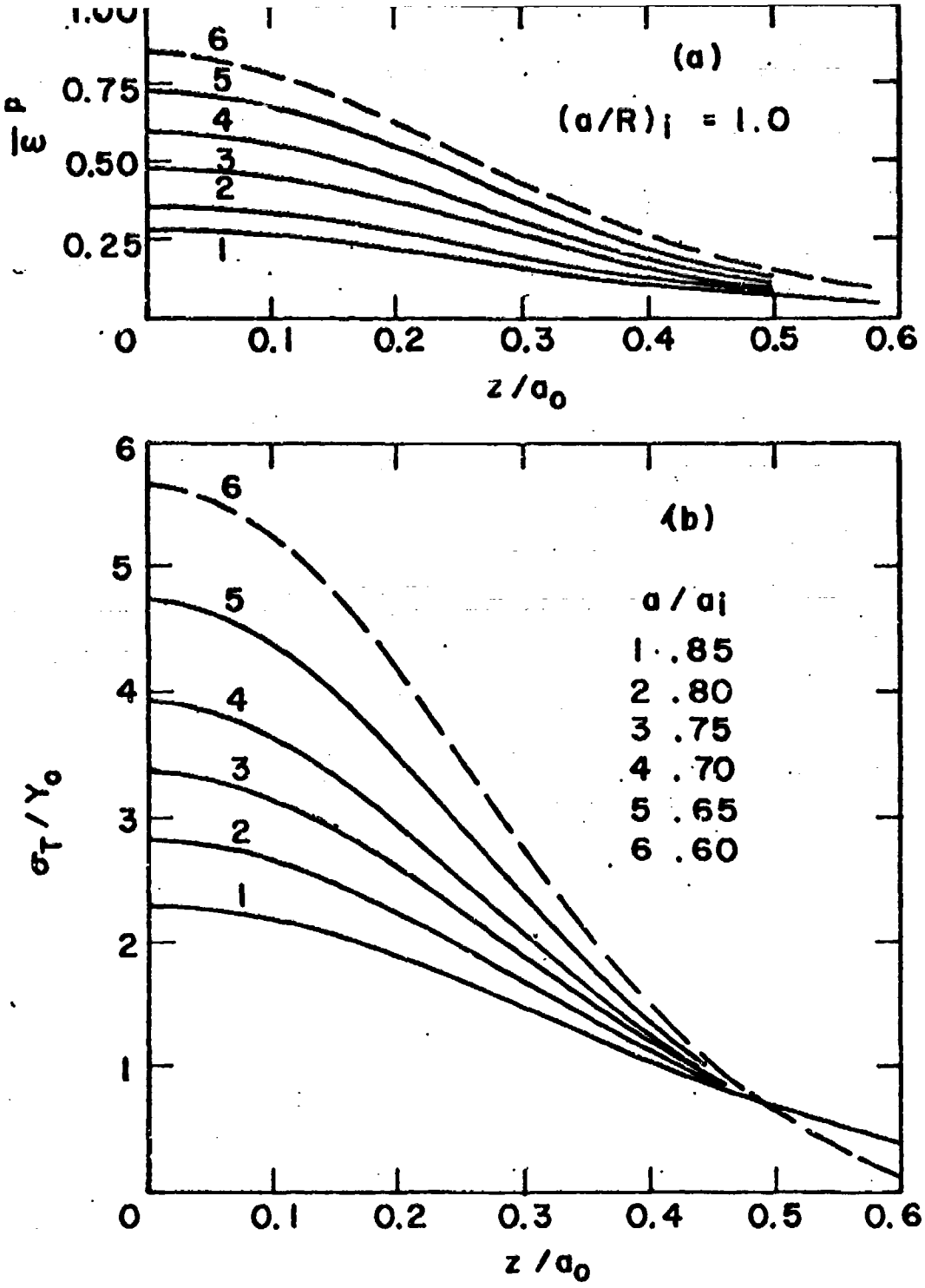

Fig. 8. Distribution of equivalent plastic strain (a), and triaxial tensile stress (b) for 1045 steel bar with $(a/R)_i = 1.0$, $(a/R)_f = 2.4$, $\varepsilon_y = 0.0094$, $n = 4$.

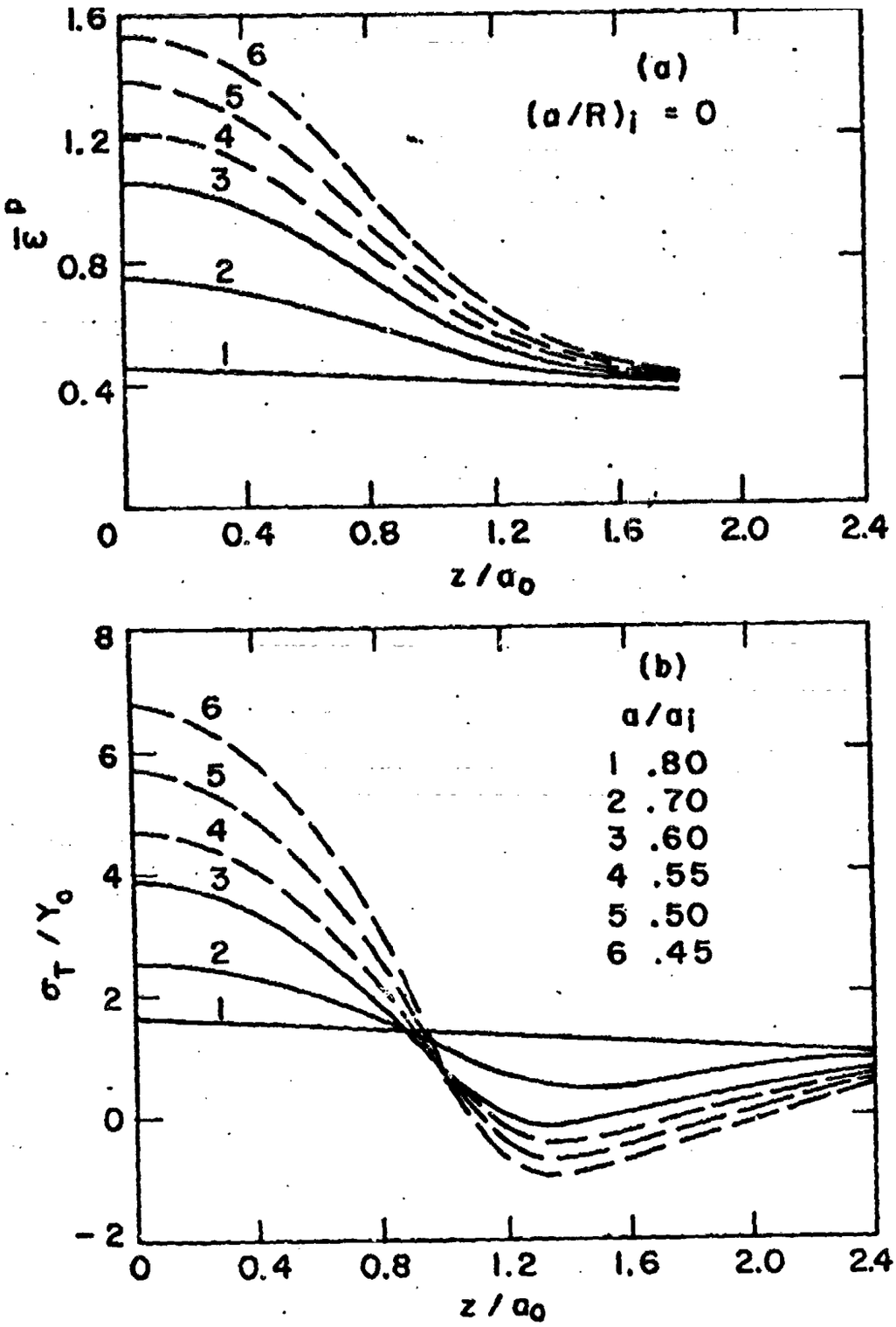

Fig. 9. Distribution of equivalent plastic strain (a), and triaxial tensile stress (b) for Cu - 0.6% Cr bar with $(a/R)_i = 0$, $(a/R)_f = 0.95$, $\dot{\varepsilon}_y = 0.00$, $n = 3$.

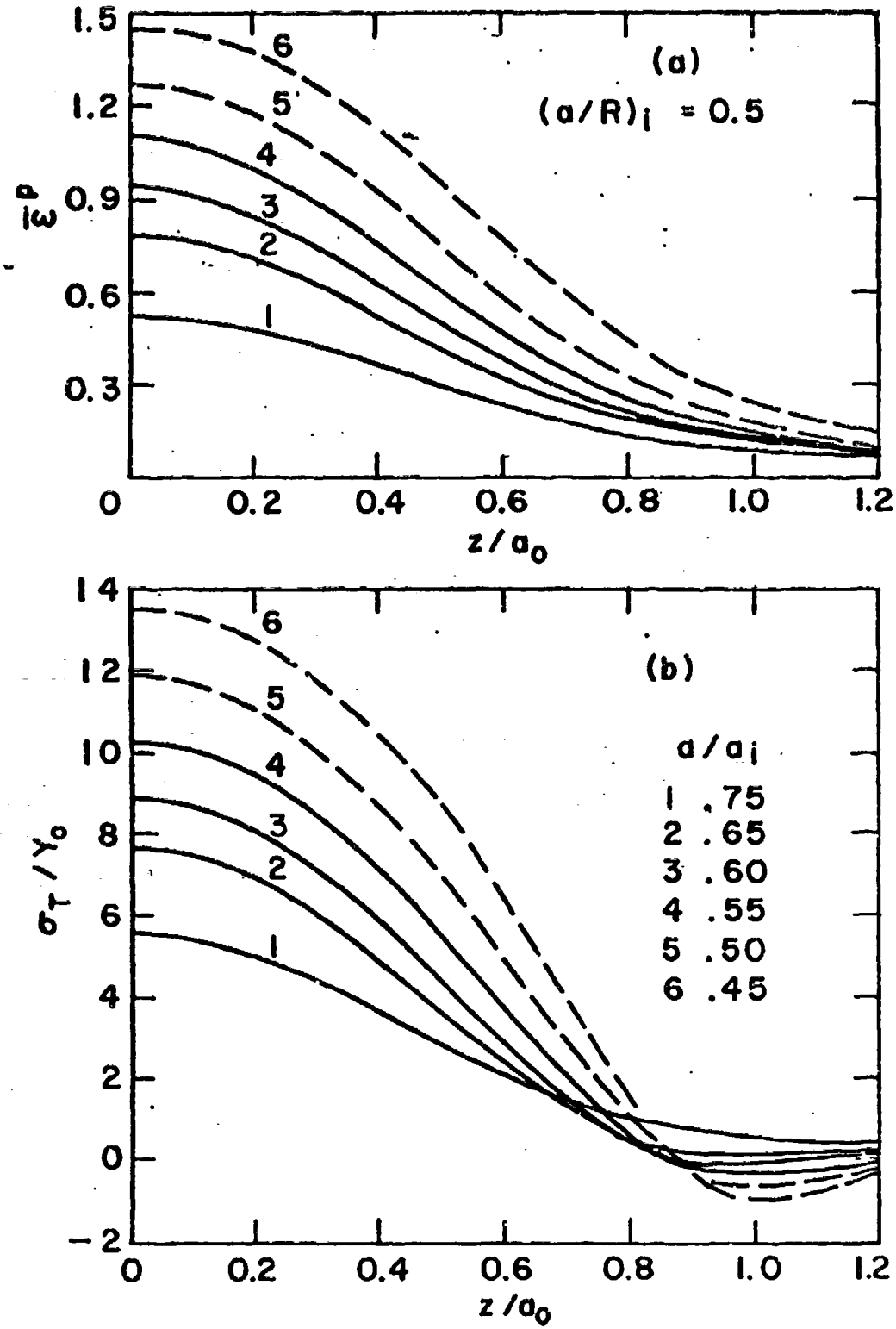

Fig. 10. Distribution of equivalent plastic strain (a), and triaxial tensile stress (b) for Cu - 0.6% Cr bar with $(a/R)_i = 0.5$, $(a/R)_f = 2.75$, $\varepsilon_y = 0.00416$, $n = 2.5$.

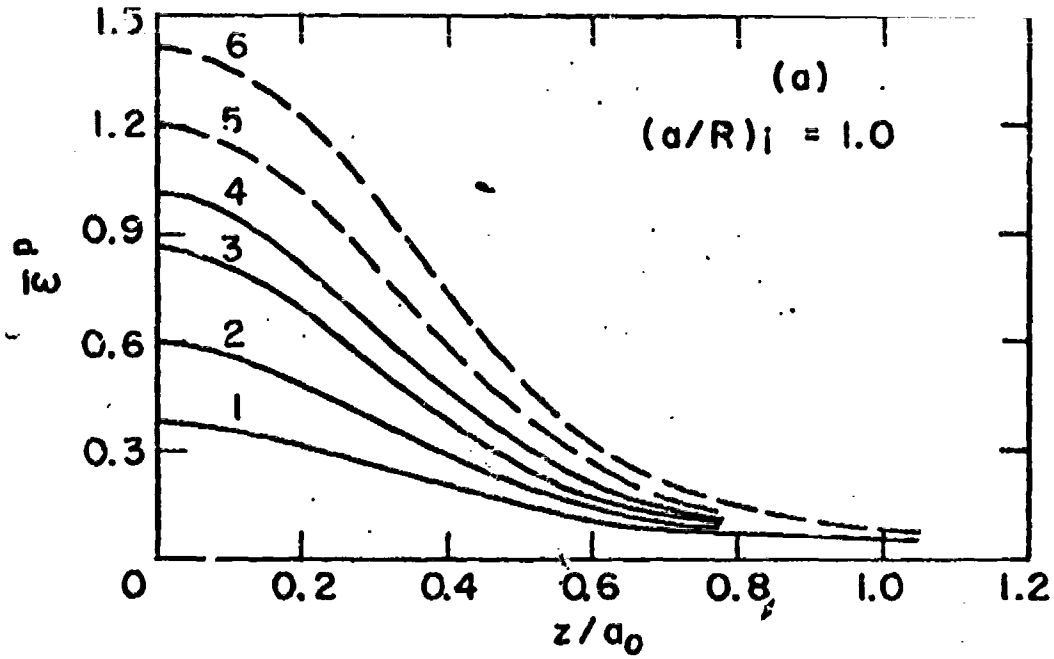

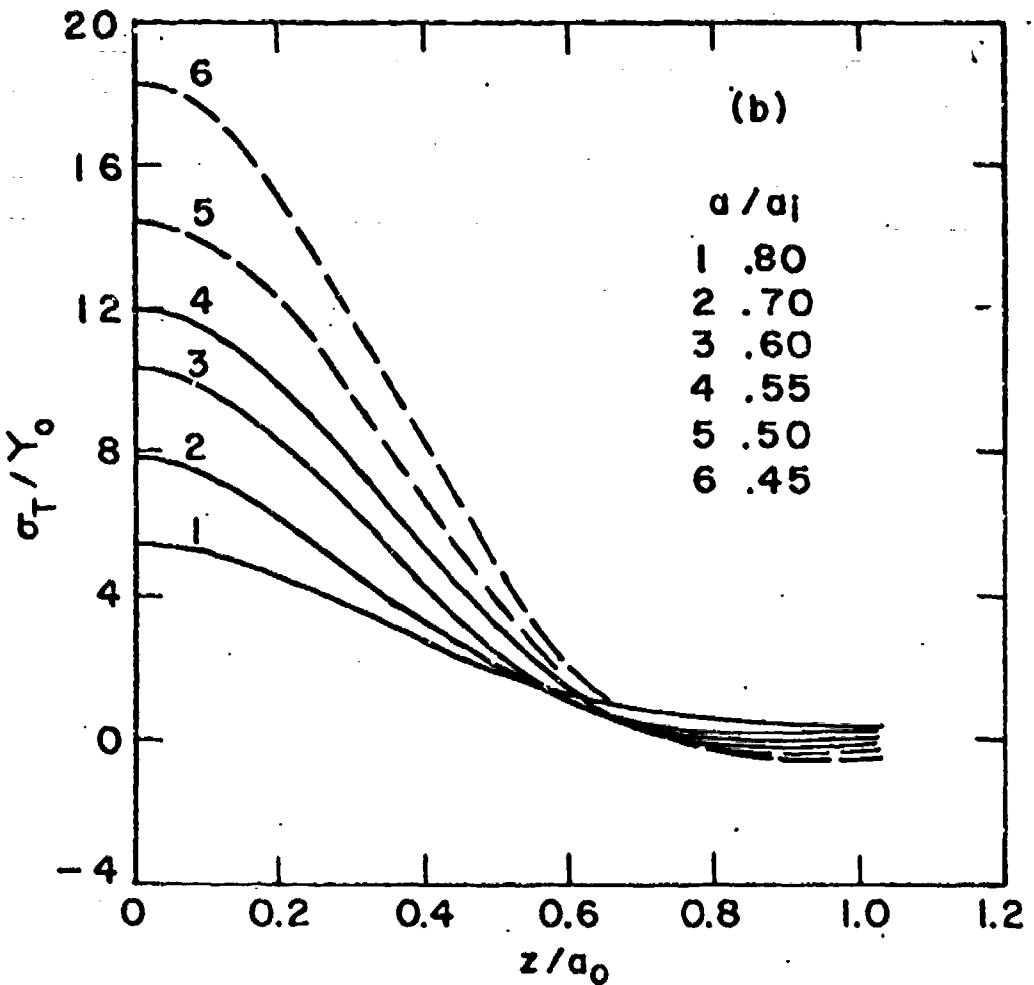

Fig. 11. Distribution of equivalent plastic strain (a), and triaxial tensile stress (b) for Cu - 0.6% Cr bar with $(a/R)_i$ = 1.0, $(a/R)_f$ = 3.82, ϵ_y = 0.00416, n = 2.5.

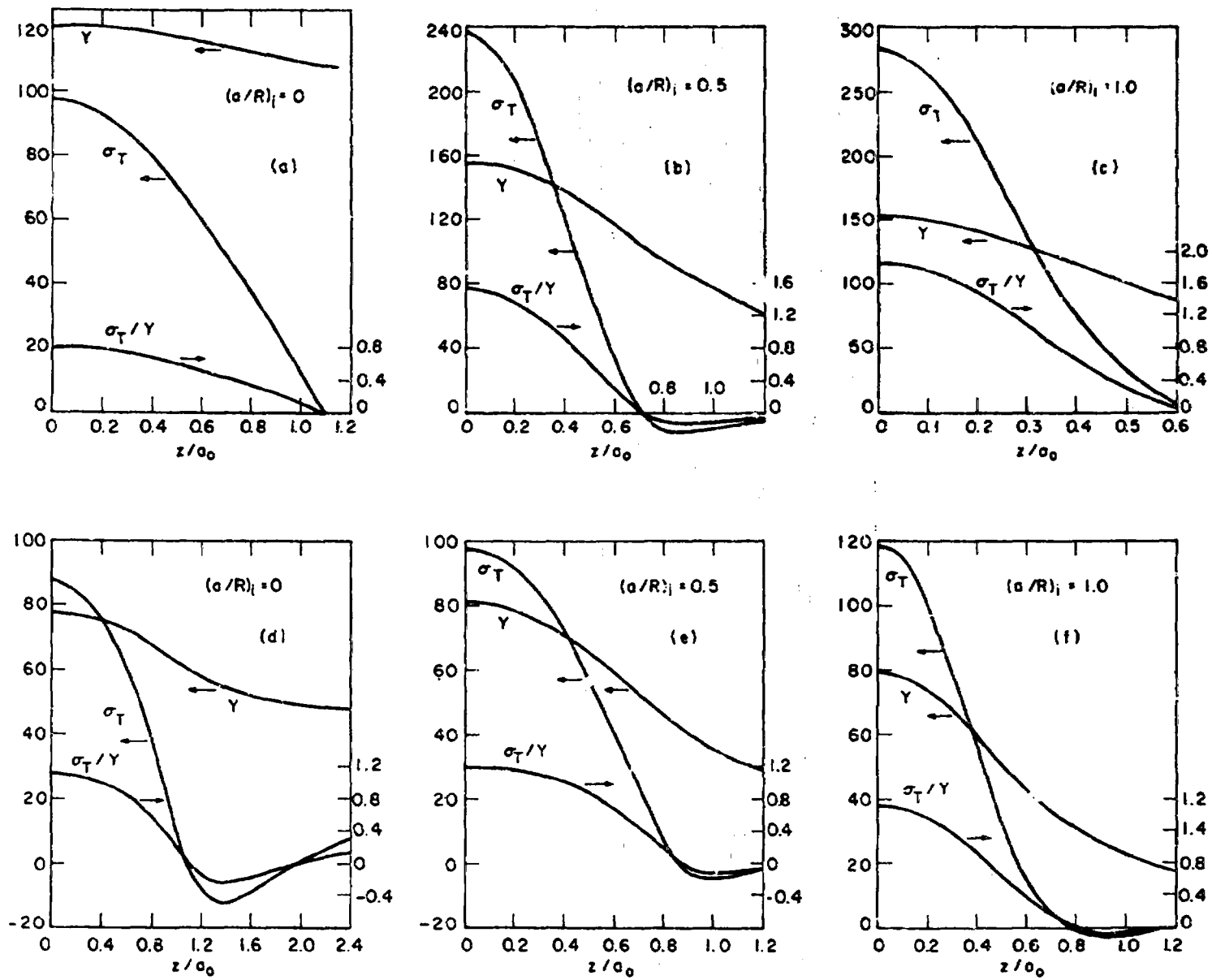

Fig. 12. Distribution of tri-axial tensile stress, σ_T, flow stress, Y, and tri-axiality, σ_T/Y, in: a) Steel wit $(a/R)_i$ = o, at a/a_i = 0.75; b) Steel with $(a/R)_i$=0.5, at a/a_i=0.60; c) Steel with $(a/R)_i$=1.0, at a/a_i=0.60; d) Cu=0.6%Cr with $(a/R)_i$=0, at a/a_i=0.45; e) Cu=0.6%Cr with $(a/R)_i$=0.5, at a/a_i=0.50; f) Cu-0.6%Cr with $(a/R)_i$=1 at a/a_i=0.50.

Cavity Formation from Inclusions in Ductile Fracture(*)

A. S. Argon(**), J. Im(**), and R. Safoglu(***)

Massachusetts Institute of Technology, Cambridge, Mass. 02139

Abstract

The previously proposed conditions for cavity formation from equiaxed inclusions in ductile fracture have been examined. Critical local elastic energy conditions are found to be necessary but not sufficient for cavity formation. The interfacial strength must also be reached on part of the boundary. For inclusions larger than about 400Å the energy condition is always satisfied when the interfacial strength is reached and cavities form by a critical interfacial stress condition. For smaller cavities the stored elastic energy is insufficient to open up interfacial cavities. Approximate continuum analyses for extreme idealizations of matrix behavior furnish relatively close limits for the interfacial stress concentration for strain hardening matrices flowing around rigid non-yielding equiaxed inclusions. Such analyses give that in pure shear loading the maximum interfacial stress is very nearly equal to the equivalent flow stress in tension for the given state of plastic strain. Previously proposed models based on a local dissipation of deformation incompatibilities by the punching of dislocation loops lead to rather similar results for interfacial stress concentration when local plastic relaxation is allowed inside the loops. At very small concentrations of second phase the inclusions

---

(*) This work has been presented in part orally at the Third International Conference on Fracture in Munich, Germany, during April 1973.

(**) Department of Mechanical Engineering, M.I.T.

(***) Department of Mining and Metallurgy, Technical University of Istanbul, Turkey.

do not interact for very substantial amounts of plastic strain. In this regime the interfacial stress is independent of inclusion size. At larger concentrations of second phase, inclusions begin to interact after moderate amounts of plastic strain, and the interfacial stress concentration becomes dependent on second phase concentration. The many reported instances of inclusion size effect in cavity formation can be satisfactorily explained by variations of second phase concentration from point to point.

I. Introduction

It appears that Joseph Henry[1], of electro-magnetism fame, has recognized as early as 1855 that metals fracture prematurely by a process of internal necking when extended by stretching. He advised that wire drawing and rolling were preferable operations (for this and other interesting historical perspectives on deformation processing see Backofen[2]). In more recent times Puttick[3] traced the cause of ductile fracture to the development of holes from inclusions (for a summary of earlier views on ductile fracture and their inadequacy see Orowan[4]). The process has since been investigated extensively both experimentally and theoretically. The current level of understanding of the role of inclusions in ductile fracture has been reviewed by Rosenfield[5]. It has now been generally established that once internal cavities are nucleated from inclusions of second phase particles, they can be plastically expanded under various combinations of shear stress and negative pressure. Analyses of homogeneous plastic cavitation by McClintock[6], Rice and Tracy[7] and others have elucidated the importance of negative pressures in the flow field in hastening the plastic hole expansion process. Comparison of such analyses with experiments have shown that local ductile fracture requires considerably smaller average plastic strain as a result of localization of dilational deformation into zones[8], followed by formation and propagation of cracks where the hole expansion process is sharply confined into portions of the highly strained zone in front of the crack[9,10]. Although these processes of terminal ductile separation are not yet fully understood, they are in a far better level

of development than the initial processes which lead to the nucleation of holes from second phase inclusion particles[5]. On the experimental side there have been conflicting observations reporting the nucleation of cavities from inclusions anywhere from immediately upon yielding to after the development of very large plastic strains. Cavities have been reported to nucleate both on interfaces by tearing the inclusion away from the ductile matrix, and by cracking of non-deformable inclusions. On the other hand semi quantitative theoretical studies have been made, based on release of stored elastic energy[11,12], production of high stresses by impingement of dislocation pile-ups on inclusions[11,13], and by reverse pile-ups of plastic accommodation loops initiated by punching from the interface[14]. More phenomenological models have also been advanced based on the development of high local shear strains at particle interfaces[15]. Here we will briefly review these mechanisms of cavity nucleation and present new analytical developments on a local stress criterion of interfacial separation. In the accompanying paper[16] we compare the results of experiments on a number of inclusion-bearing metals with these new analytical developments.

II. Criteria for Inclusion Separation

A. Assessment of Earlier Developments

Although it has often been assumed by the advocates of hole growth that non-deformable inclusions are either initially not stuck to the matrix or that they can be separated immediately upon plastic yielding from the matrix in which they are embedded, there are many observations which show that this can only be true in restricted cases and that most often large plastic strains are required to clear inclusions free. Hence we assume together with most of the former workers who have considered the problem of cavity nucleation that such holes are a result of a more or less extensive pre-processing. It has been generally observed that while inclusions with large aspect ratio may undergo multiple internal fracturing, equiaxed inclusions almost always nucleate holes by interfacial separation. Here we confine our attention only to the equiaxed inclusions which we will consider as a first approximation as rigid and plastically non-deformable. The problem of non-equiaxed inclusions, whose behavior depends on their shape and orientation in addition to their size and spacing is a complex problem and will not be discussed here.

As already mentioned in the previous section, the earlier considerations of inclusion separation can be grouped into three categories, energy criteria, local stress criteria, and local strain criteria.

Gurland and Plateau[11] proposed that interfacial cracks could form when the locally concentrated elastic strain energy becomes comparable to the energy of the surfaces to be generated. Considering no local plastic accommodation and without investigating whether or

not the stored elastic energy could actually be released by crack formation, they based their arguments on dimensional analysis and concluded that cracks would form at lower applied stresses on large inclusions. As pointed out by Brown and Stobbs[17] the analysis of Gurland and Plateau is only a necessary condition for inclusion separation. A more correct analysis by Tanaka, Mori, and Nakamura[12] has shown that in a purely elastic situation, the energy criterion is always satisfied for particles above a diameter of about 250Å, almost upon yielding. Since in many instances inclusions of more than hundred times this size have been observed to remain attached to the matrix at strains more than hundred times the yield strain it must be concluded that the energy requirement is only a necessary one and that actual separation requires reaching the interfacial strength at the interface, at least at some local points, to provide a nucleus of separation. It must then follow that for very small particles of diameter much less than the critical diameter of 250Å where the energy criterion may not be satisfied even when local stresses reach the interfacial strength, stable cavities can not form. The interface would merely separate a distance of the order of atomic dimensions relieveing much of the elastic strain energy but still transmitting long range attractive forces. Similar problems of this nature related to the very short range singular stress fields around dislocation cores have been discussed by Stroh[18].

Gurland and Plateau[11] and also Broek[13] have attributed cavity formation to impingement of dislocation pile-ups at inclusions in the manner proposed by Zener[19] and analysed by Stroh[20]. At low

temperature where slip tends to be planar, cavities can be produced by this mechanism especially if the inclusions have a large aspect ratio increasing the probability for them to interfere with such planar slip. Some of the observations on the splitting elongated inclusions is probably due to this mechanism. At moderate temperatures in close packed metals where many equivalent slip systems become operable and slip tends to become wavy, the ease of secondary slip will make the development of high stresses difficult or almost impossible. Therefore, in ductile fcc metals and even in bcc metals at moderate temperatures this mechanism is almost certainly not responsible for cavity formation around inclusions. Ashby[14] has discussed an interesting alternative in which primary deformation incompatibilities do not produce cavities directly, but initiate highly organized secondary slip by punching out dislocation loops from the interface of the inclusion with the matrix to reduce the local shear stresses. These loops then form reverse pile-ups and can build up interfacial tensile stresses until they reach the interfacial strength when a cavity is formed. Ashby's model amounts to a special upper bound analysis for plastically dissipating primary deformation incompatibilites; it is however not an upper bound analysis for the total problem since the assumed flow field is only local and does not satisfy the distant deformation boundary conditions of the entire body. Ashby has shown that this model can also be formulated completely as a macroscopic slip line field in which positive and negative deformation incompatibilities around the particle can be balanced against each other by a closed slip line field of four lobes[21]. Thus, in spite of the fact that the interfacial stresses calculable by this model are no better than a high upper bound, the model is

conceptually simple and as we will show later can account readily for interactions between particles to explain why large particles lead to cavity formation before small particles.

McClintock[15] has given an extensive elastic-plastic continuum analysis of stress distributions around cylindrical particles in anti-plane strain, where it is shown that large strain concentrations can develop around non-deforming particles in non-strain hardening matrices. Arguing that similar strain concentrations must also occur in plane strain deformation and that such high strain concentrations in crystal plasticity are usually composed of dislocation pile-ups, McClintock has suggested that cavity formation at interfaces may obey a critical local strain criterion, or alternatively a criterion that may be a mixture of a critical interfacial shearing strain and an interfacial normal stress. The nature of this combined criterion has not been clarified. Most investigators have adopted one of the above criteria to explain their results.

Below we will consider the separation primarily of only large particles for which the energy criterion is always satisfied and cavity formation can be expected to depend on reaching locally a critical interfacial tensile strength.

B. Critical Stress Criteria Based on Continuum Deformation

In most instances ductile fracture results from cavities formed around inclusions of micron size. On the other hand, transmission electron microscopy of dislocation structures around inclusions of sub-micron size have shown that the spacing of the surrounding dislocations in the high strain gradient zones are very much smaller than the particle

diameter, suggesting that at least for large particles a continuum analysis of deformation is proper. On the other hand dislocation structures around small particles of only several hundred Angstroms diameter are usually highly organized prismatic loops,[17,22] requiring a more discrete dislocation analysis for the interfacial stresses. Below we will discuss both approaches in order.

Considering the particle as a rigid cylinder and the surrounding matrix as an elastic, plastic strain hardening continuum, the development of interfacial stresses is desired for pure shear deformation. The solution for any other state of deformation having a negative pressure component can then be obtained by superimposing this negative pressure on the interfacial stresses of the pure shear solution. Some solutions of this type already exist. Huang[23] has presented a deformation theory solution for a rigid cylindrical inclusion embedded into an incompressible Ramberg-Osgood (power-law) material with a stress exponent of 7. He finds that a strain independent constant interfacial tensile stress concentration develops which is maximized at an angle of about 12° toward either side of the principal tension axis, and has a magnitude of 1.36 times the distant boundary shear traction. Huang also showed that for a decrease in the stress exponent corresponding to increasing strain hardening behavior the stress concentration increases steadily (and presumably approaches asymptotically the solution for an incompressible linear material). Orr and Brown[24] have considered the same problem in which the matrix was modelled as an incompressible elastic-plastic material with either no hardening or a linear hardening rate equal to 1/40 of the Young's modulus. Orr and Brown too find that the interfacial tensile stress reaches a maximum value away from the

principal tensile direction but at an angle of about 17° toward either side of this direction. Unlike Huang, Orr and Brown find, however, that the magnitude of the interfacial tensile stress concentration increases steadily as the distant plastic strain increases both for the non-hardening as well as the hardening material, and shows little change in this behavior even at distant plastic strain levels 15 times the yield strain. At that time the maximum interfacial stress is 3.03, and 2.52 times the boundary shear traction for the non-hardening and linearly strain hardening material respectively. Because of this difficulty of a lack of steady state for the non-hardening material even at large plastic strains we find the solution of Orr and Brown not very useful.

Rhee and McClintock[25] have demonstrated by means of a number of specific examples that the strain concentrations in inhomogeneous deformation fields in strain hardening materials can be bounded by two limiting idealizations of the plastic behavior of the material: a non-hardening rigid plastic behavior and a linear behavior with zero yield stress as shown in Fig. 1. Assuming that the same idea may also extend to stress concentrations we have obtained a finite element solution for the pure shear deformation of an elastic-ideally plastic, non-hardening continuum around a rigid cylindrical inclusion and compared this with the available linear solution as the other form of extreme idealization.

The chosen net configuration for the finite element solution corresponding to 0.01 volume fraction of second phase is shown in Fig.2. The elastic-plastic program of Marcal and King[26] was used for six increments of constant tensile and compressive boundary displacements

equivalent to pure shear, starting from the point where some elements in the chosen network just become plastic. The solution was obtained for conditions encountered in copper, i.e. for a Young's modulus of 10^4 ksi, a Poisson's ratio of 1/3, and a yield stress in tension of 15.9 ksi, giving $\varepsilon_y = 1.59 \cdot 10^{-3}$. The spreading of the plastic zones with these increments is shown in Figs. 3a-e as the shaded regions. The computed interfacial tensile stresses and tangential shear strains around the inclusion as a function of an angle θ measured from the direction of principal tension are given in Tables 1a - c. Unlike the two solutions discussed above our solution shows a flat maximum for the interfacial stress in the principal tensile direction without a significant drop before an angle of about 15°. Since the finite element net is quite coarse and other unevennesses of stress are apparent from Table I, we attribute this to defects in the program and accept the maximum interfacial stress at $\theta = 0°$ as an appropriate measure of the concentrated interfacial tensile stress. The change of this maximum stress in units of the yield strength in shear k of the matrix is given as a function of the increasing distant shear strain in Fig. 4, and indicates that a fairly stable solution was reached. The maximum interfacial tensile stress is found to be 1.5 k which is somewhat higher than the stress obtained by Huang. The distribution of equivalent shear strain which is mapped out by the spreading plastic zones shown in Fig. 3a - e resemble closely that obtained by Orr and Brown. We note further from Table 1c that there is only a very moderate interfacial shear strain concentration of about 1.10 on the interface parallel to the planes of maximum shear strain in the distant field (i.e. at $\theta = 45°$).

The second bounding solution for the interfacial stresses around a

rigid inclusion in an incompressible (i.e. $\nu = 0.5$) linear material can be obtained directly from the theory of elasticity (see Muskhelishvilli[27] or Savin[28]) and are

$$\sigma_{rr} = p\left[4\left(\frac{\rho}{r}\right)^2 - 3\left(\frac{\rho}{r}\right)^4 + 1\right]\cos 2\theta \qquad [1]$$

$$\sigma_{\theta\theta} = p\left[3\left(\frac{\rho}{r}\right)^4 - 1\right]\cos 2\theta \qquad [2]$$

$$\sigma_{zz} = p\,2\left(\frac{\rho}{r}\right)^2\cos 2\theta \qquad [3]$$

$$\sigma_{r\theta} = p\left[2\left(\frac{\rho}{r}\right)^2 - 3\left(\frac{\rho}{r}\right)^4 - 1\right]\sin 2\theta \qquad [4]$$

where p is the boundary shear traction and ρ the radius of the cylinder. The interfacial tensile stresses and shear strains around the inclusion are plotted in Fig. 5 as a function of the angle θ. We see that the tensile stress is maximized at $\theta = 0$ and is equal to 2 times the boundary shear traction. Similarly the interfacial shear strain is maximized at $\theta = 45°$ and is also equal to twice the distant boundary shear strain.

Figure 6 shows the distribution of the total principal strain ε_{xx} outside the inclusion for the two bounding solutions, in units of the total distant strain. The solid curve represents the distribution obtained from the final increment in the finite element analysis, while the broken curve is computed from Eqns. [1] and [2] by means of the elastic stress strain relations.

If the distant deformation field were not pure shear but had a negative pressure component σ_T, this negative pressure would have to

be added to the plastic drag induced interfacial stresses computed by the two limiting solutions discussed above. Thus, based on Rhee and McClintock's hypothesis the actual interfacial stresses could now be bounded as

$$\frac{3}{2}k \leq \sigma_{rr} - \sigma_T \leq 2k \qquad [5]$$

where the left hand bound is for the non-hardening idealization while the right hand bound is for the linear idealization where k is considered as the flow stress in shear. If Huang's solutions for the Ramberg-Osgood material with power-law hardening were to be extrapolated to non-hardening behavior and were taken for the lower limit it may be as low as k. Since for most of the strain hardening behavior of interest, i.e. for the exponents n between 2 and 8, Huang's solutions either fall slightly below the lower limit or between the limits, we will take the above limits as bounds for the plastic drag induced interfacial tensile stress. Since these limits are rather close together and since their mean value of 1.75 k is very nearly the flow stress in tension, Y, we take for the total interfacial tensile stress

$$\sigma_{rr} \simeq Y(\bar{\varepsilon}^p) + \sigma_T \qquad [6]$$

where $Y(\bar{\varepsilon}^p)$ is the flow stress in the region of the inclusion for the average local plastic strain of the region, had the inclusion not been present.

Equation [6] shows that the interfacial stress will increase with strain hardening and with triaxiality. Both of these effects are known to promote cavity formation. The above continuum analysis for an isolated inclusion predicts an interfacial stress dependent only on

the surrounding strain state and negative pressure but not on the size of the particle. We will see below that the particle size effects are a result of particle interactions which occur at large local second phase concentrations and at large plastic strains.

C. Critical Stress Criteria Based on Dislocation Models

In a study of enhanced work hardening due to non-deformable inclusions Ashby[14] proposed a plastic accommodation model of displacement incompatibilities which develop between a homogeneously shearing continuum and a rigid inclusion. The model which is based on Eshelby's[29] approach of considering transformation problems is illustrated in Fig. 7. In a thought experiment the non-deformable spherical inclusion of radius ρ shown in Fig. 7a is removed and replaced by a sphere of parent material. The continuum is plastically sheared by an amount γ which distorts the sphere of parent material into an ellipsoid as shown in Fig. 7b. The distorted ellipsoid is now removed and the non-deformable sphere is to be re-inserted. This requires the elimination of the displacement incompatibilities of a maximum amount of $\gamma\rho/2$. For small shear strains such incompatibilities could be accommodated in the matrix by local elastic deformation. If the inclusion is very small and if the surrounding material lacks operable dislocation sources the elastic stresses could rise until the ideal shear strength is reached at the interface and dislocation loops are punched out to form a plastic accommodation zone shown in Fig. 7c. This plastic accommodation zone reduces the shear stresses around the inclusion. The interfacial normal stresses, however, continue to rise to form a cavity across the principal tensile direction when the interfacial stress reaches the interfacial strength. Although this model is not a fully acceptable upper bound flow field for the reasons already

given above, it is simple and lends itself to the incorporation of many important details. Therefore, we will develop it further.

We assume, together with Ashby, that the ideal shear strength is reached at the interface before the ideal cohesive strength (Kelly, Tyson, and Cottrell[30] have discussed the atomic bonding requirements in different materials for this condition to be satisfied) and that circular loops are punched out and moved away from the spherical inclusion against an effective shear drag k_s. We simplify the problem by considering the dislocation loops as a continuously distributed dislocation density and idealize the model as a cylindrical punch indenting an elastic-plastic cylinder either into or out of a cylindrical hole in a rigid semi-infinite medium against a wall frictional drag of amount k_s which can be taken as the critical resolved shear stress of yielding of a single crystal, as shown in Fig. 8a . We find it necessary to distinguish a number of important alternatives.

a) Very small spherical inclusions ($\rho \lesssim 100$Å): The idealized model is as shown in Fig. 8a. The cylinder of radius $\rho/\sqrt{2}$ is extracted outward (punched outward) by interfacial normal surface tractions σ_{rr} against only a wall friction, it contains no dislocations inside, hence is incapable of undergoing internal plastic relaxation. The normal stresses become dissipated by the wall friction k_s over a length $\lambda/2$ which we term the secondary plastic zone. Choosing coordinates x as shown in Fig. 8a the differential equation for the change of the normal stress along the cylinder is

$$\frac{d\sigma}{dx} - \frac{2\sqrt{2}\,k_s}{\rho} = 0 \qquad [7]$$

where

$$\sigma = E\,\frac{du}{dx} \qquad [8]$$

The boundary conditions are $u = du/dx = 0$ at $x = 0$ (i.e. $\sigma = 0$, at $x = 0$). which gives immediately

$$\sigma = \frac{2\sqrt{2}\,k_s}{\rho}\,x \qquad [9]$$

The extent of the secondary plastic zone is obtained from the displacement incompatibility at the interface, i.e. $u = \gamma\rho/2$ at $x = \lambda/2$, and is

$$\frac{\lambda}{2} = \rho\sqrt{\frac{\gamma E}{2\sqrt{2}\,k_s}} \qquad [10]$$

This gives finally the interfacial tensile stress at $x = \lambda/2$ as

$$\sigma_{rr} = k_o\left(1 + \sqrt{\frac{6\sqrt{6}}{m}\,\frac{\gamma}{\gamma_y}}\right), \qquad [11]$$

where the first term represents the contribution of the distant field and the second term the interfacial stress due to the secondary plastic zone. In Eqn. [11] k_o is the yield stress in shear of the polycrystal and m the well known Taylor factor, i.e. $k_o/k_s = m/\sqrt{3}$, where m is generally taken as 3.1. This stress is again independent of size of the inclusion but increases reatively rapidly with increasing plastic strain as shown in Fig . 9. A cavity would form after a critical plastic strain γ_c when the interfacial stress equals the interfacial strength σ_i i.e. when

$$\gamma_c = \frac{\gamma_y m}{6\sqrt{6}}\left(\frac{\sigma_i}{k_o} - 1\right)^2. \qquad [12]$$

As discussed in Sect. 2.1 reaching the interfacial strength is necessary but not sufficient for cavity formation. The latter requires also that there be enough elastic energy stored in the region to provide for the energy of the free surfaces i.e. the ratio

$$\frac{(\alpha - \alpha_i)\pi\rho^2}{\beta\left(\frac{\sigma_i^2}{2E}\right)\left(\frac{2\pi\rho^3}{3}\right)} < 1 \qquad [13]$$

where the numerator is the surface energy of the cavity and the denominator the elastic energy that can be released by a cavity. In Eqn [13] α is the surface free energy of the cavity, α_i the interfacial energy, and the factor β of order 0.5 is to account for the sharply decreasing tensile stress away from the interface. Considering that $(\alpha - \alpha_i) \approx \sigma_i b/4$ (where b is a lattice dimension), and that $\sigma_i/E \approx 0.02$ one finds that cavities can only open up when

$$\frac{\rho}{b} > \frac{3}{2}\frac{E}{\sigma_i} \approx 75 \qquad [14]$$

For smaller inclusions no stable cavities can form. The inclusion will separate from the matrix a certain distance of atomic dimensions to relieve part of the elastic energy, but long range forces will still act across the interface. In some cases the inclusions may only be very poorly adhered to the matrix, and it can be assumed that $\sigma_i \approx 0$. Then the tensile incompatibility can be accommodated at the interface from the beginning by the formation of a cavity without punching out any secondary plastic zone.

To meet the condition given in Eqn.[14] the inclusion must have a diameter of 400Å or over. For such relatively large inclusions it becomes more and more likely that some retained primary dislocations tangled around the inclusion act as sources and that the punched cylinder can undergo internal plastic relaxation as well.

b) Large spherical inclusions ($\rho > 250$Å):

With internal plastic relaxation inside the punched cylinder the

idealized model is still as shown in Fig. 8a, giving rise to the same differential equation for the change in the normal stress σ by Eqn. [7]. The stress-strain law now is non-linear and may be taken as

$$\frac{\varepsilon}{\varepsilon_y} = \frac{1}{\varepsilon_y}\frac{du}{dx} = \left(\frac{\sigma}{Y_o}\right)^n \qquad [15]$$

where ε_y and Y_o are the yield strain and yield stress in tension respectively, and where the exponent n can be anywhere from 2 to 8 representing decreasing capacities for strain hardening.

The solution of Eqn [7] together with the new non-linear constitutive law, and the same boundary conditions as before can be obtained readily analytically for any exponent n and leads to (see Appendix)

$$\sigma_{rr} = k_o\left[\left(\frac{r}{r_y}\right)^{\frac{1}{n}} + \sqrt{3}\left(\frac{\sqrt{6}(n+1)}{m}\frac{r}{r_y}\right)^{\frac{1}{n+1}}\right] \qquad [16]$$

where again the first term represents the contribution of the distant field. The secondary plastic zone now becomes

$$\frac{\lambda}{2} = \rho\frac{m}{2\sqrt{2}}\left(\frac{\sqrt{6}(n+1)}{m}\frac{r}{r_y}\right)^{\frac{1}{n+1}}. \qquad [17]$$

The increase of stress with plastic strain due to punching of the secondary plastic zone is now considerably slower than in the previous case where plastic relaxation inside the punched out cylinder was not possible. Figure 9 shows the rise of the portion of the interfacial stress resulting from the punching of the secondary plastic zone for the case without relaxation and one where the hardening exponent $n = 2.5$ corresponding to copper. As the strain hardening rate becomes less with increasing exponents n, the rate of rise due to this

component would become progressively less.

It is of interest to compare the above solution for the dislocation loop punching model with the continuum solution. When the hardening rate decreases as $n \to \infty$ the interfacial stress concentration goes asymptotically to

$$\lim_{n \to \infty} \left(\frac{\sigma_{rr}}{\sigma_{\varphi}} \right) = 1 + \sqrt{3} \qquad [18]$$

This value is 89% higher than the lower limit given in Eqn [6] to which it should correspond. Although this solution is not to be preferred to the continuum solution discussed in the preceding section, it gives a result well within a factor of 2 of the latter, and will be useful to investigate specific effects.

c) Interacting Inclusions:

Many investigators have reported that in a given sample large inclusions appear to produce cavities sooner than small ones—a particlularly well reported case being that of Palmer and Smith[31]. Some of the previous explanations of this effect appear to be erroneous such as for instance the energy explanation of Gurland and Plateau[11] which was discussed above to be only a necessary condition for cavitation. The explanation advanced by Palmer and Smith that large inclusions may act as a more efficient sink for embrittling impurities could certainly be valid but cannot likely be responsible for this phenomenon in all cases. It is reasonable to expect that the effect may have its origin in interaction between inclusions. From dimensional analysis it is clear that the stress concentration can not be dependent on inclusion size for the case of an isolated large inclusion (surface energy

restrictions being unimportant) in an infinite medium where there is only one length dimension. When inclusions are in very finite media or when many inclusions are present in a body so that their spacing becomes of the order of their diameter a new length parameter appears in the analysis. It can be readily seen, however, that even in this case the stress concentration will be dependent only on the ratio of inclusion size to spacing. If all inclusions are of the same size this would make the stress concentration dependent only on the volume concentration of second phase but not directly on the inclusion size. It is clear, therefore, that an inclusion size dependence of the stress concentration can occur, at a given volume concentration of second phase, only if local variations of concentration exist, making it possible for some larger than average inclusions to be near neighbors at a spacing equal to or smaller than the average spacing. The situation is sketched out in Fig 8b where the ratio of the net particle distance to the particle size is given by the local concentration c of second phase. Assuming that the interior of the punched cylinder of the secondary plastic zone can undergo plastic relaxation as in the previous case so that a constitutive equation of the type given in Eqn [15] is valid, the interfacial tensile stress can be calculated analytically for a fixed ρ/λ by the previously outlined appraoch only for an exponent of $n = 2$ (see Appendix). A much simpler approximate method can be used, however, to obtain the interfacial stress for any exponent n by breaking down the contributions to the interfacial stress into three sources: a) the strain hardening contribution resulting from the extension of the cylindrical zone as if it were an isolated tension specimen, b) the plastic drag contribution

rising linearly from the center of the cylinder to the interface, and c) the contribution of the distant flow stress. This gives for the interfacial stress

$$\sigma_{rr} = k_0\left[\sqrt{3}\left(\frac{\sqrt{3}\,(\gamma/\gamma_y)}{\sqrt{\frac{2\pi}{3c}}-\sqrt{\frac{8}{3}}}\right)^{\frac{1}{n}} + \frac{\sqrt{6}}{m}\left(\sqrt{\frac{2\pi}{3c}}-\sqrt{\frac{8}{3}}\right)+\left(\frac{\gamma}{\gamma_y}\right)^{\frac{1}{n}}\right] \qquad [19]$$

(see Appendix), where the well known expression for the ratio of the net particle spacing to particle radius in a plane

$$\frac{\lambda}{\rho} = \sqrt{\frac{2\pi}{3c}} - \sqrt{\frac{8}{3}}\ , \qquad [20]$$

was used for a local concentration c of second phase. The change of the interfacial stress with increasing plastic strain is plotted in Figs. 10a, and 10b for two values of n representing those for copper ($n = 2.5$) and steel, ($n = 4$) and for a variety of values of the concentration c. As can be seen from the figure for small concentrations there is no interaction between inclusions.

We now consider first that all particles are of constant size but are distributed randomly in space or on any planar section. If the area allocated per particle is a, then the probability of finding n particles in an area of size A is given by a Poisson distribution as

$$P(n,a) = \frac{1}{n!}\left(\frac{A}{a}\right)^n \exp\left(-\frac{A}{a}\right). \qquad [21]$$

Considering that the chosen area A together with n corresponds to a new concentration

$$c = \frac{n\pi\rho^2}{A} \qquad [22]$$

for a particle radius of ρ, we can obtain readily the probability for finding a local concentration c in integer multiples of the average concentration $\bar{c}$ by letting the area A go to a, i.e.

$$P(c/\bar{c}) = \frac{1}{e}\left(\frac{\bar{c}}{c}\right)! \quad , \left(\frac{c}{\bar{c}} = 0, 1, 2, 3 \cdots\right) \quad [23]$$

To obtain the probability for finding any arbitrary non-integer local concentration between c and c + dc we merely let $n = c/\bar{c}$ become a continuous variable by introducing the gamma function to obtain

$$dP(c/\bar{c}) = \frac{dn/\Gamma(n+1)}{\int_0^\infty dn/\Gamma(n+1)} \quad \left(\text{where } n = \frac{c}{\bar{c}}\right). \quad [24]$$

This leads finally to the probability of having a local concentration variation equal to or greater than c as,

$$1 - P(c/\bar{c}) = \frac{\int_{c/\bar{c}}^\infty dn/\Gamma(n+1)}{\int_0^\infty dn/\Gamma(n+1)} = 0.431 \int_{c/\bar{c}}^\infty \frac{dn}{\Gamma(n+1)} \quad , \quad [25]$$

where the integrals in the numerator and denominator are the incomplete and complete Neumann functions which can be readily evaluated (see E.H. Erdelyi, et al.[32])

This probability is plotted in Fig. 11 as a function of the concentration ratio $c/\bar{c}$. To find the dependence of the plastic strain on the local concentration of second phase we equate the interfacial stress in Eqn [19] to the interfacial strength σ_i. With increasing plastic strain γ, the

separation condition is reached first for closely spaced large inclusions (large local concentration of second phase) followed by inclusions with decreasing size and increasing spacing. The fraction f of the separated inclusions of the total population is then given directly by the cumulative probability of finding regions of local concentration having a concentration in excess of that for which the current plastic strain is sufficient for cavity formation, i.e.

$$f(\gamma) = 1 - P(c/\bar{c}) = 1 - P(c(\gamma)/\bar{c}) . \qquad [26]$$

The application of this approach to inclusions in steel and copper is discussed in the accompanying paper by Argon and Im[16].

Finally, it is of interest to prescribe when inclusions can be considered non-interacting, and when their interaction must be taken into account. Interaction between particles occur when the secondary plastic zones of neighboring particles in the plane of punching touch, i.e. when λ/ρ of Eqn [17] equals that of Eqn [20]. This gives a critical strain ratio $(\gamma/\gamma_y)_{crit}$. above which interactions must be considered.

$$\left(\frac{\gamma}{\gamma_y}\right)_{crit} = \frac{m}{\sqrt{6}(n+1)}\left[\frac{\sqrt{2}}{m}\left(\sqrt{\frac{2\pi}{3c}} - \sqrt{\frac{8}{3}}\right)\right]^{n+1} . \qquad [27]$$

The dependence of this critical strain on the concentration of second phase is shown in Fig. 12 for two strain hardening exponents.

III. Experiments

A direct experimental verification of the approximate analyses presented above was found desirable. Since no meaningful and reliable method of direct interfacial stress measurement could be conceived, it was considered useful to measure the plastic strain distribution around non-deforming inclusions to compare them with the strain distributions obtained for the limiting non-hardening and linear behaviors plotted in Fig. 6. To do this, a model experiment was designed in which the plastic strain distribution in a soft copper matrix could be measured around a hardened cylindrical copper-beryllium inclusion which could be heat treated to have a yield strength about 10 times that of the copper matrix. The model specimen was prepared by drilling a central 0.25 inch hole almost through a 2.5 inch diameter OFHC copper cylinder. This piece together with a graphite funnel containing an amount of castable charge of Cu-Be alloy was placed into a vacuum furnace where the specimen and the inside of the drilled hole was evaporation-cleaned by maintaining the assembly 100°C below the solidus point of the alloy for 45 minutes. The temperature was then raised to above the melting point to cast the charge in place. After this the specimen was cooled to 800°C and maintained there for two hours to homogenize the alloy followed by quenching and tempering at 300°C for two hours to obtain peak hardness. The cylindrical bar with the Cu-Be core was then machined into two 1.75" square blocks of 1.5" thickness with the cylindrical core running along the short length and through the center of the square faces. All faces of the blocks were then polished and

one of the square faces was provided with a fine, scratched square grid of 0.017" spacing running parallel to the edges of the block. The two blocks were then put together face to face so that the grid remained between the blocks. The pair were then compressed 10% in a plane strain compression jig as shown in Fig. 13. The compression faces and the two outside faces touching the jig were coated with a MoS_2 spray to reduce friction. This presented barelling of the specimen. After compression the blocks were removed from the jig, taken apart to reveal the internal grid, which was then measured to compute the distribution of the lateral strain parallel to the principal extension direction. This distribution of the measured normal strains is shown in Fig. 6 for comparison with the theoretically determined bounds for the strain distribution. The actual measured strains are greater than the plastic strains near the inclusion but become smaller than the plastic strains at greater distances. Since the inclusion was not rigid but actually had a fairly high compliance and showed signs of some plastic straining these departures from expected behavior are considered not surprising. In any event the experimental distribution lies nearer to the plastic non-hardening solution than to the linear solution. This lends support to the bounding analysis discussed in Section 2.2

IV. Discussion

The various approximate analyses presented above show that for very small inclusions where no local diffuse plastic relaxation is possible because of the complete absence of dislocations in the surroundings, the shear stresses on the inclusion interface can be relieved by punching out dislocation loops as suggested by Ashby[14]. This can not relieve the interfacial tensile stresses which may reach the interfacial strength. When the inclusion diameter is less than about 400Å there is insufficient elastic energy stored in the surroundings of the inclusion and stable cavities can not form. When the inclusion diameter exceeds this cut-off limit, stable cavities can form. In this range of increasingly larger inclusions, however, local plastic relaxations become more and more likely and a continuum analysis for the stress concentrations becomes appropriate. All such continuum analyses give a rather mild stress concentration factor which for a pure shear mode of deformation is only of the order of $\sqrt{3}$, i.e. the interfacial stress is of the order of the local equivalent flow stress in tension. When the volume concentration of second phase is small so that the secondary plastic zones of particles do not touch, then the particles act in isolation and the interfacial stress is independent of the particle size but depends only on the local flow stress and any local long range triaxial stress. When the volume concentration is large or when the shear strain is large so that the secondary plastic zones of particles touch, the particles interact. If the particles are of uniform size and quasi-uniform spacing, the interfacial stress becomes in addition to the plastic strain, dependent also on the concentration of the second phase but remains still independent of the particle size, i.e. at constant concentration any increase in

particle size is balanced by a proportional increase in particle spacing. The interfacial stress becomes particle size dependent only if there are significant local variations of second phase concentration from point to point for a given average second phase concentration. Such concentration variations actually exist in many inclusion bearing alloys and can account for the often reported effects of particle size on local strain for cavity formation. Experimental evidence for such effects will be presented in the accompanying paper by Argon and Im[16].

References

1. J. Henry: Proc. Am. Assoc. Advancement Science, 1855, vol. 9, p.102.
2. W. A. Backofen: Met. Trans. (Campbell Memorial Lecture, 1973) in the press.
3. K. E. Puttick: Phil. Mag. 1959, vol. 4, p. 964.
4. E. Orowan: Rept. Progress in Physics, 1949, vol. 12, p. 185.
5. A. R. Rosenfield: Metall. Reviews, (No. 121), 1968, vol. 13, p.29.
6. F. A. McClintock: in Fracture (H. Liebowitz, ed.) vol. 3, p. 106. Academic Press, New York, 1971.
7. J. R. Rice, and D. M. Tracey: J. Mech. Phys. Solids, 1969, vol. 17, p. 201.
8. C. A. Berg: in Inelastic Behavior of Solids (M. F. Kanninen et.al.eds.) p. 171, McGraw-Hill, New York, 1970.
9. F. A. McClintock: in Physics of Strength and Plasticity (A. S. Argon, ed.) p. 307, M.I.T. Press, Cambridge, Mass. 1969.
10. J. R. Rice: in Proc. Third Intern. Conf. Fracture (Munich) Part II. (paper I-441), 1973.
11. J. Gurland, and J. Plateau: Trans. A.S.M. 1963, vol. 56, p. 442.
12. K. Tanaka, T. Mori, and T. Nakamura: Phil. Mag. 1970, vol. 21, p. 267.
13. D. Broek: A Study on Ductile Fracture, Ph.D. Thesis Delft, Netherlands, 1971.
14. M. F. Ashby: Phil. Mag. 1966, vol. 14, p. 1157.
15. F. A. McClintock: in Ductility, p. 255, A.S.M. Metals Park, Ohio, 1968.
16. A. S. Argon, and J. Im: Met. Trans., 1974, this issue.
17. L. M. Brown, and W. M. Stobbs: Phil. Mag. 1971, vol 23, p. 1201.
18. A. N. Stroh: Proc. Roy. Soc. (London) 1955, vol. A232, p. 548.
19. C. Zener: in Fracturing of Metals, p. 3 A.S.M., Metals Park, Ohior, 1949.
20. A. N. Stroh: Proc. Roy. Soc. (London) 1954, vol. A223, p. 404.
21. M. F. Ashby: private communication.

22. P. B. Hirsch and F. J. Humphreys: in Physics of Strength and Plasticity (A. S. Argon, ed.) p. 189, M.I.T. Press Cambridge, Mass. 1969.

23. W. C. Huang: Int. J. Solids, Structures, 1971, vol. 8, p. 149.

24. J. Orr, and D. K. Brown: Elasto-Plastic Solution for a Cylindrical Inclusion in Plane Strain, Dept. of Mech. Eng. Report, University of Glasgow, 1973.

25. S. S. Rhee, and F. A. McClintock: in Proc. Fourth U.S. Nat. Cong. Appl. Mech., vol 2, p. 1007, ASME, New York, 1962.

26. B. V. Marcal and I. P. King: Int. J. Mech. Sci. 1967, vol. 9, p. 143.

27. N. I. Muskhelishvilli: Some Basic Problems of the Mathematical Theory of Elasticity, p. 355, P. Noordhoff Ltd. Groningen, Netherlands, 1963.

28. G. N. Savin: Stress Concentration around Holes, p. 260, Pergamon Press, N.Y., 1961.

29. J. D. Eshelby: Proc. Roy. Soc. (London) 1957, vol. A241, p. 376.

30. A. Kelly, W. R. Tyson, and A. H. Cottrell: Phil. Mag., 1967, vol. 15, p. 567.

31. I. G. Palmer, and G. C. Smith: in Proc. Second Bolton Landing Conf. on Oxide Dispersion Strengthening, p. 253, Gordon and Breach, N.Y., 1968.

32. A. Erdelyi, W. Magnus, F. Oberhettinger, and F. G. Tricomi: Higher Transcendental Functions, Vol. 3, p.217, McGraw-Hill, New York 1955.

Appendix

A.1. Interfacial stresses around large spherical inclusions:

The first integral of the differential equation for the normal stress along the secondary plastic zone (Eqn [7], gives

$$\sigma(x) = \frac{2\sqrt{2}\,k_s}{\rho}\,x + C \qquad [A-1]$$

where x is measured from the end of the secondary plastic zone. Using the non-linear constitutive equation of Eqn [15] gives

$$\frac{\varepsilon}{\varepsilon_y} = \left(\frac{2\sqrt{2}\,k_s\,x}{Y_0\,\rho} + \frac{C}{Y_0}\right)^n \qquad [A-2]$$

which when integrated gives the displacement u, also measured from the end of the secondary plastic zone as

$$u = \frac{\varepsilon_y\,Y_0\,\rho}{2\sqrt{2}\,k_s\,(n+1)}\,\xi^{n+1} + D \qquad [A-3]$$

where

$$\xi = \frac{2\sqrt{2}\,k_s\,x}{Y_0\,\rho} + \frac{C}{Y_0} \qquad [A-4]$$

When $x = 0$, $\xi = \frac{C}{Y_0}$ and $u = 0$. This gives

$$u = \frac{\varepsilon_y\,Y_0\,\rho}{2\sqrt{2}\,k_s(n+1)}\left[\left(\frac{2\sqrt{2}\,k_s\,x}{Y_0\,\rho} + \frac{C}{Y_0}\right)^{n+1} - \left(\frac{C}{Y_0}\right)^{n+1}\right] \qquad [A-5]$$

The other boundary condition is that $u = \gamma\rho/2$ when $x = \lambda/2$. This gives

$$\frac{Y\rho}{2} = \frac{\varepsilon_y Y_0 \rho}{2\sqrt{2}\, k_s (n+1)} \left[\left(\frac{\sqrt{2}\, k_s \lambda}{Y_0 \rho} + \frac{C}{Y_0} \right)^{n+1} - \left(\frac{C}{Y_0} \right)^{n+1} \right] \qquad [A-6]$$

← from which the integration constant C could be determined as a function of the yet unknown extent of the secondary plastic zone $\lambda/2$. The secondary plastic zone can then be obtained by substituting $C(\lambda/2)$ into Eqn. [A-1] and setting $\sigma = 0$ at $x = 0$. This, however, tells immediately that $C = 0$, which can only be satisfied if λ is chosen to satisfy Eqn [A-6] for the special value of $C = 0$. This gives the extent of the secondary plastic zone as

$$\frac{\lambda}{2} = \frac{\rho}{2\sqrt{2}}\, m \left(\frac{\sqrt{6}\,(n+1)}{m} \frac{\gamma}{\gamma_y} \right)^{\frac{1}{n+1}} \qquad [A-7]$$

where $m = \sqrt{3}\, k_o / k_s$ and $\varepsilon_y = \gamma_y / \sqrt{3}$ was used in the evaluation.

We now obtain the interfacial stress due to the punching out of the secondary plastic zones as

$$\sigma = k_o \sqrt{3} \left(\frac{\sqrt{6}\,(n+1)}{m} \left(\frac{\gamma}{\gamma_y} \right) \right)^{\frac{1}{n+1}} \qquad [A-8]$$

The distant stress governing the distant plastic strain will also appear across the boundary and must be added to the above stress to obtain the total interfacial stress. This stress is $k_o(\gamma/\gamma_y)^{1/n}$ giving for the total interfacial tensile stress σ_{rr} finally,

$$\sigma_{rr} = k_o \left[\left(\frac{\gamma}{\gamma_y} \right)^{\frac{1}{n}} + \sqrt{3} \left(\frac{\sqrt{6}\,(n+1)}{m} \frac{\gamma}{\gamma_y} \right)^{\frac{1}{n+1}} \right] \qquad [A-9]$$

A-2 Interacting inclusions.

When the secondary plastic zones of particles touch at large concentrations of second phase, or at large plastic strains, the interfacial stress becomes dependent also on the local concentration of second phase. For this case analytical solutions are difficult to obtain and it is more instructive to resort to approximate solutions. An approximate solution can be obtained readily by dividing the interfacial stress up into three parts. The first contribution to the interfacial stress comes from considering the cylindrical interconnecting plastic zone between particles as shown in Fig. 8b as a round tensile bar which has undergone a plastic extensional strain of $\gamma\rho/\lambda$ which results in a stress of

$$\sigma_1 = Y_0\left(\frac{\varepsilon}{\varepsilon_y}\right)^{\frac{1}{n}} = \sqrt{3}\,k_0\left(\frac{\rho}{\lambda}\,\frac{\gamma}{\gamma_y}\sqrt{3}\right)^{\frac{1}{n}} \qquad [A-10]$$

The second contribution comes from the plastic shear drag on the extending cylinder along its walls which is

$$\sigma_2 = k_s\sqrt{2}\left(\frac{\lambda}{\rho}\right) \qquad [A-11]$$

where the shear drag along the wall $k_s = \sqrt{3}\,k_o/m$, can be taken as the critical resolved shear stress for slip in a single crystal, which is the polycrystal yield strength in shear k_o divided by the Taylor factor for shear, i.e. $m/\sqrt{3} = 3.1/\sqrt{3}$.

The third contribution comes from the boundary tractions governing the distant field. This contribution is

$$\sigma_3 = k_0 (\gamma/\gamma_y)^{\frac{1}{n}} \qquad [A-12]$$

The sum of all three contributions gives the total interfacial tensile stress and is the quantity in Eqn. [19].

An analytical solution for the dislocation loop punching component of the interfacial stress, i.e. components 1 and 2 above, can be obtained again readily for $n = 2$, by substituting Eqn [A-6] into Eqn [A-1] and letting $x = \lambda/2$. This would give the interfacial stress as a function of λ/ρ which now, as shown in Fig. 8b is governed by the local concentration of second phase c. The end result is obtained readily as

$$\sigma_m = k_0 \left[\left(\frac{\gamma}{\gamma_y}\right)^{1/2} + \frac{\sqrt{6}}{2m}\left(\frac{\lambda}{\rho}\right)\left(1 + \sqrt{\frac{2\sqrt{3}\, m^2 (\gamma/\gamma_y)}{(\lambda/\rho)^3} - \frac{1}{3}}\right)\right] \qquad [A-13]$$

where

$$\frac{\lambda}{\rho} = \sqrt{\frac{2\pi}{3c}} - \sqrt{\frac{8}{3}} \qquad [A-14]$$

is the ratio of the net distance in the plane of plastic punching to the radius of the particle.

Table Ia. Normalized Radial Stresses σ_{rr}/k around the Inclusion, Measured form a Point under the Tensile Direction

	θ				
γ/(k/G)	4.5°	13.5°	22.5°	31.5°	40.5°
0.770	1.495	1.400	1.025	0.765	0.160
0.848	1.606	1.535	1.125	0.825	0.175
0.925	1.550	1.510	1.070	0.905	0.180
1.000	1.480	1.440	1.000	0.875	0.150
1.080	1.425	1.380	0.930	0.875	0.140
1.158	1.400	1.380	0.900	0.870	0.100

Table Ib. Normalized Tangential Stresses $\sigma_{\theta\theta}/k$ around the Inclusion, Measured from a Point Under the Tensile Direction.

	θ				
γ/(k/G)	4.5°	13.5°	22.5°	31.5°	40.5°
0.770	0.745	0.700	0.510	0.365	0.080
0.848	0.800	0.765	0.560	0.435	0.090
0.925	0.780	0.755	0.535	0.420	0.100
1.000	0.740	0.720	0.500	0.500	0.090
1.080	0.710	0.690	0.465	0.500	0.090
1.158	0.700	0.690	0.450	0.520	0.060

Table Ic. Magnitude of Normalized Tangential Shear Strain $\gamma_{r\theta}/(k/G)$ Around the Inclusion, Measured from a Point Under the Tensile Direction

	θ				
γ/(k/G)	4.5°	13.5°	22.5°	31.5°	40.5°
0.770	0.026	0.570	0.615	0.950	0.970
0.848	0.032	0.622	0.675	1.060	1.080
0.925	0.032	0.610	0.660	1.225	1.250
1.000	0.032	0.675	0.725	1.220	1.240
1.080	0.026	0.692	0.740	1.255	1.275
1.158	0.026	0.725	0.770	1.340	1.360

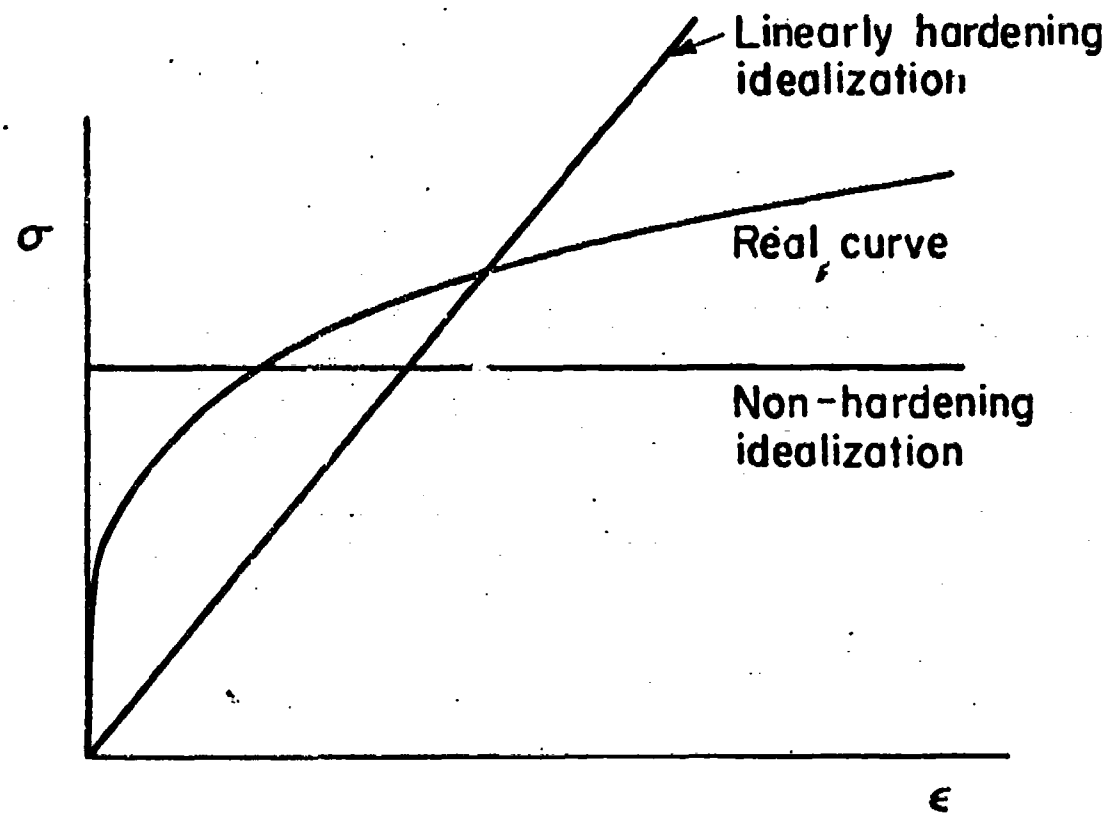

Fig. 1. Idealization of actual plastic behavior by two limiting forms of non-hardening rigid plastic, and linear behavior.

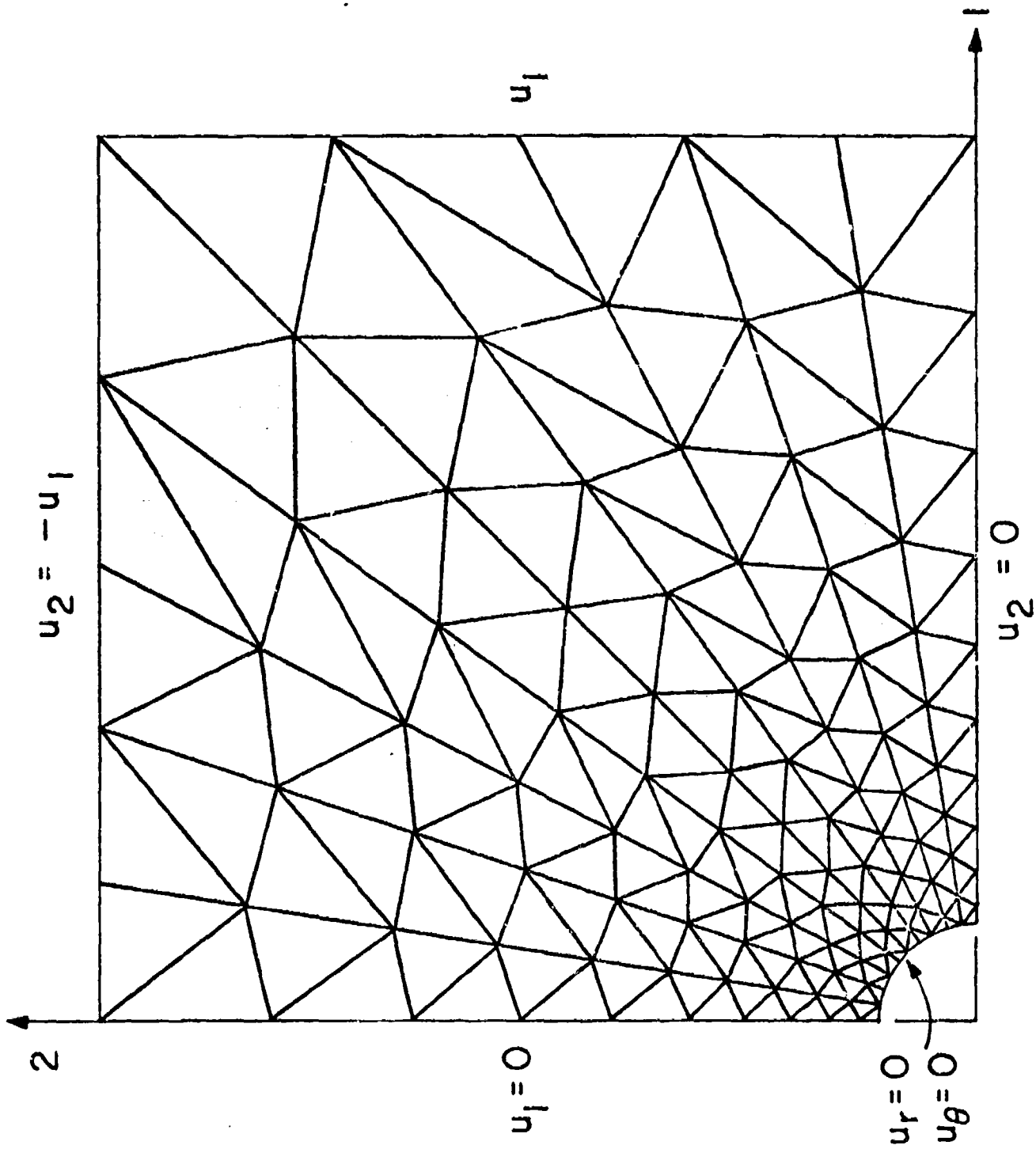

Fig. 2. One quadrant of grid for finite element solution of initiation of plastic flow in pure shear around a rigid cylinder.

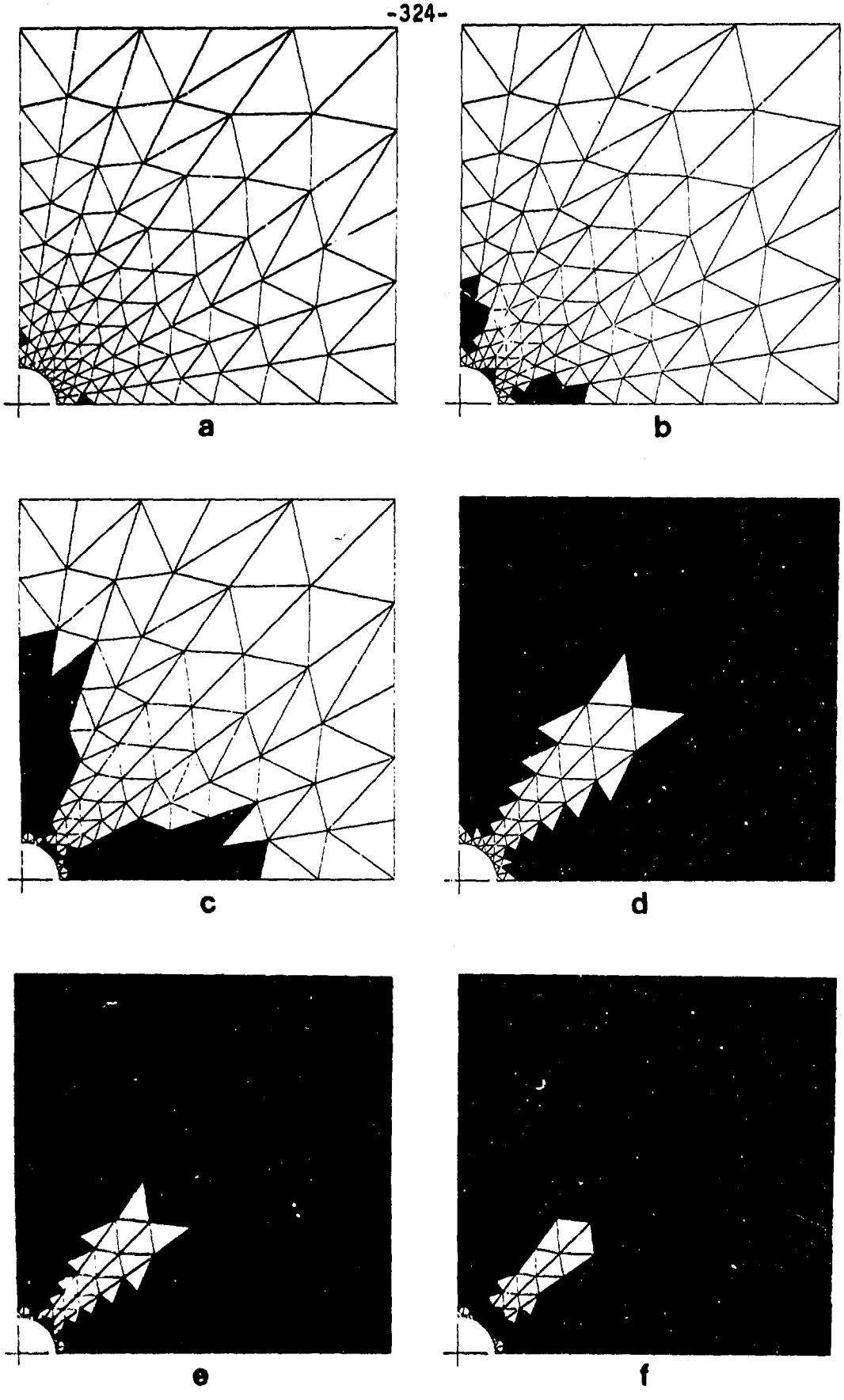

Fig. 3. Spreading of the plastic region (shaded) with increasing boundary displacements for elastic, non-hardening plastic idealization: a) $u_1 = u_o$ where plastic flow is just initiated, b) $u_1 = 1.1\ u_o$, c) $u_1 = 1.2\ u_o$, d) $u_1 = 1.3\ u_o$, e) $u_1 = 1.4\ u_o$, f) $u_1 = 1.5\ u_o$

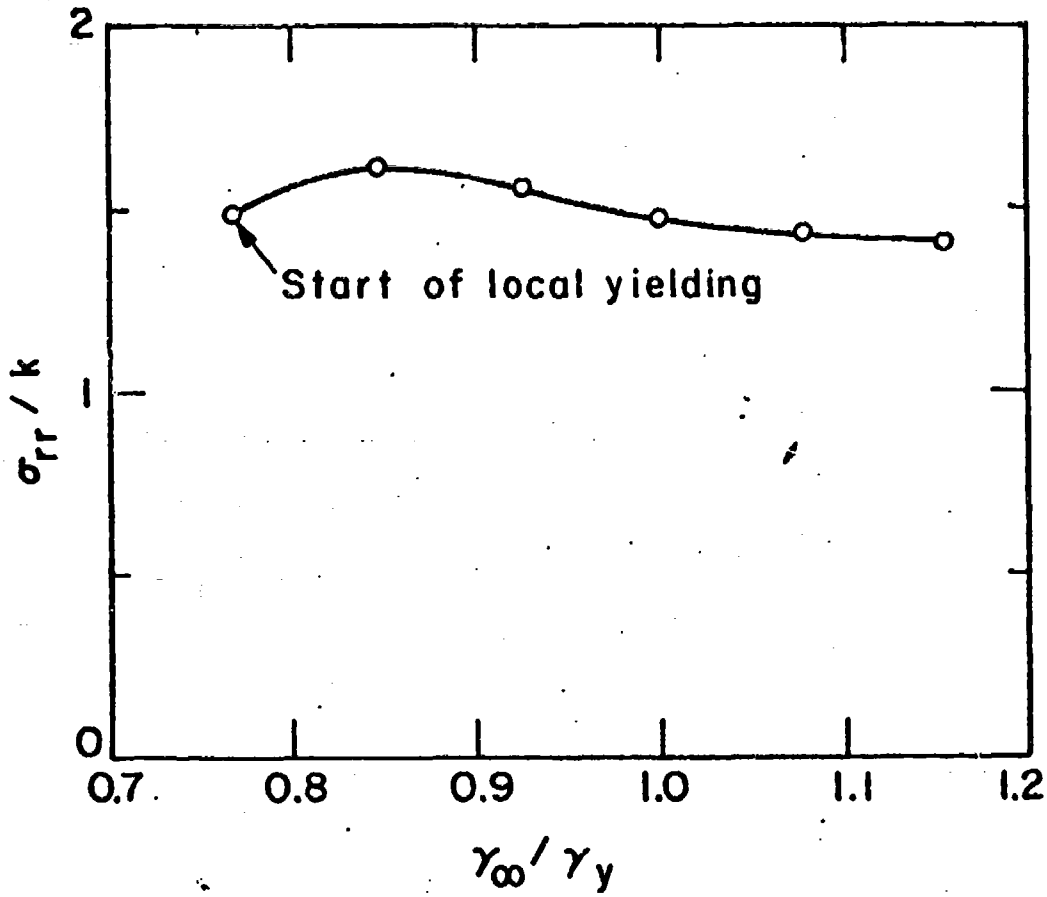

Fig. 4. Change of maximum interfacial tensile stress with increasing boundary strain in non-hardening material.

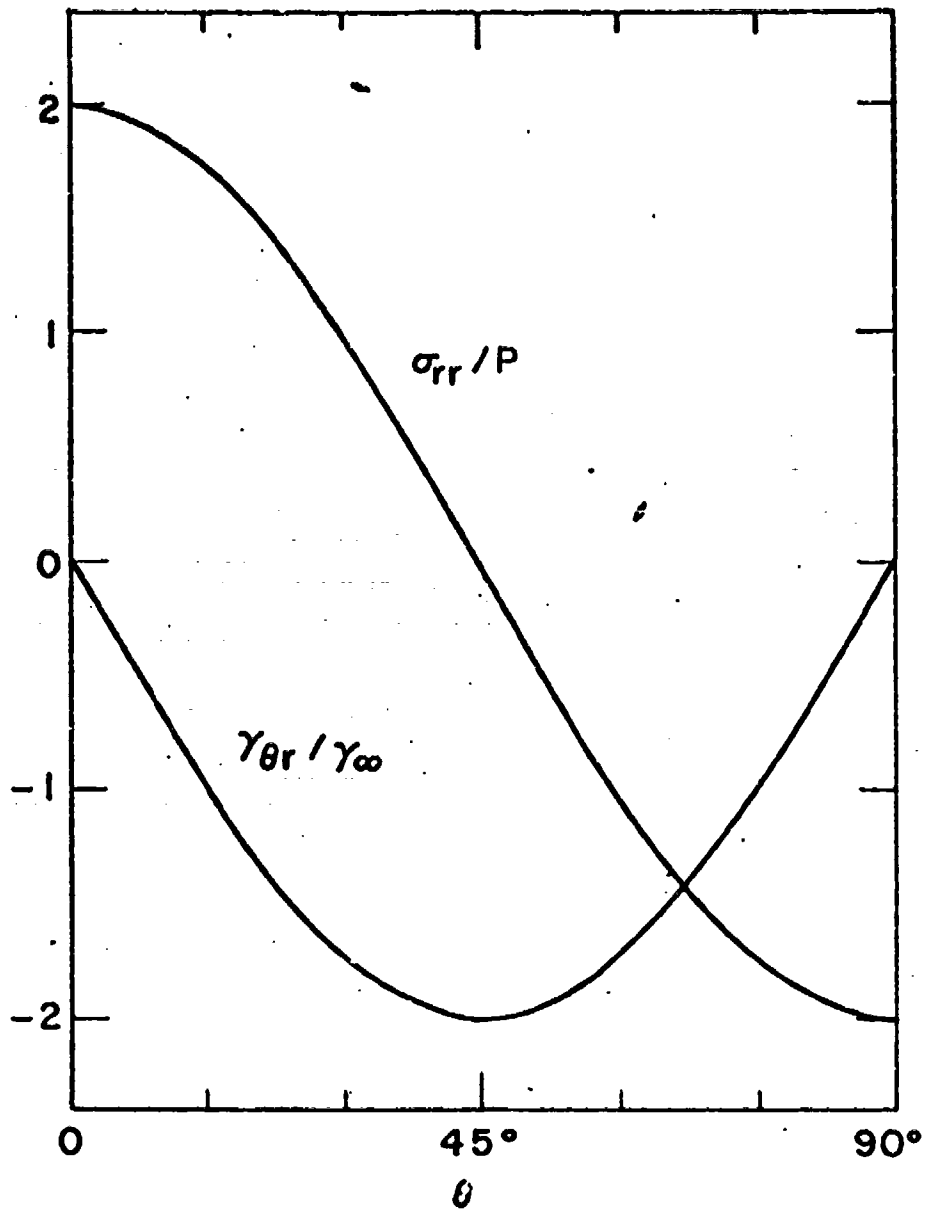

Fig. 5. Distribution of interfacial tensile stress and shear strain around a rigid particle in an incompressible linear matrix.

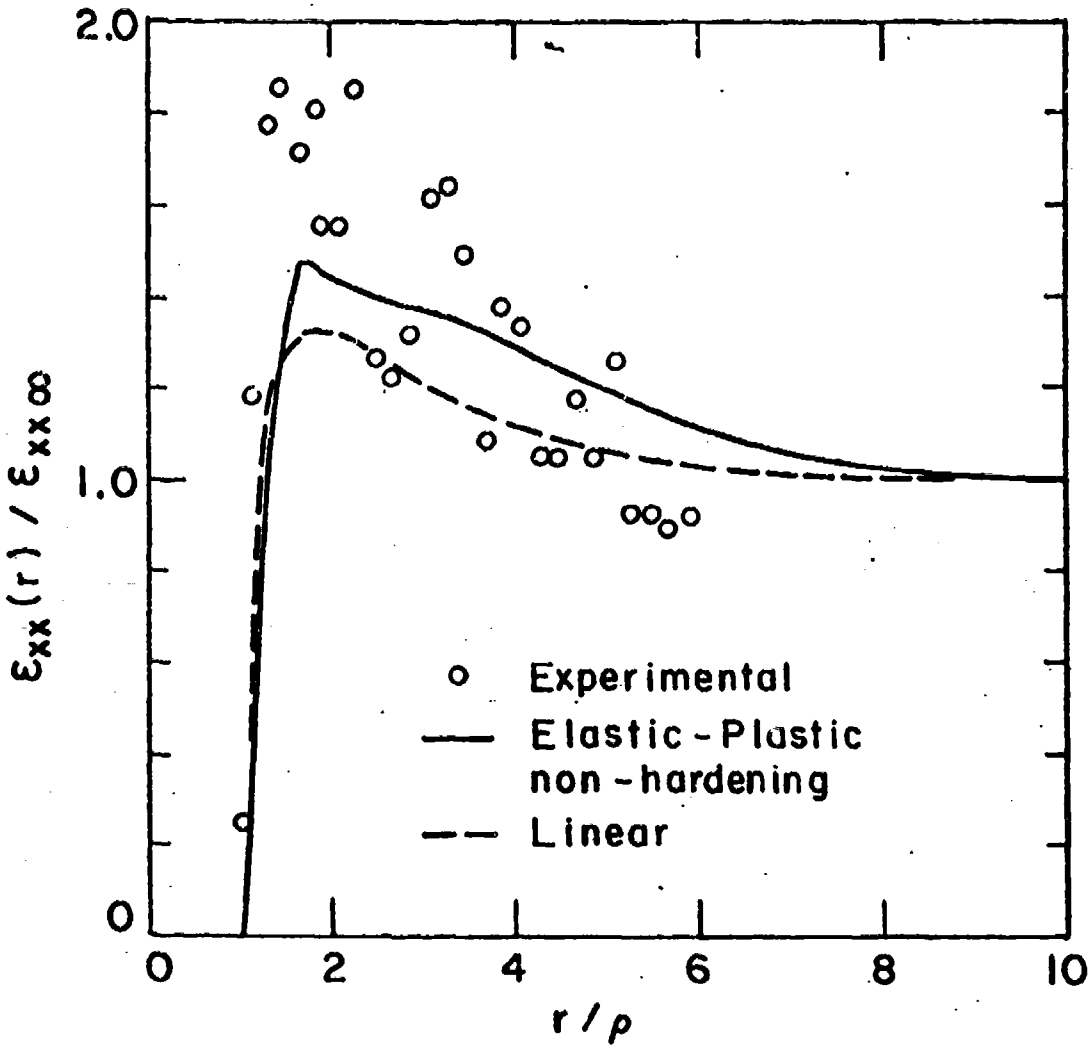

Fig. 6. The distribution of principal total strain ε_{xx} parallel to the tension direction for the elastic, non-hardening plastic material, the linear incompresible material, and experimental measurements on a model copper specimen with a hardened cylindrical Cu-Be "inclusion".

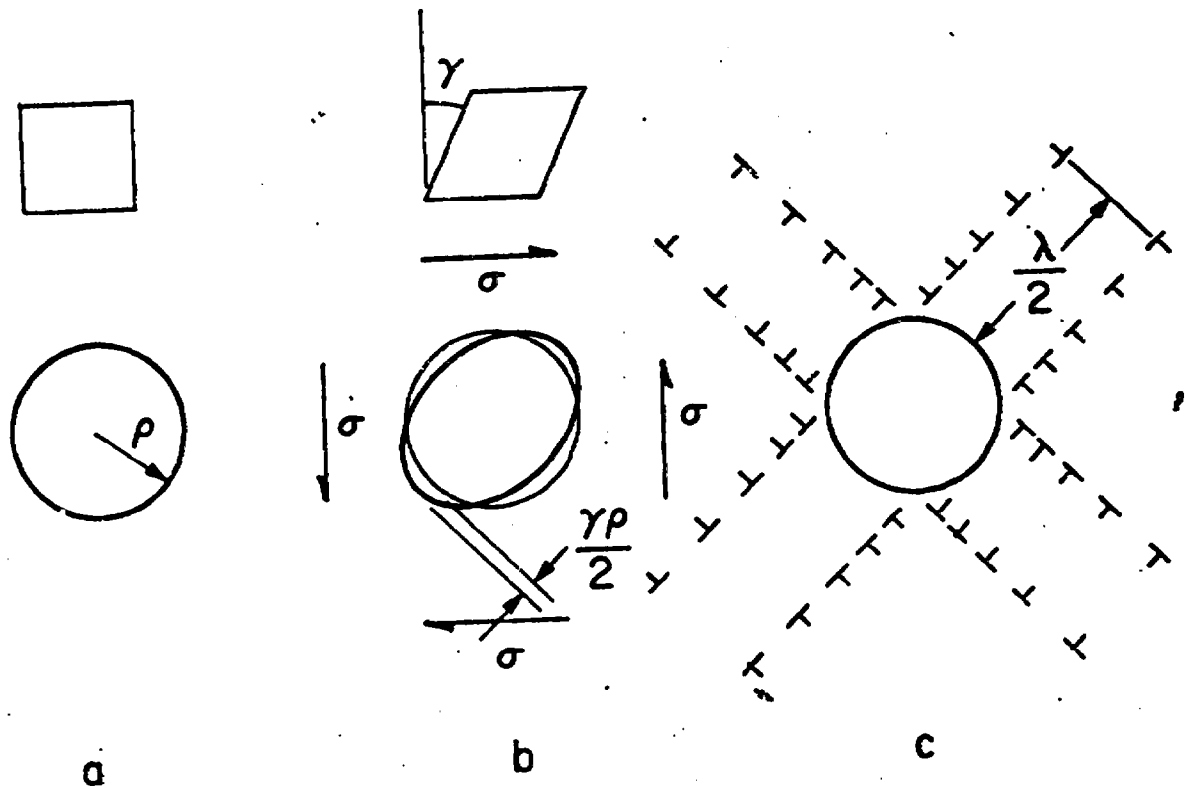

Fig. 7. Ashby's model of the production of a secondary plastic zone to dissipate the elastic shear stresses arising from the interfacial displacement incompatibility upon plastic straining of the matrix.

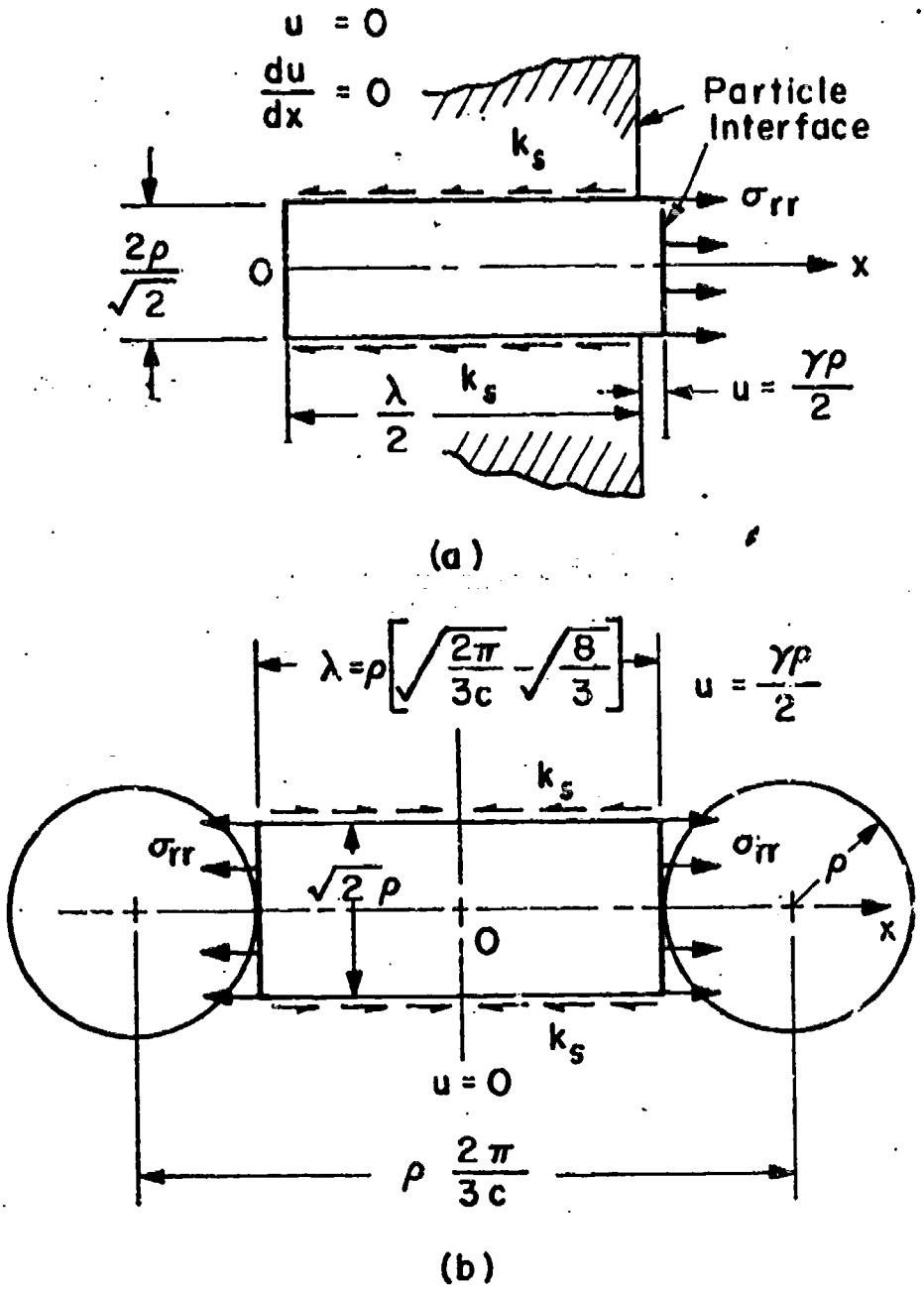

Fig. 8. a) Idealization of the cylindrical plastic punching by a cylinder elastically or plastically extended in a rigid cavity against wall friction; b) Plastic punching between two interacting particles.

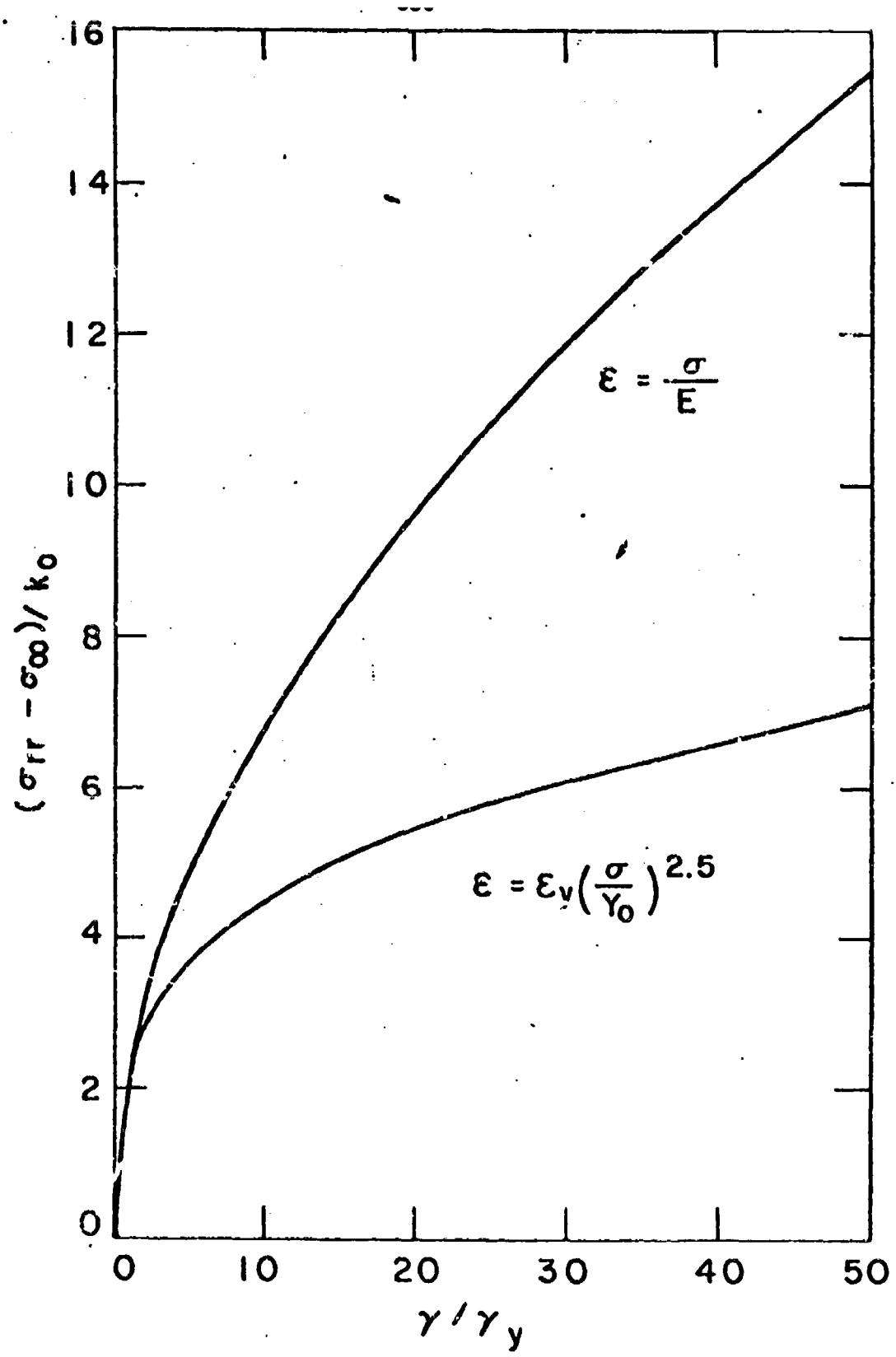

Fig. 9. Change of interfacial stress with increasing distant plastic strain for an elastic plug and a plastic, strain hardening plug.

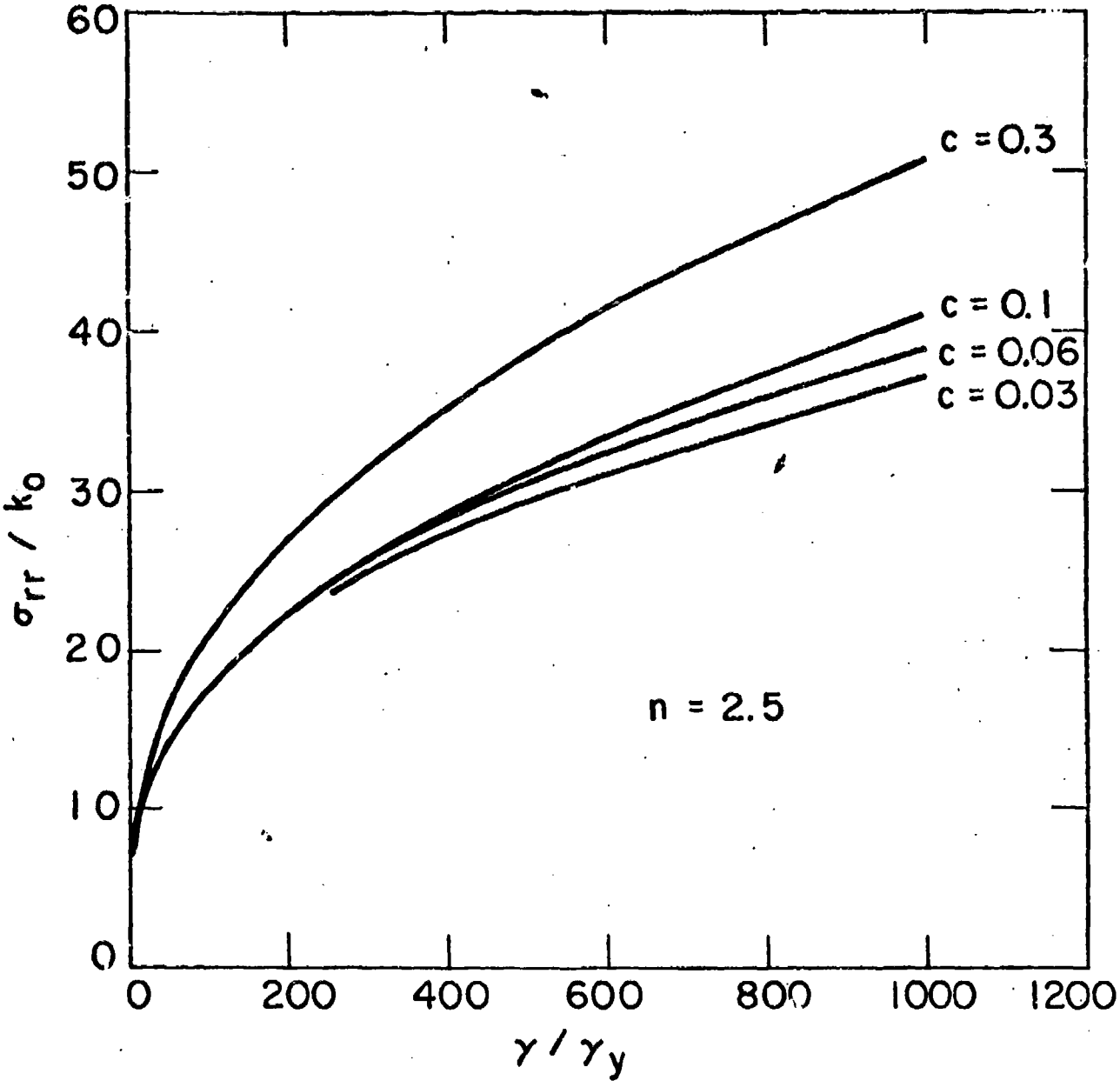
60
50
40
30
20
10
0
0
200
400
600
800
1000
1200
σ_{rr} / k_o
γ / γ_y
c = 0.3
c = 0.1
c = 0.06
c = 0.03
n = 2.5

Figure 10a

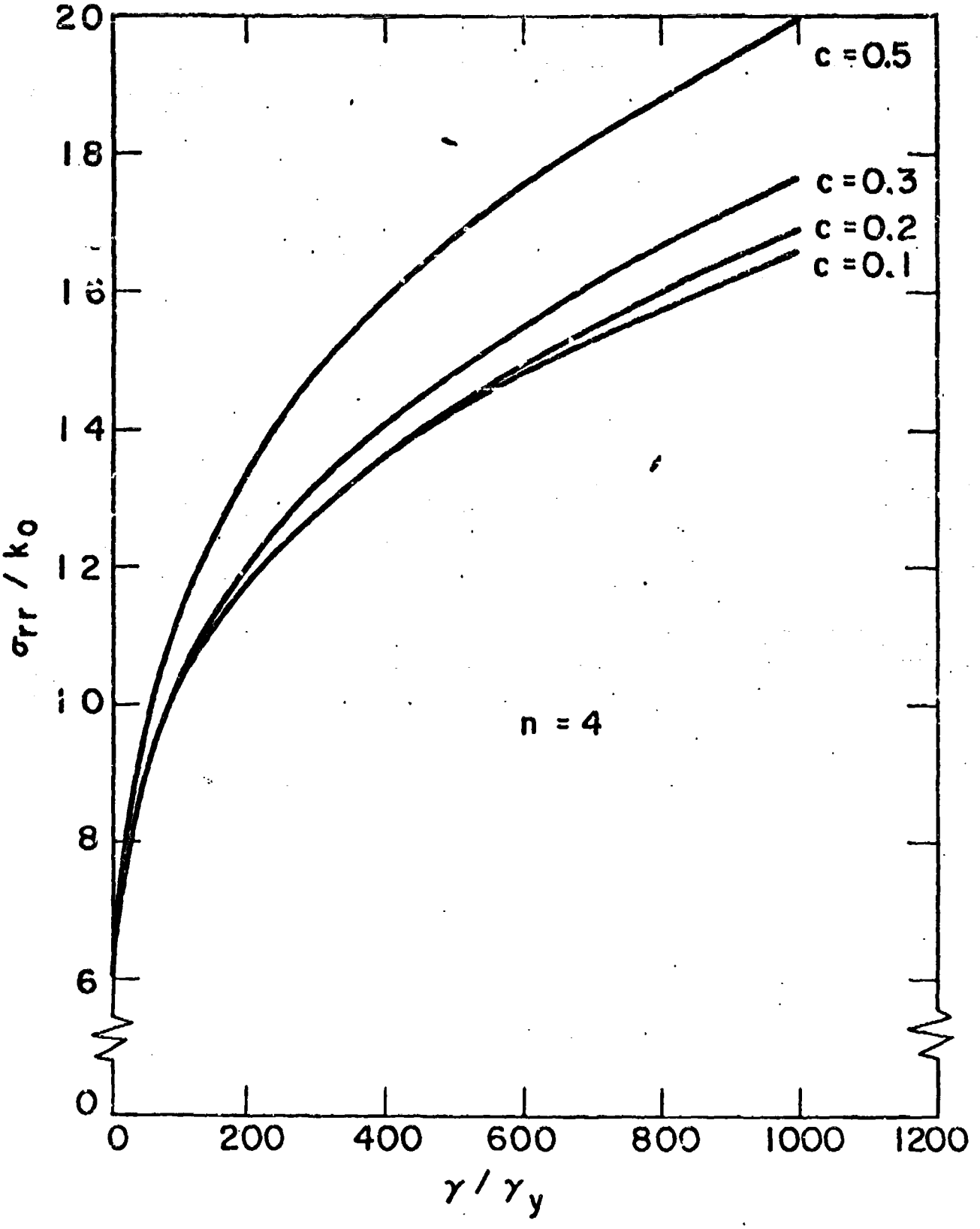

Fig. 10. Dependence of interfacial stress on local second phase particle concentration, a) for copper, n = 2.5, b) for 1045 steel, n = 4.

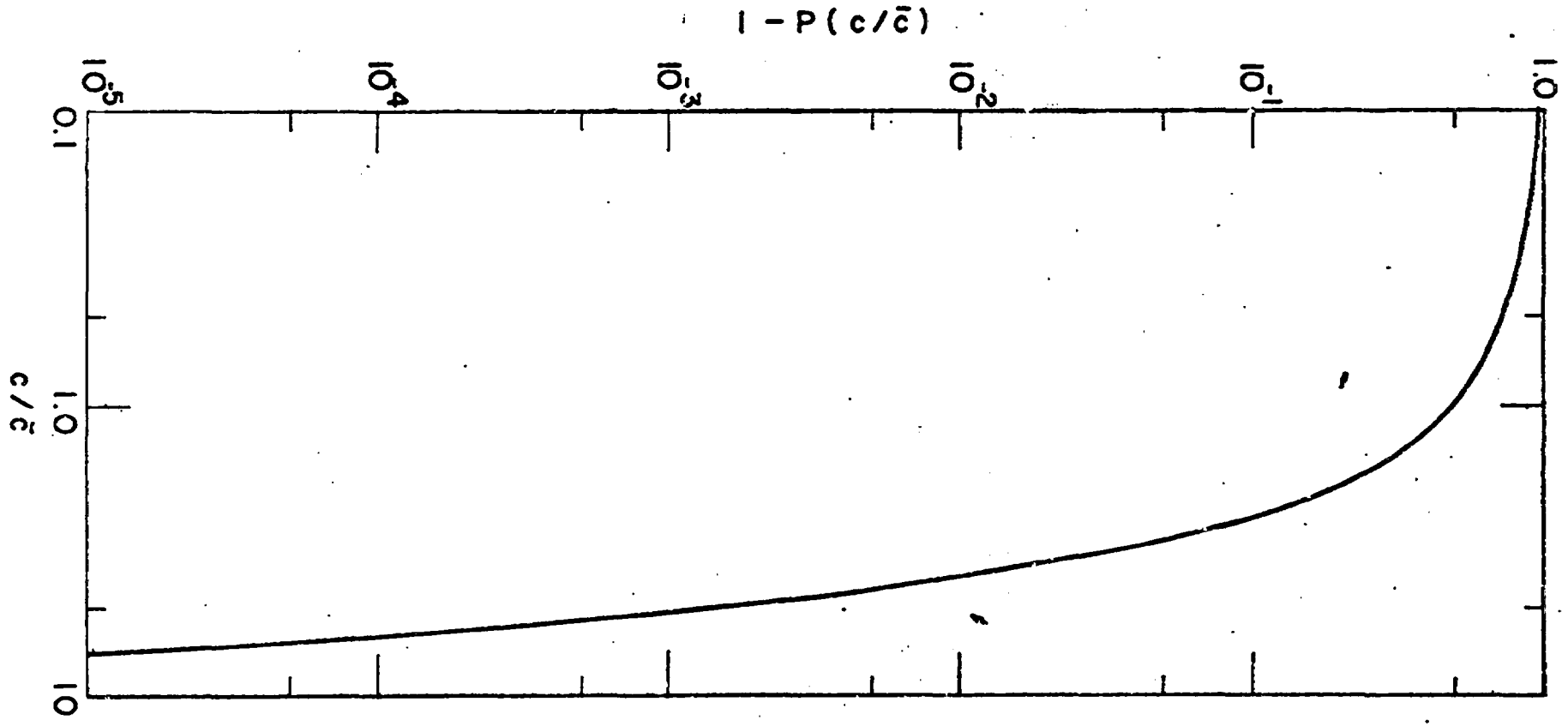

Fig. 11. Probability $(1 - P(c/\bar{c}))$ of finding a local second phase particle concentration in excess of c, when the overall average is $\bar{c}$.

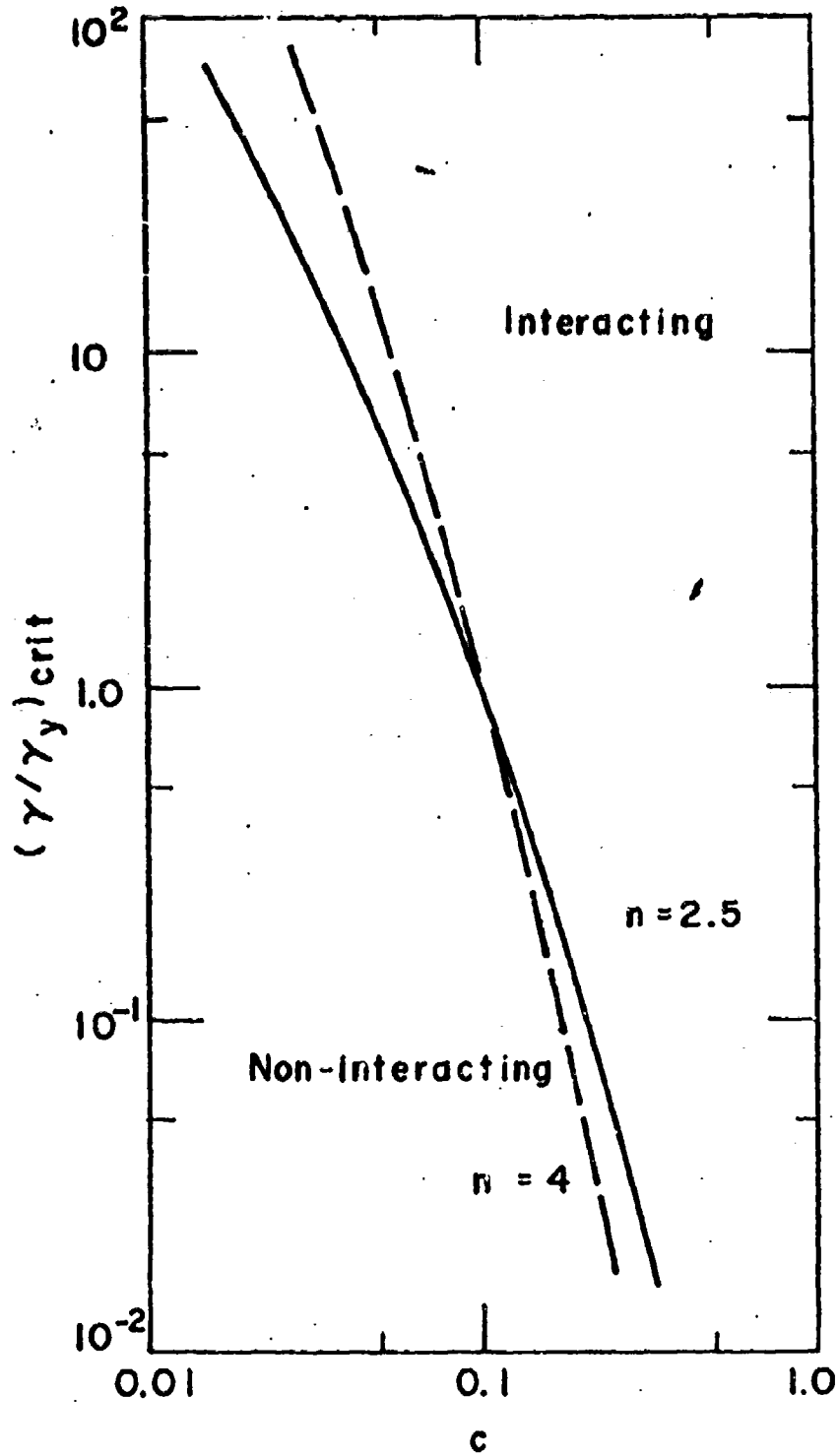

Fig. 12. The dependence of the critical strain ratio for particle interactions as a function of local second phase concentration for two hardening exponents.

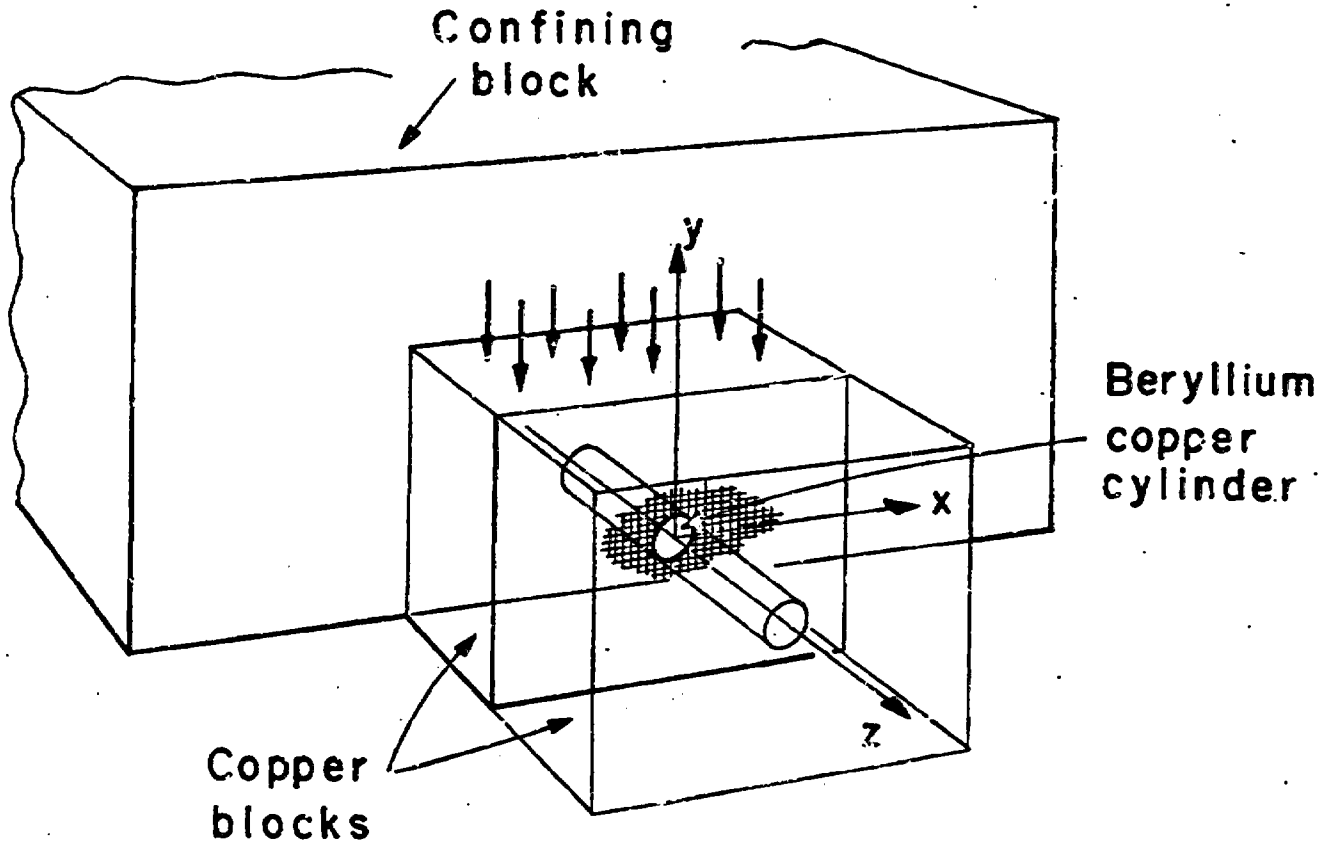

Fig. 13. Experimental arrangement for determining local plastic strains in a copper block with a hardened, cylindrical Cu-Be "inclusion".

SEPARATION OF INCLUSIONS IN SPHEROIDIZED 1045 STEEL, Cu-0.6% Cr ALLOY, AND MARAGING STEEL IN PLASTIC STRAINING (*)

A. S. Argon,(**) and J. Im(**)

Massachusetts Institute of Technology, Cambridge, Mass. 02139

ABSTRACT

Experiments were performed on spheroidized 1045 steel, Cu - 0.6% Cr alloy, and maraging steel containing respectively Fe_3C, Cu-Cr, and TiC inclusions of nearly equiaxed shape. The local interfacial stresses for separation of these inclusions during plastic deformation were evaluated by the methods described in the two preceding papers. The results show that the interfacial strengths for these inclusions in their respective matrices are 254 ksi, 144 ksi, and 264 ksi. In the spheroidized steel the average diameter of the separated inclusions is distinctly larger than the average diameter of the whole population. This is quantitatively explained by the enhanced interfacial stresses developed in regions of above average concentration of second phase which frequently occur in very dense population of inclusions. No such effect was observed in the other two systems which is consistent with their much lower volume fraction of second phase. Some tension experiments have also been performed with the spheroidized 1045 steel at elevated temperature, giving results qualitatively similar to those at room temperature.

---

*This work has been orally presented in part at the Third International Conference on Fracture in München, Germany during April, 1973.

** Department of Mechanical Engineering

I. Introduction

Since the work of Puttick[1] it has been well established that inclusions play a fundamental role in the ductile fracture of metals as the sources of the holes which grow by plastic deformation and link together to produce dimpled rupture. There have been a large number of observations made of these phenomena which have recently been reviewed by Rosenfield[2]. Most such experimental investigations, however, have remained either at the observational level or have been confined to reporting to the concentration dependence of the strain to fracture.[3-6] Furthermore, the majority of the experimental investigations have concentrated on the total problem of ductile fracture which has primarily been viewed from the point of view of plastic hole growth making the tacit assumption that inclusions are synonomous with holes. This is in spite of the fact that problems such as temper embrittlement, where "debonding" trace impurities segregate at interfaces, can only be explained by drastic reductions of the required strain to nucleate cavities at inclusions. In the few experimental investigations which have addressed themselves to the problem of cavity formation at inclusions, Palmer and Smith[7] have found that for spherical SiO_2 inclusions in copper, although small inclusions are more plentiful, the fewer large inclusions form cavities first. In a corresponding study on spheroidized carbon steel, Inoue and Kinoshita[8] have found the strain to fracture (not necessarily the strain for cavity formation) independent of carbide diameter, but the strain for cavity formation increasing with increasing interparticle spacing. There has been no investigation to our knowledge which has

concentrated quantitatively on the conditions for cavity formation. This investigation to be reported below attempts to fill this gap.

II. Experimental Procedure

The goal of this investigation was to study the behavior of equiaxed inclusions in plastic deformation fields of known plastic strain and triaxial stress distribution[9] to determine by means of some approximate analysis of the local interfacial stress concentrations,[10] the actual local conditions for cavity formation. To keep the problem relatively manageable, equiaxed inclusions were chosen for which no shape parameter need be considered. It can be expected that plate-shaped or needle-shaped inclusions will behave differently not only based on their large aspect ratio but also on the orientation of their principal geometrical shape axes relative to the principal axes of the local strain field. This would introduce in addition to two principal aspect ratio parameters, three angular orientation parameters and make the problem immediately very complex. (See also Broek[11]).

The inhomogeneous strain field which was chosen for studying the cavity formation conditions was the round tension specimen with and without initially machined natural neck profiles. Although the triaxial tensile stress (negative pressure) can not be controlled independently from the local plastic strain, it is possible to obtain a large range of triaxiality (ratio of triaxial tensile stress to equivalent flow stress) by providing the bar with initial neck profiles. The distributions of local flow stress and triaxiality in a number of strain hardening materials in round bars with a variety of initial natural neck

profiles have been calculated by Argon, Im, and Needleman[9] for this purpose and are reported in one of the companion papers.

The local interfacial stress for separation of inclusions from the matrix was obtained by plotting the areal density of separated inclusions on an axial section of a fractured bar as a function of the distance z_f away from the fracture surface. The point along the axis where this density of separated inclusions drops to zero is taken to give the local condition for inclusion separation for which the interfacial stress is evaluated by means of the approximate bounding analysis of Argon, Im, and Safoglu [10] which gives this stress as

$$\sigma_{rr} = \sigma_T + Y(\bar{\varepsilon}^p) \qquad [1]$$

for very dilute concentrations of second phase, where σ_T is the local triaxial tensile stress and Y the plastic resistance in tension corresponding to the local average plastic strain, had the inclusion been absent. When the second phase concentration is high and inclusions interact, the interfacial stress increases above the value given by Eqn. [1] and corrections need to be made for such interaction, as described by Argon, et al.[10]

Inclusions in three materials were investigated: Fe_3C inclusions in spheroidized 1045 steel, Cu-Cr inclusions in Cu-0.6% Cr, and TiC inclusions in unaged maraging steel.

The 1045 steel was spheroidized by putting all carbon in solution at 900°C - with nearly finished specimens sealed in Vycor tubes. The steel specimens were then quenched into ice brine immediately after

the Vycor tubes were broken by a heavy pair of steel tongs. This produced a very fine lamellar martensite with a hardness in excess of Rc64. The specimens were then aged in a vacuum system at 700°C for about six days followed by furnace cooling. This produces nearly equiaxed Fe_3C inclusions shown in Fig. 1 of a volume concentration of 0.229 and a mean particle diameter of 0.44 micron. The ferrite grain size was about 5-10 microns. The stress-strain curve of the spheroidized material is given in Fig. 3 of Argon, Im, and Needleman.[9]

The copper with 0.6% chromium was purchased in 5" long swaged bars of roughly 0.75" diameter from American Metal Climax, Inc. Specimens of nearly final shape were machined from these bars and aged at 700°C for over a week to produce a volume concentration of C.0059 of second phase Cu-Cr inclusions of 0.89 micron average diameter. As Fig. 2 shows, these inclusions were not always equiaxed. A small fraction had aspect ratios greater than one, with the largest being about 4. The grain size of the final material was in the range of 20-30 microns. A chemical and spectrographic analysis of the final material gave a composition of 0.005 Cr, 62 ppm C, 5 ppm Fe, less than 1 ppm Ca and Mg. with the balance being copper. The stress strain curve of the fully aged material is given in Fig. 4 of Argon, Im, and Needleman[9].

The maraging steel (VM-300) with a nominal composition of 0.0004 C, 0.001 Mn, 0.001 Si, 0.18 Ni, 0.09 Cr, 0.045 Mo, 0.006 Ti, 0.001 Aℓ with the remainder being iron was purchased from Teledyne Vasco Co. in the form of 0.75" diameter rod. No heat treatment was given to the material tested. The stress-strain curve of the material is given in Fig. 3. In the unaged condition the material had a grain

size of about 10-20 microns and contained two distinctly different types of inclusions: TiC inclusions of a volume concentration of 0.011 and average diameter of 5.3 microns and a much smaller set of Ni_3Mo inclusions of about 0.5 micron diameter or smaller, both shown in Fig. 4. In this study we will concentrate only on the effect of the larger TiC inclusions.

The test specimens were round cylindrical bars of normally 0.375" diameter at the gage section. Some of these bars were machined further to have natural neck profiles according to the empirical neck profile formula given by Eqns. [8] and [9] in Argon, Im, and Needleman[9] to reach different levels of triaxiality and plastic strain distribution in the center portion of the bar when strained. The different initial acuity of the machined neck is given as the neck radius to profile radius ratio a/R in the data below. All specimens were strained to fracture. A 0.5" section from both sides of the fractured pieces was removed. The fracture surface of one side was viewed with the SEM. The other side was given an extra heavy nickel plating, mounted on its side in metallographic compound, sectioned along the axis, and metallographically polished down to 0.25 micron finish. In the case of the copper specimens, best results were obtained with a vibratory polish (Syntron) over prolonged periods. The polished sections were then very lightly etched to delineate the inclusions (Nital or Pickral for 1045 steel and maraging steel, and very dilute HNO_3 for Cu-Cr). The separated inclusions could then be easily seen in the SEM, such as the cases in Figs. 2 and 5.

Some tensile fracture experiments on spheroidized 1045 steel were also conducted at 450°C and 630° in which the same techniques were

followed. Since the specimens were tested in air the fracture surfaces were always oxidized to some extent, so not much meaning was attached to these surface observations.

III. Experimental Results

A. Spheroidized 1045 Steel

As mentioned in Section 2 above, the Fe_3C inclusions in the spheroidized 1045 steel produce a rather concentrated second phase of 0.229 volume fraction of nearly equiaxed inclusions. Some important statistical parameters pertaining to these inclusions were measured on planar sections in the unstrained material. Figure 5 shows the cumulative density of inclusions as a function of their diameter, 2ρ. The mean diameter of the inclusions was found to be 0.443 micron. The cumulative distribution of the net spacing between nearest neighbors of inclusions is shown in Fig. 6. This distribution was obtained by assigning a number to every inclusion in a micrograph of a large area containing a large number of inclusions, drawing inclusion numbers at random, and measuring the distance from the picked inclusions to their nearest neighbor. The figure shows that the mean net distance to the nearest neighbor is nearly equal to the mean diameter of the inclusions. In the separation of the inclusions interaction between nearest neighbors is important and is accentuated by a large ratio ρ/λ_c of inclusion radius to spacing between centers. Figure 7 gives the measured frequency distribution of the ρ/λ_c ratio.

Six tension experiments were performed with three different initial specimen profiles, given by a/R ratios of 0, 0.5 and 1.0. The

specimens were pulled to fracture at a standard extension rate of 10^{-4} in-sec^{-1}. The initial and final dimensions of the specimens are given in Table I. One piece of all fractured specimens was sectioned along the axis, metallographically polished, and etched to reveal the distribution of the density of separated inclusions along the axis. Figure 8a and 8b show the fracture surface dimples and a region near the fracture surface on an axial section where many separated inclusions can be seen. It is readily observable from Figs. 8a and 8b that the spacing of the fracture surface dimples corresponds closely with the spacing of inclusions demonstrating that the Fe_3C inclusions are the sole source of the ductile fracture process. The density distributions of separated inclusions along the specimen axis measured by means of detailed SEM traverses along the axial cross sections of the broken specimens are given in Figs. 9a, 9b, and 9c for the three different initial specimen profiles. The position z_f along the specimen axis where the measured density of separated inclusions goes to zero is given in Table I. The local equivalent plastic strain and triaxiality corresponding to these points were determined from the distributions of plastic strain and triaxiality for the required specimen profiles obtained by Argon, Im, and Needleman[9] (their Figs. 6, 7, and 8). These values are also given in Table I. Finally the last column in Table I gives the computed total interfacial stress at inclusion separation obtained according to Eqn. [1]. The average equivalent strain to fracture obtained from the final and initial radii of the neck which is also given in Table I shows that in each case a very substantial portion of the total strain has gone toward generating

the holes. Inspection of the computed interfacial strengths shows some scatter but no orderly trend with any other parameter. Considering that there is some scatter apparent in the distribution of the density of separated inclusions and that the identification of the position of the last separated inclusion along the axis requires extrapolation, we consider the results satisfactory and compute an average interfacial strength of 203 ksi for Fe_3C in ferrite. This computed strength is an underestimate as Eqn [1] with which it is obtained is valid for non-interacting inclusions. As we will consider further below, the inclusions in 1045 steel are strongly interacting. This could make the actual interfacial strength about 25% higher, i.e. 254 ksi (See Fig. 10b in Argon, et al.[10]).

The dependence of the density of separated inclusions on the inclusion diameter was determined both immediately underneath the fracture surface and a distance $z = 0.32a_o$ away from the fracture surface. These distributions are also shown in Fig. 5 as the two lower curves. The mean diameter, 0.65 micron, of the separated inclusions immediately underneath the fracture surface is 46% larger than the mean diameter of the total population of inclusions. The mean diameter, of 0.732 microns, of the separated inclusions a distance $0.32a_o$ away from the fracture surface is fully 65% larger than the average of the total population. This demonstrates that larger than average size inclusions separate first and that other inclusions of smaller diameter separate at progressively larger plastic strains in a certain inverse relation to their size. Thus the region away from the fracture surface, representing an earlier state of development has a larger fraction of the

large inclusions separated than the region nearer to the fracture surface.

B. Copper with Cu-Cr Inclusions

The Cu-Cr inclusions in copper prepared by the aging treatment discussed in Section 2 above formed a very dilute volume concentration of second phase particles in comparison with the Fe_3C particles in spheroidized steel. Nine specimens were tested having the same three initial profiles as those of the steel specimens, i.e. $a/R = 0$, 0.5, and 1.0.

The dependence of the cumulative density of the Cu-Cr inclusions on their diameters is shown in Fig. 10. As can be seen these inclusions were on the average larger than the Fe_3C inclusions, but their size distribution looks rather similar to the distribution of the latter inclusions.

The results of the tension tests together with pertinent dimensions of the specimens are given in Table II. The appearance of the fracture surface dimples is shown in Fig. 11 where it can be seen clearly by comparing the size of the central holes of the inclusions to the size of the dimples that the inclusion population was quite sparse consistent with the micrograph of Fig. 2. The density distributions of separated inclusions measured on an axial section on the central median plane are given in Figs. 12a, 12b, and 12c. Because of the much sparser overall density of inclusions the distribution along the axis of the separated inclusions shows considerable scatter. The extrapolated values for the position of the last separated inclusion along the axis are given in Table II together with the local plastic

strains, local flow stresses, triaxiality of stress, and finally the computed interfacial strength, all obtained from the analysis of Argon, Im, and Needleman[9] for necked copper bars (their Figs. 9, 10, 11). The average interfacial strength obtained from the last column in Table II is 144 ksi. Once again comparison of the plastic strain for hole nucleation with the overall plastic strain to fracture shows that the nucleation strain is a substantial fraction of the total.

As in spheroidized steel the dependence of the cumulative density of separated inclusions on their size was determined immediately underneath the fracture surface and is shown plotted in Fig. 10. The mean diameter of the separated inclusions is 0.76 micron which is 14.6% less than the mean diameter of the total population. Considering that the total inclusion population is sparse, that the separated inclusions are only about a third of the total, makes this measurement subject to considerable error. We consider this difference not significant and conclude that in this case there is no preference for selecting large inclusions for earlier separation. This as we will discuss below is quite consistent with the sparsity of the second phase concentration, making the inclusions essentially noninteracting.

C. Unaged Maraging Steel

There were two types of inclusions in the maraging steel in the as-received condition on which the tests were performed. Of interest here is only the population of large TiC inclusions forming a volume fraction of 0.011 with an average diameter of 5.3 microns and an average spacing of 45 microns. No statistical measurements

were performed on the size distribution of these inclusions beyond obtaining these average values. Inspection of planar sections of the as-received material showed no separated or cracked inclusions in the as-received material.

Four tensile tests were performed on specimens with four different profile geometries given in Table III, where other dimensions of the specimen before and after the test are recorded. As before the density distribution of separated inclusions was measured on the axial section of the fractured specimens and is given in Figs. 13a and 13b. The location of the last separated inclusion along the axis is also given in Table III. Since the inclusion spacing was quite large and the density sparse, the distribution shows considerable scatter and the position of the last separated inclusion determined by extrapolation is again subject to some scatter. Since no special computation was made for the distribution of plastic strain and triaxiality for this material according to Needleman's method, and since the strain hardening rate was extremely low, the extension of the Bridgman analysis discussed by Argon, Im, and Needleman[9] was used to compute the interfacial strength of the inclusions. In view of the approximations made the results are not considered to be as reliable as those for the 1045 steel and the Cu-0.6% Cr discussed above. In any event the end result shows very little scatter and gives an average interfacial strength of 264 ksi. Since the density of TiC inclusions was quite low they were not interacting (see Fig. 12 in Argon et al[10]) and no correction is necessary on this value. Finally Fig. 14 shows the appearance of the fracture surface dimples. The large dimples of the TiC inclusions stand out clearly from

Ni_3Mo inclusions which produce dimples of a diameter an order of magnitude smaller than the TiC inclusions.

D. Spheroidized 1045 Steel at Elevated Temperature

To compare the behavior of inclusion bearing structural material at elevated temperature with that at room temperature it was considered advisable to perform a number of tests at elevated temperatures on the spheroidized 1045 steel.

Specimens were prepared for elevated temperature deformation in the same manner as for room temperature. No special profiles were machined into the bars since no reliable method of evaluation of local stress existed for the highly rate dependent deformation to which the specimens were subjected. Tests were performed at 450°C and 630°C in air in a resistance heated furnace, at a conventional extension rate of 10^{-4} in sec^{-1}.

Statistical measurements were made on the inclusions on planar sections before and after the experiments. Because of a somewhat less successful spheroidization the Fe_3C inclusions were not fully equiaxed and even had a characteristic pearlite type structure. This was particularly so in the material used for the 450°C tests, as can be seen from Fig. 15 showing the microstructure after the test along an axial section. The microstructure of the corresponding specimen used in the 630°C test is shown in Fig. 16. As a result of this difference the mean nearest neighbor distance of the 450°C material was only $\bar{\lambda} = 0.134$ micron while that of the 630°C material was $\bar{\lambda} = 0.182$ — both being considerably less than that in the material used for the room temperature tests. Figures 17 and 18 give the dependence of the

inclusion density or average inclusion diameter (average diameter being defined as the geometric mean value of the two extreme dimensions of the inclusions).

The specimens were sectioned along the axial median plane as before to determine the density distribution of separated inclusions along the axis. These distributions are shown in Fig. 19. The difference in the spatial densities of separated inclusions for the 450°C and 630°C experiments shown in Fig. 19 is entirely a result of the larger size inclusions existing in the material used for the 630°C experiments. The size distributions of the separated inclusions was also measured immediately underneath the fracture surface as before and are plotted in Figs. 17 and 18 for the respective cases. In both cases the mean diameter of the separated inclusions is larger than the mean diameter of the total population — being a result of interaction between inclusions. The difference between the two mean diameters is larger for the 630°C experiment which is nearly of the same ratio as that in the room temperature experiments. The smaller difference between the mean diameters of the separated inclusions and that of the total population in the 450°C is most likely a result of the extremely elongated nature of the inclusions in this material. Apart from these minor differences the results at these two temperatures are rather similar and qualitatively the same as the room temperature experiments.

Because of the strongly rate dependent nature of the deformation the necks formed on the specimens were rather drawn out. This and the formation of a heavy oxide layer made it not very meaningful to try to compute interfacial stresses by invoking Hoff's[11] analogy

for rate dependent materials obeying a power law creep. Finally the appearance of the fracture surfaces for the 450°C and the 630°C experiments are shown in Figs. 20 and 21 where it is clear that the surface features have been markedly affected by both oxidation and diffusional smoothing.

IV. Discussion

Inspection of the results in Tables I - III for the three materials tested indicates that, as suspected, cavity formation occurs at inclusions when the interfacial stress produced by the combined effect of both the drag of the plastically flowing surrounding matrix, and the local triaxial tensile stress reaches the interfacial strength. The computed interfacial strengths of 254 ksi (with a correction for inclusion interactions) 144 ksi, and 264 ksi for the Fe_3C, Cu-Cr, and TiC inclusions in their respective matrices must be compared first with the ideal cohesive strengths of the matrices. Taking the respective Young's moduli as a scale parameter of the ideal cohesive strengths one obtains ratios of σ_{rr}/E for the three cases of 0.0088, 0.008, and 0.009 respectively. The ideal cohesive strength of a perfect close packed metal is likely to be no less than 0.05E.[12] It is known from the experiments of McClintock and O'Day[13] on the strengths of soap bubble rafts which can be made to simulate the interatomic forces between metal atoms, that high angle grain boundaries have a cohesive strength of about half the value of the perfect lattice. Such experiments have demonstrated visually possible grain boundary phase transformations occurring prior to cavity formation which have also been discussed

theoretically by Hart.[14] It is not unlikely that the strength of interfaces are less than the strength of high angle boundaries of the parent material as there are no observations of separation of grain boundaries accompanying separation of inclusions in ductile fracture. Based on this it can be expected that the cohesive strength of interfaces be somewhat lower than $0.025\underline{E}$ in the materials which we have considered. This is within a factor of 3 of the actual interfacial strengths reported above. Considering that the analysis employed in arriving at the reported values of interfacial strengths is relatively crude, that there are additional stress amplification effects that result from departures from spherical shape in the actual inclusions, and considering that the presence of embrittling trace impurities can reduce the interfacial strength markedly[15], the computed results are taken to be the actual interfacial strengths between the inclusions and the respective matrices. As mentioned in the introduction any reduction of interfacial strength by undesirable impurities would reduce the strain for inclusion separation and thereby the tensile fracture toughness. Any other effect which accentuates the development of interfacial stress such as large aspect ratios of inclusions, interaction between inclusions arising from a high concentration of inclusions, or an increase of the flow stress by various diffuse hardening mechanisms will all hasten the separation of inclusions to decrease the fracture toughness. The widely known empirical correlation between hardening and decreased ductility is at least in part a result of a reduction of the strain for inclusion separation. The well known reduction in ductility to fracture with increasing second phase particle concentration

reported first by Edelson and Baldwin[3] is of course not directly related to the effect we have been discussing; it is primarily a result of the reduction of the strain for plastic growth and linking of the holes after their formation.

In his review Rosenfield[2] concluded that the available evidence was not consistently demonstrating that large inclusions separate before small ones do for a given second phase concentration of particles. The considerations of Argon, Im, and Safoglu[10] on inclusion interaction furnish a ready explanation. As Fig. 12 in the paper of the above authors shows, when the second phase has a volume fraction of around 0.01 the inclusions will on the average not interact and behave as if they were isolated to very large plastic strains, of the order of 10^3 times the yield strain. For such cases all inclusions of a diameter in excess of about 200 Å (for which the necessary energy conditions for free surface production are satisfied[10]) will separate at approximately the same pre-strain. When the volume concentration of inclusions becomes of the order of 0.1 or larger, as in the case of the spheroidized 1045 steel, the inclusions interact almost from the very beginning of plastic straining. Such interactions produce accentuated interfacial stresses on larger than average inclusions situated at spacings less than average, i.e. regions in which the local concentration of second phase exceeds that of the average will be preferencially cavitated first. This will be followed by regions in which the second phase concentration is progressively lower. It is possible to account for the distribution of the observed density of separated inclusions along the axes of the fractured specimens, as well as the increase of the average diameter of separated

inclusions with increasing distance from the fracture surface by the interactions of inclusions as discussed by Argon, Im, and Safoglu.[10] The distribution of the ratio of inclusion radii to spacing given in Fig. 7 can be shown more instructively as a distribution of local second phase concentration by plotting it as a function of the square of the abscissa. If this distribution is normalized with its mean value it gives directly the cumulative probability $(1 - P(c/\bar{c})$ for finding a local concentration ratio in excess of $c/\bar{c}$ which as discussed by Argon, Im and Safoglu[10] obeys a distribution given by a ratio of incomplete and complete Neumann functions (see their Fig. 11). The experimental distribution for Fe_3C particles is plotted in Fig. 22 together with the theoretical distribution of Argon, Im, and Safoglu. The agreement is good. Argon, et al[10] have also shown that when the local inclusion concentration c is high their secondary plastic zones interact to increase the interfacial stress for a given plastic strain above the level of noninteracting inclusions. The result of their development is re-drawn in Fig. 23. If inclusions separate when the interfacial strength reaches a critical value this would occur first in regions of large concentration, $c > \bar{c}$ resulting in the separation of the fraction of inclusions which forms a local concentration in excess of c given by the function shown in Fig. 22. As the material is strained further, regions of lower inclusion concentration continue to undergo separation and the state of the cavitation advances along the curve in Fig. 22 from the lower right toward the upper left. In the neck region of a specimen (such as specimen 5 or 6 of the spheroidized steel) the cavitation history is stored advancing along the axis toward the fracture surface.

The separated fraction of inclusions given in Fig. 9b for specimens 5 and 6 is replotted as a function of total local equivalent strain in Fig. 24 as the six points by using the equivalent strain distribution computed for these specimens by Argon, et al [9] (their Fig. 7). To determine the theoretical distribution of the separated fraction as a function of strain, the intercepts of the curves for interfacial stress in Fig. 23 with the interfacial strength is necessary. Along the axis of specimens 5 and 6, however, there is also a sizable component of triaxial stress which can not be ignored. The local triaxial tensile stress obtained from Fig. 7 in Argon, Im, and Needleman is plotted in Fig. 23 below the abscissa axis as a function of the local equivalent plastic strain. The total difference between the curves above and below the abscissa axis in Fig. 23 gives the total interfacial tensile stress. When that difference equals the interfacial strength, inclusions separate. The computed distribution curve for the fraction of separated inclusions given by the solid curve in Fig. 24 is obtained by choosing $\underline{\sigma_{rr}} + \underline{\sigma_T} = 18.5\underline{k_o}$. Since $\underline{k_o} = 28.9$ ksi, see Table II of Argon et al[9] the required interfacial strength to obtain the theoretical curve is fully 535 ksi - far in excess of the value obtained by the direct evaluation discussed above. This apparent discrepancy is partly attributable to the approximate nature of the computation of the stresses around inclusions, resorted to analyze the interaction between inclusions. As discussed by Argon, et al[10] the approximate analysis gives values 89% higher than the more preferable continuum analysis which, however, has not been developed for interaction effects. Allowing for this excess in the analysis which lead

to the curves in Fig. 23, one requires only an interfacial strength of 283 ksi to obtain the agreement in Fig. 24. This is to be compared with the strength of 254 ksi obtained by the direct method after correction was made for inclusion interactions. The agreement between the two approaches is still somewhat poor, but in view of the many approximations made and possible experimental errors the model for the computation of the distribution of separated inclusions along the axis of a specimen discussed here is considered valid.

We close by reaching several general conclusions:

1. The criterion for the separation of inclusions from a deforming matrix is a critical interfacial stress criterion.

2. When inclusion concentrations are large, they interact to enhance the interfacial stress and hasten separation.

3. In normally annealed material without pre-processing, the plastic strain required to separate the inclusions often exceeds one half the total strain to fracture.

4. In as-received material previously subjected to cold working, inclusions may already be separated if the cold working strain exceeds a critical amount.

5. In deformation processing if no damage is to be produced which would reduce service ductility or toughness, the increments of deformation between annealing operations will have to be governed by the critical strain for inclusion separation.

6. Further quantitative progress on this problem requires more accurate solutions for interacting inclusions.

REFERENCES

1. K. E. Puttick: Phil. Mag. 1960, vol. 5, p. 759.

2. A. R. Rosenfield: Metall. Reviews, (No. 121), 1968, vol. 13, p. 29.

3. B. I. Edelson, and W. M. Baldwin, Jr.: Trans ASM, vol 55, p. 230, 1962.

4. J. Gurland, and J. Plateau: Trans. ASM, vol. 56, p. 442, 1963.

5. D. Brock: A Study on Ductile Fracture, Ph.D. Thesis Delft, Netherlands, 1971.

6. L. M. Brown, and J. D. Embury: in Abstracts, Third International Conference on Strength of Metals and Alloys, Cambridge, England, Aug. 20, 1973.

7. I. G. Palmer and G. C. Smith: in Proc. Second Bolton Landing Conf. on Oxide Dispersion Strengthening, p. 253, Gordon & Breach, N. Y., 1968.

8. T. Inoue and S. Kinoshita: in Abstracts, Third International Conference on Strength of Metals and Alloys, Cambridge, England, Aug. 20, 1973.

9. A. S. Argon, J. Im, and A. Needleman: Met. Trans, 1974 this issue.

10. A. S. Argon, J. Im, and R. Safoglu: Met. Trans, 1974, this issue.

11. N. J. Hoff: Quart. Appl. Math., 1954, vol 12, p 49.

12. A. Kelly: Strong Solids, p 5, Oxford University Press, 1966.

13. F. A. McClintock, and W. R. O'Day, Jr.: in Proc. First International Conference on Fracture, (T. Yokobori, et al eds.) vol 1, p 75, Japanese Society for Strength and Fracture, Sendai, 1966.

14. E. W. Hart: in Nature and Behavior of Grain Boundaries (H. Hu, editor) p. 155, Plenum Press, New York, 1972.

15. H. L. Markus, L. H. Hackett, Jr., and P. W. Palmberg: in Temper Embrittlement of Alloy Steels, ASTM-STP-499, p 90, ASTM Philadelphia, 1972.

TABLE I Spheroidized 1045 Steel, Stress for Separation of Fe_3C Inclusions

Spec. No.	$(a/R)_i$	$(a/R)_f$	a_o mm.	a_i mm.	a_f/a_i	$\bar{\varepsilon}^p_f$	z_f/a_o	$\bar{\varepsilon}^p_n$	$Y(\bar{\varepsilon}^p_n)$ ksi	σ_T/Y	σ_{rr} ksi
1	0	1.00	4.76	4.76	0.589	1.06	0.575	0.64	121	0.470	178
2	0	0.95	4.76	4.76	0.589	1.06	0.550	0.67	122	0.580	193
5	0.5	1.35	6.35	3.54	0.680	0.77	0.400	0.40	127	0.740	221
6	0.5	1.44	6.35	3.54	0.650	0.86	0.430	0.40	127	0.720	219
7	1.0	2.13	6.35	2.80	0.600	1.02	0.383	0.28	117	0.735	203
8	1.0	2.33	6.35	2.80	0.632	0.92	0.367	0.27	113	0.780	201

a_o = shoulder radius

a_i = initial radius of the neck

a_f = final radius of the neck at fracture

$(a/R)_i$ = initial ratio of neck radius to profile radius at fracture

z_f = position along the axis of the last separated inclusion

$\bar{\varepsilon}^p_n$ = equivalent plastic strain at the site of the last separated inclusion

$Y(\bar{\varepsilon}^p_n)$ = equivalent tensile flow stress at $\bar{\varepsilon}^p_n$

σ_T/Y = triaxility ratio

σ_{rr} = interfacial stress at separation of inclusions

$\bar{\varepsilon}^p_f$ = equivalent plastic strain at fracture

Table II Copper - 0.6% Chromium, Stress for Separation of Cu-Cr Inclusions

Spec.No	$(a/R)_i$	$(a/R)_f$	a_o mm	a_i mm	a_f/a_i	$\bar{\varepsilon}_f^p$	z_f/a_o	$\bar{\varepsilon}_n^p$	$Y(\bar{\varepsilon}_n^p)$ ksi	σ_T/Y	σ_{rf} ksi
1	0	1.10	4.760	4.760	0.452	1.58	0.570	1.27	73	0.87	13
2	0	1.25	4.760	4.760	0.424	1.72	0.590	1.33	74	0.92	14
3	0	1.09	4.760	4.760	0.517	1.28	0.680	0.99	67	0.63	10
4	0.5	2.07	5.715	3.190	0.489	1.44	0.340	1.06	75	1.09	15
5	0.5	2.00	5.715	3.190	0.495	1.56	0.380	0.97	72	1.05	14
6	0.5	1.88	5.715	3.190	0.502	1.38	0.315	1.03	74.5	1.09	15
7	1.0	2.89	5.715	2.515	0.509	1.35	0.287	0.81	66.5	1.20	14
8	1.0	2.54	5.715	2.515	0.557	1.17	0.262	0.72	63.5	1.14	13
9	1.0	2.67	5.715	2.515	0.490	1.43	0.254	0.93	70.5	1.29	16

Table III Unaged Maraging (VM300) Steel, Stress for Separation of TiC Inclusions

Spec. No.	$(z/R)_i$	$(z/R)_f$	a_i mm	a_f/a_i	$\bar{\varepsilon}^p_f$	z_f/a_i	$\bar{\varepsilon}^p_n$	$Y(\bar{\varepsilon}^p_n)$ ksi	(σ_T/Y)*	σ_{rr} ksi
1	0.10	0.36	3.17	0.516	1.32	0.705	0.844	200	0.34	268
2	0.25	0.62	3.17	0.562	1.15	0.591	0.660	193	0.36	263
3	0.50	0.73	3.17	0.562	1.15	0.678	0.660	193	0.34	258
4	1.00	1.07	3.17	0.580	1.09	0.360	0.532	187	0.48	277

(*) Computed by means of the Bridgman method.

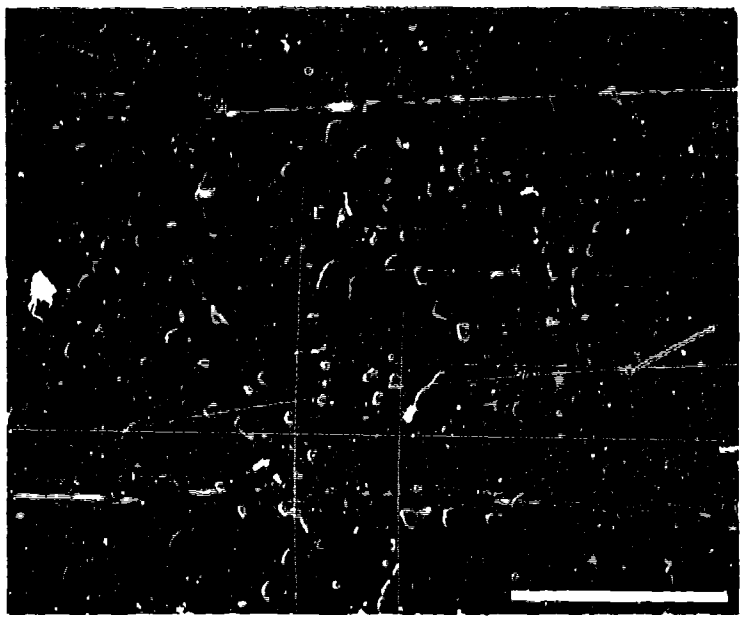

Figure 1 Fe_3C inclusions in spheroidized 1045 steel (bar is 10μ).

Figure 2 Cu-Cr inclusions in a plastically strained sample of Cu-0.6% Cr alloy (bar is 10μ).

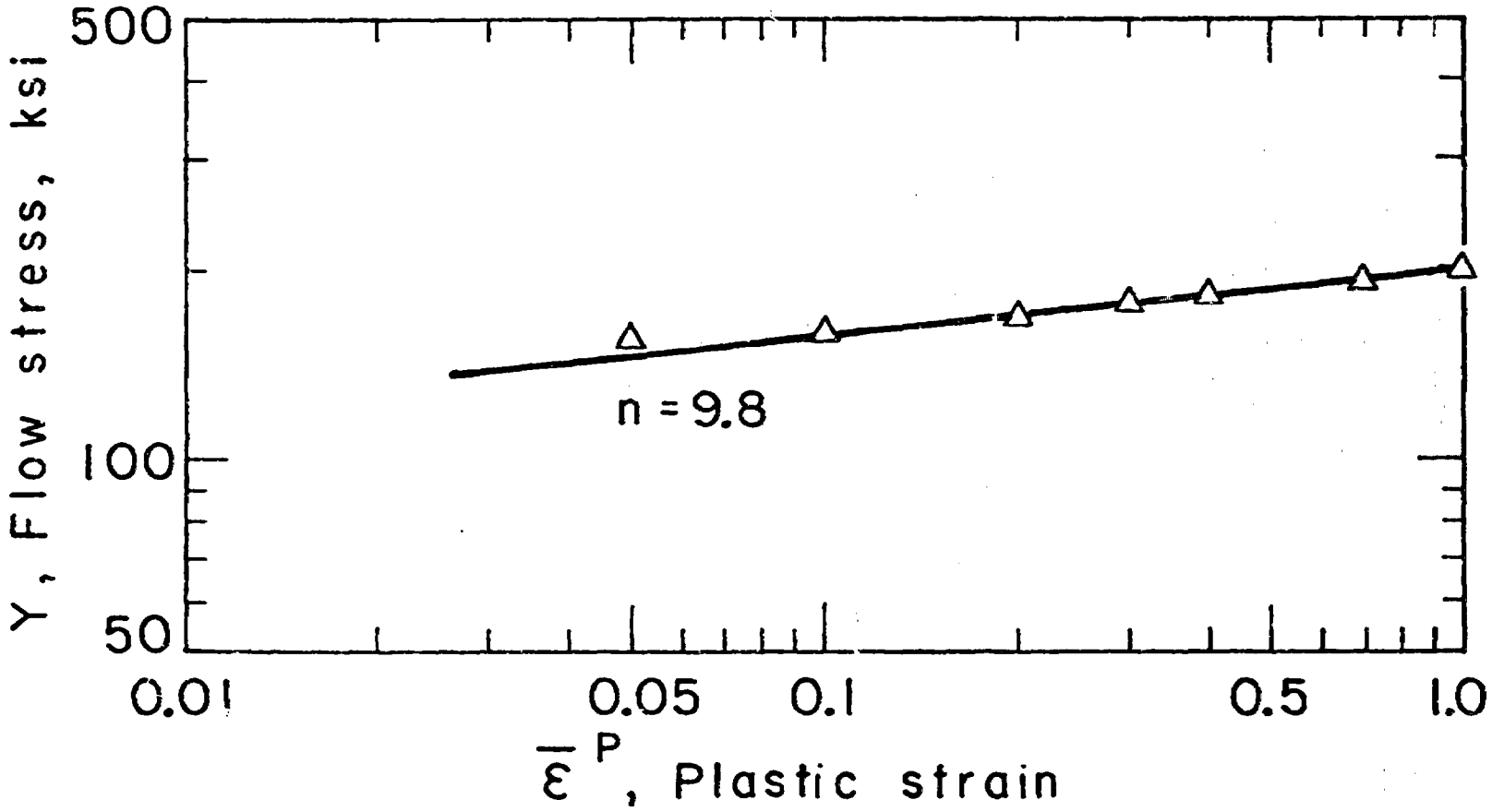

Figure 3 Stress-strain curve of unaged maraging VM300 steel.

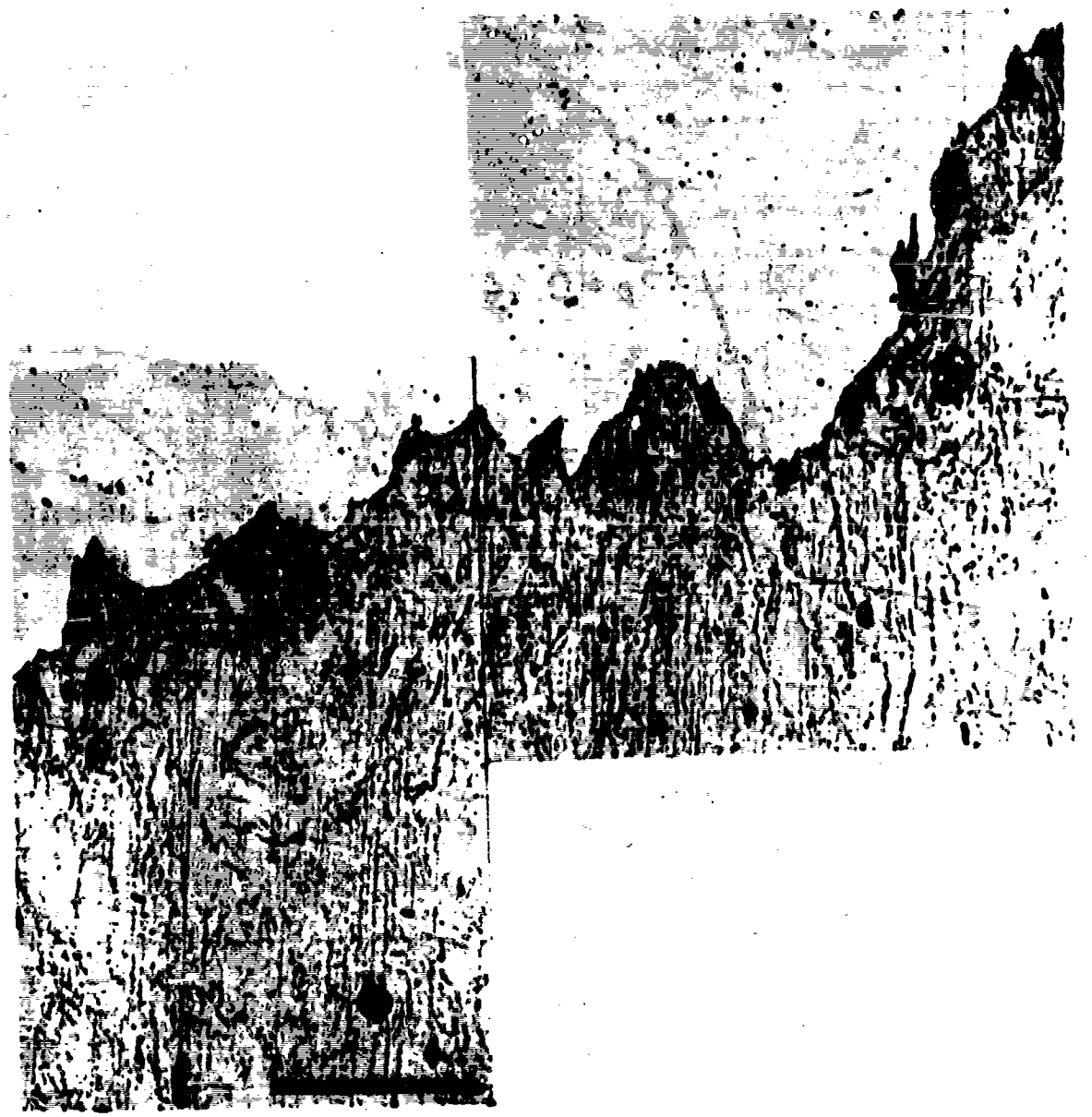

Figure 4 Section of maraging steel showing fracture surface outline and large internal holes from which TiC inclusions have been removed in the course of polishing (bar is 50μ)

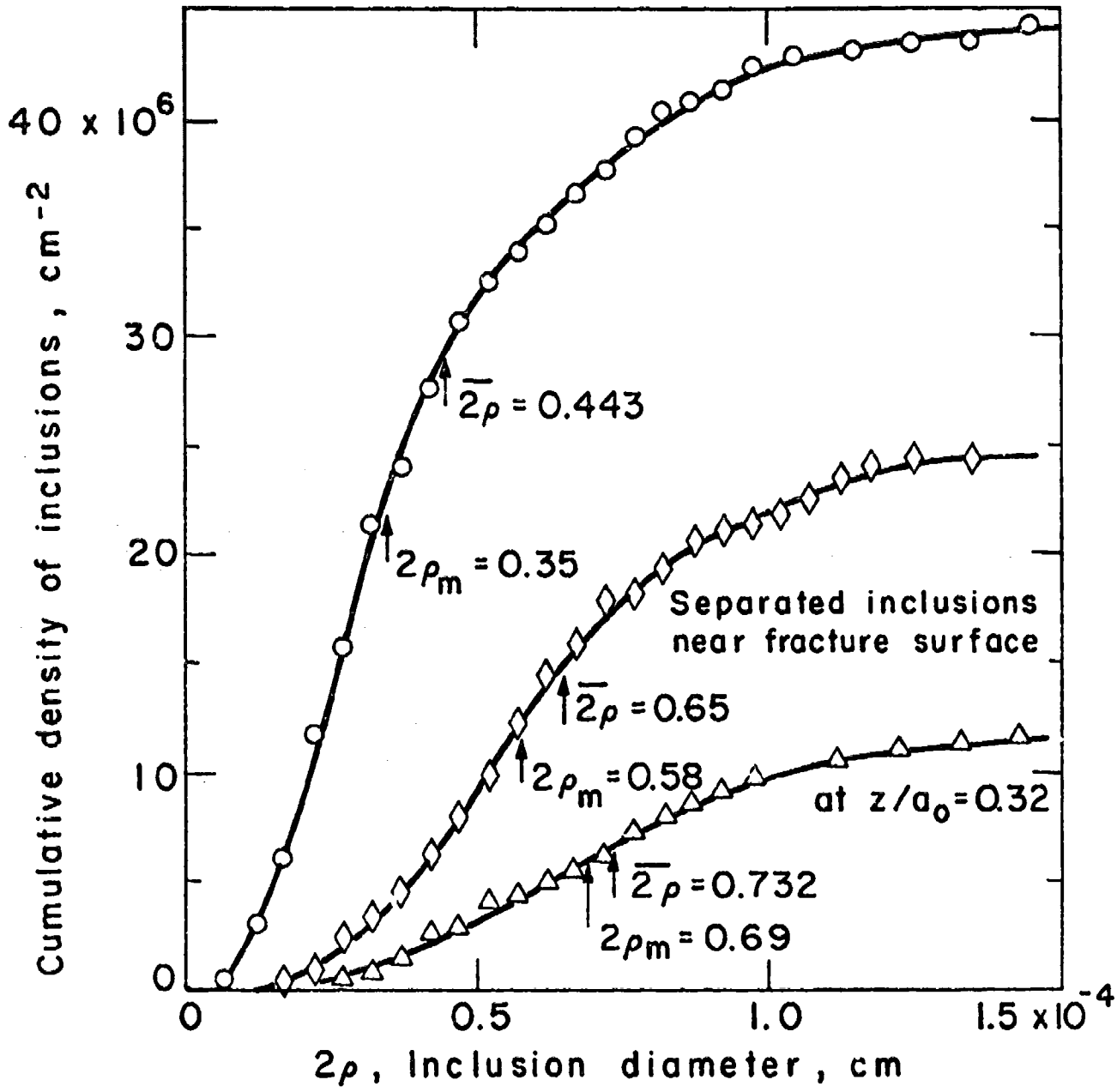

Figure 5 Cumulative density distribution of diameters of Fe_3C inclusions: upper curve, prior to straining; middle curve, separated inclusions underneath fracture surface; lower curve, separated inclusions, a distance $z = 0.32a_o$ away from fracture surface.

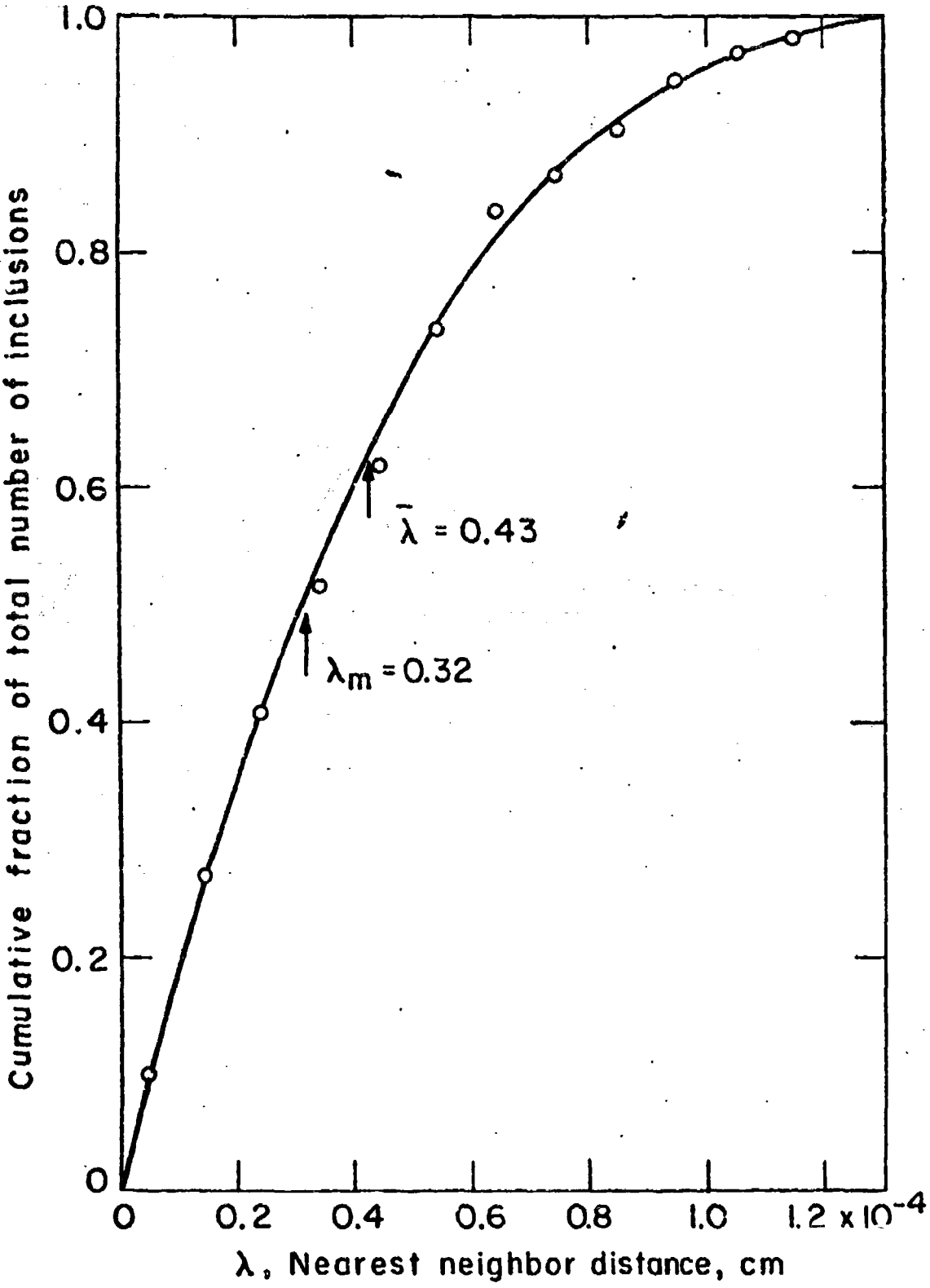

Figure 6 Cumulative distribution of net nearest neighbor distances between Fe_3C inclusions.

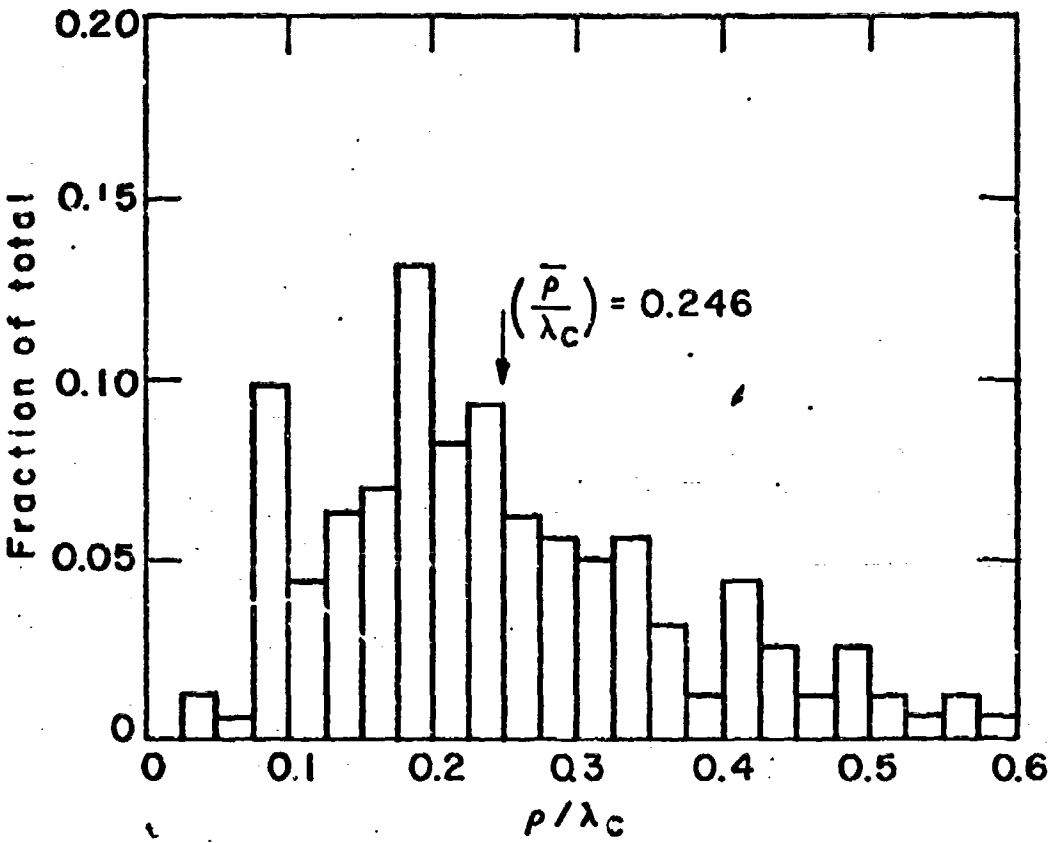

Figure 7 Frequency distribution of the ρ/λ_c ratio of Fe_3C

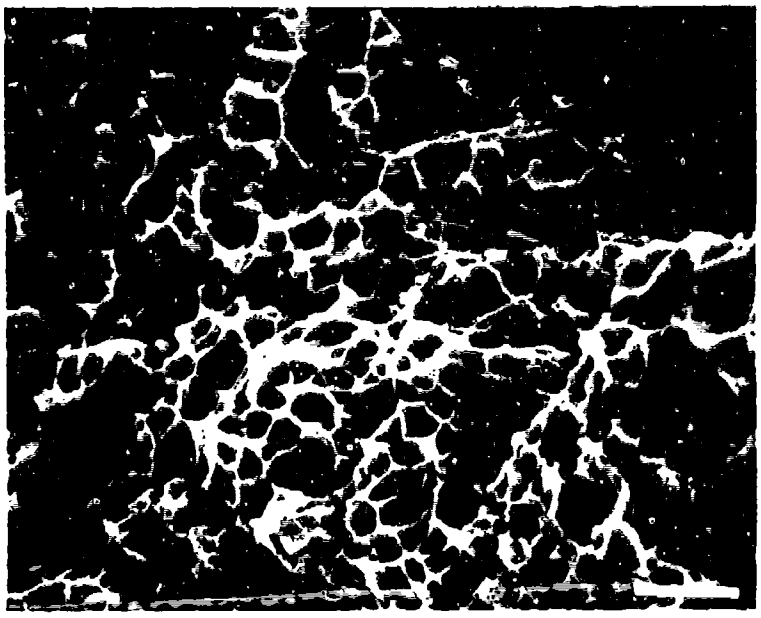

Figure 8 a) Fe_3C inclusions and holes on axial section of fractured specimen; b) fracture surface dimples (bar is 5μ).

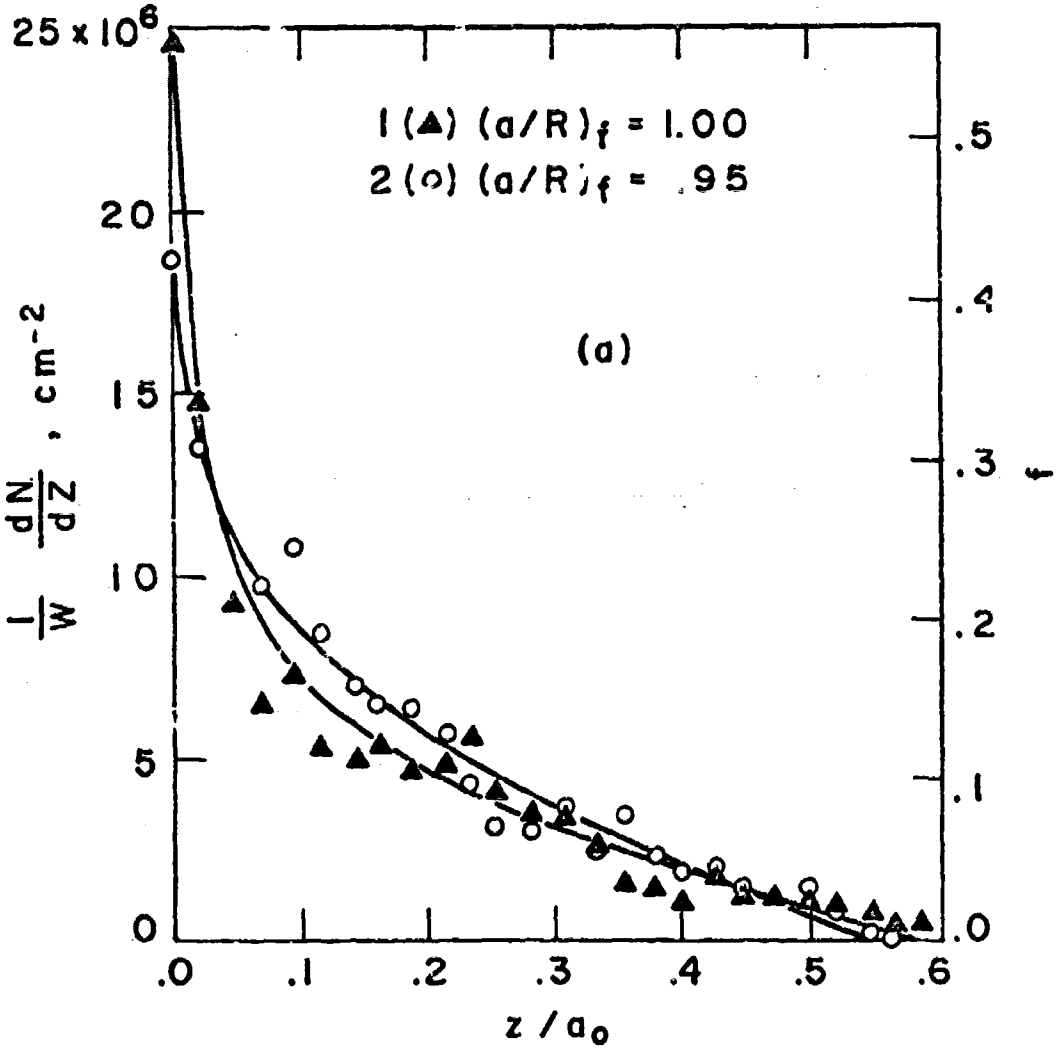

Figure 9a

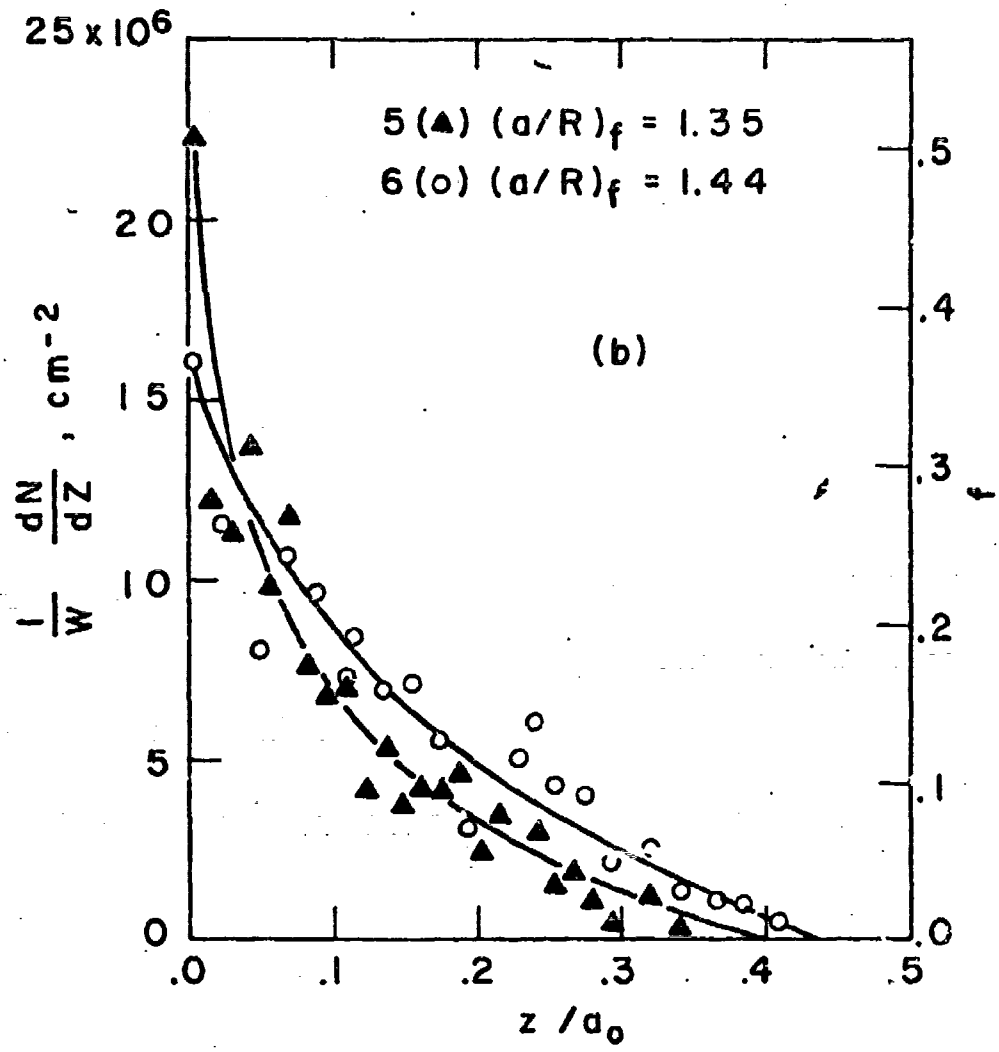

Figure 9b

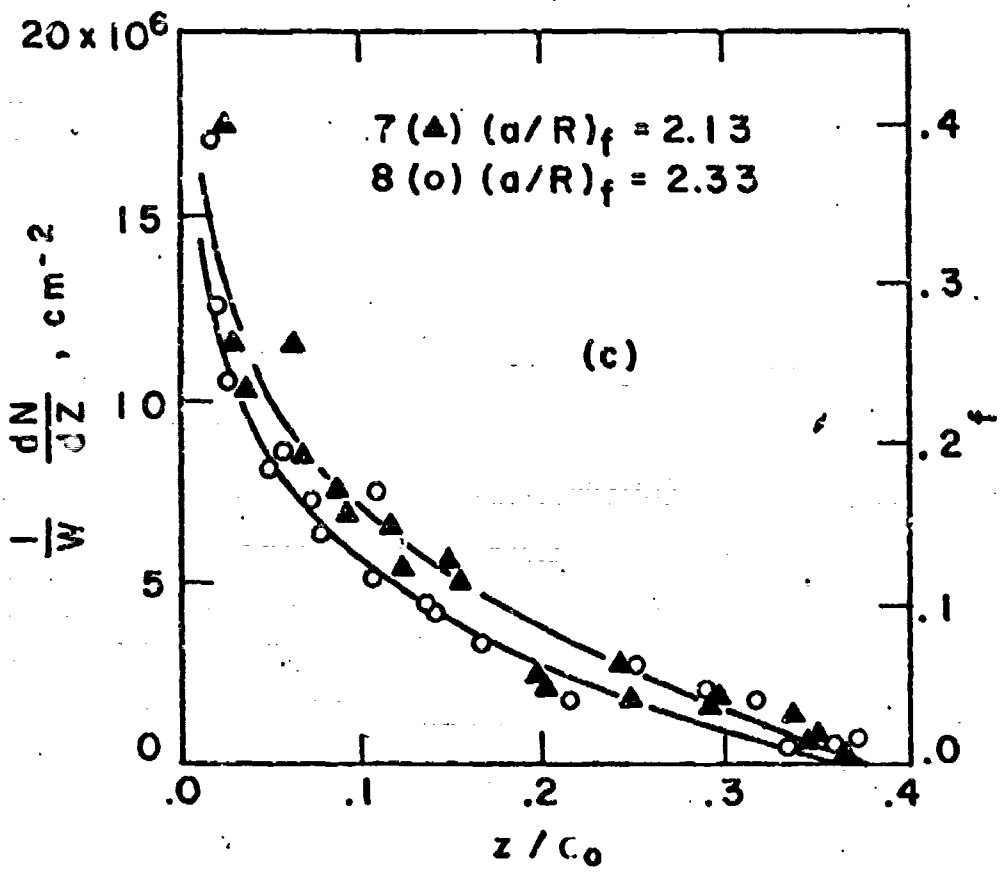

Figure 9 Density of separated Fe_3C inclusions, and fraction of inclusions separated along axes of spheroidized steel specimens: a) $\underline{(a/R)}_i = 0$; b) $\underline{(a/R)}_i = 0.5$; c) $\underline{(a/R)}_i = 1.0$.

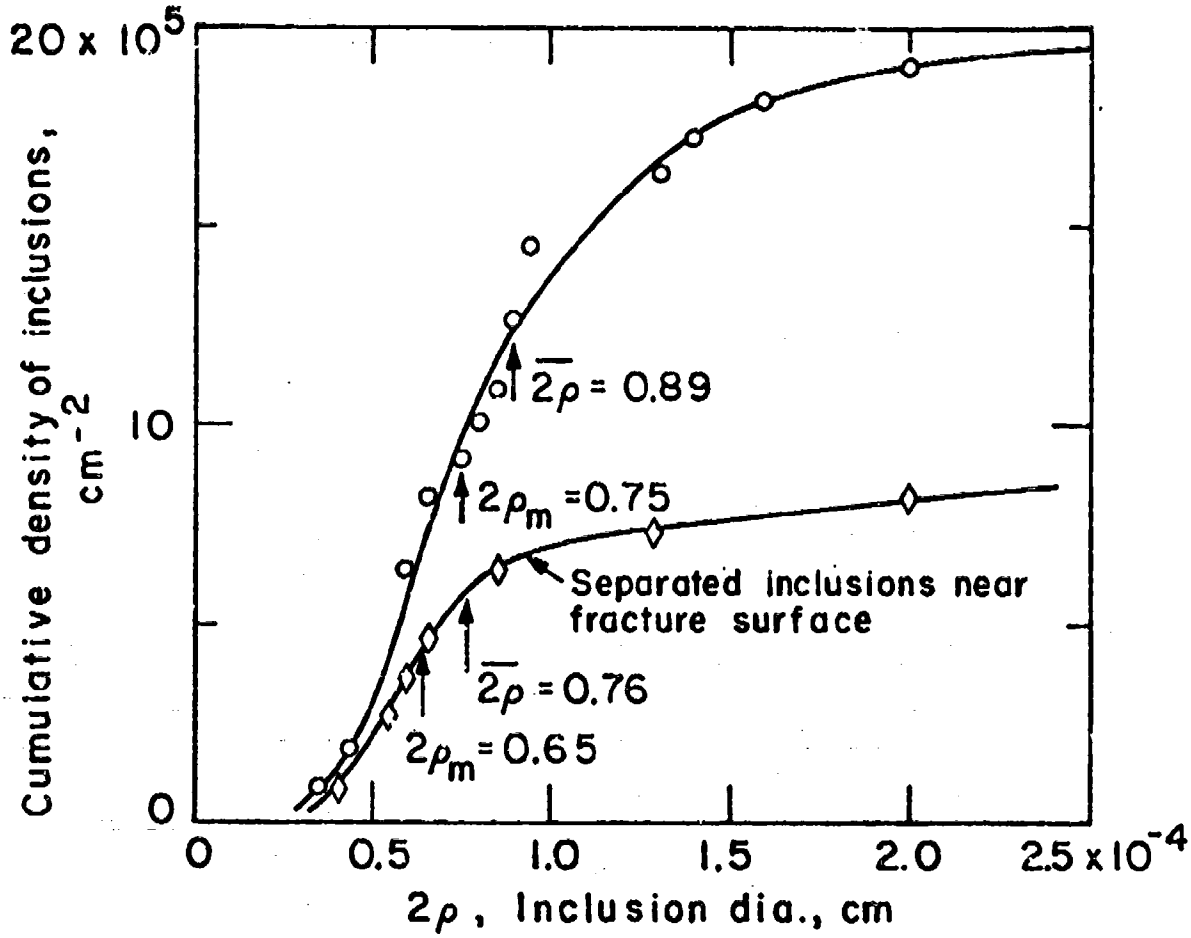

Figure 10 Cumulative density distribution of diameters of Cu-Cr inclusions in Cu-0.6% Cr alloy: upper curve, prior to straining; lower curve separated inclusions underneath fracture surface.

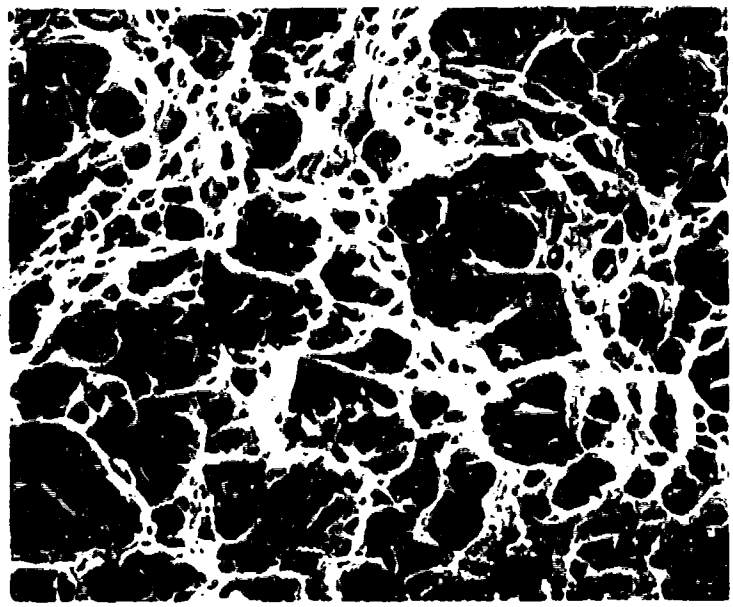

Figure 11 Dimples on fracture surface of copper with Cu-Cr inclusions (bar is 10μ).

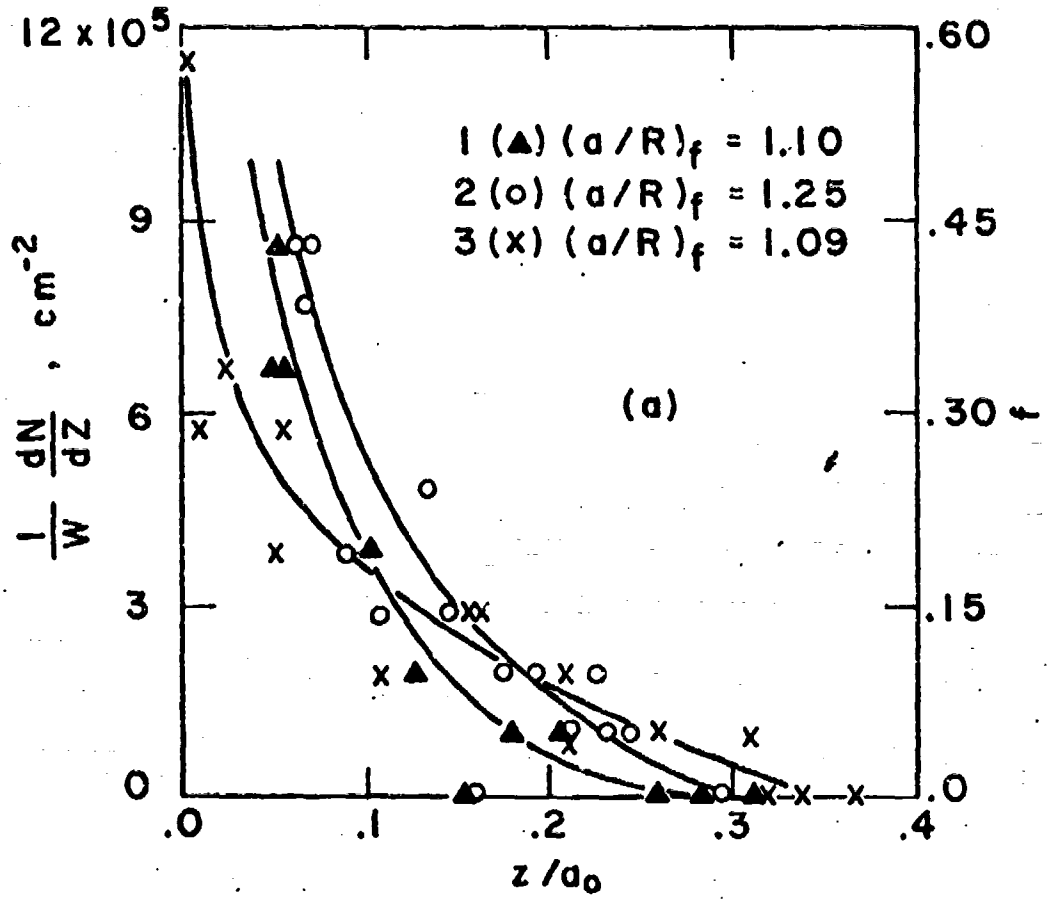
12 x 10^5
9
6
3
0
.60
.45
.30
.15
.0
.0
.1
.2
.3
.4
z /a_o
1/W dN/dZ , cm^-2
1 (▲) (a/R)_f = 1.10
2 (o) (a/R)_f = 1.25
3 (x) (a/R)_f = 1.09
(a)

Figure 12a

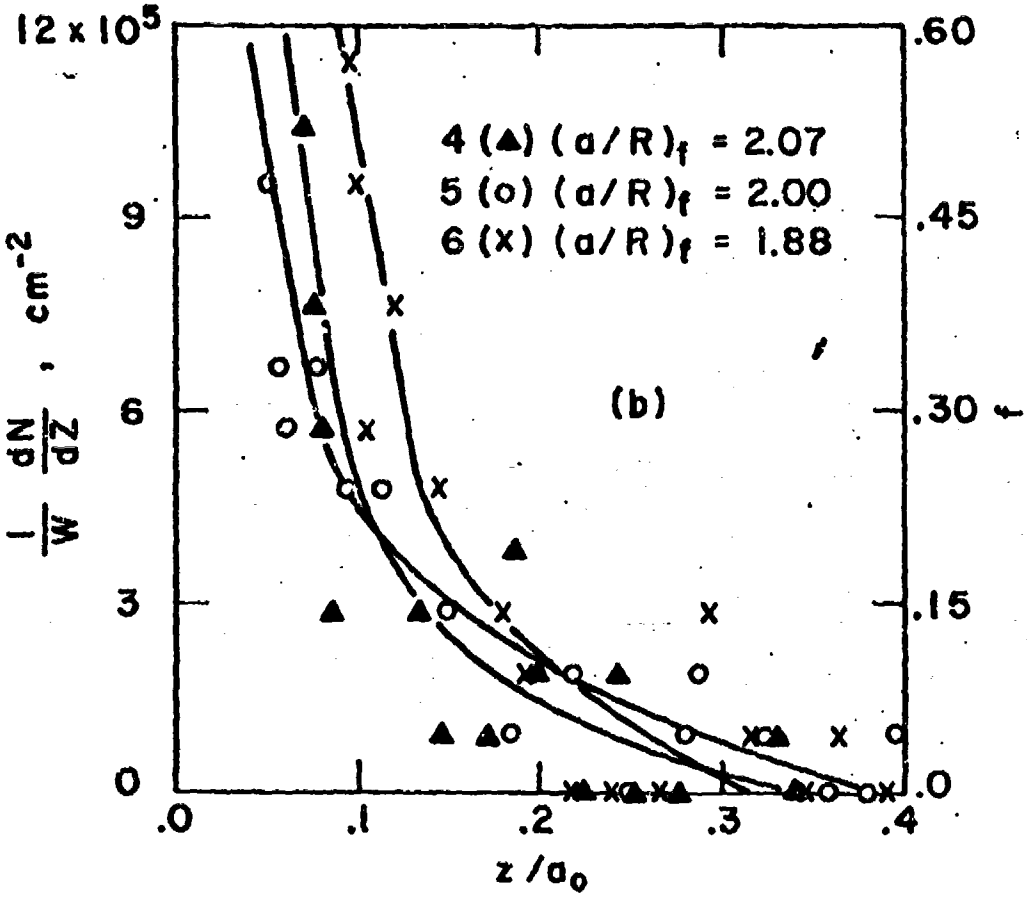
12 x 10^5
9
6
3
0
.60
.45
.30
.15
.0
.0
.1
.2
.3
.4
z / a_0
1/W dN/dZ , cm^-2
4 (▲) (a/R)_f = 2.07
5 (o) (a/R)_f = 2.00
6 (x) (a/R)_f = 1.88
(b)

Figure 12b

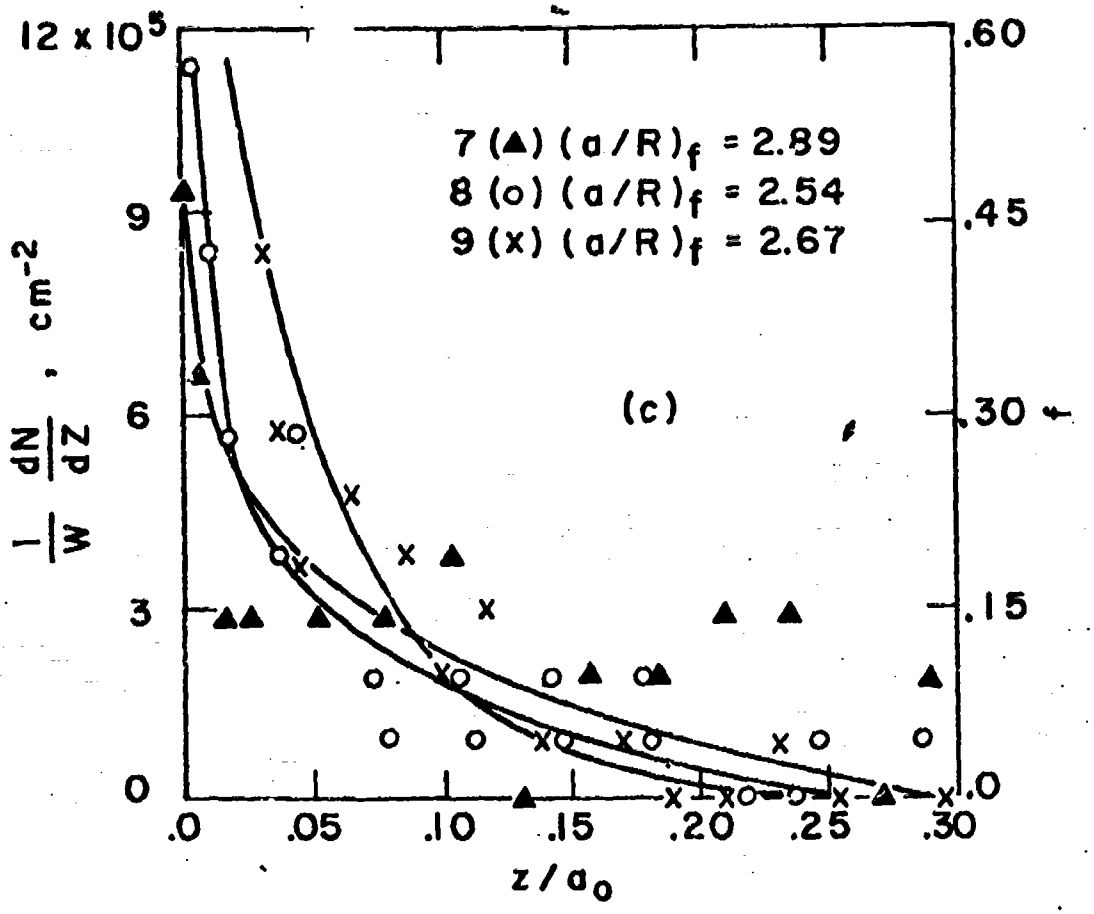

Figure 12 Density of separated Cu-Cr inclusions and fraction of inclusions separated along axes of Cu-0.6% Cr alloy: a) $\underline{(a/R)}_i = 0$; b) $\underline{(a/R)}_i = 0.5$; c) $\underline{(a/R)}_i = 1.0$.

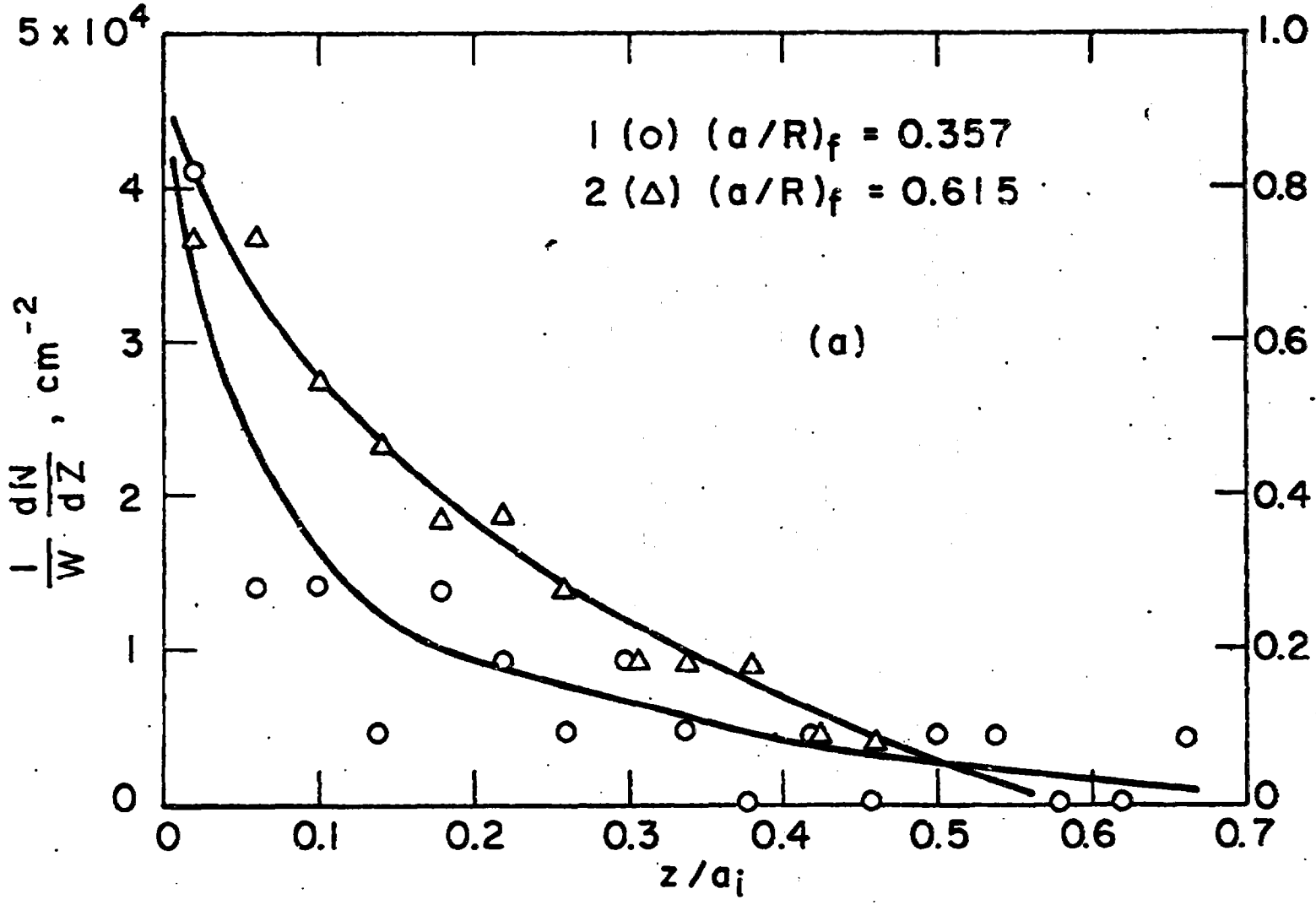
5 x 10^4
4
3
2
1
0
1/W dN/dZ , cm^-2
1.0
0.8
0.6
0.4
0.2
0
f
1 (o) (a/R)f = 0.357
2 (Δ) (a/R)f = 0.615
(a)
0
0.1
0.2
0.3
0.4
0.5
0.6
0.7
z/ai

Figure 13a

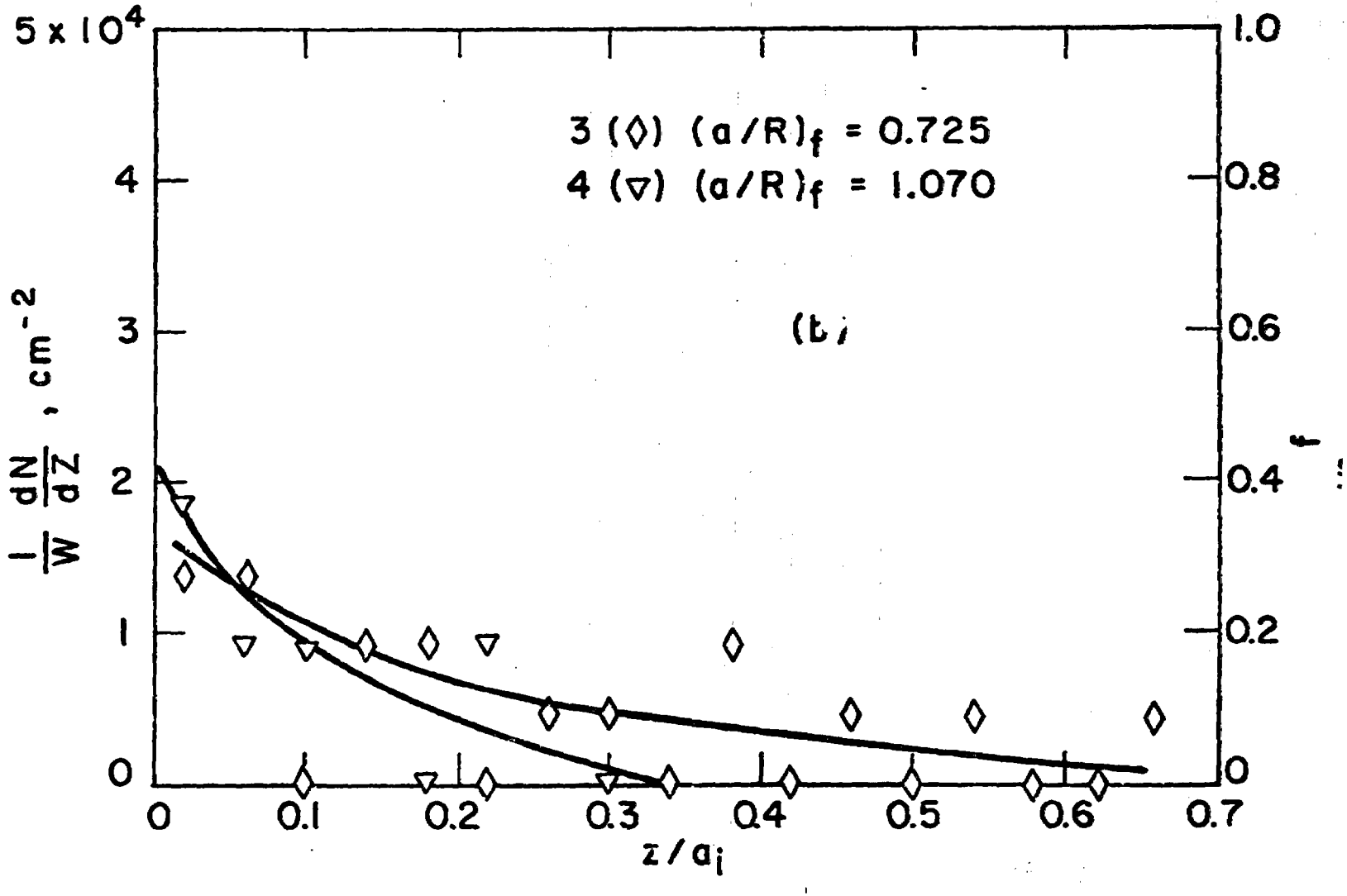

Figure 13 Density of separated TiC inclusions, and fraction of inclusions separated along axes of maraging steel: a) $\underline{(a/R)}_i$ = 0.1 and $\underline{(a/R)}_i$ = 0.25; b) $\underline{(a/R)}_i$ = 0.5 and $\underline{(a/R)}_i$ = 1.0.

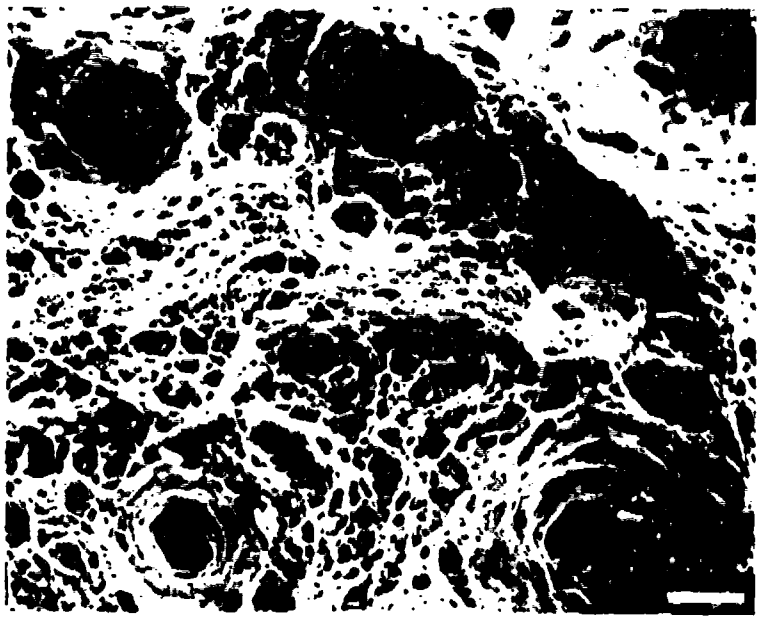

Figure 14 Dimples on fracture surface of maraging steel showing large dimples of TiC inclusions, and small dimples of Ni_3Mo inclusions (bar is 10μ).

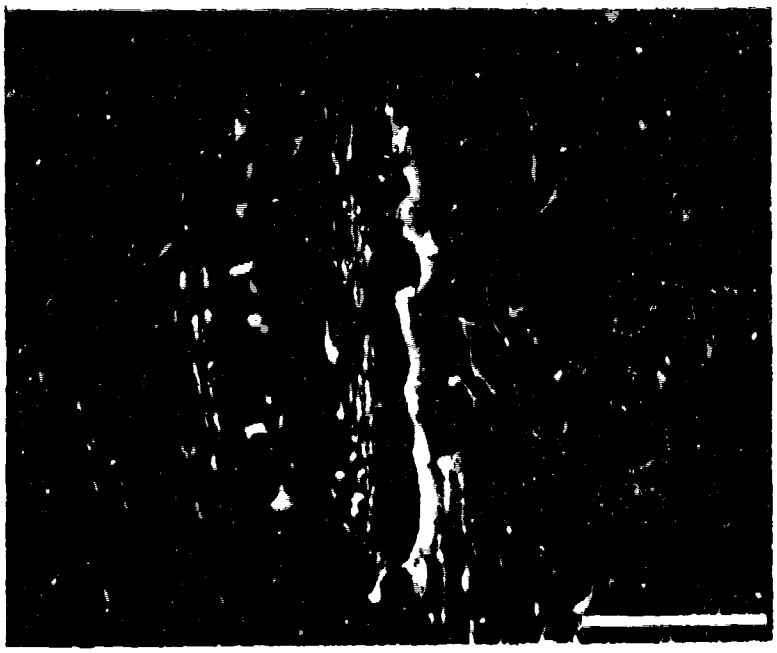

Figure 15 Fe_3C inclusions and holes in specimen strained at 450°C (bar is 5μ)

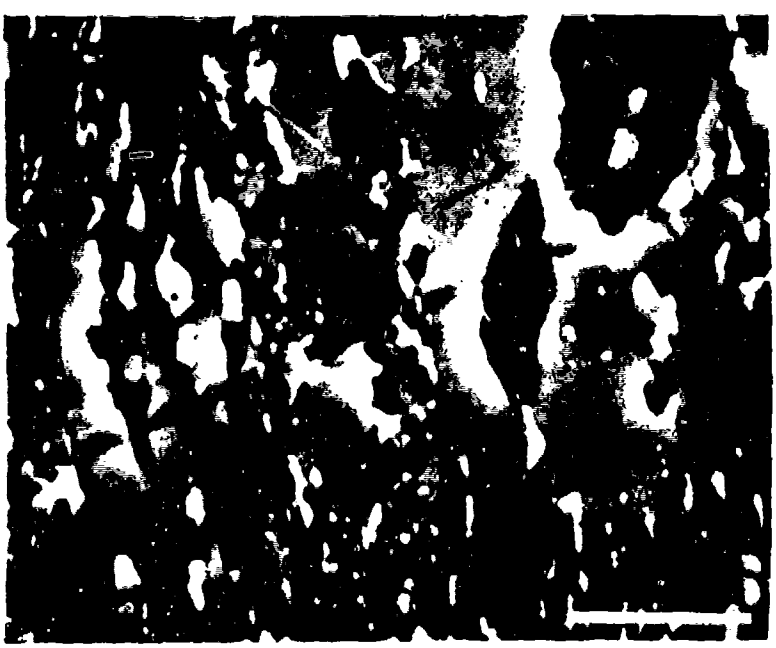

Figure 16 Fe_3C inclusions and holes in specimen strained at 630°C (bar is 5μ)

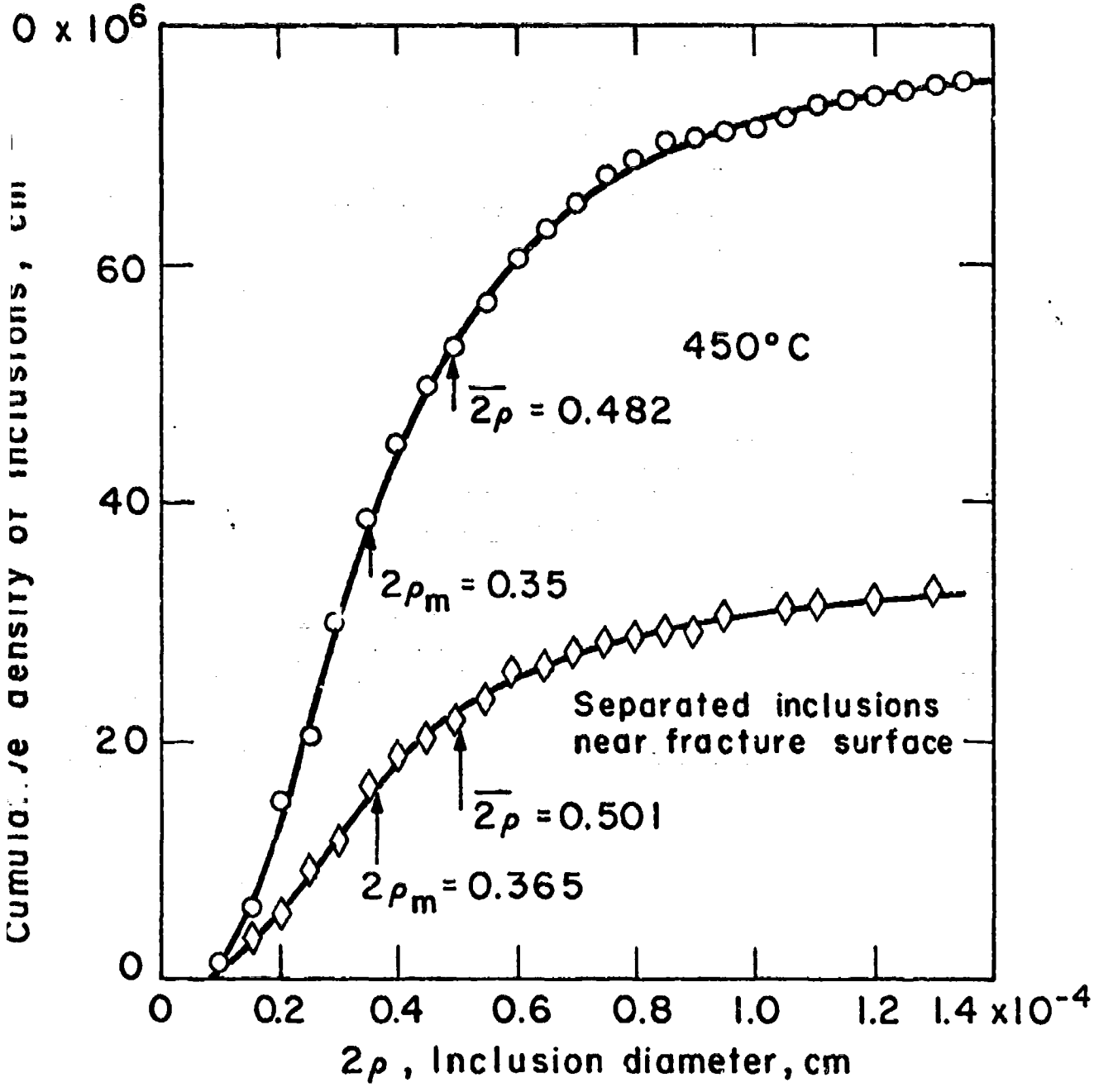

Figure 17 Cumulative density distribution of effective diameters of Fe_3C inclusions in material strained at 450°C: upper curve, prior to straining; lower curve, separated inclusions underneath fracture surface.

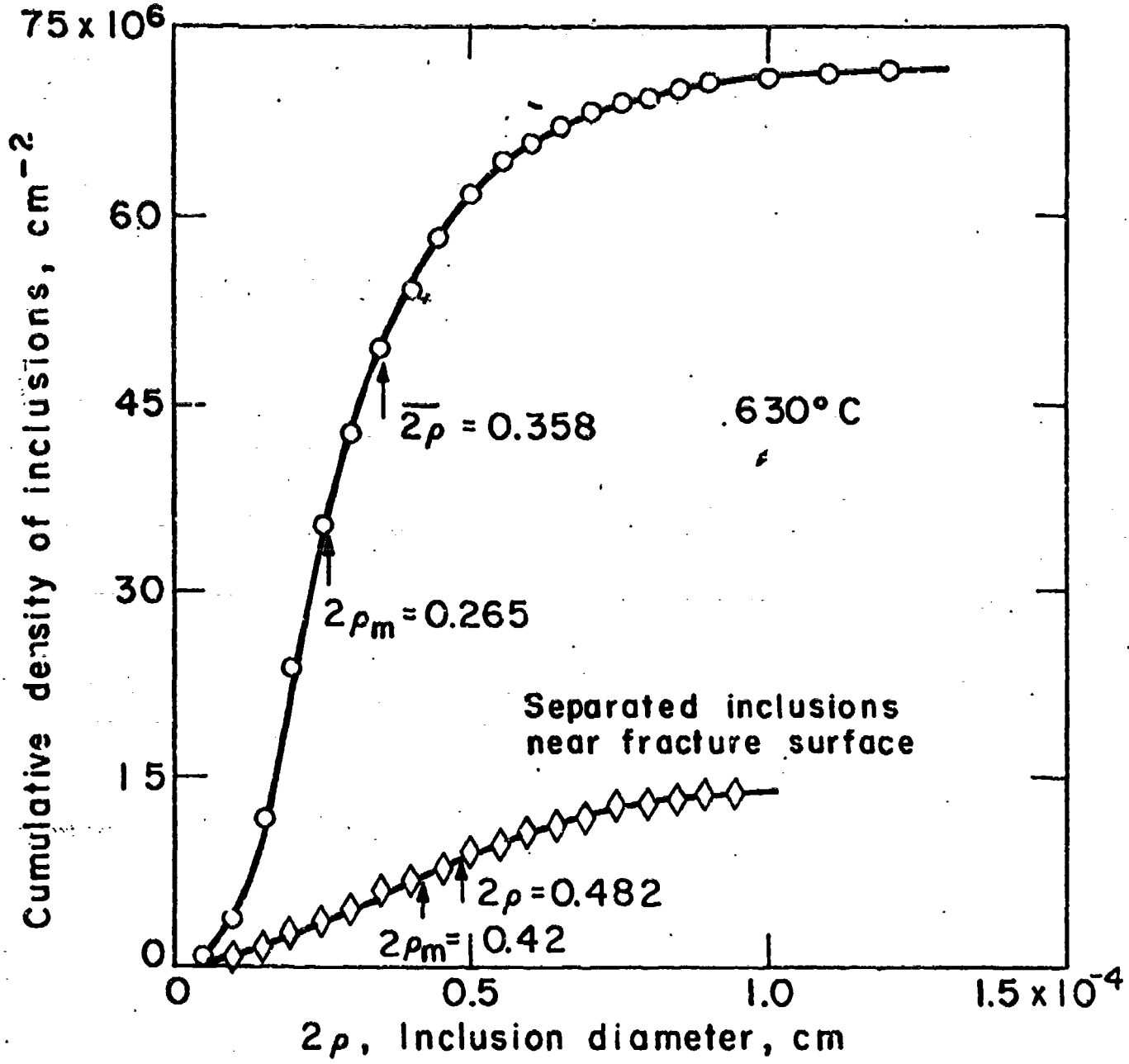

Figure 18 Cumulative density distribution of effective diameters of Fe_3C inclusions in material strained at 630°C: upper curve, prior to straining; lower curve, separated inclusions underneath fracture surface.

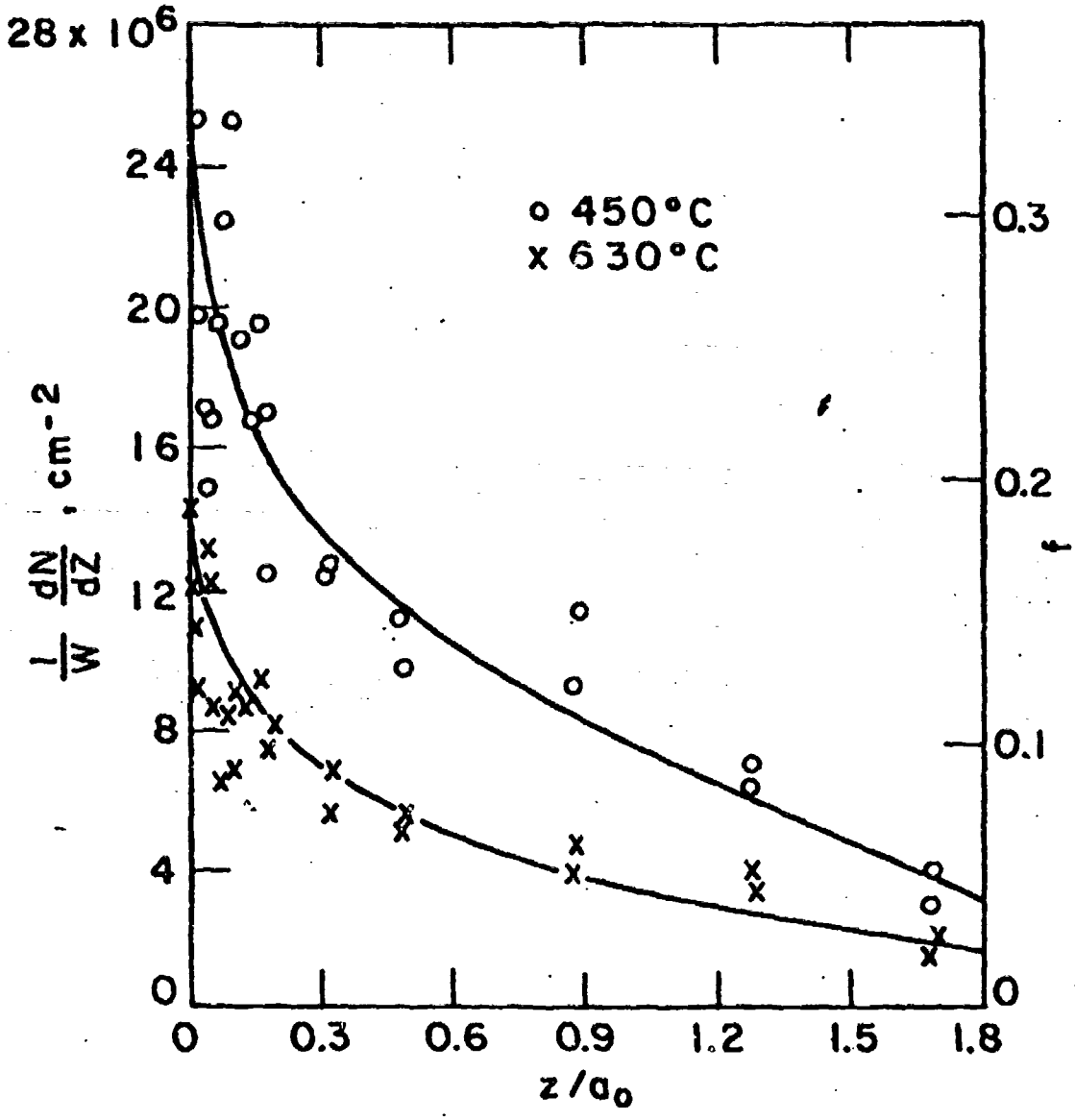

Figure 19 Density of separated Fe_3C inclusions and fraction of inclusions separated along axes of 1045 steel specimens strained at 450°C and 630°C.

Figure 20 Dimples on fracture surface of Fe_3C-bearing 1045 steel, fractured at 450°C (bar is 10μ).

Figure 21 Dimples on fracture surface of Fe_3C-bearing 1045 steel, fractured at 630°C (bar is 10μ).

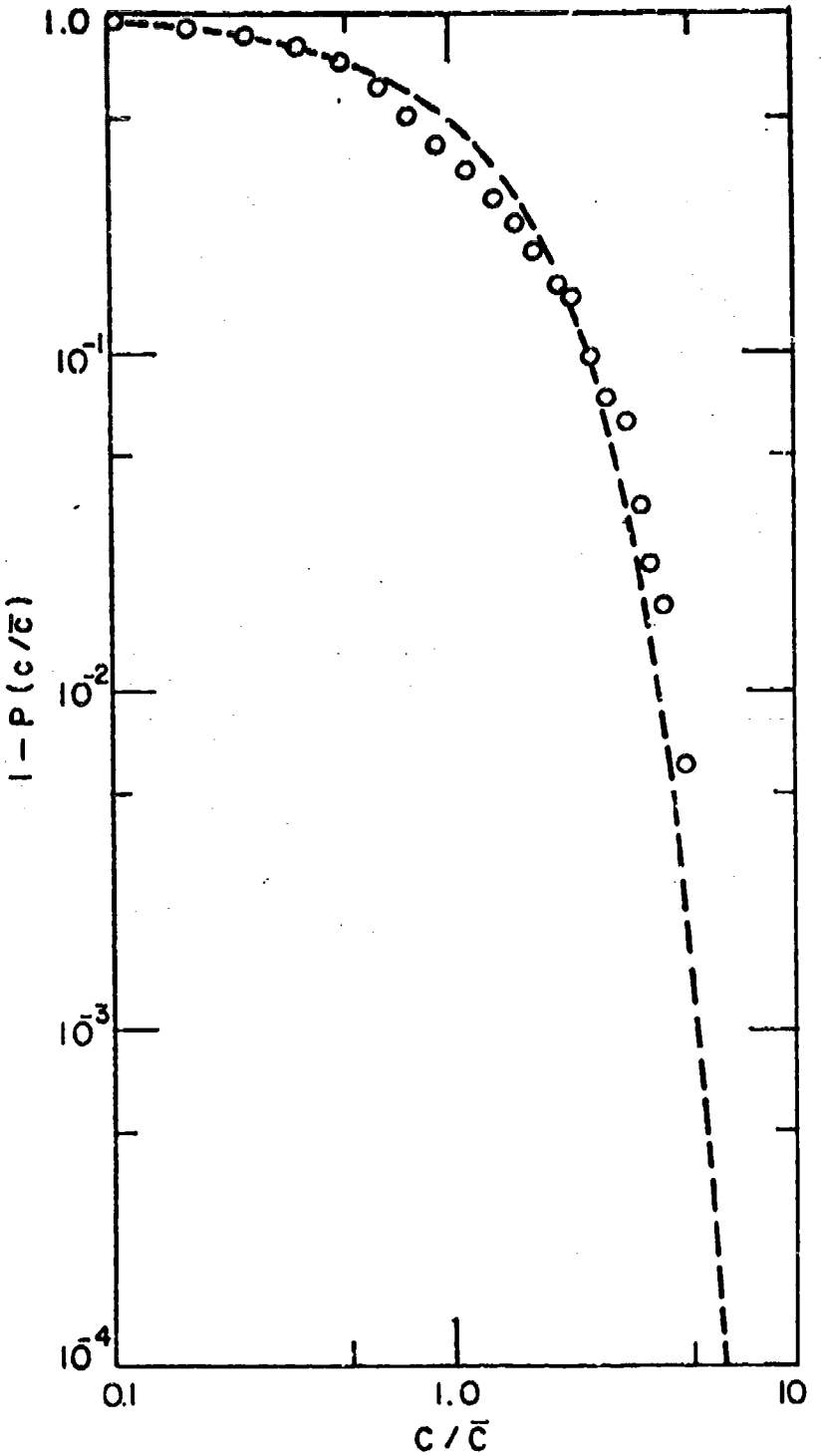

Figure 22 Probability of finding a local concentration of second phase in excess of c in specimen with average concentration $\bar{c}$, as a function of $c/\bar{c}$. Circles are experimental, broken curve from theory of Argon et al[10].

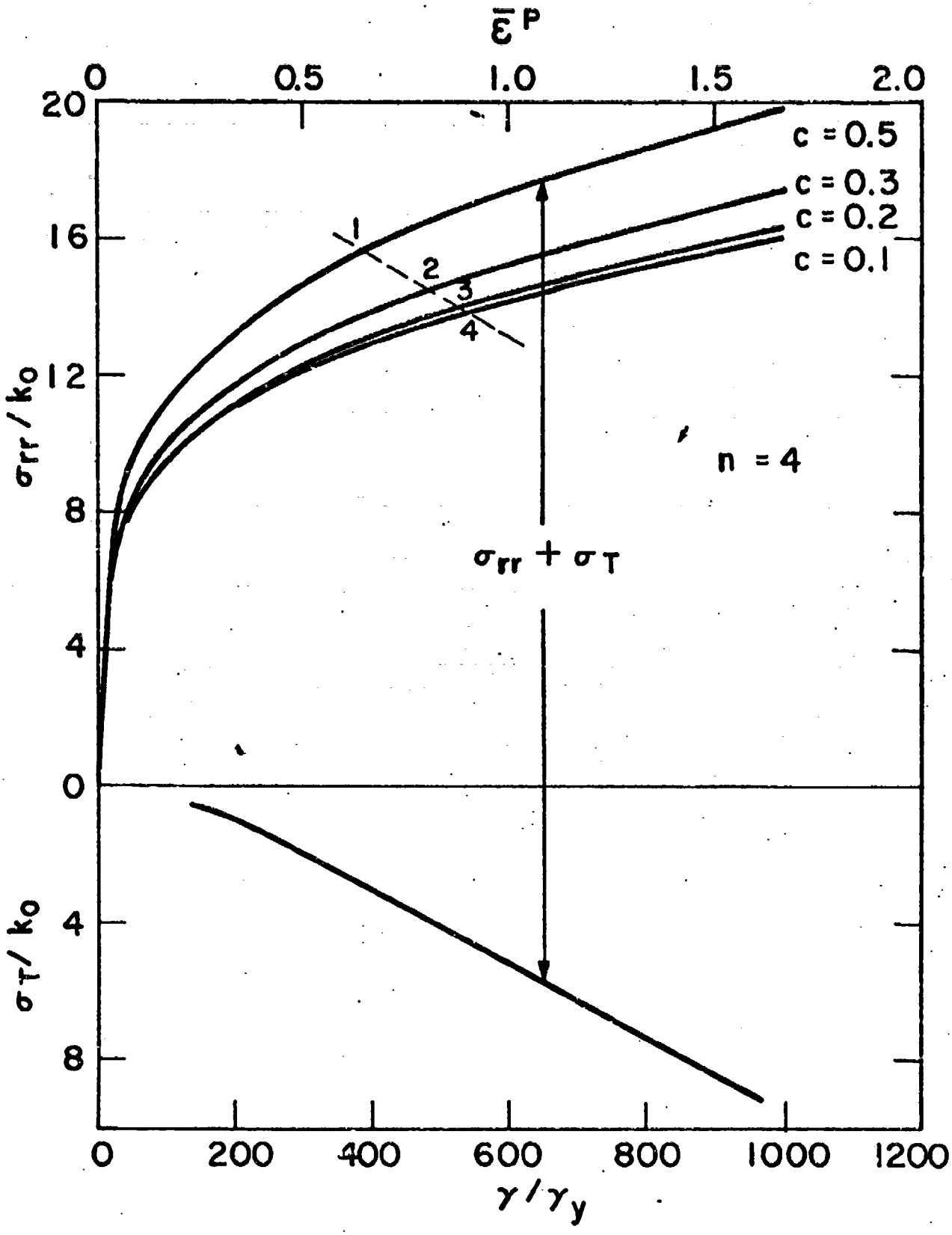

Figure 23 Construction for determination of the distribution of separated Fe_3C inclusions along the axis of a fractured specimen of spheroidized 1045 steel containing a large concentration of interacting inclusions.

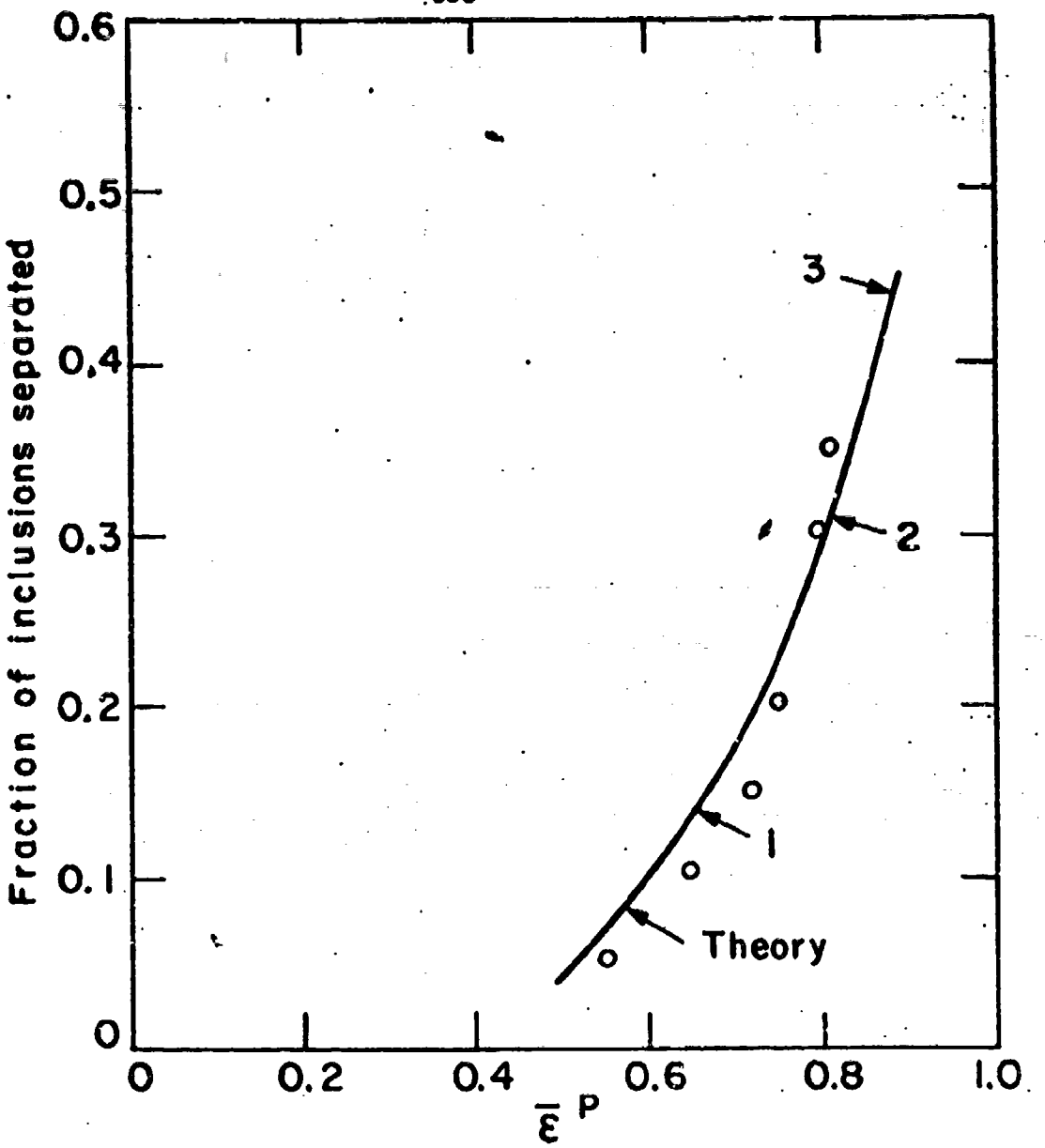

Figure 24 Fraction of separated inclusions as a function of equivalent plastic strain: dots determined from specimens 5 and 6 of 1045 steel, curve obtained from construction given in Fig. 23.